Synthesis and on surface self-assembly properties of π-extended tribenzotriquinacenes

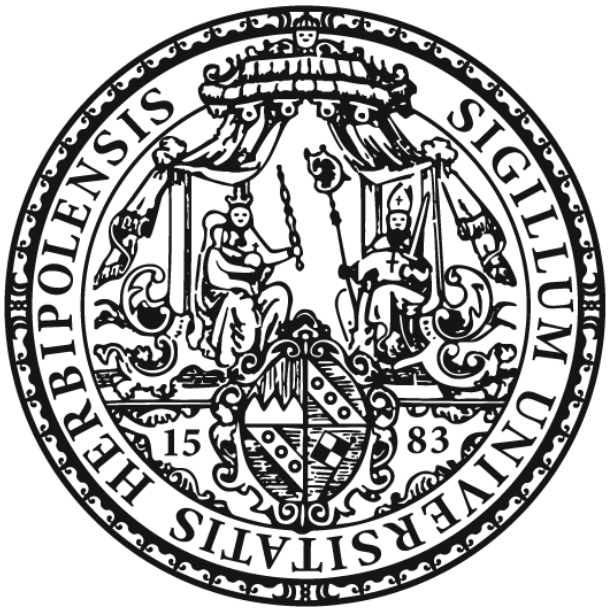

Dissertation zur Erlangung des naturwissenschaftlichen Doktorgrades
der Julius-Maximilians-Universität Würzburg

vorgelegt von
Sinem Toksabay

aus
Izmir, Türkei

Würzburg, 2021

Eingereicht bei der Fakultät für Chemie und Pharmazie am

13.07.2021

Gutachter der schriftlichen Arbeit

1. Gutachter: Prof. Dr. Anke Krüger

2. Gutachter: Priv.-Doz. Dr. Florian Beuerle

Prüfer des öffentlichen Promotionskolloquiums

1. Prüfer: _____

2. Prüfer: _____

3. Prüfer: _____

Datum des öffentlichen Promotionskolloquiums

_____

Doktorurkunde ausgehändigt am

_____

for my precious family

"It was the best of times, it was the worst of times, it was the age of wisdom, it was the age of foolishness, it was the epoch of belief, it was the epoch of incredulity, it was the season of light, it was the season of darkness, it was the spring of hope, it was the winter of despair" ***Charles Dickens, A Tale of Two Cities***

Die vorliegende Arbeit wurde im Zeitraum von Januar 2017 bis Februar 2021 am Institut für Organische Chemie der Julius-Maximilians-Universität Würzburg angefertigt

Weitere Veröffentlichung:

M. Vogt, R. Buschmann, S. Toksabay, M. Schmitt, M. Schwab, M. Bode, A. Krueger, „Self-Assembly and Electronic Structure of Tribenzotriquinacenes on Ag (111), *J. Phys. Chem. C* **2019**, *123*, 5469–5478."

Acknowledgements

First and foremost, I want to express my gratitude to Prof. Anke Krüger, my supervisor, for allowing me to complete this research in her group. Her scientific knowledge, advice, and enthusiasm were invaluable. I'd like to express my appreciation to her for always assisting, understanding, finding solutions, and most importantly, listening to me whenever I needed it. Thank you very much.

Prof. Matthias Bode deserves special recognition for providing me with the opportunity to learn a new instrument and for enabling me to complete an outstanding study. Apart from him, I'd like to express my gratitude to Markus Leisegang, Andreas Christ, and Patrick Härtl for their invaluable assistance in teaching and explaining STM to me and patiently answering all of my questions. Without your assistance and interesting and informative discussions, this study would not be completed. Dr. Jing Qi and Paula Weber receive my special thanks for continuing the research.

I would also like to express my sincere gratitude to the employees of the Organic Chemistry institute: I am indebted to Dr. Matthias Grüne, and Patricia Altenberger for advice when measuring and interpreting NMR spectra, as well as Juliane Adelman for mass measurements. I would especially like to thank Liselotte Michels and Sabine Timmroth for the elemental analysis measurements, Michael Ramold and Markus Braun for their help with repairs and the steady dry ice supply, Bernd Brunner for his help with IT issues and everyone at the chemical store.

I'm grateful to the DFG GRKs 2112 for their financial support, as well as the members for the stimulating discussions and new perspectives on my work. For the x-ray crystal structure determination, I would like to thank Johannes Krebs and Prof. Todd Marder.

I had the pleasure of supervising Fabian Pascher, Jessica Rühe and Julian Herbert.

The members of the Krüger group deserve a special mention, for the enjoyable working environment and their intellectual and emotional support. It was fun to share one of the most challenging part our life together. Thank you, Dr. Adam Day, for reading, correction, and the fruitful discussions. From each person in the group, I was able to learn something new, so thanks to Dr. Rachel Buschmann, Dr. Stefan Wachtler, Christian Bauer, Johannes Ackermann, Sebastian Vettermann. Tobias Neff, and Max Kirchner. My warm gratitude goes to Lena Roos for being a wonderful fume hood companion, the best

"Deutschlehrerin" in the world, for all the valuable discussions and moments, and for her unwavering support. I'm overjoyed that Julia Puck shares my passion for cats. Meow! I'd like to thank Viktor Merz for sharing his "sense of humor" and teaching me some of the most useful words (!) in German literature. I owe a huge debt of gratitude to Dr. Sarah Ranjbar, for her invaluable advice, our sushi and wine dinners and making me feel like I wasn't alone in Würzburg.

I owe Öznur Singin and Fulya Ersoy a debt of gratitude for making me feel that I am home in Germany. Thank you for all of the amusing, enjoyable, and unexpected moments we had on our trips. It's a priceless pleasure to be with you both and to travel with you.

I would like to give my special gratitude to Tuncay Dogan and Tülin Arslan always being there and supporting me whenever I need. Your friendship is very precious to me.

Dr. Sinem Demirci, Isilay Sheridan Gün, and Selcan Sengül deserve special thanks for their unwavering support, sisterhood, and demonstration that distance does not matter in our friendship. The last eighteen years would have been meaningless without them.

I'd like to express my heartfelt gratitude to Fazilet Gürer. It would have been impossible to get through this difficult journey without her friendship and support. Our friendship means a lot to me. Thank you for everything!

Lastly, I am grateful to my parents, Serdar and Suzan, as well as my brother Sinan and sister-in-law Türkan, and our lovely cat Minnos, without whom I would not be where I am today. Thank you for always believing in me and loving me. I believe I am incapable of fully expressing my emotions, but I am the luckiest person ever to have you all!

Table of Contents

CHAPTER 1

1.1 Introduction

1.1.1 Graphene

Graphene is a one-atom-thick layer of sp^2 hybridized carbon atoms tightly packed in a honeycomb crystal lattice in two dimensions. Since its discovery in 2004, it has been the subject of intense research. Geim and Novoselov et al. defined a micromechanical division technique for graphite exfoliation based on repetitive peeling of highly ordered pyrolytic graphite (HOPG).[1] Due to its special properties, such as high current density, high theoretical specific surface area, high transparency, high electrical conductivity, superior carrier stability, high thermal conductivity, and power, it was suggested that it can be used as a next-generation electronic material.[2-3]

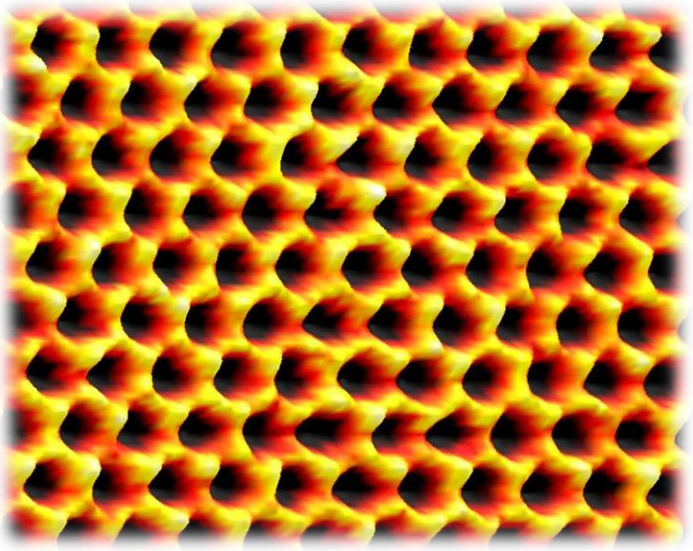

Figure 1. STM image of the graphene sheet.[4]

In addition, graphene shows roughly infinite structural flexibility, the highest tensile strength ever recorded and it has been characterized as a zero bandgap semiconductor.[5] These unique electronic properties generate surprisingly high opacity for an atomic monolayer, with a startlingly low absorption ratio of 2.3% of white light.[6]

Due to its unique properties, it has become highly desirable also to synthesize graphene. Two distinct approaches to graphene synthesis have been developed.[7] The top-down technique, is the exfoliation of bulk graphite includes mechanical cleavage with Scotch tape, direct liquid phase exfoliation of graphite/graphite intercalation compound with ultrasonication, or oxidation of graphite to graphite oxide (GO), followed by reduction process to restore electronic properties (reduced graphene oxide-RGO). (Figure 2). Direct exfoliation methods produce graphene with relatively high crystal quality (high electrical conductivity, less crystal defect), but the production yield is still insufficient for practical application. Organic impurities are common in products and controlling the number of graphene layers is difficult (whereby increasing the number of layers decrease its optical transparency).

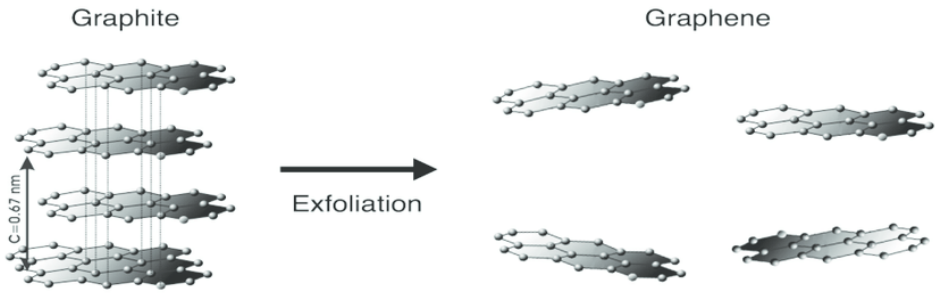

Figure 2. Schematic representation of formation of 2D-structured graphene from 3D-structured graphite by exfoliation.[8]

The alternative strategy, is the bottom-up graphene synthesis, graphene can be grown molecularly from small molecular carbon precursors using Chemical Vapor Deposition (CVD) or epitaxially on a substrate (SiC) using different substrate catalysts and growing parameters to achieve a well-controlled thickness (number of layers).[9-13] Unlike the top-the down techniques, the bottom-up method will tune (opto)electronic and spintronic characteristics with atomic precision.

The electrical and optical properties of graphene are directly affected by its quality. Perfect graphene does not show any bandgap, it hinders the straightforward application of graphene especially in field-effect transistor (FET) devices.[14] The existence of structural disorders such as impurities or defects have a significant impact, i.e. a band gap is developed, bringing a new era for graphene-like molecules in the field of electronic applications. The electronic structure of graphene with defects has been studied in an extensive amount of research.[15-16]

The electronic properties are determined by the overlap of p_z-orbitals, which is altered in the presence of structural defects. For example, bond lengths in strain fields of defects vary from those in the perfect lattice. In addition, defects lead to a local rehybridization of σ and π-orbitals which again changes the electronic structure. A local curvature around defects, due to non-hexagonal rings or adatom complexes created via chemical or physical treatment, influences rehybridization as well. Defects lead to scattering of the electron waves and change the electron trajectories.[15, 17]

1.1.1.1 Defects in Graphene

Perfect graphene comprises of sp^2-hybridized carbons arranged in a two-dimensional (2D) hexagonal lattice. In addition, many types of structural defects eventually occur during graphene fabrication, altering its mechanical, thermal, electrical, and magnetic properties by disrupting the symmetry of the π-electron system.[18-22] In graphene, there are two types of defects: intrinsic defects, which are made up of non-sp^2 orbital hybrid carbon atoms. The most common cause of these defects is non-hexagonal rings surrounded by hexagonal rings. Non-carbon atoms in graphene disrupt the crystalline order.[23] Stone-Wales defects, single vacancy defects, multiple vacancy defects, line defects, and carbon adatoms are the five types of intrinsic defects. All of these are examples called as point defects.

Stone-Wales (SW) defects are formed when a single pair of carbon atoms rotates, forming adjacent pairs of pentagonal and heptagonal rings.[19, 24] One valent bond must be rotated by 90 degrees to produce the Stone-Wales defect SW (55-77). As a result, four old valent bonds between neighbors are broken and formed four new bonds, followed by two seven- and five-membered rings instead of four hexagons of the perfect honeycomb lattice. (**Figure 3**)

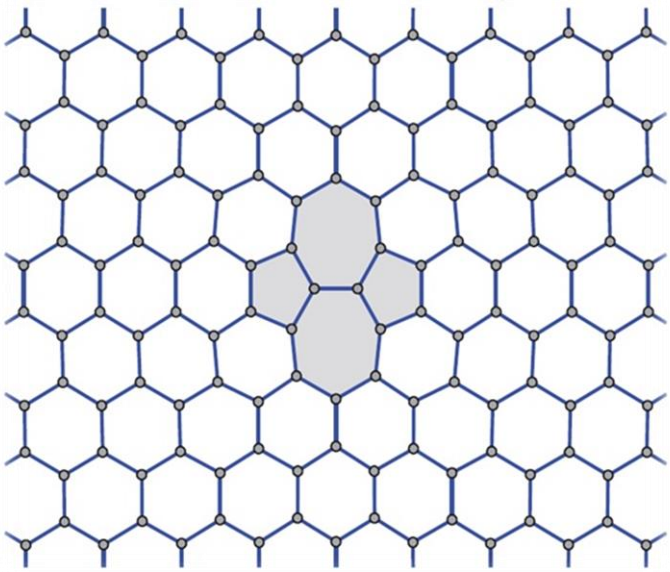

Figure 3. Formation of Stone-Wales (55-77) defect.[25]

In order to create a single vacancy V_1(5-9), one carbon atom is removed from the graphene lattice, breaking three valent bonds. The remaining lattice relaxes with two neighboring atoms linked by a new valent bond, forming a structure (5-9) with one pentagon and one nonagon instead of three hexagons (**Figure 4**). Scanning Tunneling Microscope (STM)[26] and Transmission Electron Microscopy (TEM)[27-28] have been used to observe single vacancies in graphene lattices.

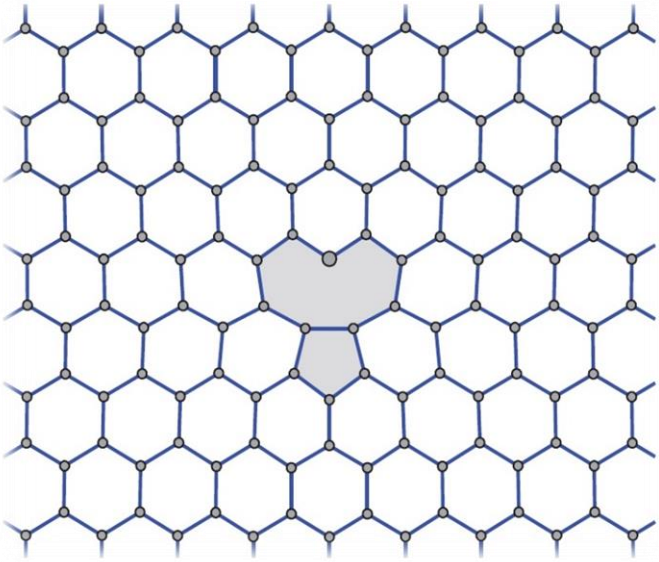

Figure 4. Formation of five and nine-membered rings by a single vacancy, a so-called V_1(5-9) defect.[25]

There are some ways to build double vacancies (DV). The creation of a double vacancy is the result of the removal of two adjacent atoms or by the combination of two single vacancies (SVs). By removing two neighboring carbon atoms and breaking four valent bonds, the double-vacancy defect V_2(5-8-5) shown in **Figure 5** can be created. Following this procedure, the remaining four neighboring carbon atoms form two new valent bonds, and the four hexagons in the lattice structure are replaced by two pentagons and one octagon.

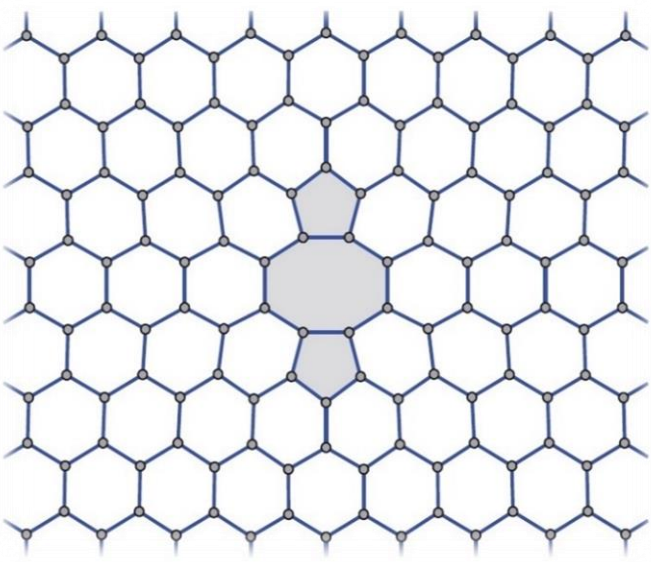

Figure 5. Formation of double vacancies V_2(5-8-5).[25]

The V_2(5-8-5) defect is transformed into a configuration of three pentagons and three heptagons by rotating one of the bonds in the octagon, similarly to the formation of a Stone Wales defect (555-777).

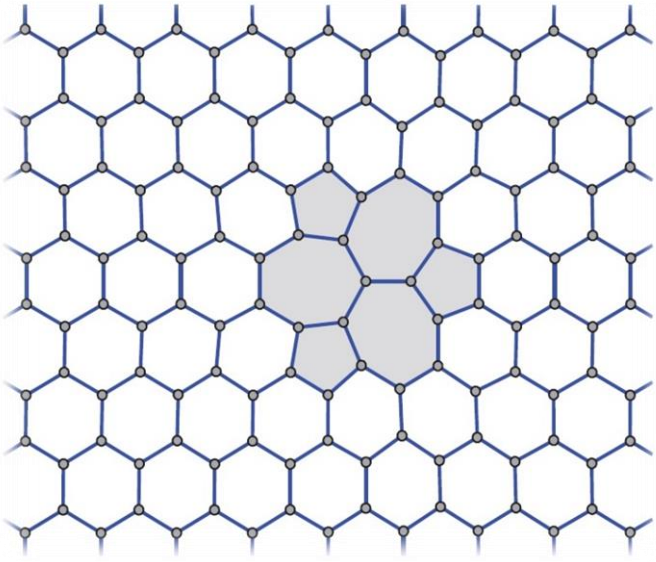

Figure 6. Formation of V_2(555-777) vacancy.[25]

Another bond rotation forms the double-vacancy defect V_2(5555-6-7777) from the defect V_2(555-777). Instead of ten perfect hexagons, the honeycomb lattice produces four pentagons, one hexagon, and four heptagons (**Figure 7**).

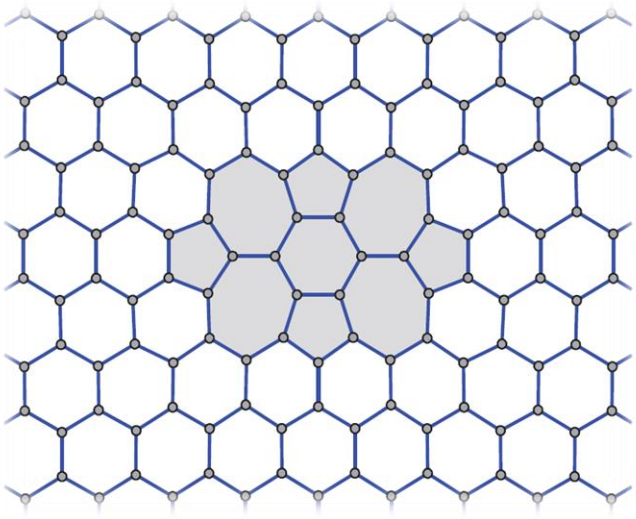

Figure 7. Formation of V_2(5555-6-7777) vacancy.[25]

When four neighboring carbon atoms with Y-shape valent bonds are removed from the graphene lattice, the largest hole appears. Following that, six carbon atoms linked to the removed atom form new valent bonds, resulting in the quadruple vacancy defect V_4(555-9). Instead of six hexagons, this defect produces three heptagons and one large nonagon (**Figure 8**).

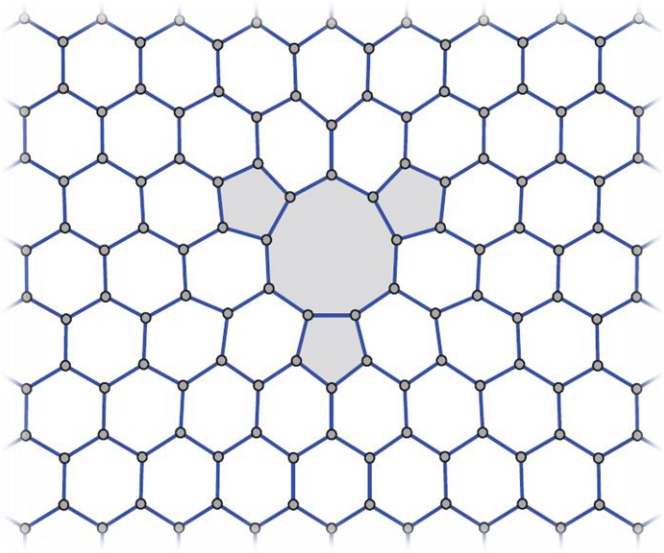

Figure 8. Formation of V_4(555-9) vacancy.[25]

In addition to the point defects described above, graphene can exhibit line defects at grain boundaries.[29-31] These line defects are often made up of non-hexagonal rings including pentagons, heptagons, and octagons, and they have a significant effect on graphene's electronic transport properties. [32]

Defects as Scattering Centres

Point defects, on the other hand, are common during fabrication and degrade the performance of graphene-based devices. In synthetic graphene, point defects are the most common[19, 28, 33-34], and their properties have been extensively studied by experiment.[19, 31, 34-36] For example, electron irradiation of graphene favorably forms zigzag-oriented divacancies and multi-vacancies composed of rotated hexagons, the former exhibiting metallic behavior[31] and the latter opening a bandgap up to 0.2 eV.[34] The imperfection of the hexagonal carbon atom network and the scattering of carriers by localized states determine the transport properties of graphene with point defects. As the defect concentration increases, n-type conduction exhibits almost insulating behavior, whereas p-type conduction exhibits metallic behavior.[37] Furthermore, for specific applications, a thorough understanding of the impact of specific point defects on graphene's electronic and transport properties is required. Lattice defects[38-39] are also likely to be present in graphene synthesized by reduction of graphene oxide[9, 12], chemical vapor deposition[40-41], or carbon segregation on the surface of SiC.[42] Intervalley scattering can also be caused by lattice defects, resulting in constant mobility and insulating temperature dependence of conductivity, both of which are much lower than those of graphene with charge impurities.[43]

Furthermore, reconstructed vacancies in graphene can be exploited to alter the local electrical and magnetic structure of graphene by acting as efficient metal atom trapping centers.[43] The electronic band structure of graphene has been shown to be significantly altered by point defects. They have the potential to induce localized and sharp resonant states at Fermi energy[37] , which act as electron scattering centers and significantly reduce graphene's electrical conductivity.[38, 44] Due to more resonant states in the transport spectrum, the conductance decreases as the defect concentration increases.[34,35]

1.1.1.2 Polycyclic Aromatic Hydrocarbons (PAHs) and Bowl-Shaped Molecules

In recent decades, polycyclic aromatic hydrocarbons (PAHs) have shown exceptional optical and electrical properties. As a result, they have received a great deal of interest in fabricating various organic electronics such as OLEDs, OFETs.[44-47] PAHs with planar structures and wide π-conjugated systems are essential for efficient intermolecular π-orbital overlaps. However, there is a possibility to decrease the chemical stability with

extending π-conjugation of PAHs which would restrict the production of organic electronics. It has also been demonstrated that losing conjugation of PAHs alters the electronic states and is certainly preferable for electrochemical applications. There are several ways to change the planarity of PAHs such as introducing hetero atoms into the π-conjugation system and inserting non-hexagonal rings into the hexagonal lattice.[48] Fused extended π-systems containing additional five-membered rings have to be well distinguished from all six-membered compounds owing to the fact that these structures are typically curved.[49-51] The developments in the field of organic synthesis have resulted in the synthesis of such complex structures that were previously impossible to synthesize. So far, much of the attention has been focused on planar PAHs, however, non-planar PAHs are interesting in their own right due to their unique physical, chemical, and assembling features.[52] After the discovery of fullerenes[53] and carbon nanotubes[54] bowl shaped aromatic molecules (so-called buckybowls), which are architectural fragments/components of fullerenes and carbon nanotubes have been gained great interest. These are considered not only as model compounds and precursors for the production of new materials but also their exceptional properties and potential applications such as host−guest recognition[55-56] chiroptical properties[57] and electronic conductivity are of interest to researchers.[58-59] There are various synthetic approaches starting from either corannulene[60-61] or sumanene[62] to understand the formation of buckybowls.

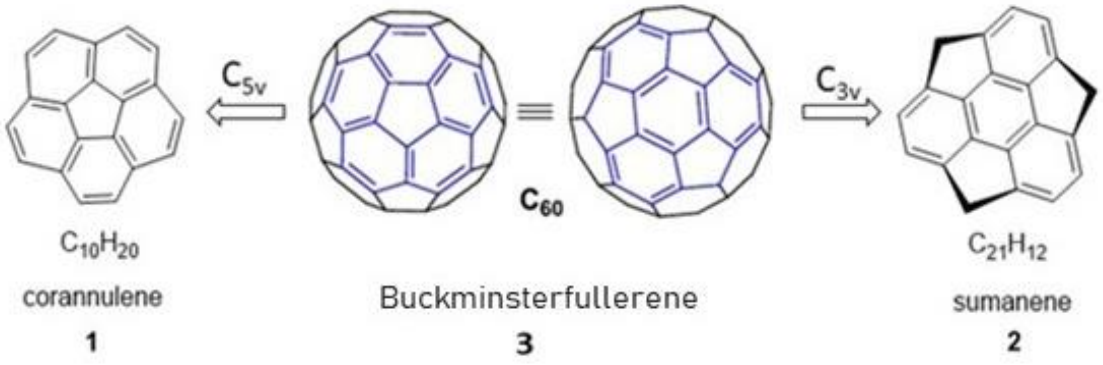

Figure 9. Structures of corannulene (**1**) and sumanene (**2**) as buckminsterfullerene (**3**) fragments.

Both are already bowl-shaped aromatic molecules[63] (**Figure 9**). The development of functional synthetic strategies is a key issue in this area, since buckybowl synthesis is difficult due to the high ring strain energy conveyed by curvature.

In contrast to planar π-conjugated molecules, buckybowls have some unique properties such as π-π interactions, convex/concave surfaces, or bowl to bowl inversion. As mentioned above, the bowl shape is created by the bond angles and the distances between the bonds and thus the distortion of π-conjugation of planar PAHs is a result of the curvature. Besides, the π-orbital overlap is weakened and decreases the π-character in sp^2 carbon compared to that of planar π-conjugated molecules. Significant changes are expected as a result of this character shift, including an increase in electron affinity, a decrease in LUMO level, and liability towards cycloaddition, all of which are typical features of fullerenes.[64]

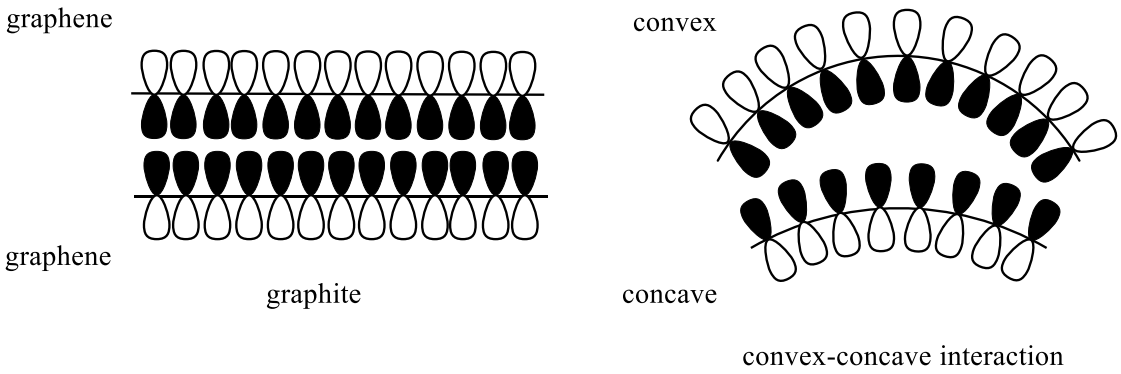

Figure 10. Schematic representation of planar and convex-concave π-π interaction.

Buckybowls have two distinct faces as a consequence of their curvature caused by π-conjugation: concave (endo) and convex (exo). These two faces have distinct properties in terms of electron densities and orbital structures. For example, metal atom coordination bonding mostly favours on the convex surface of the bowl [65-67] in contrast the π-π interactions which are mostly occur on the concave face of buckybowls. Many research have shown that the π-interaction has a significant impact on the photonic and electronic behaviour of organic functional materials.[68-69]

The interconversion of the convex and concave surfaces of open, bowl-shaped structures can be achieved by bowl inversion, which was first observed as a remarkable property of buckybowls during the corannulene synthesis.[70-71] The bowl inversion is depending in the depth of bowl and requires energy to overcome the high energy barrier of the planar transition state. The bowl inversion of corannulene and sumanene have been studied both theoretically and experimentally.[72] Because of their substituent effect on the peripheral aromatic ring, corannulene derivatives lower the bowl inversion barrier compared to its derivatives.

1.1.1.3 Nanographenes (NGRs)

Polycyclic aromatic hydrocarbon is a common name given to those aromatic hydrocarbons, which consist of more than two unsubstituted fused benzene rings. According to IUPAC rules, nanographene can be considered as a graphene fragment ranging from 1-100 nm in size the term graphene molecule is accepted for large PAHs having sizes of 1-5 nm.

As mentioned in previous section **0**, the bottom-up methods for graphene synthesis were introduced through the versatile organic chemistry of PAHs. The Scholl reaction is a straightforward method for the synthesis of graphene molecules by extending the size of PAHs. It involves a polyphenylene precursor with a topology that helps cyclodehydrogenation to completely flatten benzene rings into the PAH plane. The synthesis of hexa-*peri*-hexabenzocronene (HBC) from hexaphenylbenzene is the most significant example and considered as one of the smallest graphene molecule with a disc diameter of approximately 1.4 nm.[73]

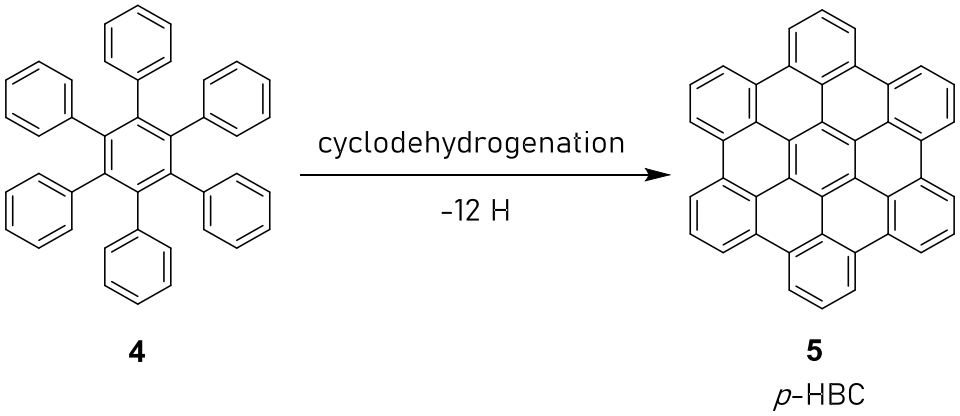

Figure 11. Synthesis of hexa-peri-benzocronen (p-HBC) through intramolecular cyclodehydrogenation.[73]

Interestingly, supernaphtalene and other higher analogues of HBC with different symmetries, such as $C_{72}H_{26}$ 6, $C_{96}H_{30}$ **7**, and $C_{138}H_{42}$ **8** were synthesized from starting from suitable polyphenylene precursors.[74-75]

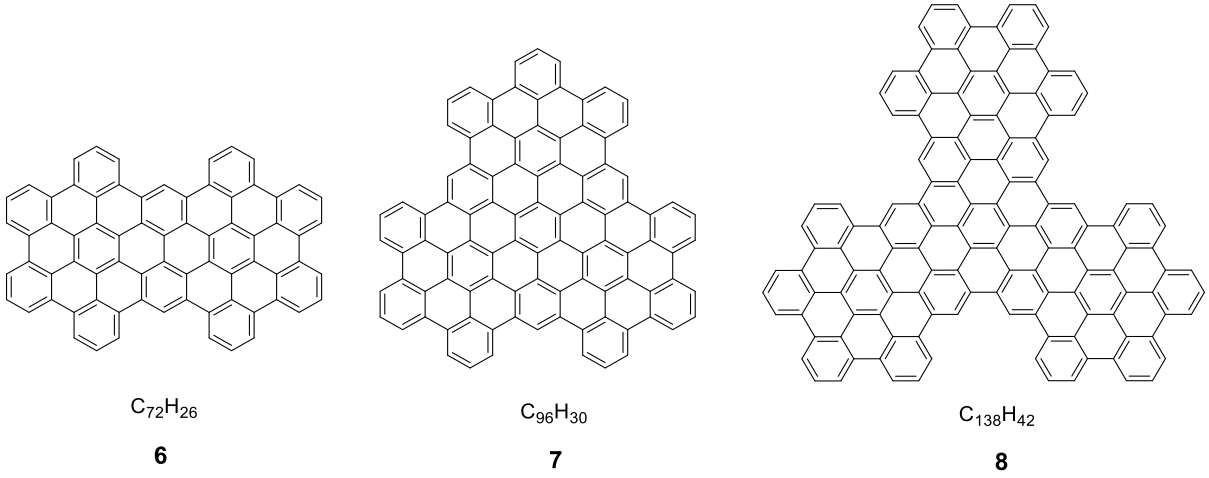

Figure 12. Chemical structures of some HBC homologues **6-8** with varying symmetries.[74-75]

Remarkably, Müllen and co-workers reported that the polyphenylene precursor **4** can be transformed into $C_{222}H_{42}$ (10) containing a C_{222}-hexagon, **9**. **10** is the largest synthesized monodisperse nanographene molecule so far, which has a disc diameter of 3.2 nm. (**Figure 13**) They were able to describe the crystal structure of the soluble precursor, which shows the existence of distorted, closely packed, and interlocked benzene rings.[76]

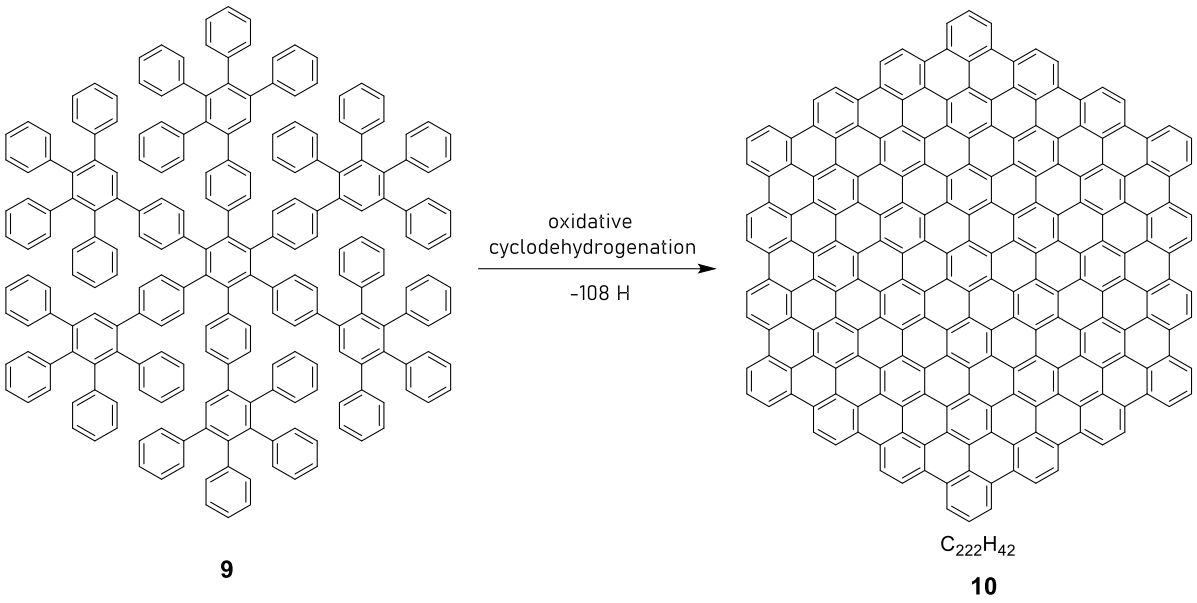

Figure 13. Synthesis of $C_{222}H_{42}$ (**10**) via oxidative cyclodehydrogenation.[76]

1.1.2 Extension of Polyaromatic Hydrocarbons (PAHs)

The fundamental point of the construction and extension of polyaromatic hydrocarbons (PAHs) is forming new C-C bonds. There are various types of π-extension approaches such as oxidative coupling and the Scholl reaction, alkyne benzannulation[77], C-H arylation[78], photochemical cyclodehydrochlorination (CDHC) and cyclodehydrofluorination (CDFC)[79-81], cross-coupling[82-86], photocyclisation[87-89], one-shot annulative π-extension (APEX)[90] and Al_2O_3-mediated hydrogen fluoride elimination.[91-92]

As one of the key topics of this thesis, oxidative coupling and the Scholl reaction will be discussed in depth in the following.

1.1.2.1 Oxidative Coupling and Scholl Reaction

The first oxidative aromatic coupling reaction (**Figure 14**) between arene compounds was reported in 1868 by Löwe[93] and similar results were observed in 1910 by Scholl for the transformation of quinone to π-extended quinone, by treatment with an excess of anhydrous $AlCl_3$ at 140–145 °C.[94]

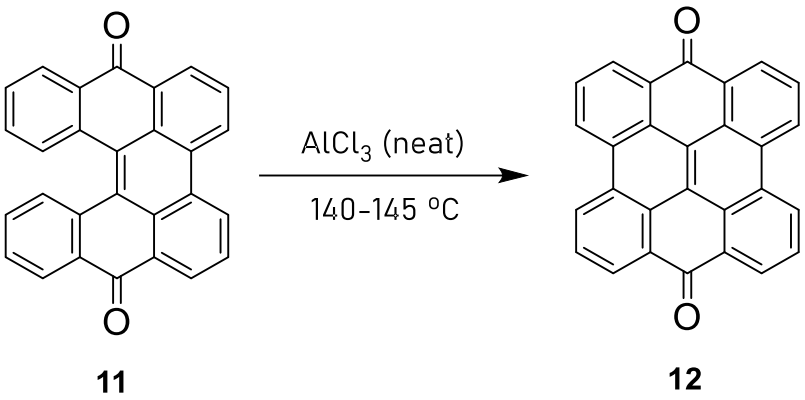

Figure 14. The first reported Scholl reaction.[94]

Despite the fact that Lewis acid-mediated cyclodehydrogenation is one of the oldest methods for obtaining polycyclic aromatic hydrocarbons[95] such as perylene[94], terylene[96-97], and dibenzotetraphenylperi anthene, the mechanism is still unclear. Gryko et al.[98] proposed a distinction between two possible mechanisms for the generation of polycyclic aromatic products prior to this discussion. One of the proposed mechanisms is known as the Scholl reaction, which occurs when an electrophilic complex, or σ-complex (shown as H^+ for simplicity in **Figure 15**, but it could also be a σ-complex formed with a Lewis acid).[98] Methodologies associated with this mechanism typically involve the use of strong Lewis acids such as $AlCl_3$ dissolved in chlorobenzene, complexes of fused salts such as $AlCl_3$/NaCl or $AlCl_3/SO_2$, among others.[99-100] The oxidative aromatic coupling, on the other hand, is another proposed mechanism for Lewis acid-mediated reactions. The formation of a radical cation is followed by intramolecular cyclization and re-aromatization to yield the polycyclic product. (**Figure 15**, left side).[98] The reaction is carried out under experimental conditions that include the use of Lewis acids such as $FeCl_3$ or strong oxidants like 2,3- dichloro-5,6-dicyano-1,4-benzoquinone (DDQ).

The ambiguity of these reactions stems from the fact that there is sometimes no clear evidence of the operating mechanism and is occurred through the Scholl mechanism without discrimination. The fact that most of the Lewis acids used in the Scholl reaction are also mild oxidants used in oxidative aromatic coupling reactions is one of the factors contributing to the confusion.[101-102]

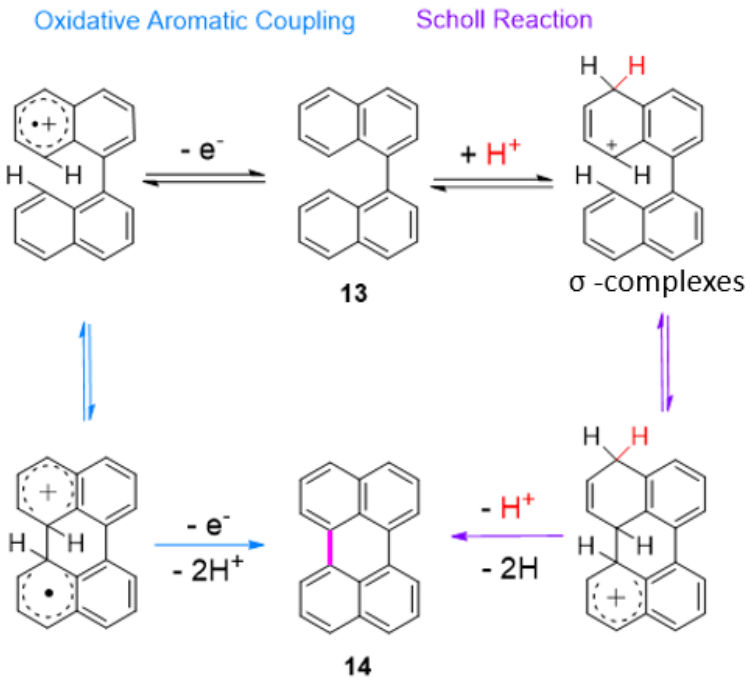

Figure 15. Archetypical oxidative aromatic coupling and Scholl reactions.[103]

The reaction of 2-naphthol in the presence of an oxidant such as $FeCl_3$ at 50 °C is a good example of how to distinguish between oxidative aromatic coupling and Scholl mechanism.[104-105] Under these circumstances, an oxidative aromatic coupling reaction produces 2,20-dihydroxy-1,10-binaphthalene (**Figure 16**). However, even when additional portions of $FeCl_3$ are added to the system, the perylene-1,12-diol compound cannot be obtained.[98] In contrast, by heating 2,20-dihydroxy-1,10-binaphthalene with $AlCl_3$ at 150 °C, the C–C bond formation (C-8 with C-8´) to give the perylene-1,12-diol can be achieved (Scholl conditions).[106]

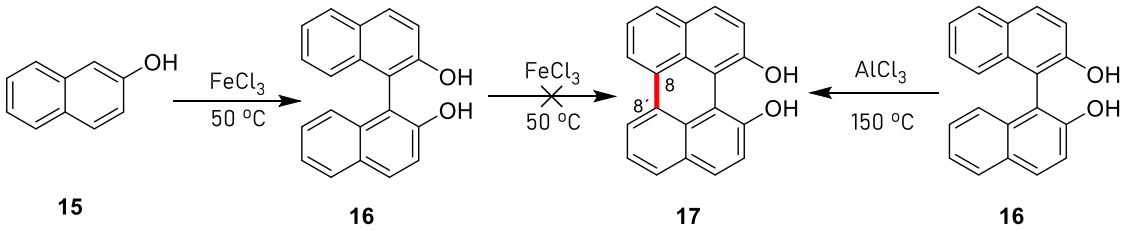

Figure 16. Formation of perylene-1,12-diol.

The Scholl reaction is particularly preferable for the oxidative cyclodehydrogenation of various types of substituted hexaarylbenzenes and *ortho*-terphenyls to generate their planar PAH analogues.[107-108] These reactions have been extensively used for the synthesis of large π-extended systems as well as smaller benzonoid or heteroatomic compounds. The Scholl reaction is undoubtedly one of the most effective reactions for the building of nanographenes [90, 109] and also, hetorocyclic counterparts.[110]

1.1.2.1.1 Mechanism of the Scholl Reaction

The reaction illustrated in **Figure 17** is the simplest intramolecular Scholl reaction and will be used as a model to describe its mechanism. Interestingly, even today its nature remains disputed and poorly known. However, there are two proposed mechanisms for the Scholl reaction a) via anarenium cation and b) via a radical cation, both are in opposition.

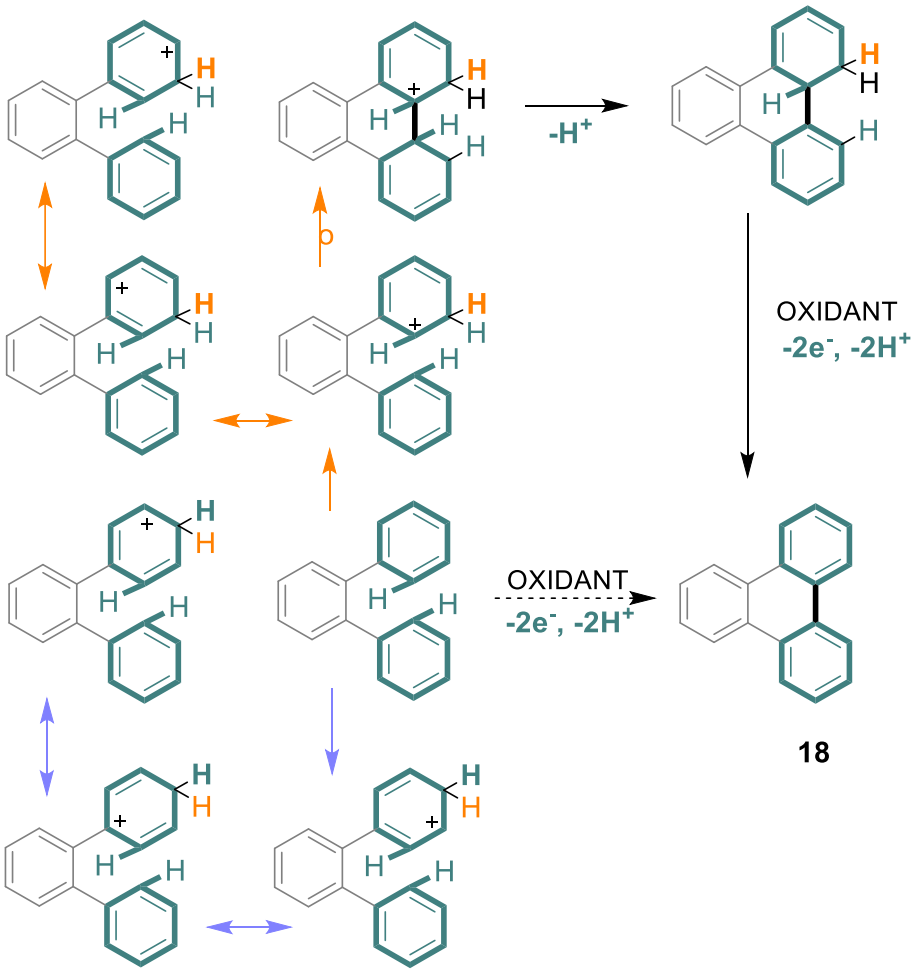

Figure 17. Proposed mechanism of the Scholl reaction via an arenium cation.[103]

The arenium cation mechanism, (**Figure 17**) starts with the protonation of the aryl moieties to form an electrophilic σ complex with a Lewis acid. Attack at the second aromatic ring forms a new C-C bond and hydrogen elimination re-establishes the aromaticity.

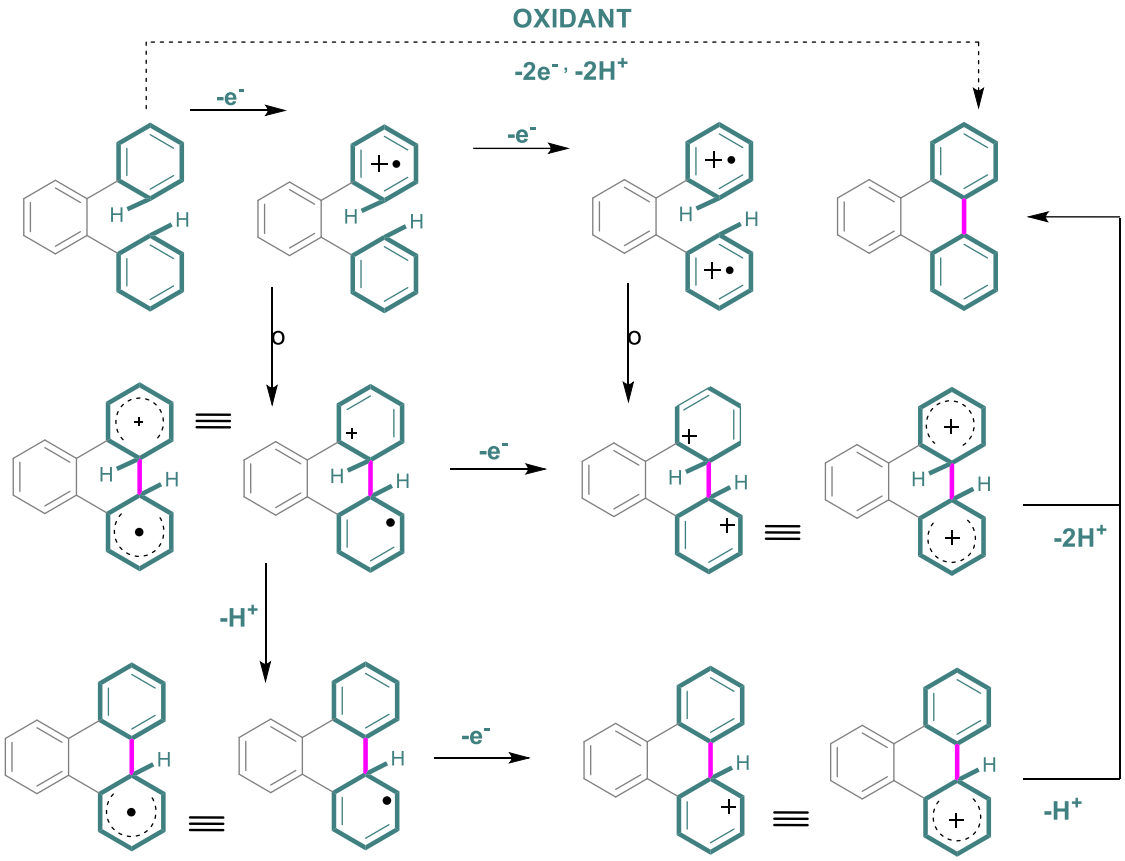

Figure 18. Proposed radical cation mechanism for the Scholl reaction.[103]

Parker and his colleagues looked into the role of radical cation intermediates in bi-aryl synthesis (**Figure 18**).[111] However, most of the Lewis acids used in the Scholl reaction are also milder or stronger oxidants and capable of catalysing a variety of reactions. As a result, distinguishing between these two possible mechanisms remains difficult.

The interest in this transition has increased over the years and many reagent systems have been introduced. Commonly used reagents include $FeCl_3$ [112-114], $MoCl_5$ [115-116], $AlCl_3$ [76, 97, 117], DDQ [118-120], and PIFA /BF_3.Et_2O.[121] Gryzbowski and co-workers reported in their review the choice of the reagent could also have an impact on the mechanism of the Scholl reaction.[98] They also categorized the reactions, and proposed that those Scholl

reactions, which occur at room temperature with a mild one-electron oxidant such as $FeCl_3$ or $MoCl_5$ probably undergo a radical cation mechanism. In contrast to this, the reactions, which take place at 120- 160 °C in the presence of strong Lewis acids, mostly follow the arenium cation mechanism.[98] As Waldwogel and colleagues reported, the Scholl reactions, which proceed in the presence of $MoCl_5$ follow the radical cation mechanism.[116] Rathore and co-workers investigated DDQ and discovered that the Scholl reaction greatly favours the radical cation system. However, because these two mechanisms will coexist and turn to each other under Scholl reaction conditions, the parallel study of the investment of arenium ion mechanism will not be fully elucidated.[103]

1.1.2.2 Drawbacks of the Scholl reaction

As specified in section **1.1.2.1**, some of the most used Lewis acid/oxidants for intramolecular Scholl reaction are metal chlorides. This usually results in the formation of hydrochloric acid during the reaction, which can quickly react under these conditions and lead to the formation of unwanted chlorinated materials.[76] Therefore, it is necessary to degas the reaction solution constantly to remove the HCl from the environment. Furthermore, rearrangements are commonly observed under Scholl reaction conditions and mostly generates the five and/or seven membered ring formation.[122]

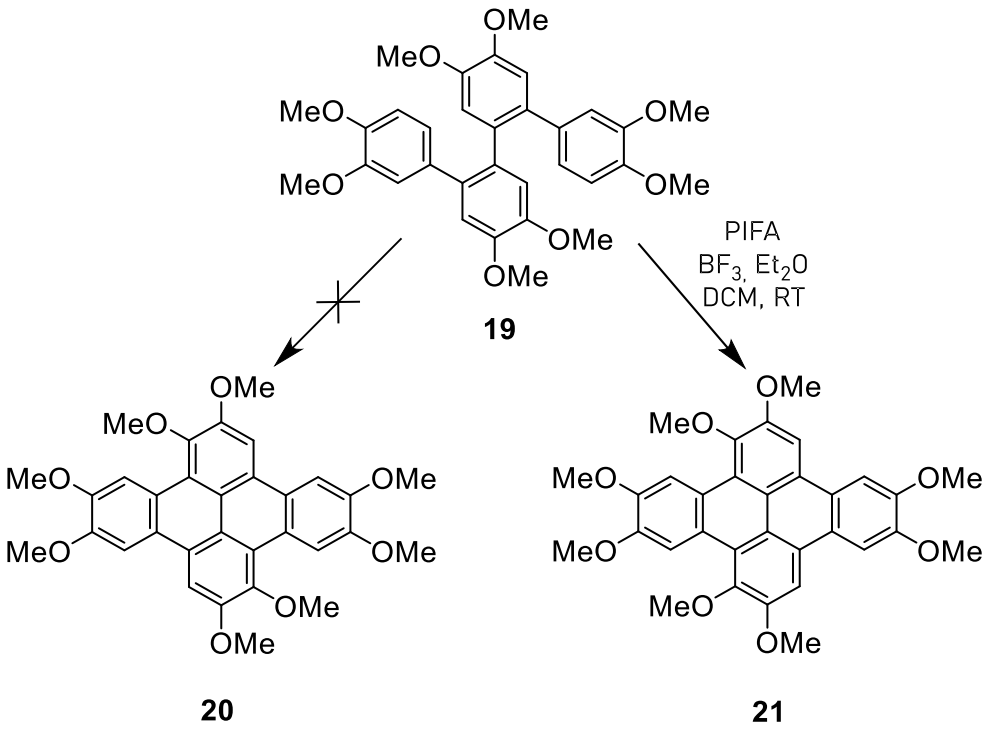

Figure 19. Example of rearrangement observable during Scholl reaction.[122]

1.1.3 Introducing strain in polycyclic aromatic hydrocarbons

Graphene's extraordinary properties are due to its pristine structure. It has been discovered that its distinctive hexagonal network and properties can be substantially altered in the presence of certain irregularities and defects. As previously mentioned in section **1.1.1.1**, vacancies containing one or two atoms missing in the lattice are commonly observed while observing defects in single layer graphene. Consequently, five or seven-membered rings or sometimes eight or nine-membered ones are common in graphene. Nanographene including non-hexagonal rings or heteroatoms can be considered as ideal models of defective graphene. As such, they can experimentally confirm theoretical studies on the impact of topological defects in graphene structures. These experimental results suggest that the existence of odd-membered rings causes planarity distortion, which has a significant impact on the physical properties of these carbon nanostructures.[123]

1.1.3.1 Five-membered rings

Due to the fact that the structures which are fused, π-extended-systems of additional five membered rings, can be curved, they must be distinguished from compounds with only six membered rings.[30] The existence of five-membered rings typically results in bowl-shaped compounds of positive curvature.

The Scholl reaction often favours the construction of a five-membered ring to a six-membered ring, with the reason for such selectivity remaining unclear. It was reported that the five-membered ring formation could stabilize the structure, thus it would be favoured. **Figure 20** represents the unexpected five-membered ring formation under Scholl reaction conditions.

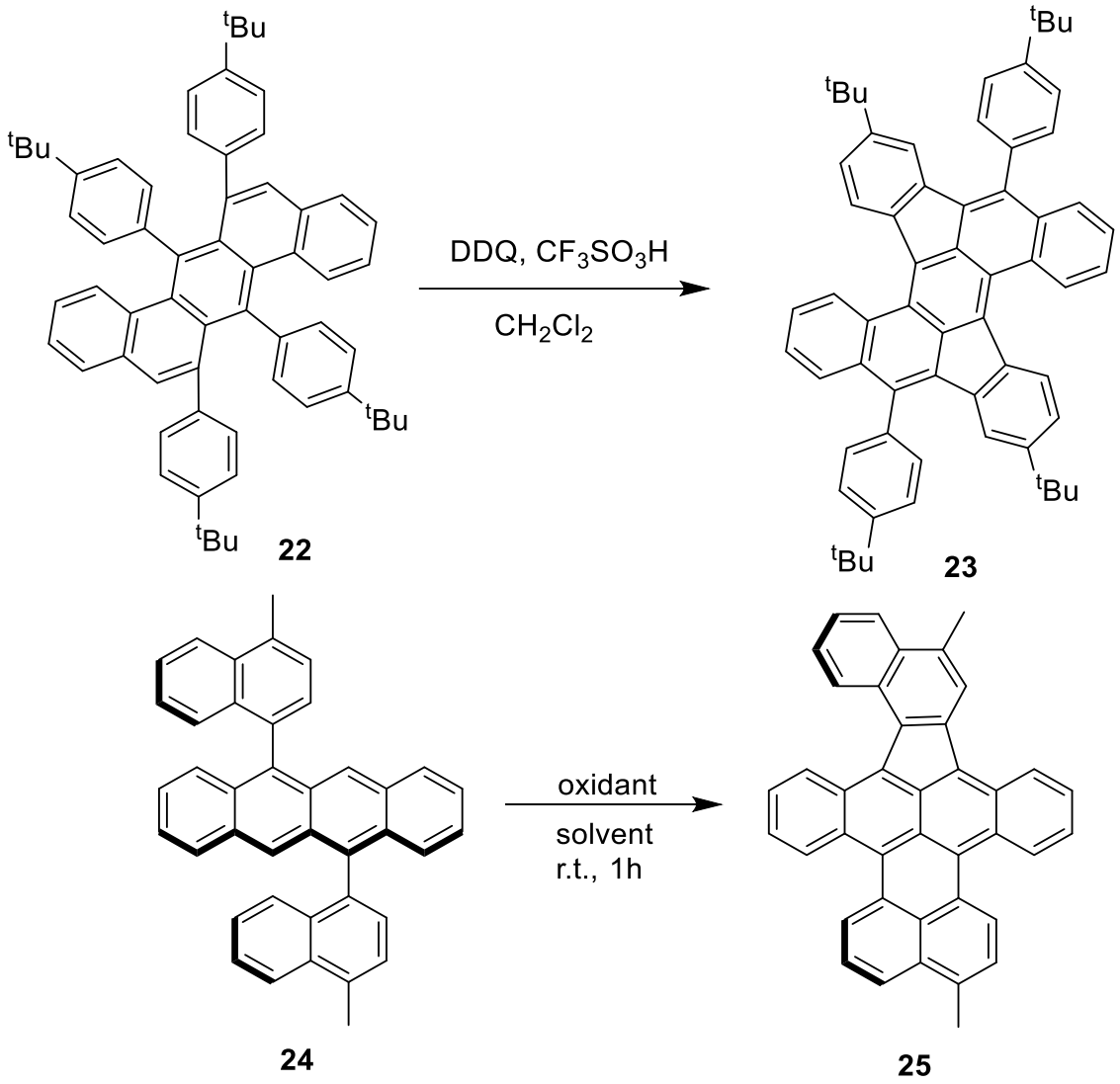

Figure 20. Formation of unexpected five-membered rings via Scholl reaction.[124-125]

Due to their unique physical and chemical properties,[126-129] such as bowl inversion,[130-131] supramolecular assembly,[132-133] electronic conductivity [58-59] and chirality[134-135] non-planar curved PAHs have taken up increasing attention in recent years. After the discovery of fullerenes[53], and carbon nanotubes,[54] bowl-shaped aromatic molecules (or buckybowls) as structural components of fullerenes and carbon nanotubes have been gained great interest not only as model compounds and precursors for the production of new materials but also for their exceptional properties and potential applications. For this reason, the five membered rings are introduced into the planar systems on purpose and the resulting compounds are being studied.

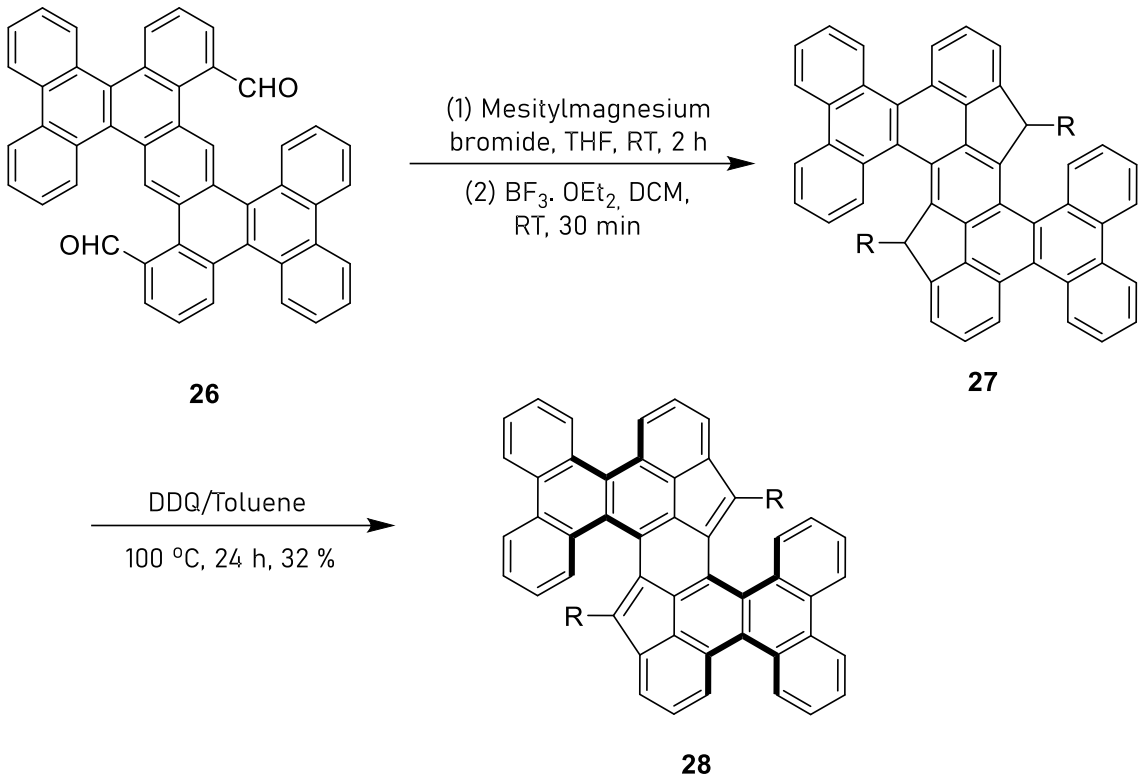

Figure 21. π-extended curved polycyclic hydrocarbon including five-membered rings.[136]

Feng and colleagues studied π-extended antiaromatic compounds by extending indenofluorene in both directions. It was revealed that they could be used as potential candidates in optoelectronic devices.

Moreover, Fasel and co-workers studied the surface assisted formation of an indenofluorene based polymer on Au(111).[137] They started with 4,4´´-dibromo-2,2-´´dimethyl-1,1´:4´,1´´- terphenyl as a precursor to grow *ortho*-methyl substituted poly(*para*-phenylene) on the metal surface under ultrahigh vacuum (UHV) and they succeeded to form five membered rings by the attack of a methyl group on the neighbouring aromatic ring.

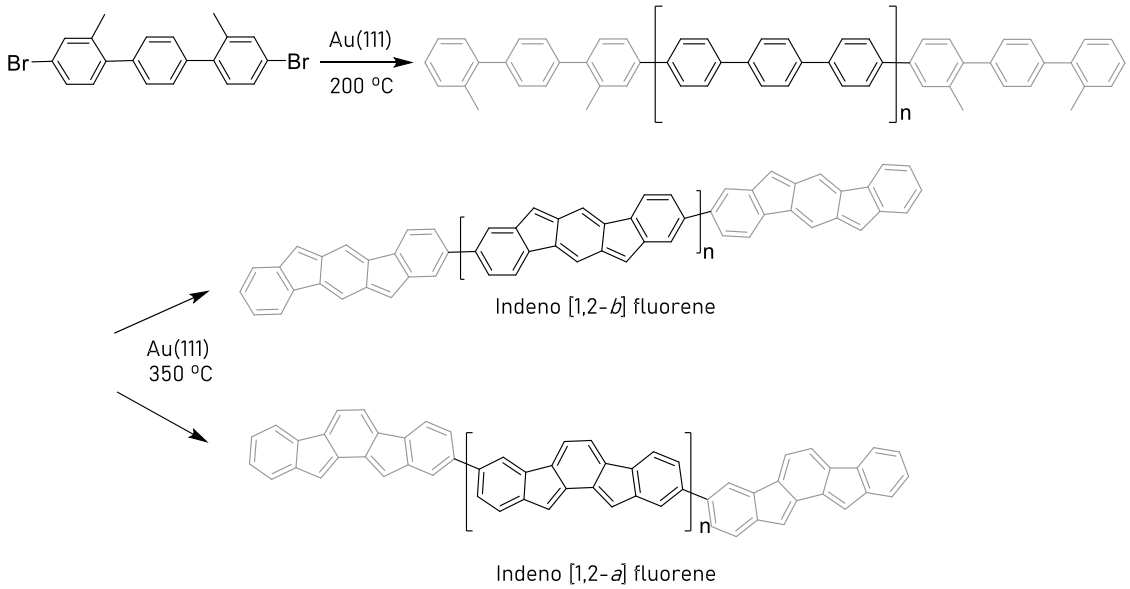

Figure 22. Surface assisted five membered ring formations on Au (111).[137]

1.1.3.2 Seven-membered rings

Besides the five membered ring formation, seven membered rings could be formed during Scholl reactions as well. The incorporation of seven-membered carbo-rings into nanographenes is a desirable objective, since by forming the aromatic cycloheptatrienyl cation the holes injected into organic p-type semiconductors are stabilized. The resulting structure including seven membered rings exhibits a stable bowl shape with negative curvature. Although it has been reported relatively rarely, Durola and co-workers observed the seven-membered ring formation first time under Scholl reaction conditions as seen in **Figure 23**.[138]

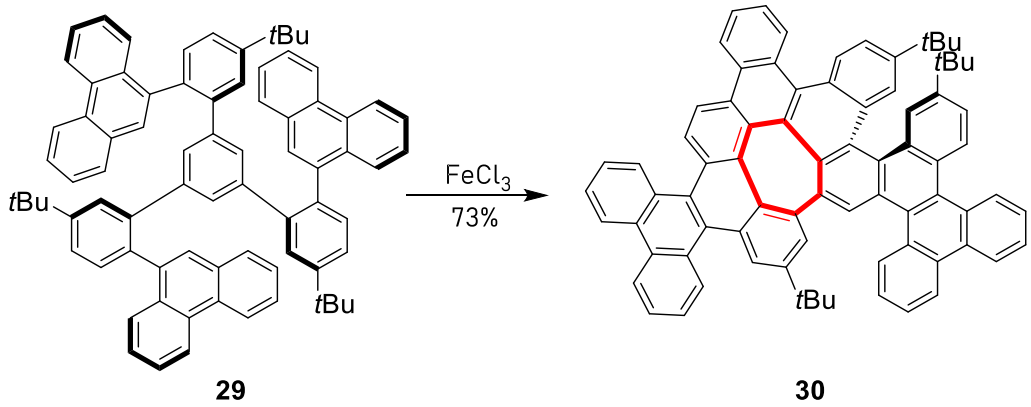

Figure 23. Unexpected seven-membered ring formation during Scholl reaction.[138]

In 2013, Itami, Scott and colleagues reported one of the most interesting odd membered ring formations (**Figure 24**).[139] They synthesized an extraordinarily distorted warped nanographene starting from commercially available corannulene in two steps, which is comprising five seven-membered and one five-membered rings. The reaction sequence comprised a C-H activation via palladium catalyst, followed by cyclodehydrogenation under Scholl reaction conditions in the presence of DDQ and TfOH. They discovered that the reaction did not stop after formation of the five-fold annulated compound but continued all the way to warped nanographene $C_{80}H_{30}$.

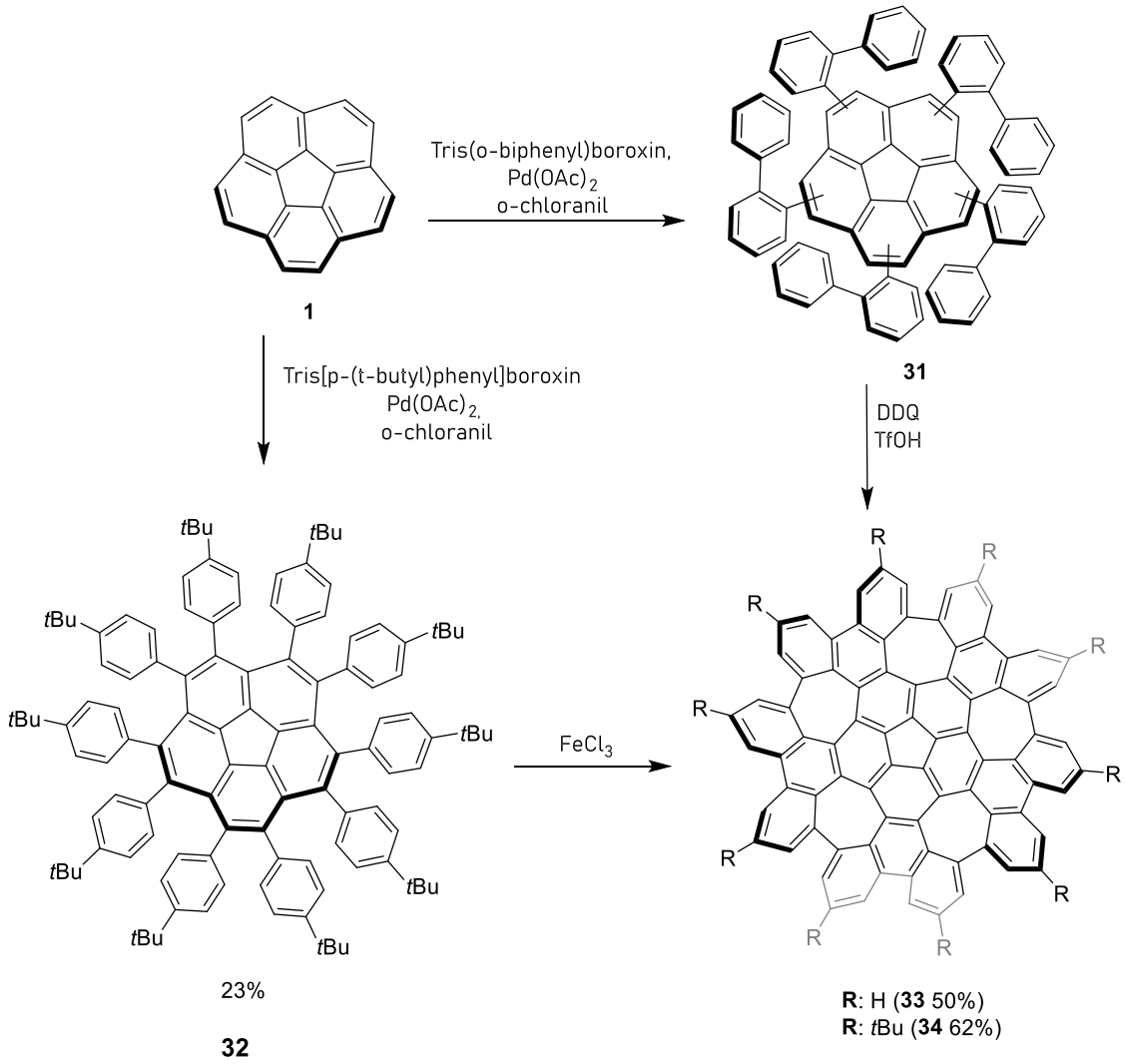

Figure 24. Synthesis of extraordinarily distorted warped nanographene **33** and **34.**[139]

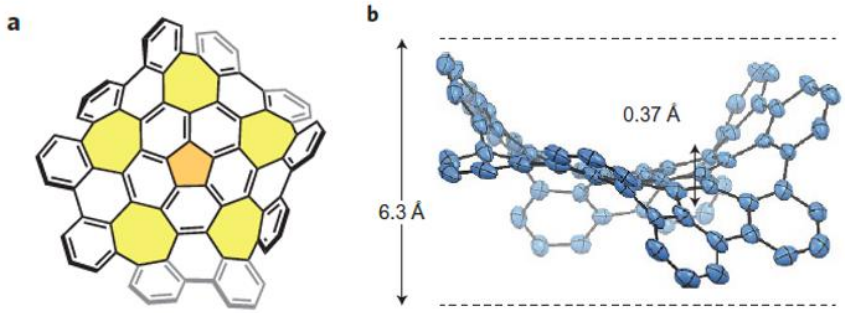

Figure 25. a) A grossly warped graphene subunit with multiple odd-membered-ring defects, b) side view of ORTEP image showing the warped structure of the new $C_{80}H_{30}$ nanographene **33,** taken from the X-ray crystal structure.[139]

At the same time, Kuck and colleagues reported the synthesis of a PAH comprising seven-membered ring.[140] As can be seen in **Figure 26**, a bowl-shaped tribenzotriquinacene, **35**, is fused with a pentaphenylphenyl unit. The final Scholl reaction was performed using $Cu(OTf)_2/AlCl_3/CS_2$ as Lewis acid and provided the expected TBTQ–HBC scaffold. It also generated a cycloheptatriene that bridges both units. Thus, the saddle-shaped heptagon connects the bowl-shaped TBTQ with the planar HBC.

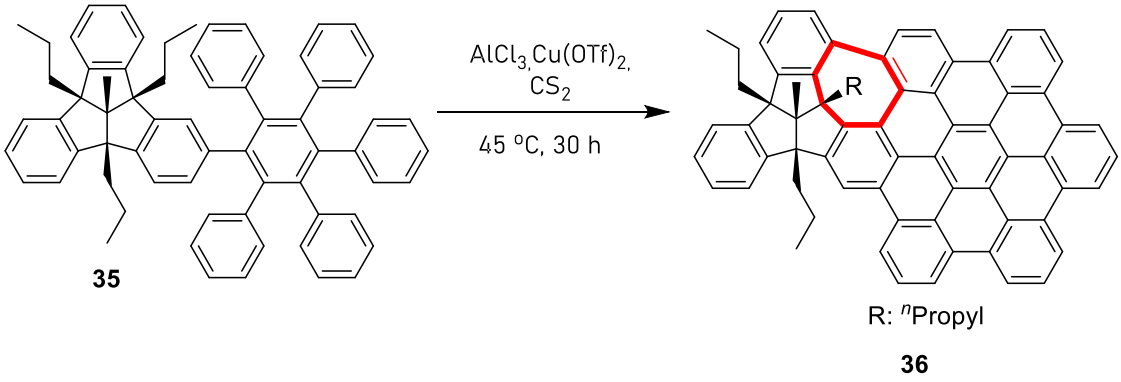

Figure 26. Seven-membered ring formation at bay-bridged position reported by Kuck.[141]

Martin et *al*. reported an intriguing study, in which the Scholl reaction is the last step leading to form different products with a different curvature depending on the oxidation conditions. In the presence of $FeCl_3$, nanographene **38** has a helical structure due to the formation of a [6]helicene and a [4]helicene, as well as positive curvature due to the presence of a five-membered ring in the corannulene fragment. In comparison, DDQ

gives rise to additional seven membered ring instead of the [6]helicene to nanographene **39** and resulting in a shallower helical structure. Furthermore, the presence of a seven-membered ring results in negative curvature and a saddle shape simultaneously. As they reported, introducing the negative curvature to the backbone has a significant impact on electronic and molecular properties compared to HBC and its analogues.[142] (**Figure 27**)

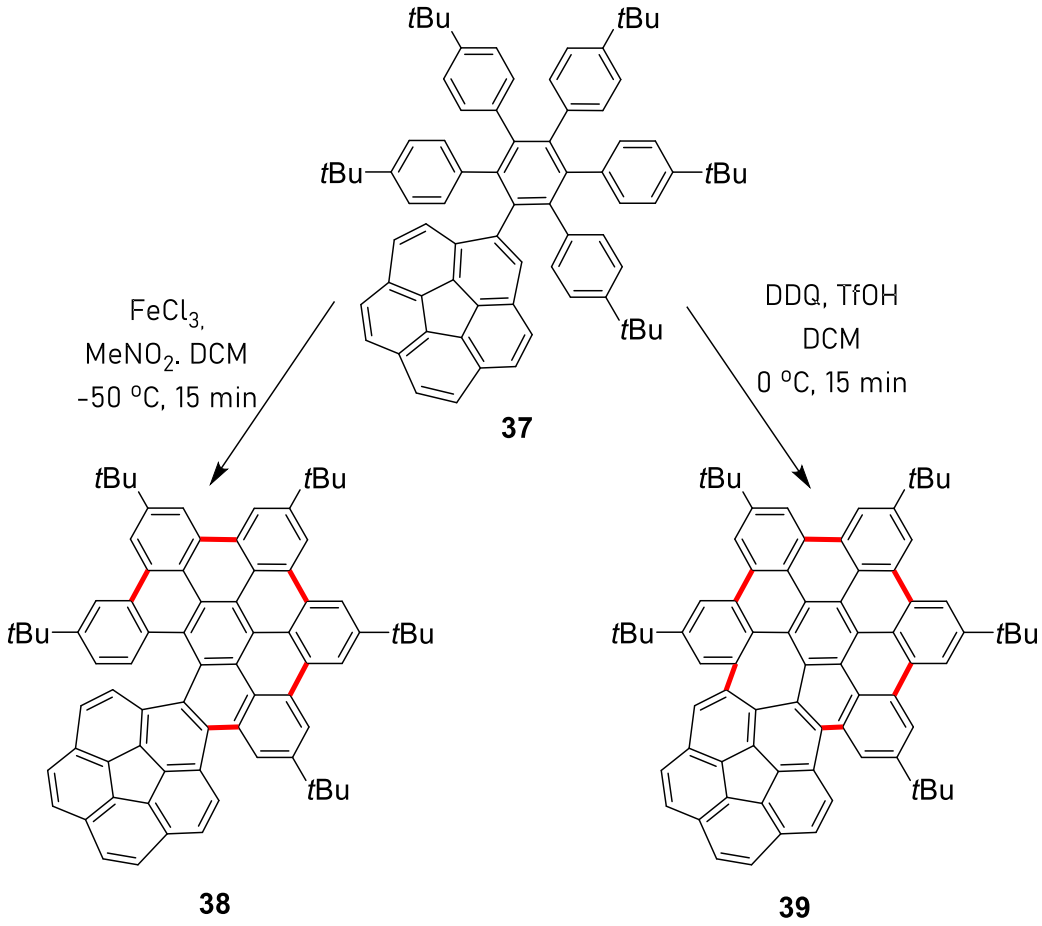

Figure 27. Selective formation of negative and positive curvature via Scholl reaction.[142]

1.1.4 Tribenzotriquinacene (TBTQ) as a defective core

Tribenzotriquinacene (TBTQ) is an interesting polycyclic aromatic framework with a particularly rigid, C_{3v} symmetrical, bowl-shaped core bearing three mutually fused indane wings (**Figure 29**, **42**). In 1999, Kuck and colleagues proposed that the structurally expanded TBTQ network could be envisioned to eventually resulted in

graphite segments, in which triquinacene (**41**) core would provide directed deformations of the nanographene.[143]

As already discussed, non.hexagonal rings are one approach to control the properties of nanographenes. In this context, extended TBTQ structures (**Figure 28**) are promising models for saturated defect structures in graphene and graphene like molecules and they could be used to investigate the role of electronic states in defected graphene.

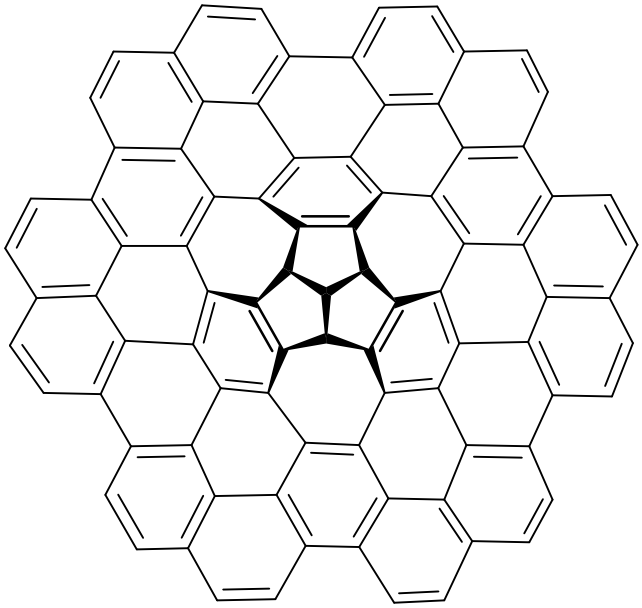

40

Figure 28. Schematic representation of a hypothetically proposed extended triquinacene bearing a completely closed arene periphery.[143]

The triquinacene (**41**) core has a conformationally rigid C_3-symmetrical structure and polyolefinic character, which exhibits intrinsic instability and high reactivity. However, it was later investigated that aromatic extension of the parent compound triquinacene to TBTQ (**42**) ensures reasonably higher stability and moderate reactivity while maintaining most of the inherent geometrical properties.[144] Therefore, TBTQ is a suitable candidate for the simulation of a strongly curved graphene defect centre.

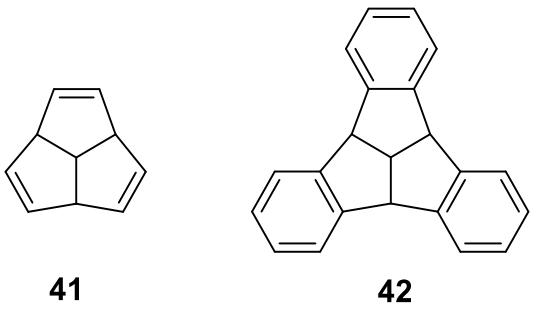

41 **42**

Figure 29. The structures of triquinacene (**41**) and tribenzotriquinacene (**42**).

1.1.4.1 Tribenzotriquinacene Synthesis

TBTQs belongs to the class of centropolyindane molecules.; They consist of three saturated, annulated five-membered carbon rings, that each carries a benzene at the outer edge. The substituents at the four saturated carbon atoms are arranged in an all-cis fashion. This leads to a special geometry, which is called bowl shaped. It has a curvature that is almost at a 90° angle.

Me-TBTQ (**50**) was first synthesized in 1984 [145] by Kuck et al. and followed by the synthesis of H-TBTQ in 1992.[146] The synthetic pathway starts with the condensation reaction between an indandione derivative and diphenylmethanol. After isolating the diketone, it is reduced to the diol and then cyclized as a last step (**Figure 30**).

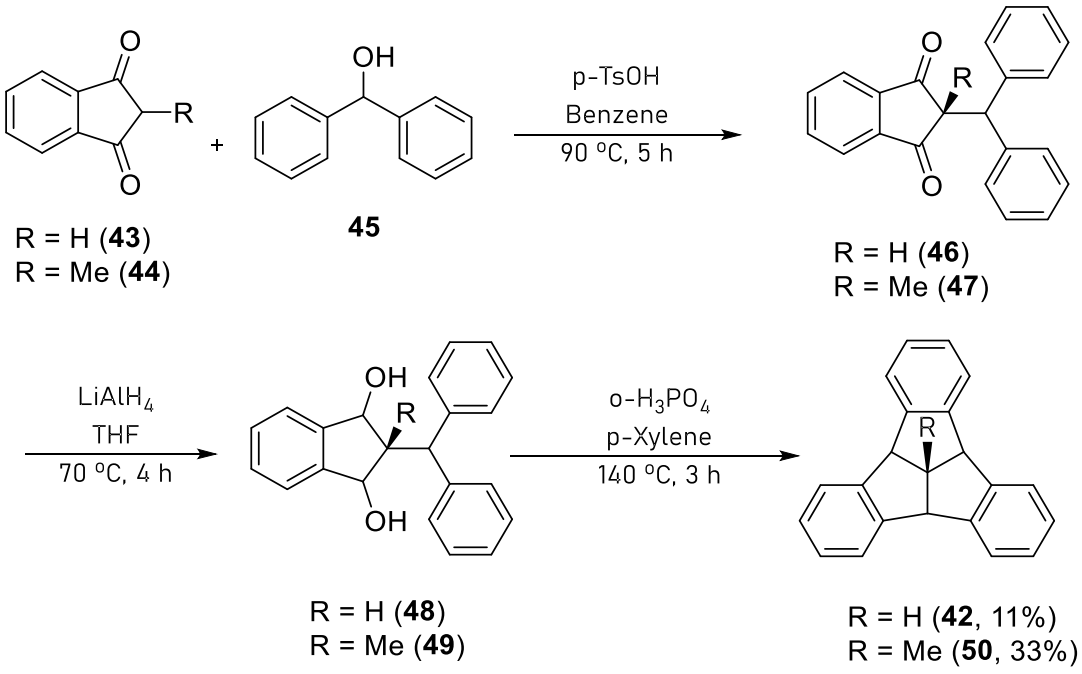

Figure 30. Double cyclization strategy to TBTQ by Kuck.[145-146]

The last step has a relatively low yield (11%) due to challenging double cyclization process. However, Hopf and co-workers reported an improved TBTQ synthesis strategy **(Figure 31**) with a 19% overall yield in only three steps and a 32% yield for the final cyclisation step.[147]

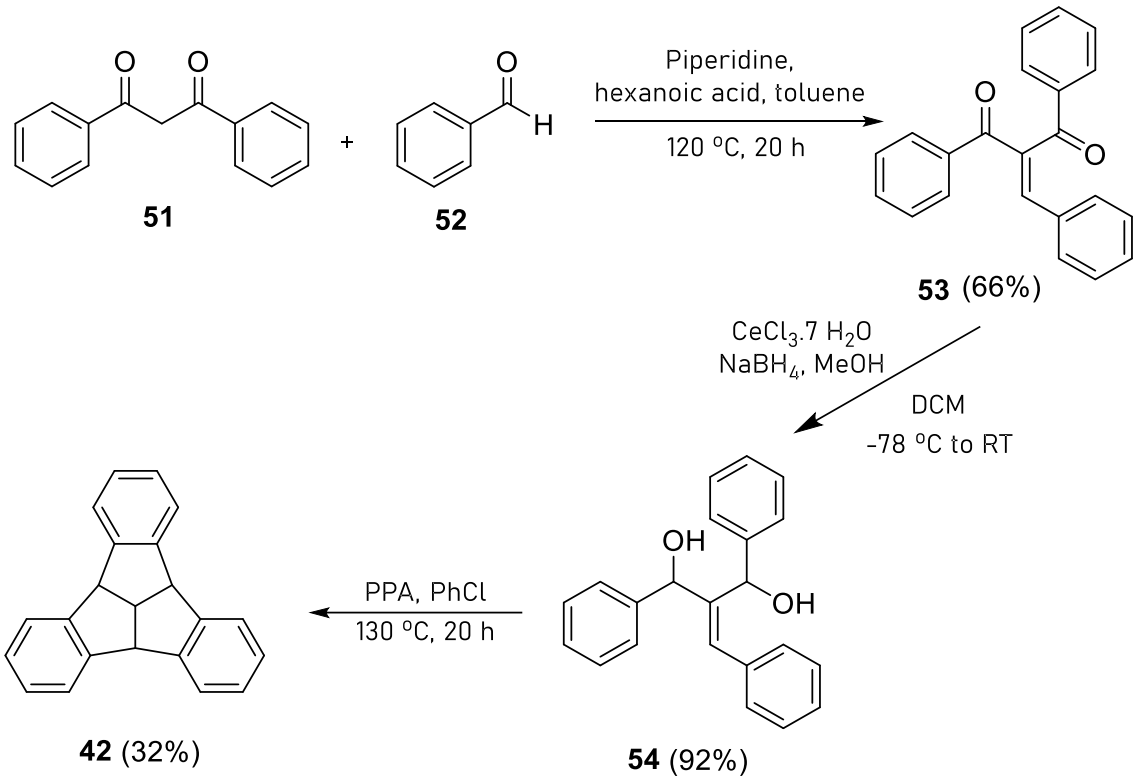

Figure 31. Tribenzotriquinacene synthesis via triple cyclization strategy by Hopf.[147]

1.1.4.2 Crystal structure of H-TBTQ and Me-TBTQ

In 2001, the single crystal X-ray structure analysis of Me-TBTQ (**50**) was reported, followed by the structure of H-TBTQ (**42**) by Kuck *et al.*[148-149] (**Figure 32**). It was revealed that both H-TBTQ (**42**) and its *centro*-methyl derivative (**50**) have perfect C_{3v} symmetry. In addition, not only Me-TBTQ but also H-TBTQ are bowl shaped and build infinite molecular stacks with entirely axial, convex-concave packing and with parallel and unidirectional orientation of the stacks. The intra-stack molecular distance was experimentally measured as 4.75 Å for H-TBTQ and 5.95 Å for *centro*-methyl derivative. It is not surprising that a 1.25 Å difference between the compounds in packing structure is observed due to the effect of the apical Me-group. Nevertheless, there is not drastic change in other geometrical parameters. While the *centro*-Me TBTQ derivative shows excellent translational symmetry within stacks in the rhombohedral space group R*3m*, H-

TBTQ exhibits space group of R*3c and* a tenuous rotation about +6° and -6° around the common axis of each stack.

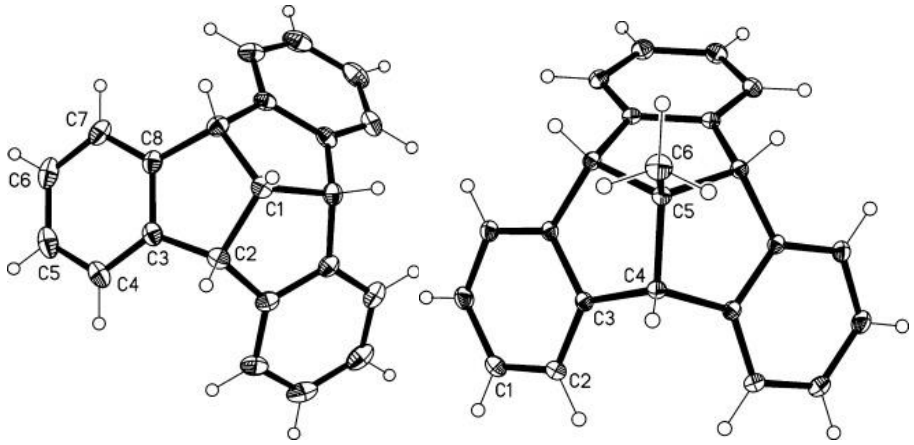

Figure 32. Crystal structures of H-TBTQ (**42**, left) and Me-TBTQ (**50**, right). The figures are taken from. (Copyright 2013, Wiley-VCH Verlag GmbH & Co. KGaA, Weinheim. Reproduced with permission.).[148]

1.1.4.3 Functionalization of Tribenzotriquinacene

The possible functionalization sites of TBTQ framework are the bridgehead, outer aromatic, *ortho*, and apical positions (**Figure 33**).[150]

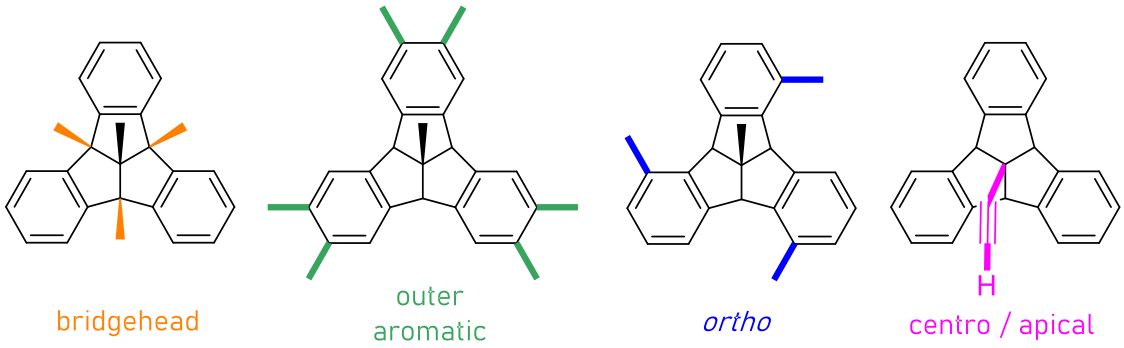

Figure 33. The four possible functionalization positions inf TBTQ.

Each functionalization type contributes the parent TBTQ molecule in a different way for further synthetic approaches. Varying the apical and the bridgehead substituents easily influence the solubility[141, 148, 151], outer rim modification can be used for incorporating the TBTQ into larger structures.[150] *Ortho*-position functionalization provides the extended polycyclic aromatic systems with a curved π-structure via ring closure with neighbouring aromatic rings.

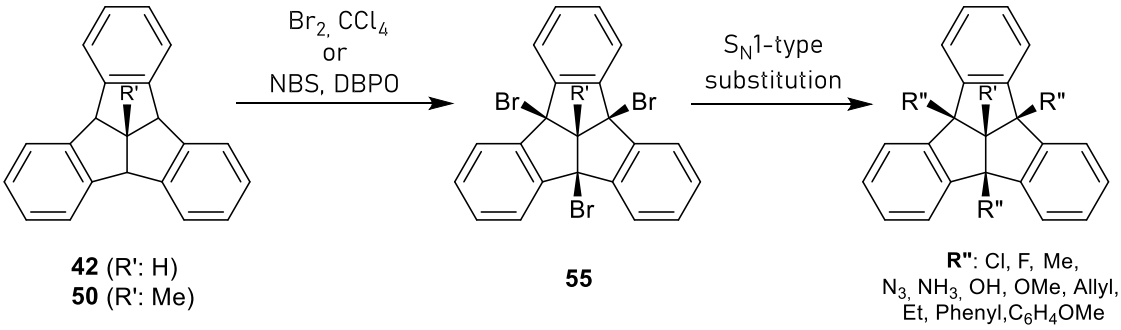

Figure 34. Bridgehead functionalization of TBTQ.[143]

Benzhydrylic bridgehead positions are the most reactive among all the C-H bonds in non-functionalized TBTQ. Bridgehead functionalization affords derivatives with various types of substituents at this position.[148, 152] Tribromo substituted TBTQ is the precursor for the facile S_N1 type of substitution reaction and can be used to synthesize an extensive amount of bridgehead functionalized TBTQ derivatives, (**Figure 34**).[148, 151, 153]

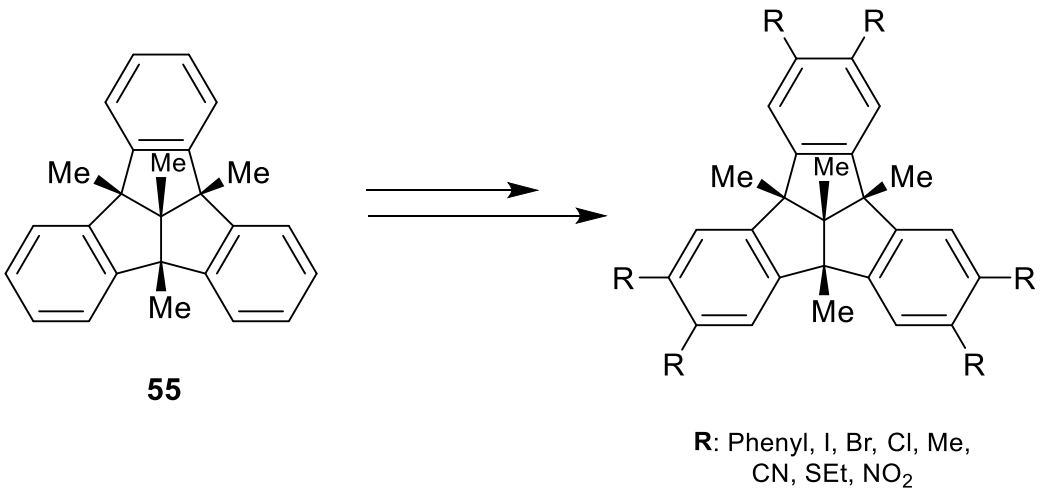

Figure 35. Outer rim functionalization of TBTQ.

For outer rim functionalization, there are basically two options. Pre-functionalization refers to the functionalization of the apical position before it is functionalized, while post-functionalization refers to the functionalization of the apical position after it has been functionalized. However, the use of pre-functionalization is limited by the required substitution of starting materials for the TBTQ synthesis, and these groups need to be inert in all steps towards the formation of the respective TBTQ derivative. Contrarily, post-synthetic functionalization is more applicable. Furthermore, methyl or propyl groups can be introduced to block the bridgehead position from any undesired functionalization. Starting from the tetramethyl substituted TBTQ derivative, there are various types of outer rim functionalized TBTQ available.[143, 148, 154-155] (**Figure 35**) Furthermore, π-extension of the three arms associated with TBTQ framework outer rim functionalization results in an expanded concave molecular principle, which is suitable for host-guest complexes with molecules of corporate architecture such as C_{60} and C_{70}.[156-160] A wide range of applications such as fluorescent chemo-sensors to detect Ag^{+} [161] and Cu^{2+} [162] selective complexation with ammonium salts [163], host-guest complexes with various quaternary ammonium halides [164] , organic cubes and cages could be envisaged.[165-167]

The *ortho*-positions are most challenging for a selective functionalization of TBTQ and are not accessible to post-synthetic functionalisation with electrophilic aromatic substitution due to sterical limitations. Besides the triple cyclization strategy by Hopf [147], Kirchwehm *et al*. reported the TBTQ derivative bearing methyl groups at all six *ortho* positions.[168]

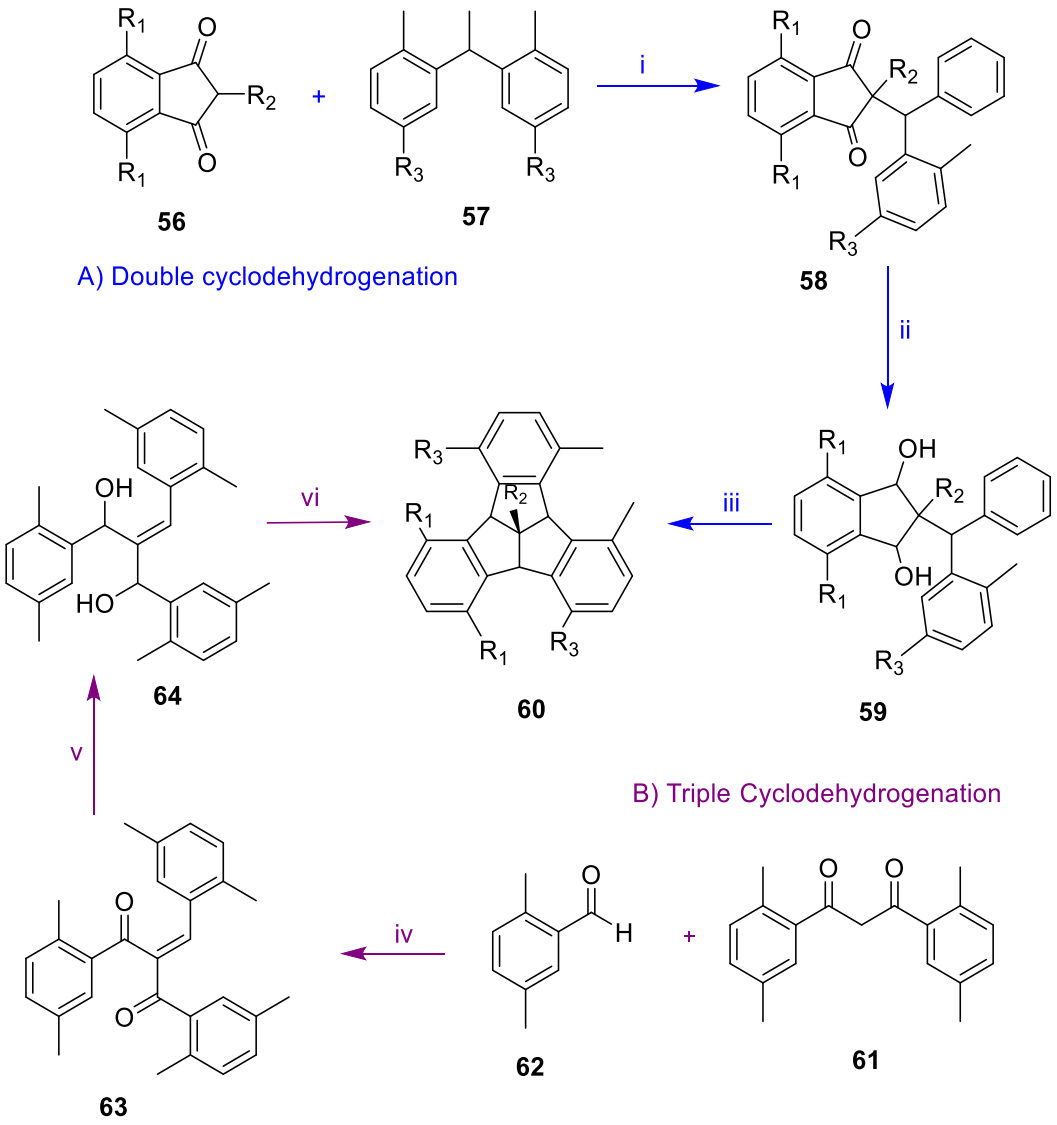

Figure 36. Two different pathways to ortho-functionalized TBTQs [168]

Substitution of the apical/centro position of TBTQ establishes the functionalization at the exo surface without disturbing the endo bowl or the three orthogonal indane side arms. Beuerle and co-workers reported that the apical functionalization of TBTQ serves the most diverse tasks such as better control of TBTQ solubility, immobilization on solid support, or exohedral functionalization of complex molecular architectures based on

TBTQ building blocks. This will significantly simplify the synthesis of derivatives for future applications based on this modular approach.[169]

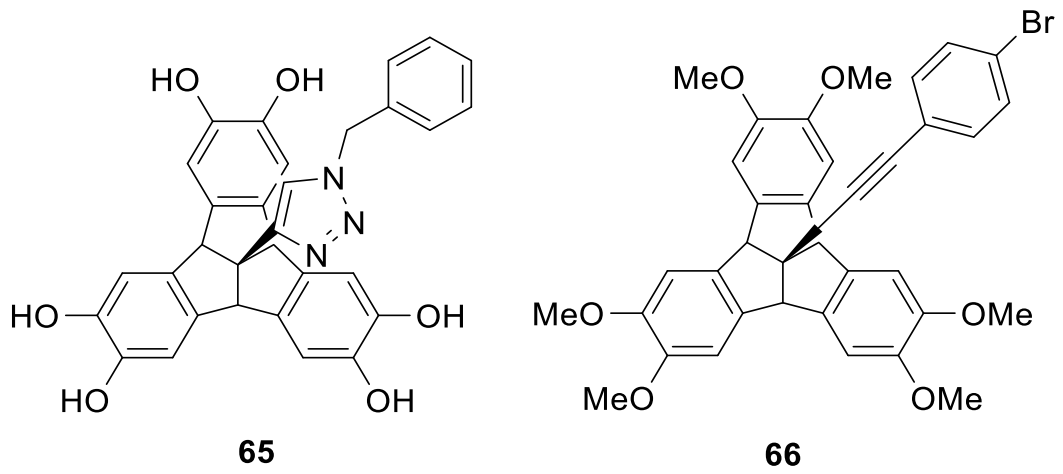

Figure 37. Some examples of apical functionalized TBTQ derivatives by Beuerle.[169]

1.1.5 Extended TBTQ

Ortho-functionalized TBTQ frameworks are promising in order to obtain defective nanographene bearing a TBTQ core. Therefore, Mughal et *al*. studied bay bridging TBTQ derivative synthesis via Scholl reaction. However, they only achieved the synthesis of one-fold cycloheptatriene ring formation at a bay position although they adapted the reaction procedure to obtain the threefold moiety.[140, 170] The main reason reported was undesired crowding at these positions.

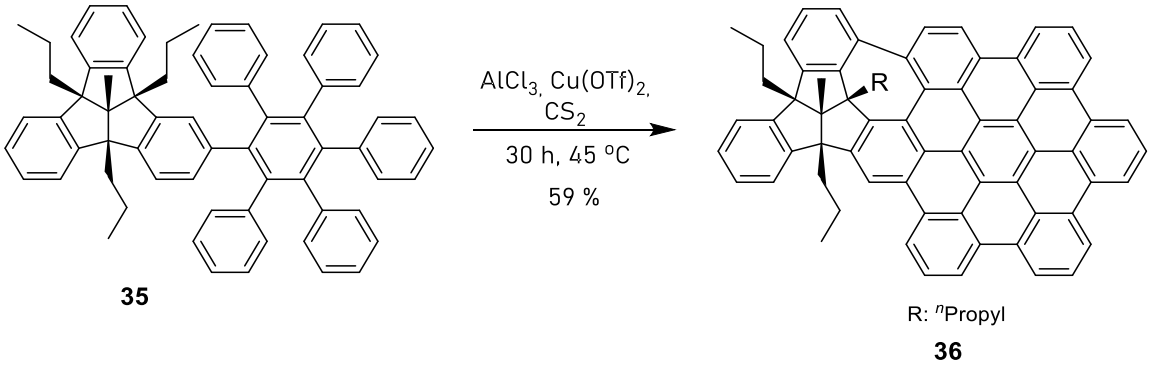

Figure 38. One fold bay bridged TBTQ.[140]

In 2014, Mughal and Kuck reported the wizard hat shape threefold bay extended TBTQ derivative starting from *ortho*-methoxy functionalized TBTQ framework.

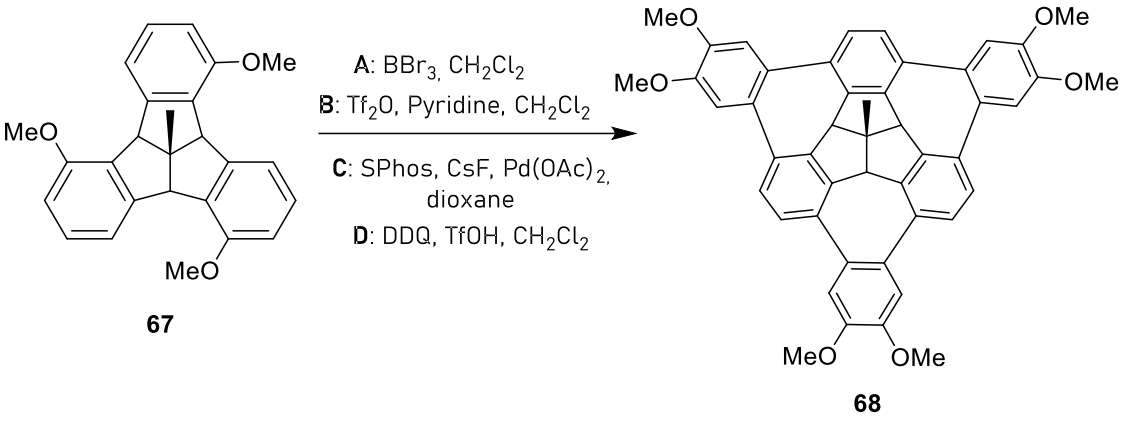

Figure 39. Synthesis of wizard hat shape extended TBTQ derivative.[171]

Furthermore, Kuck and co-workers reported multiple Scholl reaction starting from *meta* substituted TBTQ derivative and achieved porous extended TBTQ moieties under Scholl reaction conditions in a very good yield.[172]

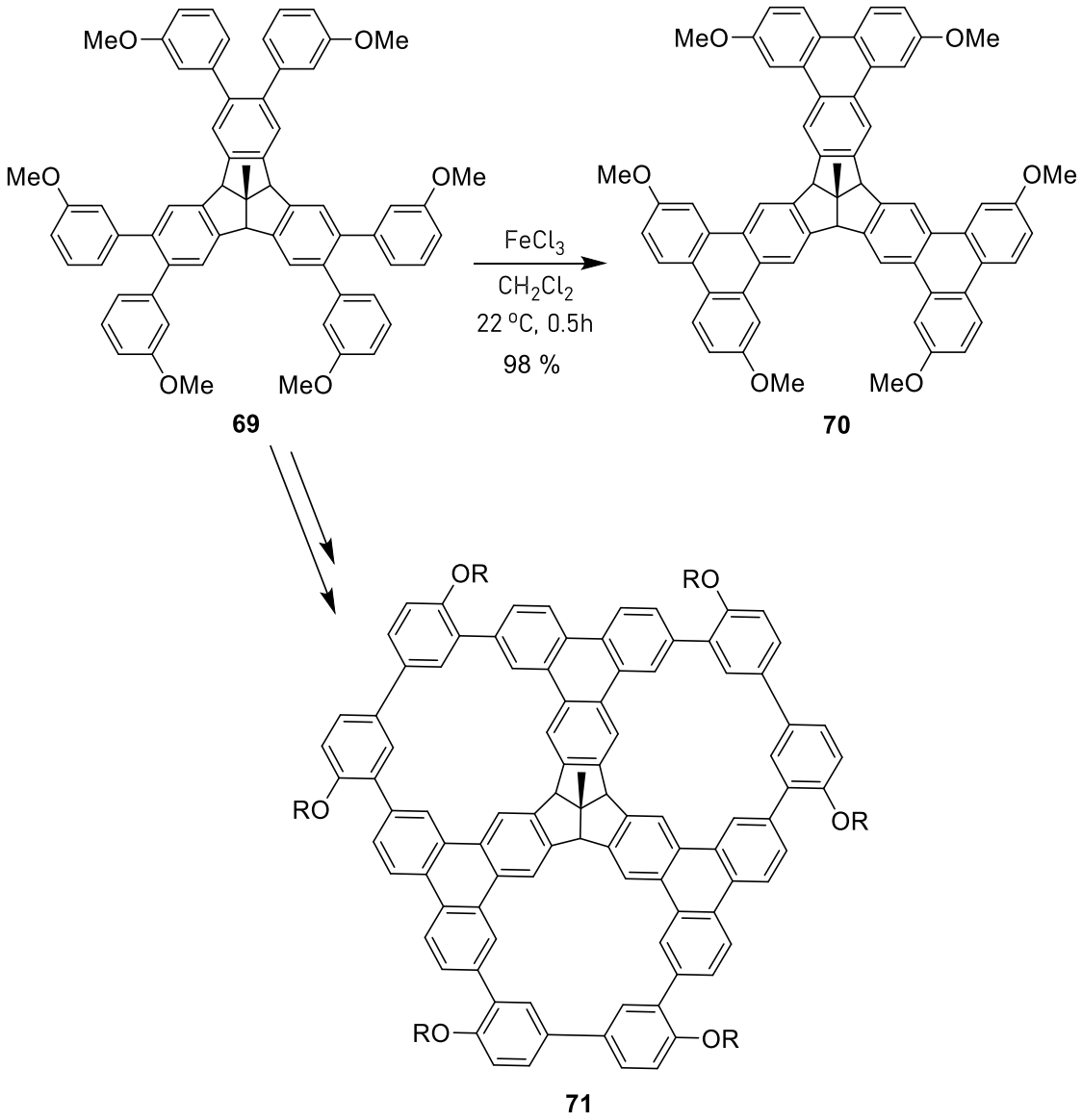

Figure 40. *meta*-functionalized π-extended TBTQ derivative molecules via Scholl reaction.[172]

They have recently reported the synthesis of a π- extended TBTQ based on the wizard hat shape ortho functionalized TBTQ. They directly installed the six phenyl rings to the sterically more hindered bay position of the wizard hat. To obtain the hexabromo derivative, the compound was first treated with a large volume of bromine. It was found that the bromination was not selective and each of the six bay regions only accommodates one bromine atom due to the steric hinderance. The regioisomeric mixture of hexabromides and thus, hexaphenylated wizard hat derivatives were obtained. The Suzuki reaction product mixture was submitted to Scholl reaction and the target compound was isolated with yield of 38%. (**Figure 41**)

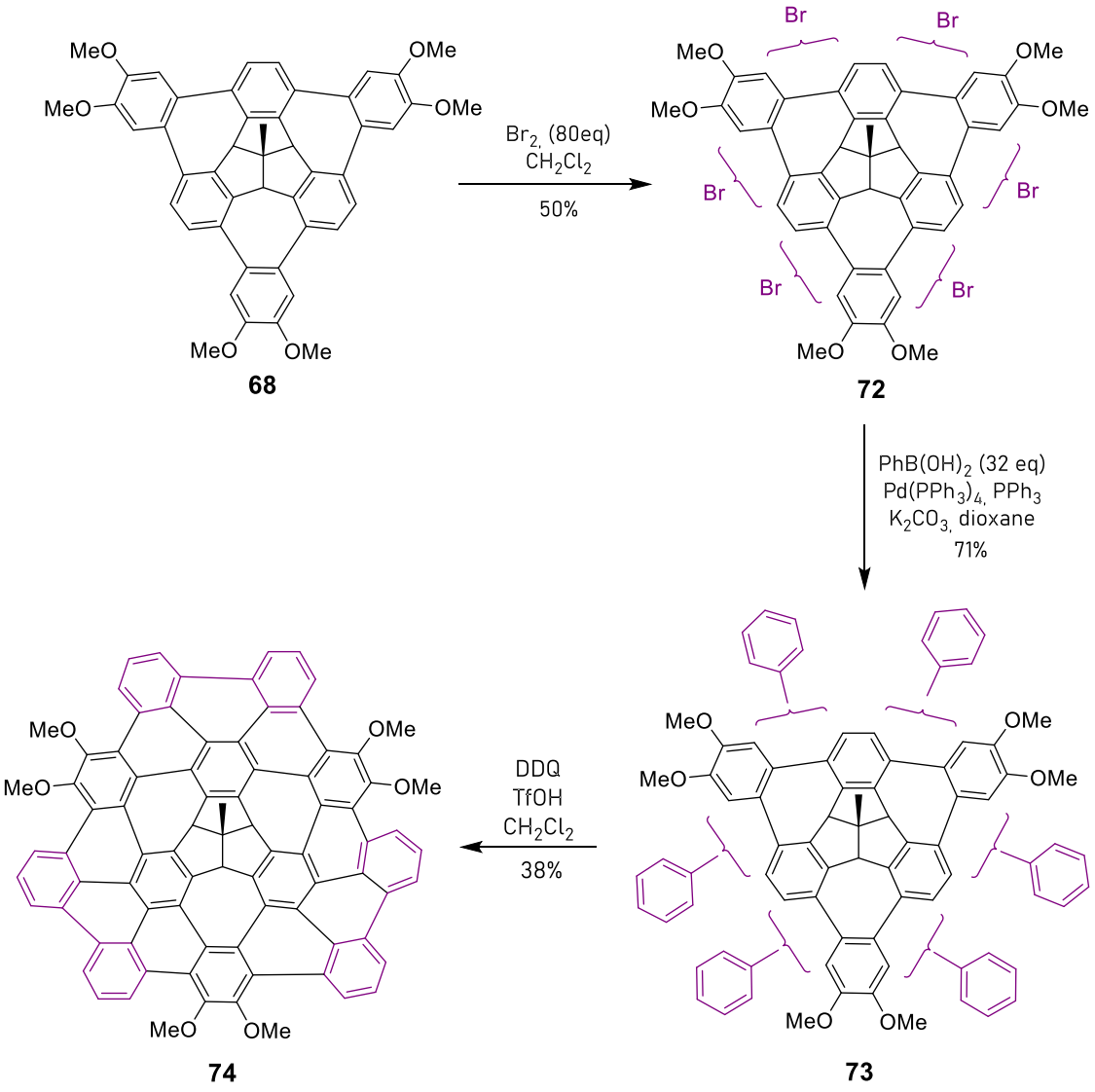

Figure 41. TBTQ based π-extended wizard hat-shaped nanographene.[173]

1.2. Aims

Defect engineering of (nano)graphenes is a fascinating subject of study, as the deliberate induction of rigid, curved deformations is likely to result in intriguing electronic properties, as seen in the literature review in the previous section. TBTQ can be thought of as a robust defect center when immersed in nanographene: rigidity comes from the tension caused by its three five-membered rings, and this core does not contribute to the conjugated π-system. Owing to the complexities of the lattice defect, a graphene-like structure with a curved defect core, which is the long-term goal of this work, cannot be obtained by subsequent alteration of defect-free graphene.

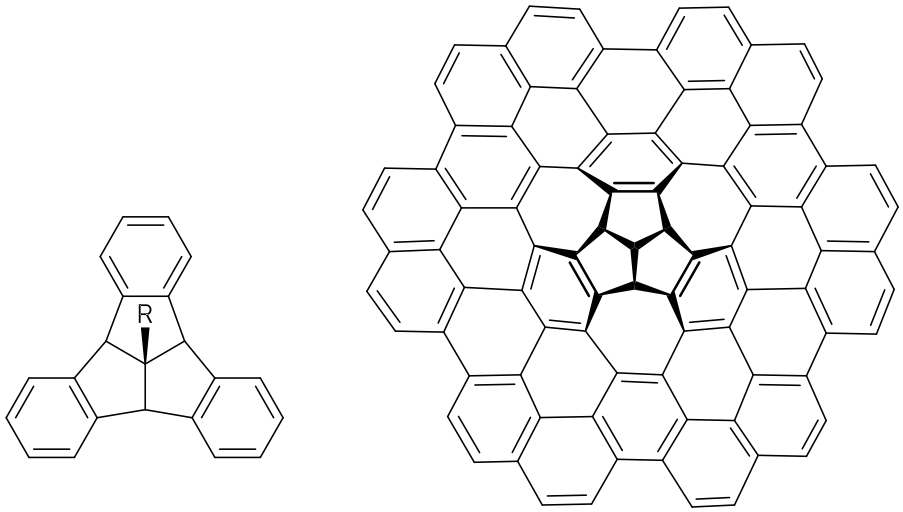

Figure 42. Me- TBTQ, **50** (left) and an extended defective graphene flake containing TBTQ at its center, **40**, (right).

Because of the wide range of transformations possible to achieve aryl-aryl coupling, as well as the distinct reactivities of the various positions in TBTQ, there are a plenty of topics that need to be researched further. Furthermore, extensive studies into the interaction of phenyl-, naphthyl-, and biphenyl- substituted TBTQ molecules with a metal substrate, Cu(111), as well as the effect on the stacking configurations of TBTQ crystal structures, will contribute the previous research and extend the π-system.

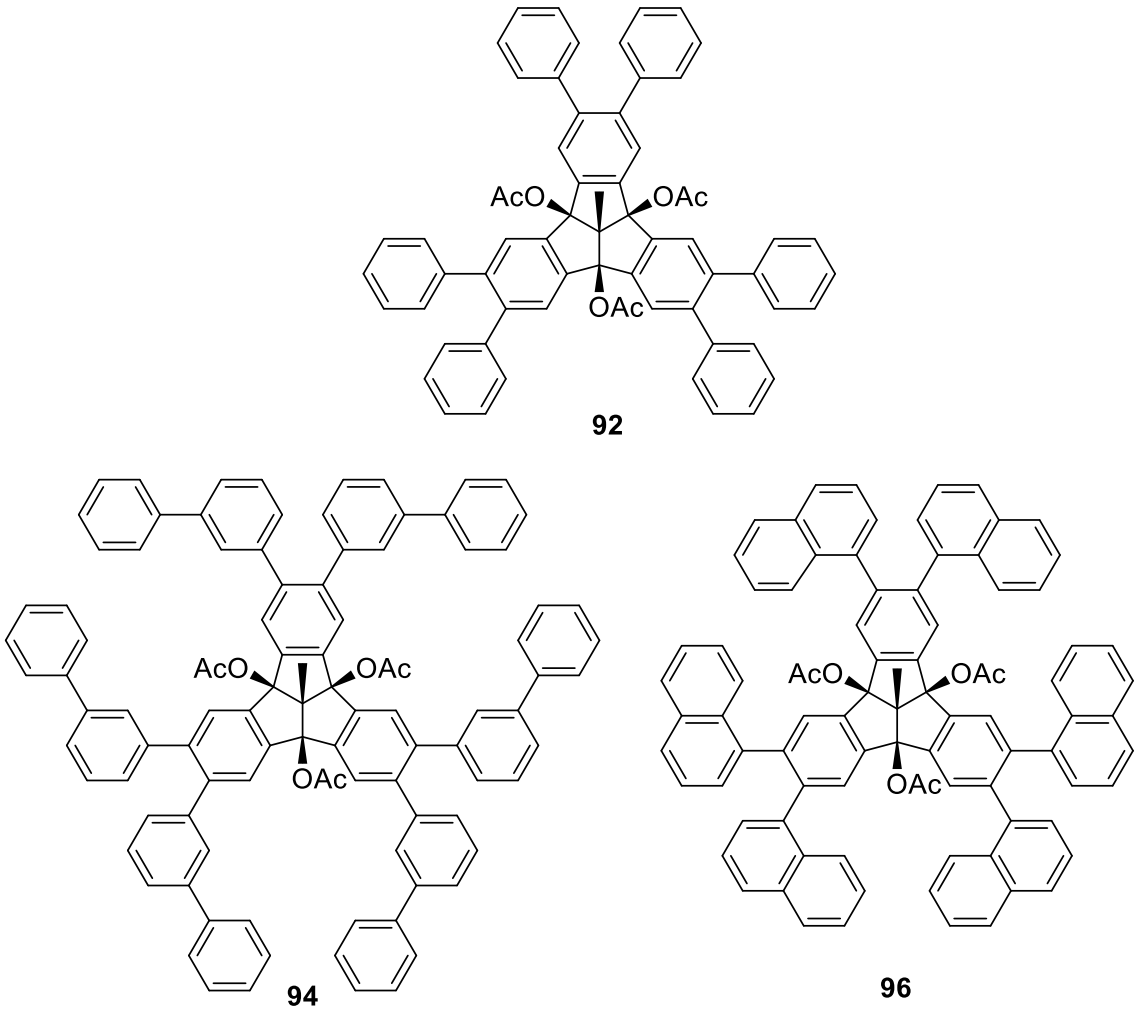

Figure 43. Three different synthesized π-extended TBTQ derivative molecules via Suzuki c ross-coupling reaction.

This work is primarily divided into two sections. One of the primary goals of this thesis is to synthesize and characterize π-extended benzannulated TBTQ derivatives, as well as to generate fully conjugated, dehydrogenated systems. The second major goal is to investigate and characterize the molecular self-assembly properties of these synthesized non-planar carbon-rich molecules, **92**, **94**, **96**, using STM spectroscopy.

With this motivation, three different bay positions protected, π-extended TBTQs were synthesized by Suzuki-Miyaura cross coupling reactions between iodo-TBTQ derivatives and various boronic acid groups (**Figure 43**). After isolation of the pure and fully characterized coupled compounds, as a next step, numerous types of Scholl reactions (see in **1.3. Results and Discussion** section) were several times performed for

benzannulation. However, due to the limitations of the Scholl reaction, attempts to synthesize benzannulated products were not achieved.

On the other hand, surface synthesis is one of the most useful and accessible method for benzannulation and can be established by STM.[174] Additionally, STM can be also used to investigate on surface molecular self-assembly characteristics of the molecules. In accordance with these properties, temperature dependent STM investigations of Me-TBTQ$(OAc)_3Ph_6$, **92**, on Cu (111) were conducted with the cooperation of the group of Prof. Matthias Bode (Department of Physics, University of Wuerzburg). It results in the formation of highly ordered 2-dimensional aggregates with distinct structural properties.

1.3. Results and Discussion

1.3.1 Protection Reaction of tertiary alcohols of TBTQ

As discussed in the introduction the bay positions of TBTQ are highly reactive. In this work, the functionalization of the TBTQ periphery is intended, thus, the bay positions need to be masked during these reactions steps. However, the established groups need to be easily removable in order to be able to eliminate them, e.g., in an attempt to aromatize the core of the TBTQ.

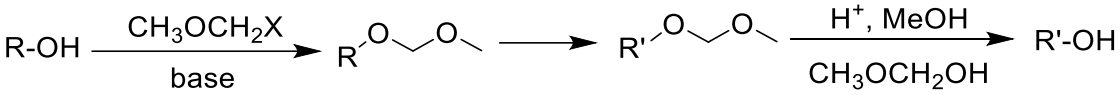

Figure 44. Schematic representation of protection reaction with MOM group in general.

In order to reduce the reactivity for further reactions, the protective group is attached only temporarily to bay positions so that the protected functional group does not react under the synthetic conditions that the molecule will be subjected to in one or more subsequent steps.

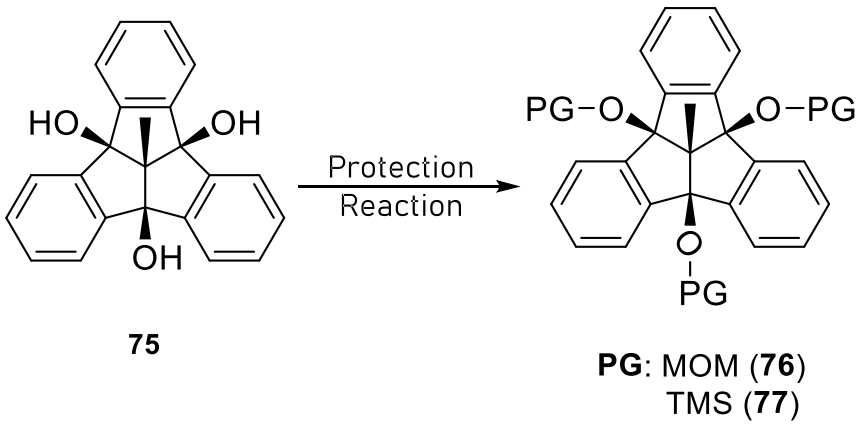

Figure 45. Protection reaction of bay positioned tertiary alcohol of Me-TBTQ(OH)$_3$ (**75**).

As it was mentioned in chapter 1.4.3, the bay position of TBTQ is the most reactive one. It is important to protect the OH groups to enable e.g., further halogenation, coupling,

and Scholl reactions. There are plenty of different protecting groups available for alcohols. Here, the position of the alcohols on the backbone is one of the most critical considerations of the protection reaction because they are tertiary. Furthermore, the selected protecting group should not be sterically hindering subsequent reactions. Thus, smaller protective groups were chosen with these considerations.

A range of different alcohol protection reactions were investigated, summarised in **Table 1**. Among the performed reactions, only the transformation using diisopropyl amine as the base was successful. The first attempted reaction was performed in the presence of NaH as a base and heated to reflux overnight. However, the isolated product did not show any characteristic peak in the NMR spectroscopy and unfortunately the product could not be obtained. In the second reaction, a NaI/DIPEA mixture was used as the base and the reaction mixture was heated to reflux for 12 h. Nonetheless, the reaction did not take place and resulted in the re-isolation of the starting material, which was observed using NMR spectroscopy. The characteristic singlet resonance, which belongs to OH groups of the precursor **75** was detected at δ= 5.70 ppm. The successful reaction conditions were adapted from Berliner *et. al.*[175] The starting material TBTQ(OH)$_3$, **75**, and 15 ml of *N*,*N*-Dimethylpyridin-4-amine (DMAP) were sequentially added to a mixture of 125 ml of toluene and 4.4 ml chloromethyl methyl ether (MOMCl, 10 Eq.). Contrary to the reported procedure, the reaction did not indicate proceed at ambient temperature after two hours. As a result, it was decided to heat the reaction mixture to reflux.

Table 1. Reaction conditions with different protecting groups

Starting Material	Base	Protecting Group	Solvent	Reaction Condition	Yield
Me-TBTQ(OH)$_3$ (**75**) 1 Eq.	NaH	MOMCl, 3.6 Eq.	THF	Overnight reflux	-
	NaI/DIPEA	MOMCl, 3.7 Eq.	DME	12 h reflux	-
	DMAP 15 Eq.	MOMCl, 10 Eq.	Toluene	18h reflux	87%
	imidazole	TMSCl	DMF	35 ^{o}C overnight under Ar	-

After 18 hours, the reaction was stopped as TLC did not indicate any remaining starting material. The work-up was performed according to the literature procedure. First, the reaction mixture was let to cool down to room temperature and then the solution was mixed with a EtOAc/sat. NH_4Cl mixture to allow decomposition of the residual starting material. The organic phase was extracted with $NaHCO_3$ several times. The product was obtained as a yellow powder with a yield of 87% after removing the organic solvent. The ^1H NMR spectrum revealed two singlet peaks, at 3.51 and 5.70 ppm, respectively. The first peak, at 5.70 ppm, represents 6H and belongs to the three MOM-CH_2 groups, while the second peak, at 3.51 ppm, represents 9H and belongs to three terminal CH_3 groups of the MOM ethers.

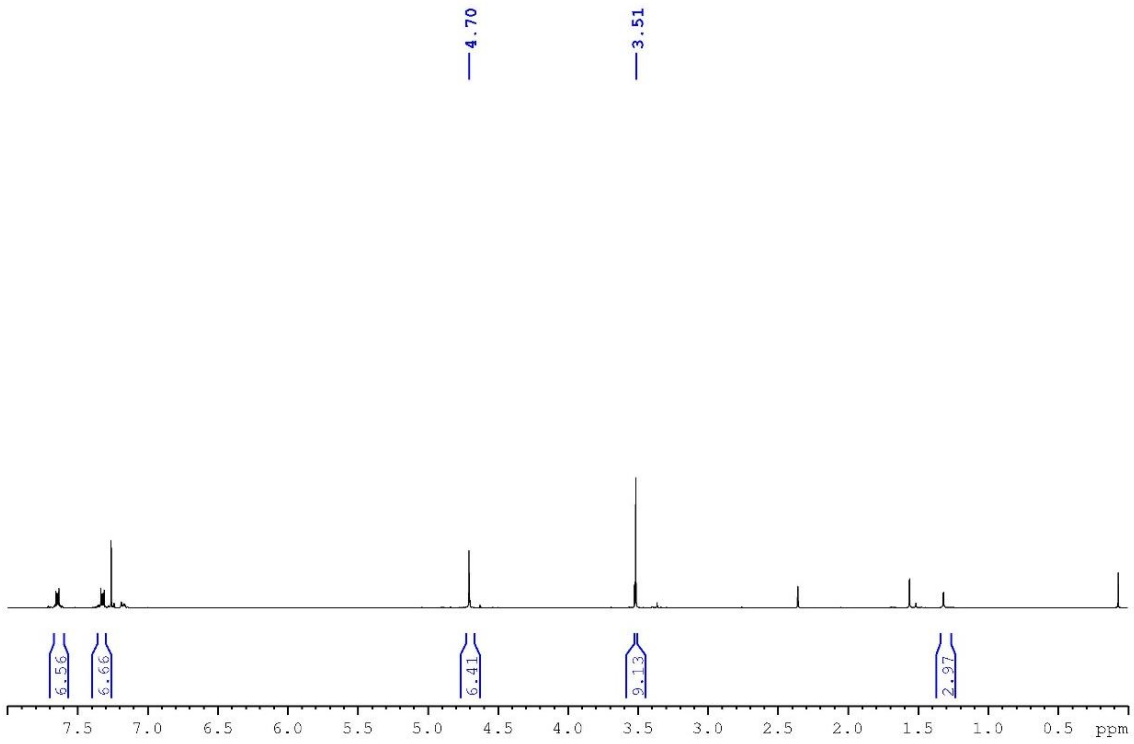

Figure 46. ^1H-NMR spectrum of TBTQ(OMOM)$_3$, (**76**).

Clearly, DMAP was the most effective base in the presence of MOMCl based on the comparison of the performed reactions.

1.3.2 Halogenation reaction of protected TBTQ derivative, 76

After protecting the OH groups in the bay positions, the next goal was the halogenation of the TBTQ framework in order to perform the outer rim functionalization of TBTQ via Suzuki cross-coupling reactions. (**Figure 47**) Therefore, a variety of reaction protocols were carried out. (Summarized in **Table 2**).

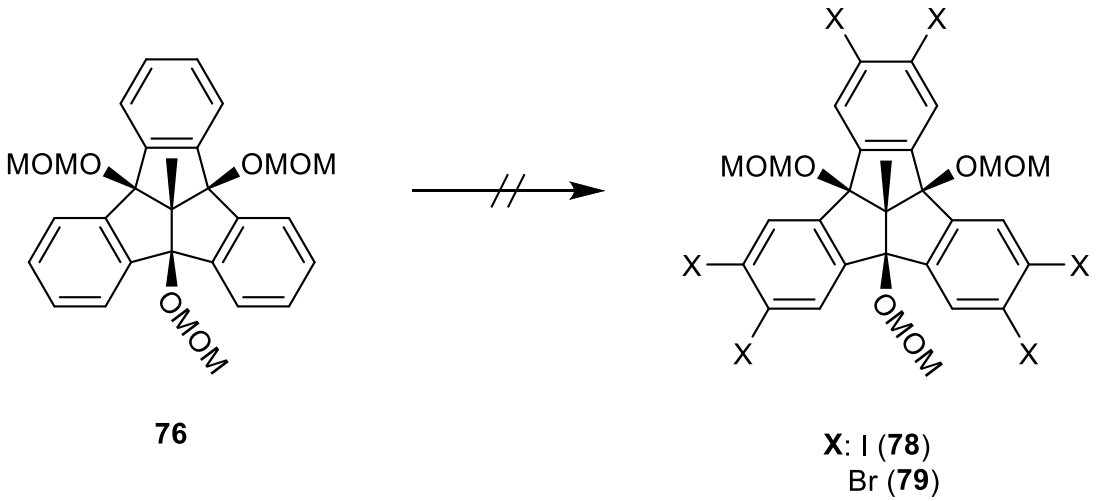

Figure 47. Attempted halogenation reaction of protected TBTQ derivative **76**

Table 2. Reaction conditions of different halogenation protocols.

Starting Material	Acid	Source of Halogen	Solvent	pH	catalyst
Me-TBTQ(OMOM)$_3$ (76) 1 Eq.	H_5IO_6 4.5 Eq.	KI 13.5 Eq.	conc. H_2SO_4	-	-
	-	Br_2	$CHCl_3$	-	Fe powder / I_2 crystals
	H_5IO_6 4.5 Eq.	KI 13.5 Eq.	1.4-dioxane H_2SO_4+ water	2.2	
	H_5IO_6 4.5 Eq.	KI 13.5 Eq.	1.4-dioxane H_2SO_4+ water	4.0	
	HBr	Br_2	HBr	-	-
	$HBF_4.Et_2O$ 7.2 Eq.	NBS 7.2 Eq	acetonitrile	-	-
	AcOH	NBS 8.0 Eq.	$CHCl_3$	≈2.0	
	-	Br_2	$CHCl_3$		Fe powder

The first attempted halogenation was iodination in the presence of periodic acid and potassium iodide with the help of conc. H_2SO_4 as a solvent at the same time. The procedure was performed according to literature.[140] The resulting product was investigated by ^{1}H-NMR spectroscopy. While a singlet resonance at δ =8.19 ppm was observed, which corresponds to six protons at the *ortho*- positions of TBTQ, no peaks were found at δ =4.70 and 3.50 ppm, which belong to the MOM groups. Furthermore, there was a rather weak resonance around 6.08 ppm as determined by ^{1}H-NMR spectroscopy (**Figure 48**), which could stem from free OH groups in bay positions. It can be understood that the six protons were belong to three outer benzene rings and therefore it was iodinated. However, the obtained product was not desired one because the lack of OMOM protons. The FT-IR spectroscopy was measured for better understanding.

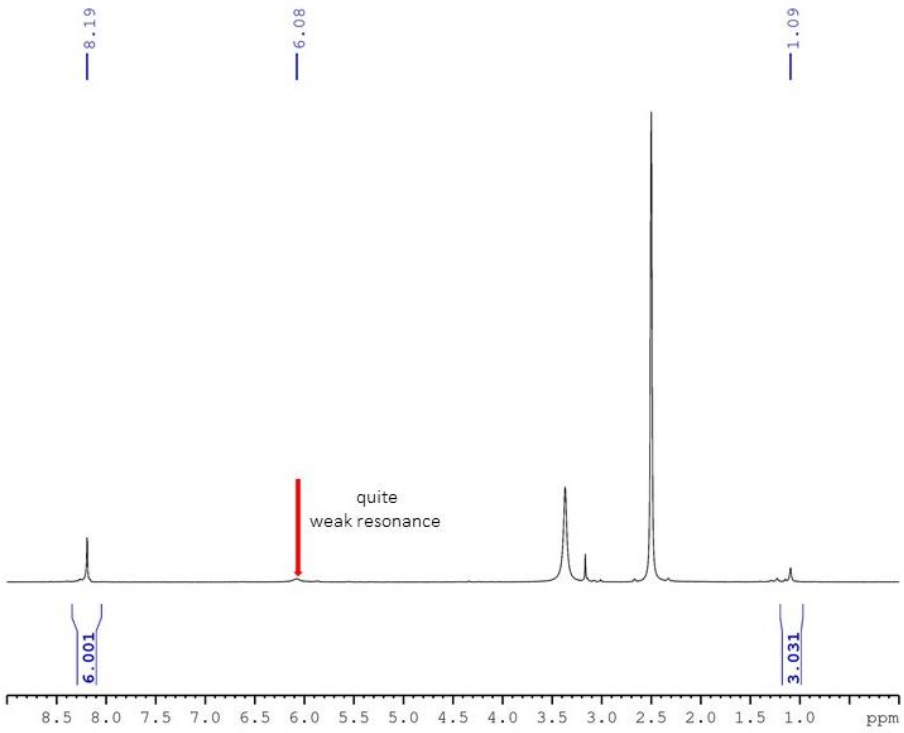

Figure 48. ^{1}H NMR spectrum of the halogenated product obtained from Me-TBTQ(OMOM)$_3$ (**76**).

Although it was not detected in ^{1}H NMR spectroscopy due to the weak resonance of OH group, FT-IR measurement unambiguously showed a typical OH peak around 3300 cm^{-1}. So, it can be interpreted that the OMOM group were cleaved and therefore it gave rise to OH groups again (**Figure 49**).

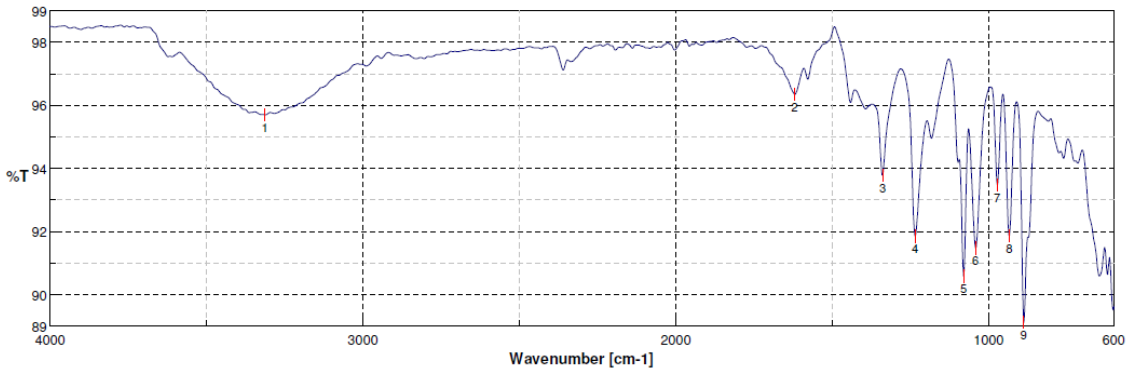

Figure 49. FT-IR spectrum of the halogenated product obtained from Me-TBTQ(OMOM)$_3$ (**76**).

Methoxymethyl ether (MOM) is a good leaving group as well. As mentioned above, the iodination reaction was partly achieved, however, none of the isolated components of bromination experiments could be identified. As it can be seen from the **Table 2**, most of the halogenation reactions require acidic conditions and none of them was successful. Although the known reaction conditions were adjusted at different pH values, the desired product could not be obtained. Furthermore, the reactions resulted in either re-isolation of the starting material or Me-TBTQ(OH)$_3$ (**75**) which is formed by deprotection of Me-TBTQ(OMOM)$_3$ (**76**). It was discovered that the MOM group is vulnerable at lower pH values and the more so for certain halogens. It is also clear from these results that the acid and the source of the halogen mixture were not strong enough to perform the halogenation reaction successfully. In addition, the acidity of the reaction was a key point, and it was quite low for the good leaving MOM group. Based on the outcomes and the unintended de-protection, the order of the halogenation and protection reactions was inverted. With this modification the Me-TBTQ(OH)$_3$ was first halogenated and subsequently the protection reaction was performed as a second step.

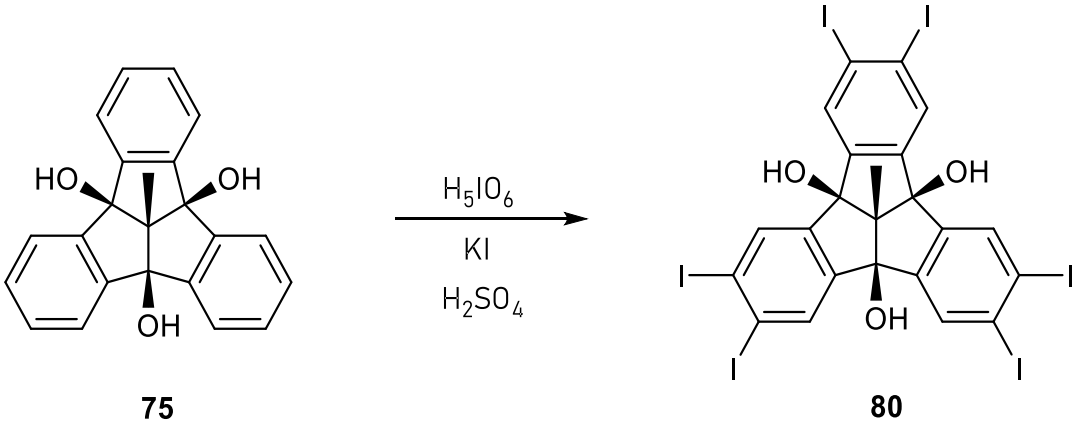

75 **80**

Figure 50. Iodination reaction of Me-TBTQ(OH)$_3$ (**75**) following the procedure by Kuck et al.[140]

The six-fold iodination at the outer rim of Me-TBTQ(OH)$_3$ (**75**) was first performed as described by Kuck *et al.* [140] (**Figure 50**). Iodine is generated *in situ* from potassium iodide and periodic acid and then oxidized by sulphuric acid, which is used as a solvent as well. Following the mechanism of an electrophilic aromatic substitution, the oxidized iodine is attacked by the benzene rings of the Me-TBTQ(OH)$_3$ (**75**). Since the reaction

conditions are quite harsh, milder ones were already tested in previous work of the group, however these were reported to be unsuccessful.

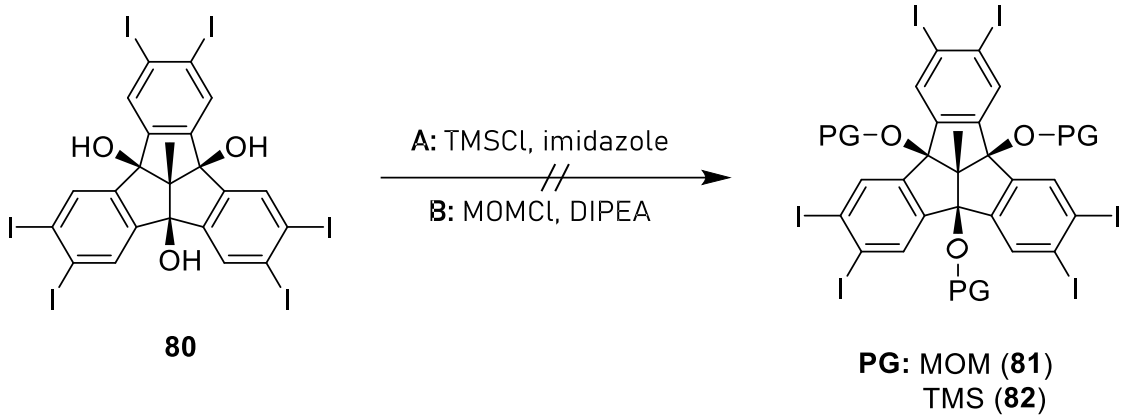

Figure 51. Protection reaction of Me-TBTQ$(OH)_3I_6$, (**80**)**,** after halogenation.

Following the halogenation reaction to **81** and **82**, several protection reactions were carried out with TMS and MOM as protecting groups. Although the reaction order was modified, the attempted protection reactions were not successful. It was determined that selecting an appropriate protective group is crucial, and in this situation, it was critical to choose a protecting group that is appropriate for tertiary alcohols.

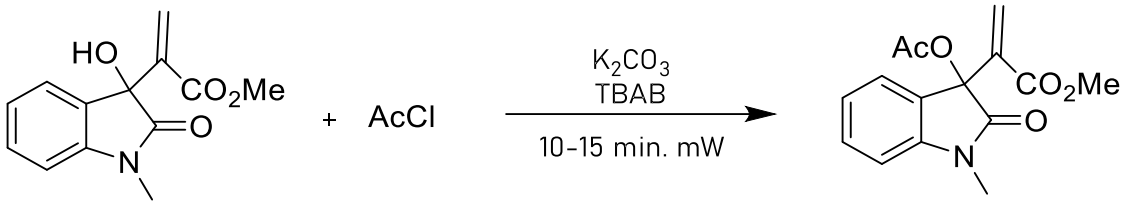

Figure 52. Microwave-assisted acetyl protection reaction of tertiary alcohols.[176]

According to literature, 4-dimethylaminopyridine (DMAP) and 4-pyrrolidinopyridine (PPY) have high catalytic activity and can be used to acylate sterically hindered secondary or tertiary alcohols using carboxylic anhydrides or acyl halides. Therefore, the most applicable protocol for protection of tertiary alcohols was identified (**Figure 54**, **A**) and performed.

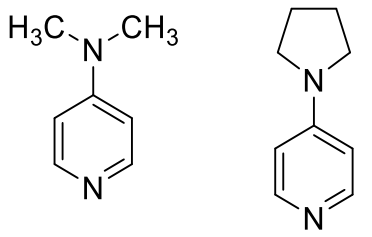

83 84

Figure 53. Molecular structure of DMAP (**83**) and PPY (**84**).

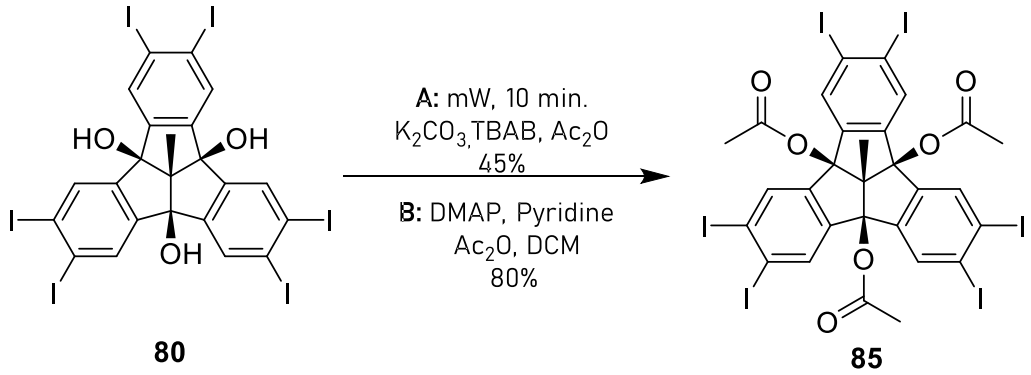

80 85

Figure 54. Different synthetic protocols of acetyl protection of TBTQ derivative, **85**.

The microwave promoted protection reaction was performed in the presence of acetic anhydride, K_2CO_3 and TBAB with yields comparable to those reported in literature. The reaction requires only microwave equipment with a power of 1000 Watt, and the reaction is carried out at 100 °C for 10 min. The work-up procedure was performed according to literature. After cooling the reaction mixture to room temperature, the crude mixture was dissolved in ethyl acetate and filtered through celite powder then purified using silica-gel column chromatography. The product was isolated as a colourless powder with a yield of 45%. It can be clearly seen from the ^{1}H-NMR spectrum of Me-TBTQ$(OAc)_3I_6$ (**85**), that the peak with the integral of 9H at δ= 2.07 ppm, which is typical for acetyl group is present. While the microwave reaction takes just a short amount of time, it does have certain limitations, such as the amount of applicable starting material. Despite the fact that the yield was not very low, the inability to accomplish the reaction with a larger amount of starting material prohibits the production of a sufficient quantity of the

product. It would be inefficient to repeat the reaction in order to collect a proper amount of product. As a result, a new acetyl protection reaction procedure was found and adjusted based on previous research.[177]

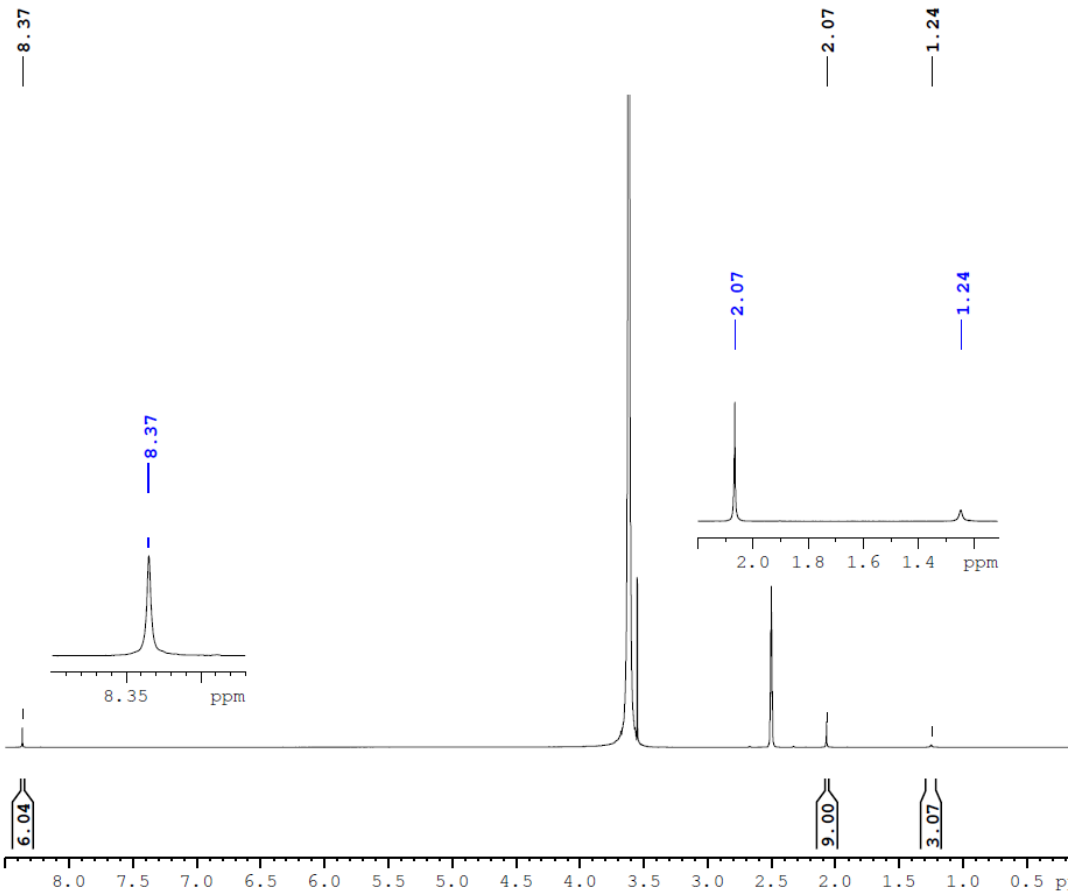

Figure 55. ^{1}H-NMR spectrum of acetyl protected TBTQ derivative, **85**.

The acetyl protective group is introduced using acetic anhydride, which is then activated by catalytic amounts of dimethyl aminopyridine (DMAP). To ensure that the reaction occurs at all three tertiary alcohol groups, a significant excess of acetic anhydride was used. The procedure was carried out under alkaline conditions using a solvent mixture of pyridine and dichloromethane. The starting material is insoluble in nonpolar solvents such as *n*-hexane and toluene due to the alcohol groups, and the large carbon-rich framework inhibits solubility in polar solvents as well. Therefore, the solubility of the starting material was a challenge during this step of the synthesis. In the end, **80** was suspended in dichloromethane using an ultrasonic bath, and then eventually dissolved by

addition of pyridine. Subsequently, acetic anhydride (Ac_2O) and DMAP were added. The reaction mixture was stirred for three days at room temperature. To complete the reaction, the resulting solution was mixed with diethyl ether and washed with unsaturated hydrochloric acid, sodium bicarbonate, and brine solutions. The product was purified by recrystallization using DCM and obtained with a yield of 80%. The compound shows two singlet peaks at δ=7.90 ppm δ=2.16 ppm in the ^{1}H-NMR spectrum. In addition, ^{13}C-NMR spectroscopy shows an individual line at δ=170 ppm which is typical for the C=O bond from the acetate group. Mass spectrometry shows an intensive peak at m/z 1164 and a quite weak peak at m/z 1223. The difference between values refers to m/z 59 due to the facile loss of one acetate group. However, all the corresponding data show that the hexaiodo-Me- TBTQ$(OAc)_3$ (**85**) was successfully synthesized.

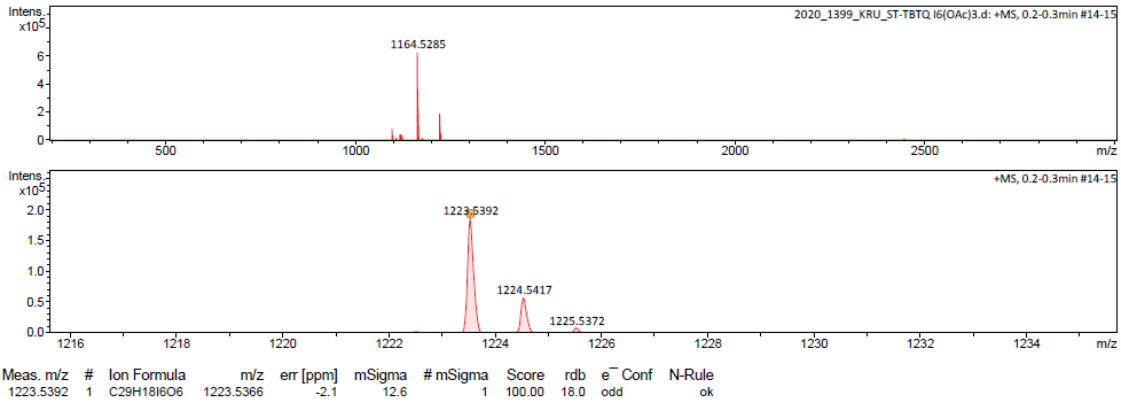

Figure 56. APCI mass spectrum of Me-TBTQ$(OAc)_3I_6$ (**85**).

1.3.3 π-Extension via Suzuki Coupling

The aim of the halogenation and protection reactions was to extend the π-system and then implement the Scholl reaction. To annulate the wings of the TBTQ core. As it was mentioned in chapter **1.1.4.3**, there are various possible approaches of π-extension. In 1999 Tellenbröker and Kuck hypothesized that TBTQ could be considered as a defect centre for nanographene.[143] Therefore, the π-extension and following cyclodehydrogenation reaction started to gain their attention.

After achieving the synthesis of Me-TBTQ$(CH_3)_3I_6$ (**86**), Tellenbröker *et al.* first introduced the phenyl rings to parent system via Suzuki cross-coupling reaction.

Following that, a photocyclodehydrogenation procedure was carried out in a falling film photo reactor by irradiating the benzene solution of the starting material under argon atmosphere in the presence of iodine and propylene oxide for 18 hours. While this approach successfully affords ed three-fold cyclodehydrogenation of **87** with relatively good yield, the hexanaphtyl substituted tetramethyl TBTQ derivative **90** only demonstrated one-fold photo-induced cyclization (**Figure 57**).

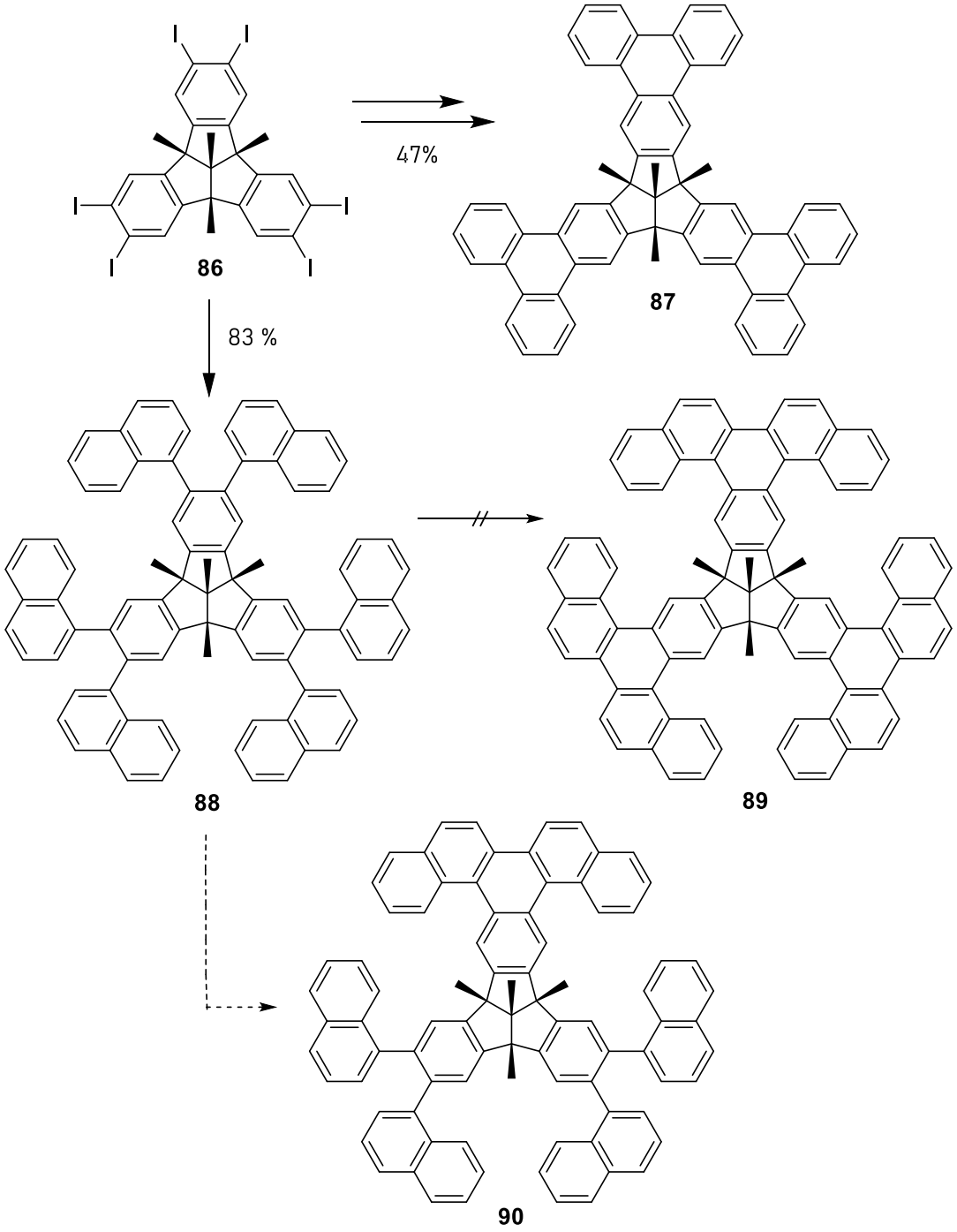

Figure 57. Synthesis of **90** by Tellenbröker.[143, 178]

In this thesis, a similar strategy was followed, however, using different protective groups (**Figure 58**). The products of the grafting of six phenyl, naphthyl or biphenyl groups are thus not literature known; however, the reactions were carried out similar to known procedures.[155] All of the reactions were performed under nitrogen atmosphere. The starting material and the boronic acids were placed into a Schlenk flask and dissolved in a nitromethane/water mixture. After adding KOH and PPh_3, the resulting solution was degassed three times.

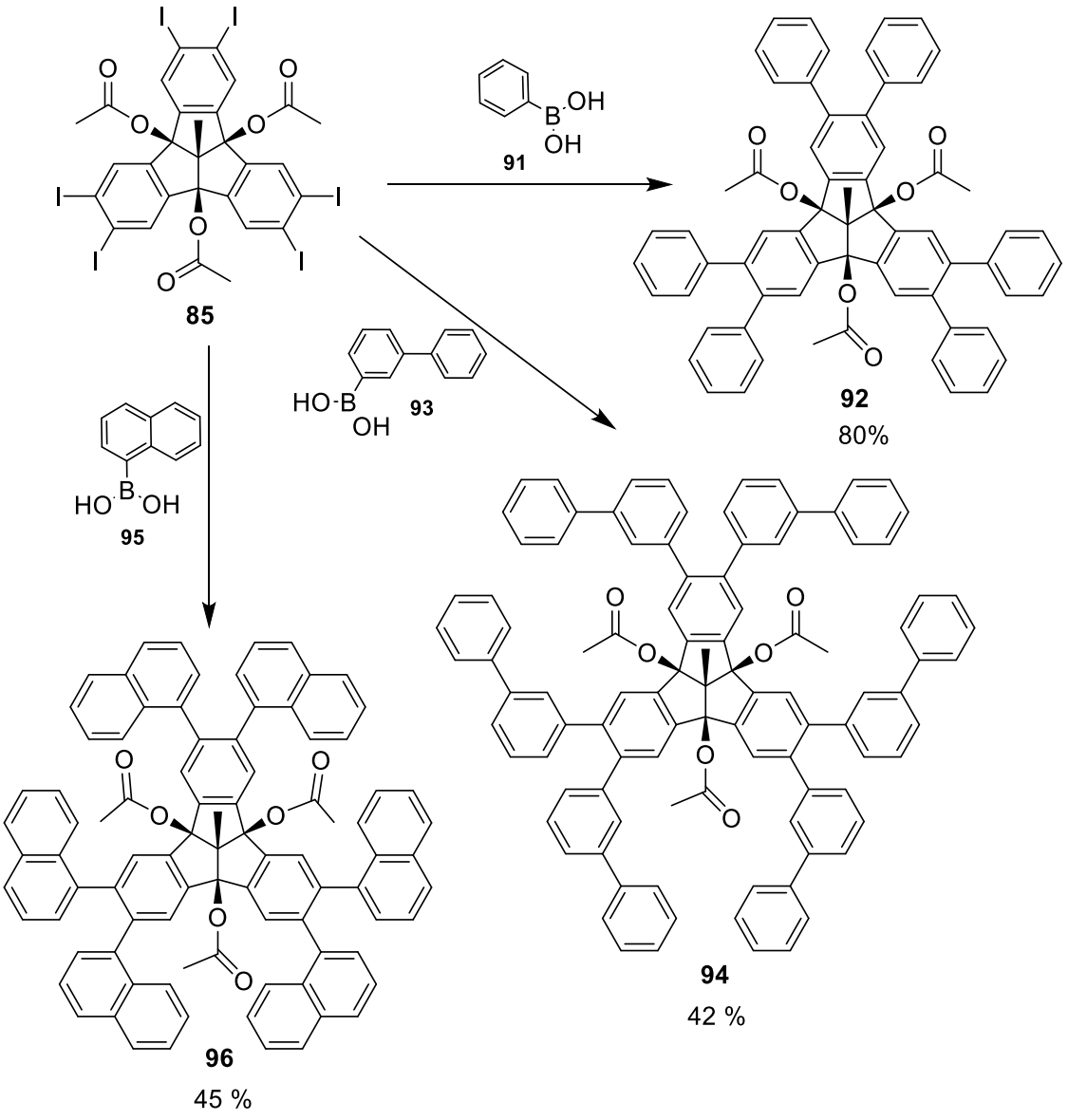

Figure 58. Overview of performed multiple Suzuki cross-coupling reactions with different boronic acids.

Subsequently, a catalytic amount of the $Pd(dba)_2$ catalyst was added and degassed once more. The reaction mixture was stirred overnight at 110 °C. TLC was used to finish the reactions until there was no more starting material left. The work-up procedure was done by removing $PhNO_2$ via cold trap under reduced pressure followed by extraction and column chromatography, affording the desired hydrocarbons in relatively high yields.

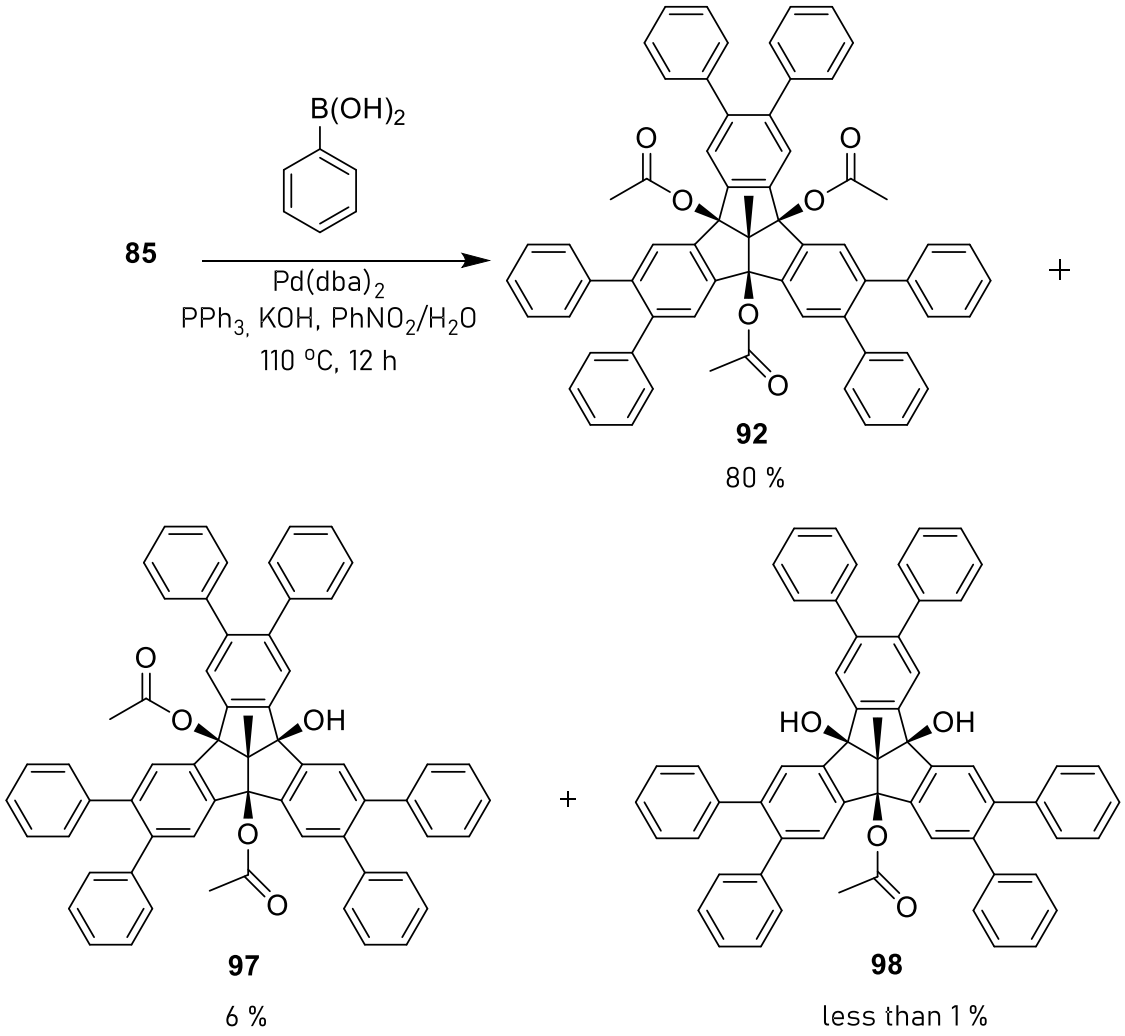

Figure 59. Multiple Suzuki cross-coupling reactions of the hexaiodotriacetate-TBTQ derivative **85** with phenylboronic acid (**91**) to **92** and the isolated side products **97** and **98.**

The molecular C_{3v} symmetry is reflected in the ^{1}H-NMR spectra. The product **92** shows a sharp singlet peak with six protons for the *ortho*-positions of the TBTQ core at $\delta = 7.59$ ppm. The six peripheral phenyl rings give rise to two multiplets with 18H and 12H.

centred at = 7.17 and 7.05 ppm, respectively. The bay-positioned acetate groups show a singlet peak at δ= 2.20 ppm with an integral of 9H

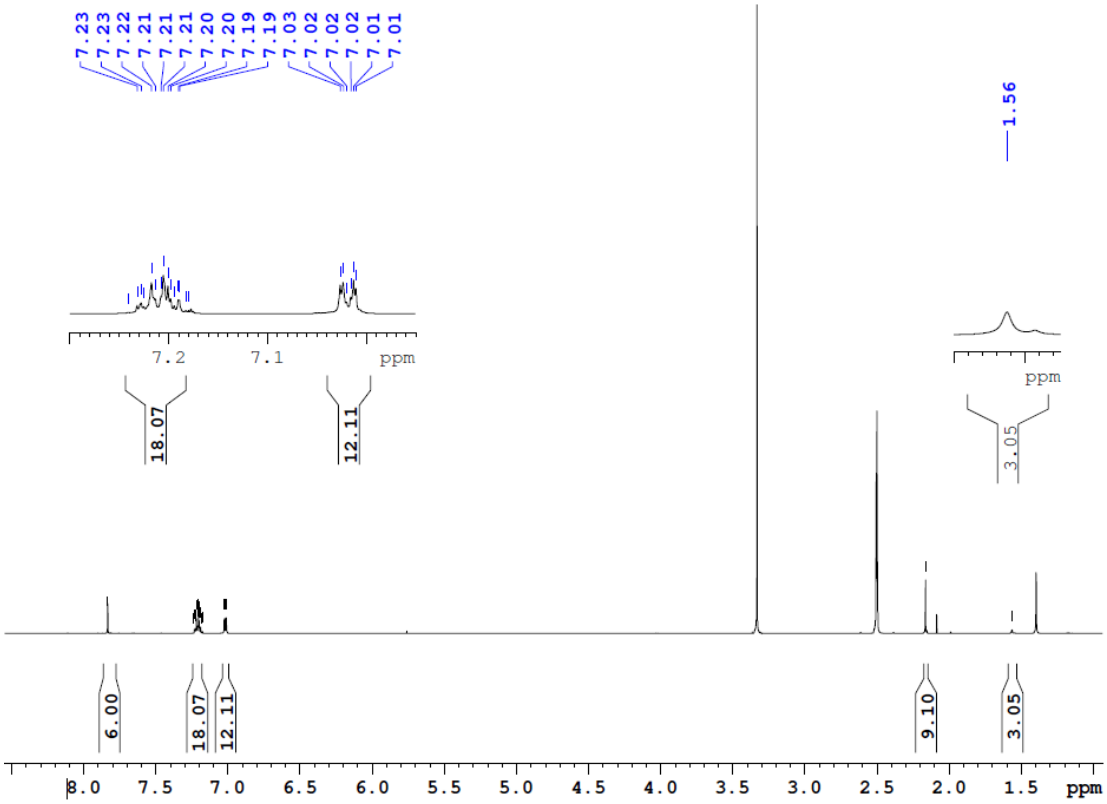

Figure 60. ^{1}H-NMR spectrum in d_6-DMSO of hexaphenyl-substituted Me-TBTQ (**92**) (The peaks which are at 1.4, 2.05 and 3.33 ppm corresponds to cyclohexane acetone and water respectively)

The 65 carbon atoms of hydrocarbon **92** give rise to only 12 individual lines in the ^{13}C-NMR spectrum. The ASAP mass spectrum of **92** exhibits a low intensity molecular ion peak at m/z 924 and the base peak at m/z 865, which again indicates the facile loss of an acetate radical group. The purity of product **92** was also verified with HPLC using ACN as the eluent. A single peak was observed with a retention time of 8.5 min with UV detection at 220 nm. Furthermore, two side products were isolated with a very low yield as well. Fortunately, the ^{1}H-NMR characterization could be done, and the products were identified as the partially deprotected derivatives **97** and **98** (**Figure 59**). The ^{1}H-NMR spectrum shows three sharp singlet peaks at δ= 7.74, 7.63 and 7.54 ppm. Each peak represents two protons which belong to *ortho*-positioned protons of parent TBTQ. Thereby, it was clear that the C_{3v} symmetry of the desired product was broken. Besides,

an additional singlet peak appears at δ= 3.05 ppm with one proton and the number of protons of acetate groups is reduced from nine to six for the peak at δ=2.20 ppm. This indicates that one OH group was placed in the bay position instead of an acetate. Further, the second isolated side product exhibits three sharp singlet peaks as well. **97** shows a singlet peak at δ=2.89 ppm with two protons and the typical acetate peak has an integration of three protons at δ=2.20 ppm. Thus, it can be concluded that two OH groups were located in the bay positions (**Figure 59**).

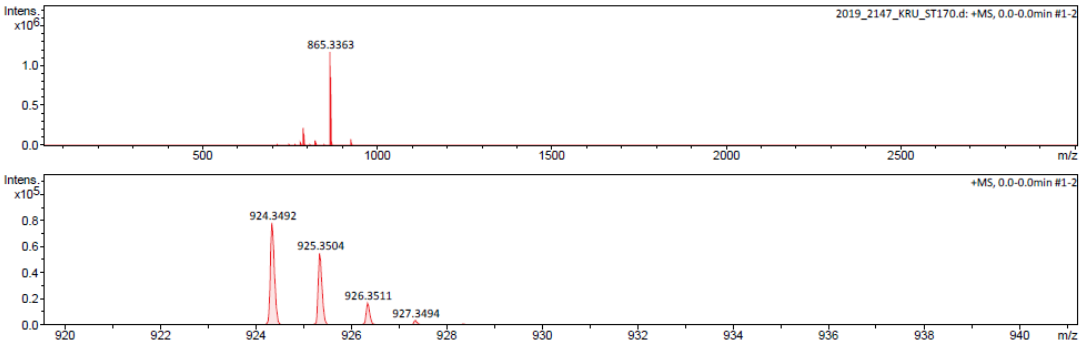

Figure 61. APCI-DIP mass spectrum of Me-TBTQ(OAc)$_3$Ph$_6$ (**92**).

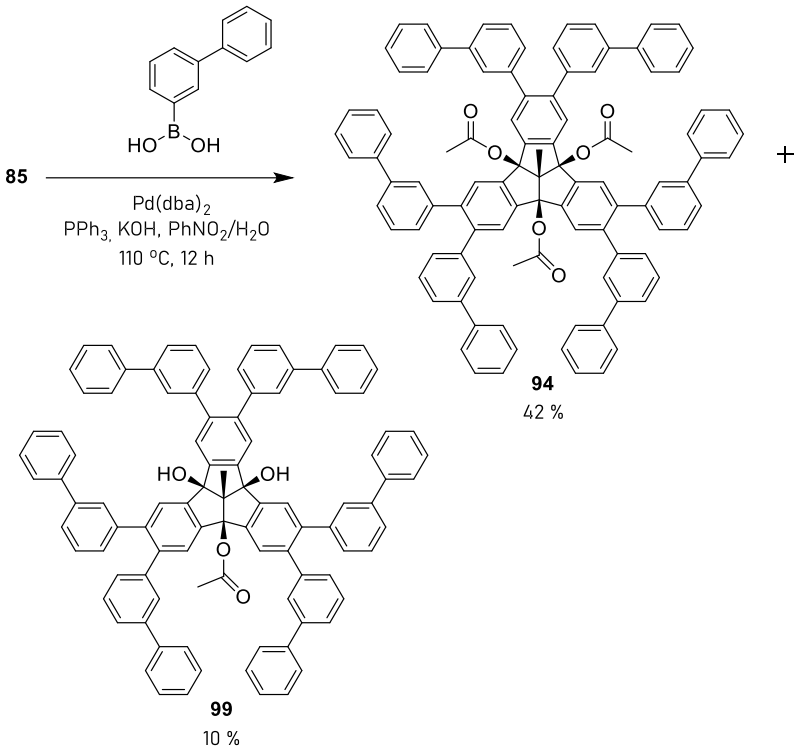

Figure 62. Multiple Suzuki cross-coupling reaction of the hexaiodotriacetate-TBTQ derivative **85** with biphenylboronic acid (**93**) to **94** and isolated side product **99**.

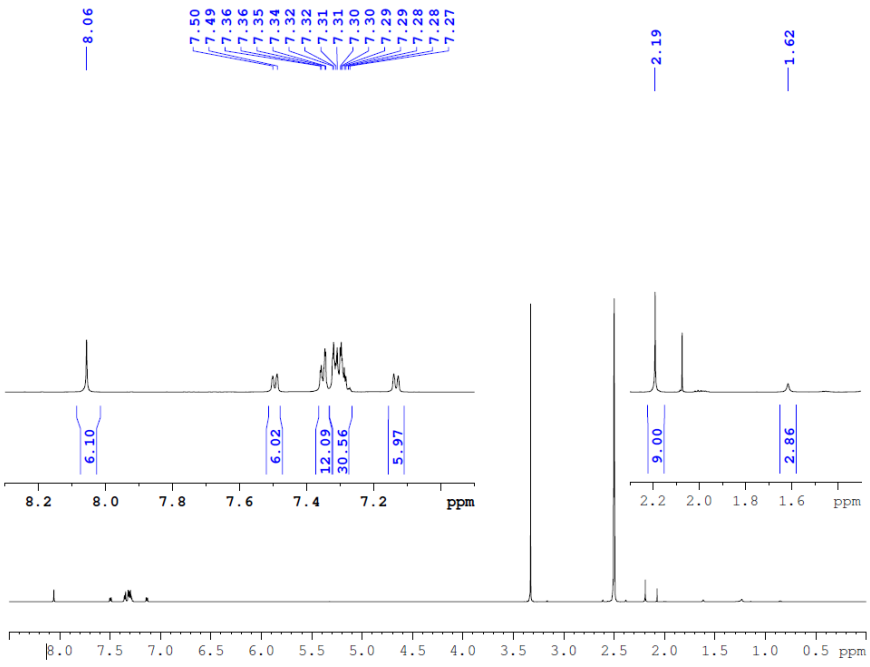

Figure 63. ^{1}H- NMR spectrum of hexa-biphenyl substituted Me-TBTQ derivative (**94**). (The peaks which are at 1.4, 2.05 and 3.33 ppm corresponds to cyclohexane acetone and water respectively)

Figure 62 illustrates the six-fold Suzuki cross-coupling reaction of hexaiodotriacetate-TBTQ **85** with biphenylboronic acid. The molecular C_{3v} symmetry is reflected in the ^{1}H- and ^{13}C-NMR spectroscopy as well. The product **94** shows a sharp singlet peak with six protons for the *ortho*-positions of the TBTQ core at δ = 7.65 ppm. The biphenyl groups possess 54 protons in the aromatic region in total and show four different multiplets centred at δ= 7.48, 7.36, 7.32 and 7.27 ppm, respectively (**Figure 63**). As it was observed, **94** shows a typical acetate peak with 9 protons at δ=2.20 ppm. **94** contains 101 carbons in total and the ^{13}C-NMR spectrum exhibits only 18 individual lines. In order to measure the exact mass of the product, various mass spectroscopies such as ASAP, MALDI-TOF and APCI-DIP were carried out. They exhibit a very low intensity molecular ion peak at m/z 1381 and the most intensive peak was at m/z 1322. The difference is due to the facile loss of acetate group and corresponds to molecular weight of a cleaved acetate (m/z 59) as well. The product was submitted to reverse phase high pressure liquid chromatography

(RP-HPLC) in order to confirm purity and a sharp peak was observed at a retention time of 27 min and UV detection at 250 nm.

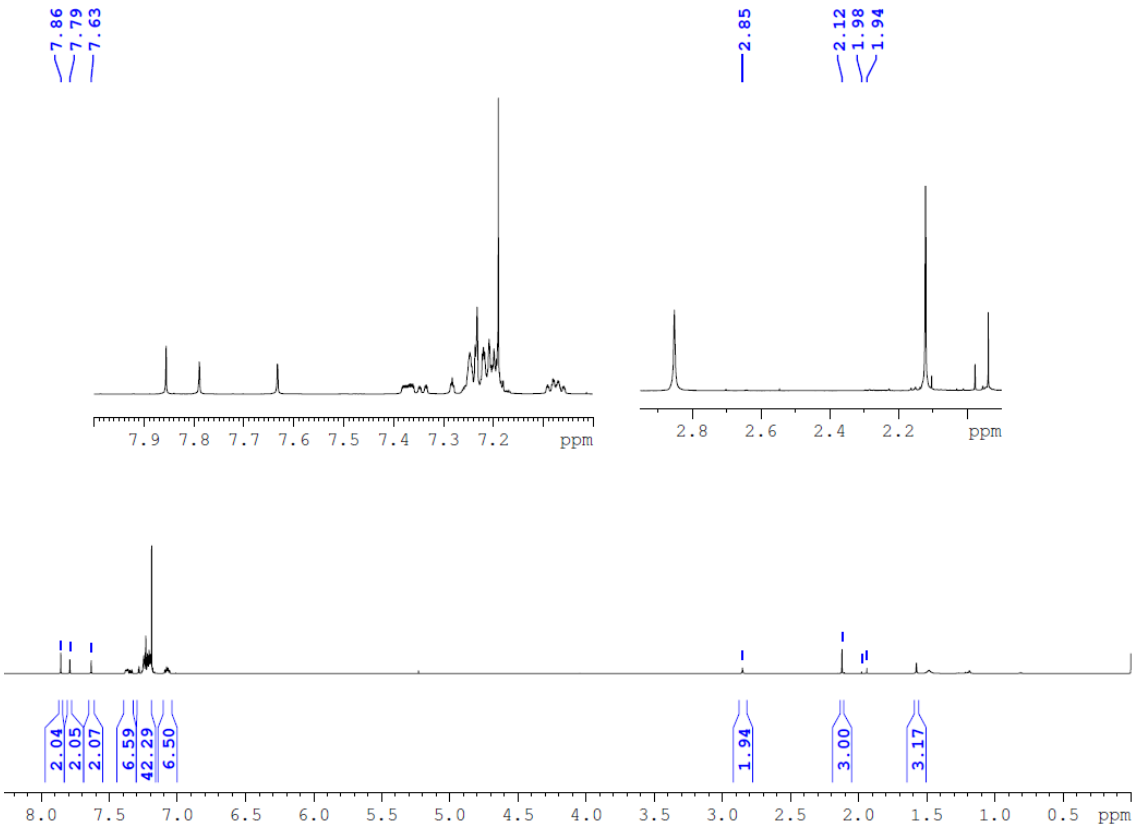

Figure 64. ^{1}H- NMR spectrum of side product (**99**), Me-TBTQ(OH)$_2$Bp$_6$

The only isolated side product is shown in **Figure 62**. Spectroscopic properties of **99**, correspond to the characteristics observed for the main product **99**. It exhibits three sharp singlet peaks at δ= 7.92, 7.86, 7.70 ppm. Each peak corresponds to two protons, which belong to *ortho*-positioned protons of the parent TBTQ. The acetate peak appears at δ= 2.19 ppm, however with three protons instead of nine. The new broad singlet peak appears at δ= 2.92 ppm representing two protons, which corresponds two OH groups. Additionally, the singlet peaks in the aromatic regions were moved to lower field due to the influence of OH groups in the bay positions. Additionally, the singlet peaks in the aromatic regions were moved to lower field due to the influence of OH groups in the bay positions.

The hexanaphthyl derivative **96** was obtained using the Suzuki cross coupling reaction of **85**-naphthyl boronic acid with hexaiodotriacetate-TBTQ **96** (**Figure 65**).

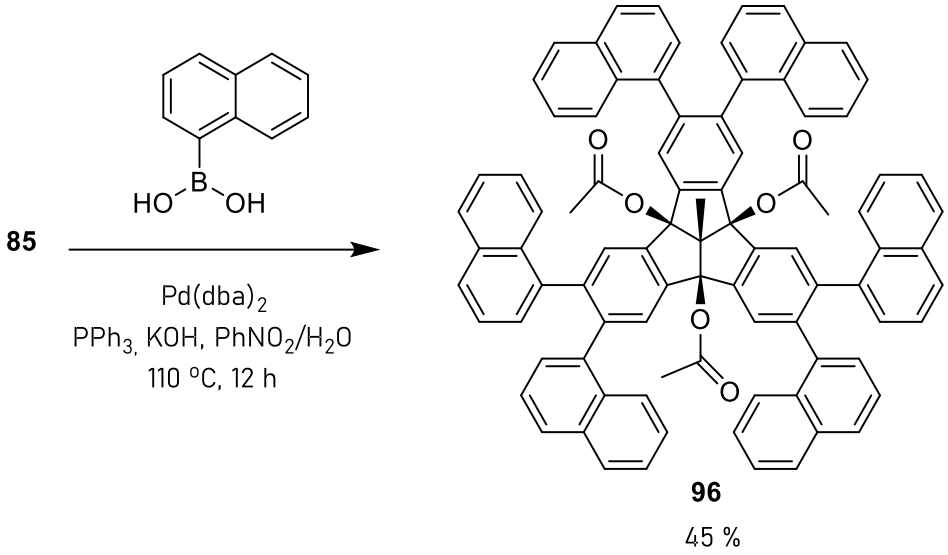

Figure 65. Multiple Suzuki cross-coupling reaction of the hexaiodotriacetate-TBTQ derivative **85** with naphthylboronic acid (**95**), to **96**

Column chromatography afforded the hexanaphthyl-TBTQ derivative **96** in a yield of 45 %. The resulting product was characterized by various mass spectroscopic methods such as MALDI-TOF, APCI-DIP ASAP which all revealed a very intensive mass peak at m/z 1165 and a quite low peak at m/z 1224 corresponding to Me-TBTQ$(OAc)_2Np_6$ and Me-TBTQ$(OAc)_3Np_6$ (**96**), respectively. An ESI (+) mass spectrum with Na, K as an additive was performed to confirm the identity of hydrocarbon **96.**

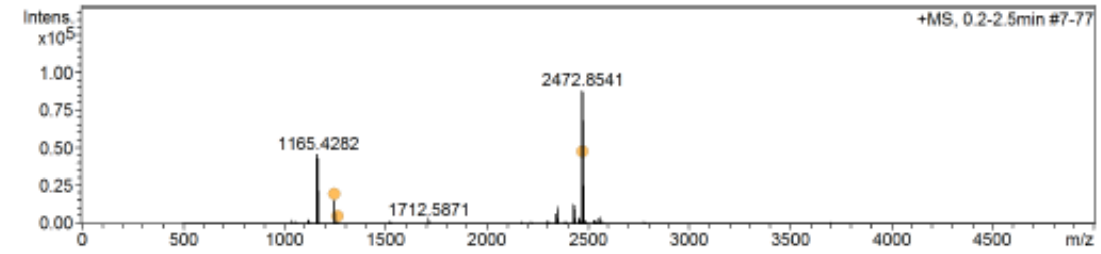

Meas. m/z	#	Ion Formula	m/z	err [ppm]	mSigma	# mSigma	Score	rdb	e¯ Conf	N-Rule
1247.4309	1	C89H60NaO6	1247.4282	-2.1	20.8	1	100.00	59.5	even	ok
1263.4054	1	C89H60KO6	1263.4021	-2.6	36.7	1	100.00	59.5	even	ok
2471.8491	1	C178H120NaO12	2471.8672	7.3	14.0	1	100.00	118.5	even	ok

Figure 66 The ESI Mass spectrum of **96**

On the other hand, in the ^{1}H and ^{13}C NMR spectra, the hexanaphthyl substituted Me-TBTQ(OAc)$_3$ (**96**) showed completely different characteristics compared to the analogues **92** and **94.** The spectra were significantly more complex than expected for a C_{3v} symmetrical structure. For instance, the ^{1}H-NMR spectrum demonstrates a broad multiplet in the aromatic region at δ= 8.16 - 6.56 ppm and several resonances for the bridgehead acetate and *centro*-methyl groups. The similar finding was reported by Linke *et al.* for the hexanaphthyl substituted tetramethyl-TBTQ derivative **88** (**Figure 57**) as well.[155] As they reported, this observation is due to the strongly hindered internal rotation of the 1-naphthyl residues at the concave TBTQ core. Moreover, the ^{13}C-NMR spectrum also demonstrates a mixture of rotamers, similar to the report by Linke *et al.* However, the lack of any diagnostic peak between iodine and aryl carbon that the starting material has at δ = 110.0 ppm proves the successful completion of the Suzuki cross-coupling reaction.

In summary, the multiple Suzuki cross-coupling reactions of Me-TBTQ(OAc)$_3$I$_6$ (**85**) were successfully carried out, leading to the hexa-substituted derivative **92**, **94** and **96**. The obtained yields were consistent with similar examples from literature. In addition, side products were identified through ^{1}H- and ^{13}C-NMR spectroscopy and mass spectrometry. The spectroscopic data of obtained products were consistent.

1.3.4 Annulation of π-extended TBTQ derivatives via Scholl reaction

In 2012 Mughal and Kuck achieved the synthesis of a TBTQ core bearing molecule containing a single PAH unit bridging one of the bay positions via Scholl reaction. The resulting structure was annulated by benzene moieties and additionally by a cycloheptatriene ring fused to mutually merged structure of both the bowl-shaped TBTQ and a (quasi-planar) hexa-peri-hexabenzocoronene (HBC) in the case of **35** as the precursor.[140]

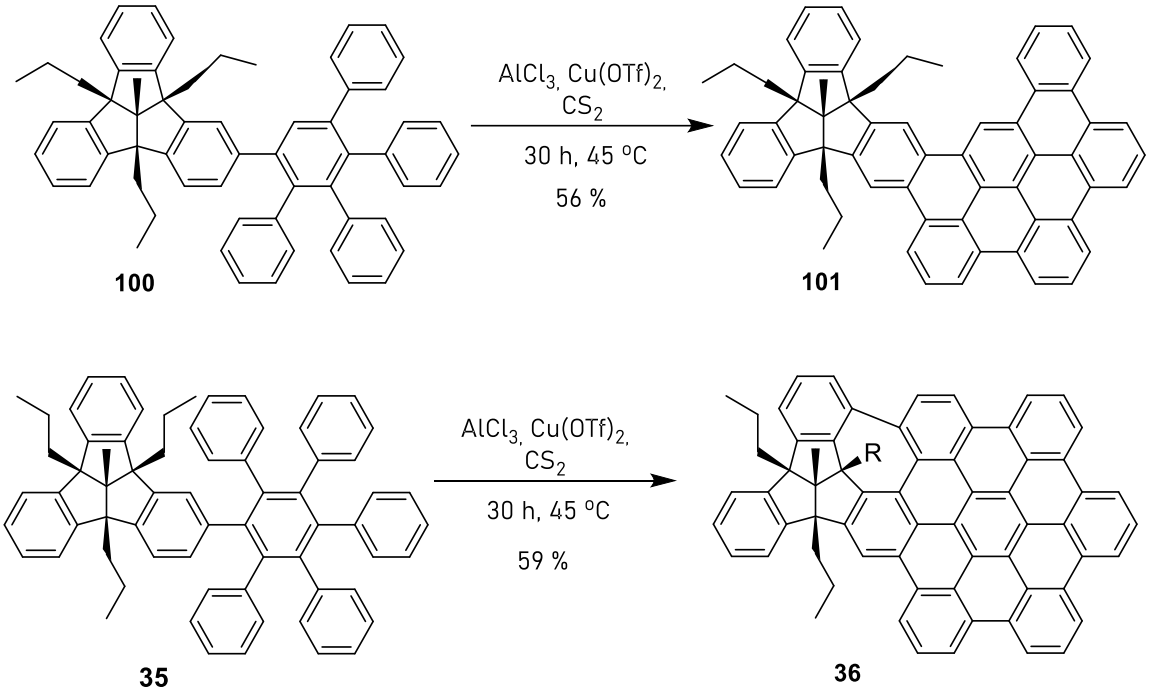

Figure 67. Bay-bridging Scholl reaction of oligophenylphenyl-TBTQ derivatives-substituted TBTQ derivatives.[140]

The cyclodehydrogenation was performed under Lewis acidic conditions. Application of the conventional Scholl reaction reagents, such as $FeCl_3$, only returned the starting material. Therefore, it was tried to use different oxidant systems containing $Cu(CF_3SO_3)_2$– $AlCl_3$–CS_2 and $FeCl_3$–$MeNO_2$–CH_2Cl_2 and as reported, the Cu $(CF_3SO_3)_2$– $AlCl_3$–CS_2 mixture gave better results regarding side reactions, chlorination or migration of alkyl. Under the chosen conditions, the Scholl reaction took place smoothly and exclusively in an intramolecular manner to provide the polycondensed

TBTQ derivatives. The product **36** contains one seven-membered ring formed between the HBC and one of the benzene rings in the triquinacene core.

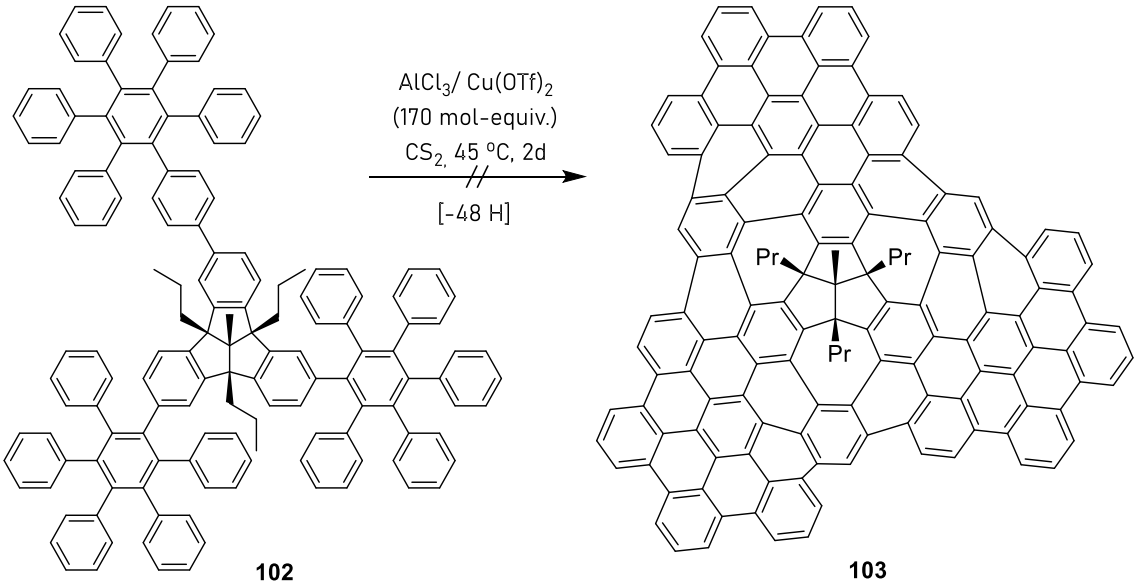

Figure 68. Attempted multiple cyclodehydrogenation of **102** to form **103** with a TBTQ core.[170]

Attempts to synthesize a C_3-symmetric analogue of **102**, containing three HBC moieties failed (**Figure 68**). Although the tris(pentaphenylphenyl)tribenzotriquinacene was successfully synthesized, multiple ring formation of **103** was not observed under similar conditions. Furthermore, only mixtures of starting material and partially dehydrogenated products were obtained. Consequently, it was concluded that the particularly bulky starting material and poor solubility of intermediates likely prevented the complete intermolecular C-C bond formation. Additionally, the concave side of the core of the TBTQ was occupied by the overcrowding of the phenyl groups, which resulted in an unintentional cyclodehydrogenation reaction.[170]

In 2012 Kirchwehm attempted to perform bay bridging Scholl reactions, however, instead an unexpected formation of a product **106** methoxylated at one of the bay positions of molecule was observed. It was only isolated a mixture of the starting material and this side product. The side product **106** was confirmed by ^{1}H NMR spectroscopy, which exhibits a peak at $\delta = 3.06$ ppm and a peak of mixture at m/z 510 (MALDI-TOF). Nevertheless, this competing reaction was not completely surprising because of the

potential chlorination in the presence of the $FeCl_3$ during Scholl reaction as already reported in literature.[179-181] As the reaction mixture was quenched with MeOH to finish the reaction, the subsequent substitution of Cl in the double benzylic positions of the TBTQ occurred, leading to the formation of methoxy substituted TBTQ **106**.[168]

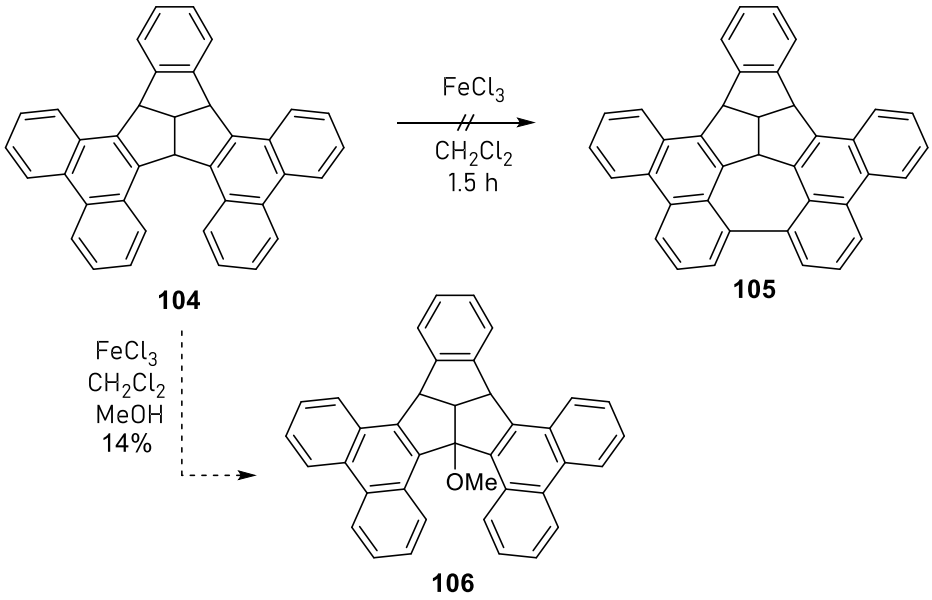

Figure 69. Attempted Scholl reaction and unexpected product by Kirchwehm.[168]

Eventually, Buschmann repeated the single cyclodehydrogenation under the same Scholl reaction conditions and achieved to synthesize the methoxy derivative **106** with a yield of 14 %, as well.[182] Additionally, it was reported, that the reaction was carried out in the dark to prevent the light inducing radical formation during chlorination. Nevertheless, the methoxylated product was the only isolated substance. It was concluded that another Lewis oxidant was needed to prohibit the chlorination.[179-180]

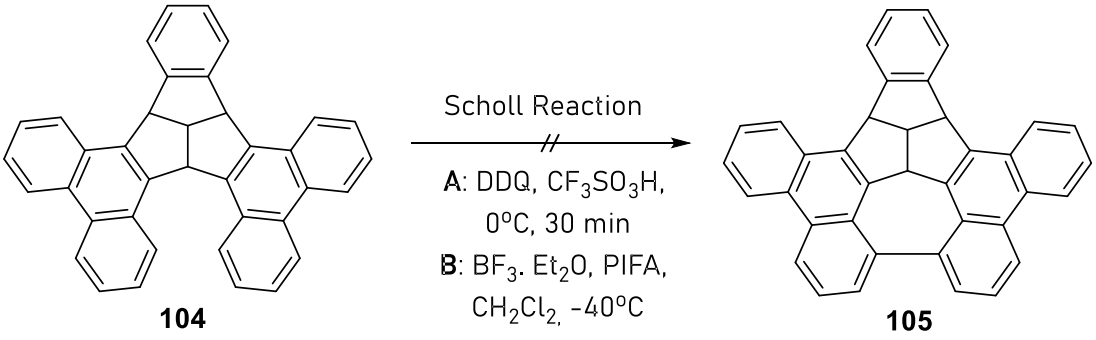

Figure 70. Attempted synthesis of bay bridged TBTQ under different Scholl reaction conditions by Buschmann.[182]

Therefore, alternative Lewis oxidants such as DDQ were tested, that are not able to form a chlorinated intermediate structure. Rathore et al. suggested 1 eq. of DDQ per C-C bond formation is sufficient.[181] Due to the proposed reaction being more challenging than the literature example, the equivalency of the oxidant was increased to 1.5. The reaction was finished in 30 min, monitored by (NP)-HPLC. Although most identified products showed peaks in the aromatic region of the ^{1}H-NMR spectrum, the number of protons did not match with the intended product.

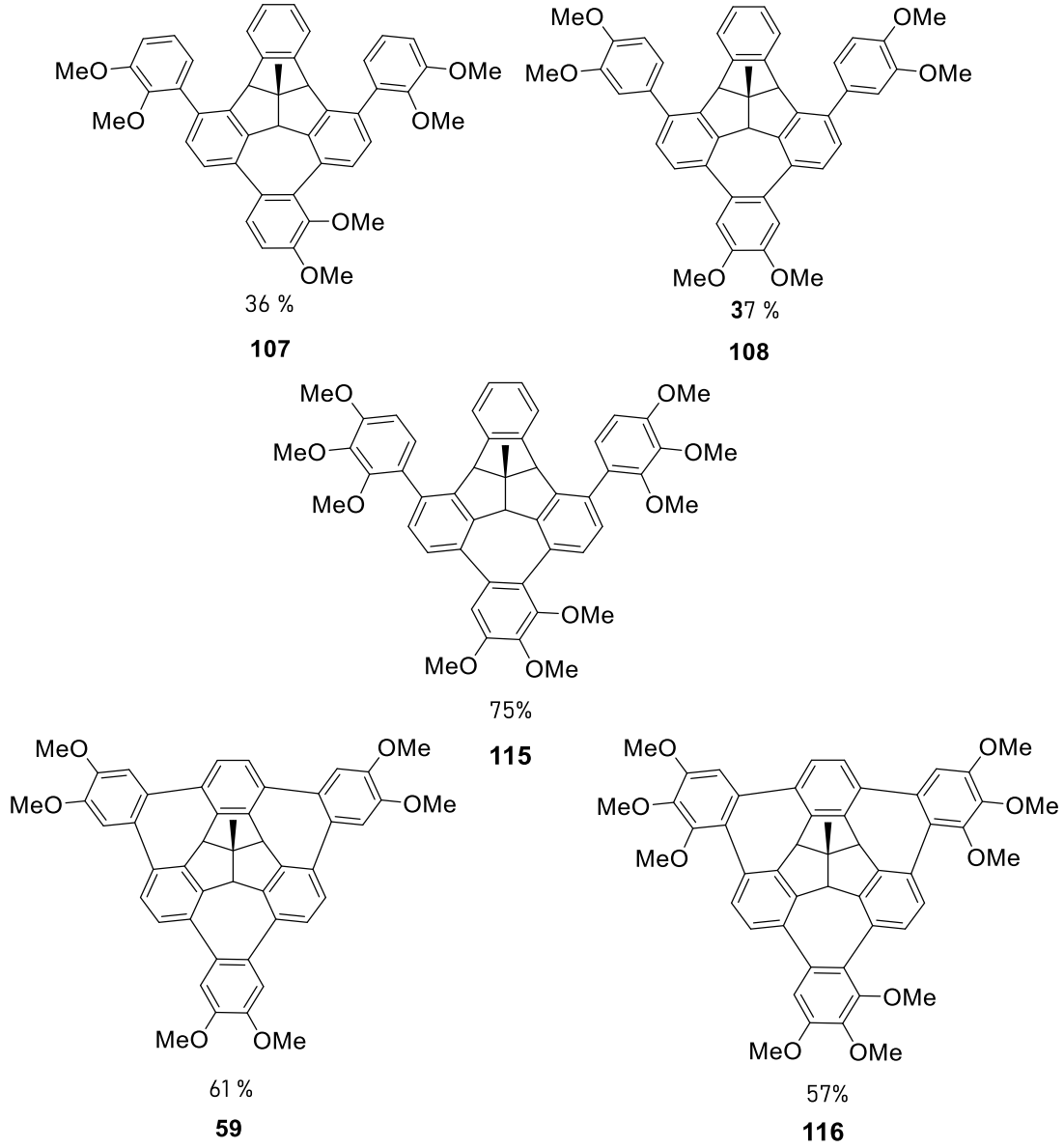

Figure 71. The products of single and triple of sterically and electrical effect of methoxy substituted TBTQs via Scholl macrocyclization.[171,183]

More favourable outcomes of the Scholl reaction were reported by Kuck, Chow and co-workers in 2017, when they studied the electronic and steric effect of the position of methoxy groups on successful Scholl reaction. They found that the bay–bridging cycloheptatriene formation in *ortho*-aryl substituted TBTQs via Scholl reaction is immensely sensitive to electronic and steric factors. As it can be seen from **Figure 71**, the bay positioned methoxy groups, even when they are double substituted, resulted in unsuccessful Scholl reactions. This result demonstrates that cycloheptatriene formation in *ortho*-aryl-substituted TBTQs via the Scholl reaction is sensitive to electronic and steric factors and emphasizes the importance of methoxy-substituted TBTQs for extending the carbon network.[171]

In conclusion, these results indicate several important points for the formation of C-C bonds between aromatic moieties and the possibility of Scholl reaction. First of all, three-fold cyclization reaction is only possible if the aryl rings are electron rich enough, single cyclization is much more favourable than two-fold or threefold cyclization. However, once the second cyclization occurs, the third one will proceed rather easily. If the substituents are located in sterically hindered bay regions, the cyclization may not occur when the aryl ring does not have sufficiently electron-rich substituents.[183]

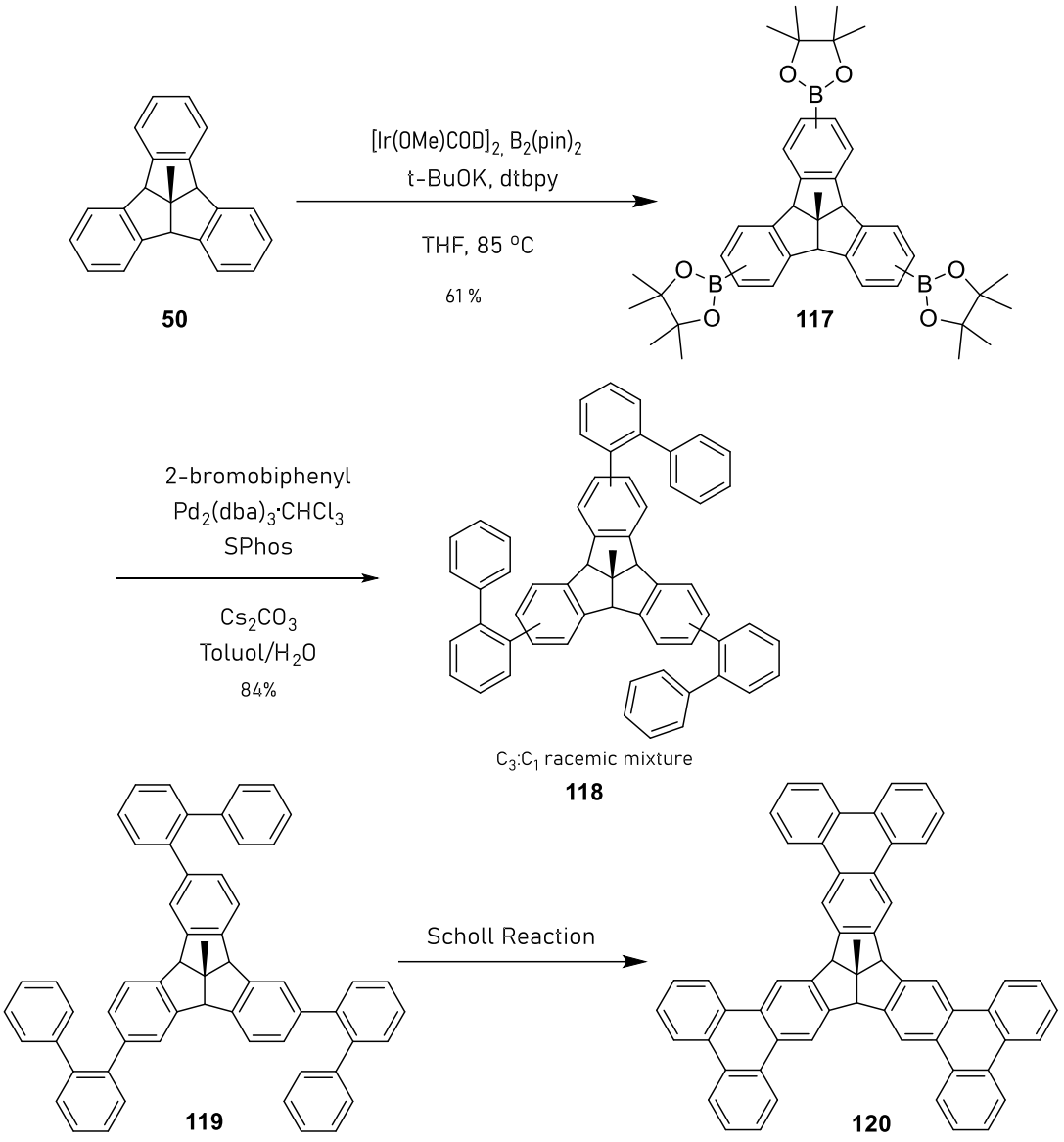

Figure 72. The summary of achieved Scholl reaction by Buschmann.[184]

Buschmann reported the successful Scholl reaction of **120** with the modification of the synthetic method based on all of the findings of attempting Scholl reactions and literature examples. (**Figure 72**) Instead of pre-functionalization of TBTQ constituents, post-functionalization of *centro* Me-TBTQ was carried out. The borylation was achieved in the presence of $B_2(pin)_2$ and $[Ir(OMe)COD]_2$ catalyst according to the literature example of Itami and Scott.[139] The resulting regioisomeric (C_3:C_1) mixture was coupled with 2-bromobiphenyl via Suzuki cross-coupling. After extensive research on various Scholl reaction conditions, the reaction was successfully carried out in the presence of PIFA and $BF_3{\cdot}Et_2O$ at -78 °C. The chemicals were added dropwise with a syringe pump over 8 h

until there was no starting material left. The resulting mixture was purified by column chromatography with a yield of 6 % for the fully annulated product **120**.

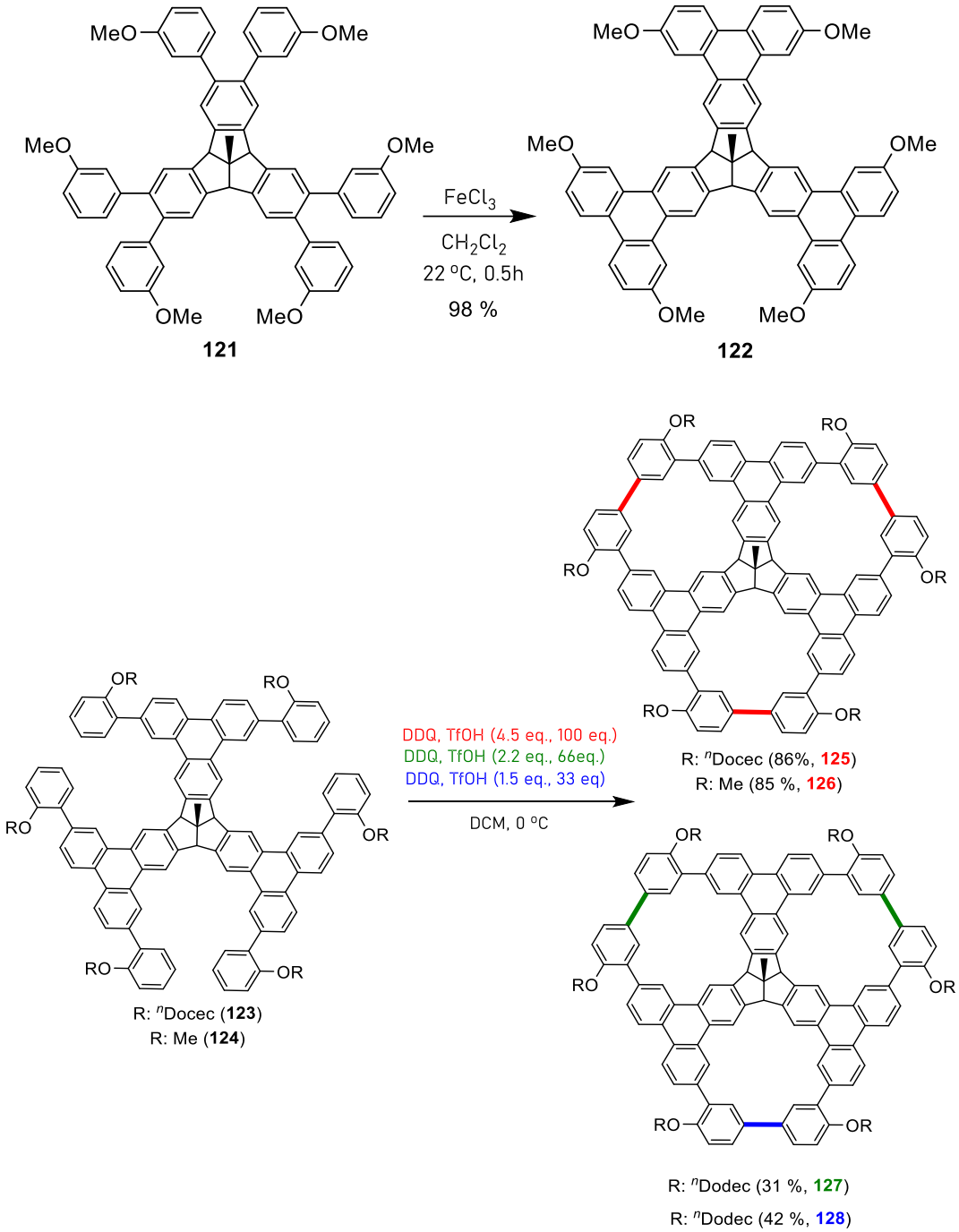

Figure 73. Scholl reaction conditions with different Lewis oxidants for TBTQ derivatives.[172]

Kuck *et al.* also reported the extension of the π-system and ultimately succeeded with a three-fold intramolecular Scholl macrocyclization with a suitably functionalized precursor with favourably positioned substituents making use of the electronic and steric effects of the electron donating groups. The readily accessible *meta*-methoxylated TBTQ was successfully submitted to three-fold Scholl reaction leading to **122** in very good yield. Subsequently, the aromatic rings were expanded to generate a closer environment and perform the formation of porous nanographene of TBTQ derivative. The high efficiency of the three-fold macrocylisation can be attributed to the rigid framework of the tris(triphenyleno)triquinacene system, which spatially prearranges the alkoxyphenyl groups for intramolecular oxidative coupling.[172]

1.3.4.1 Threefold Scholl Reaction of hexaphenyl substituted Me-TBTQ, 92

Here, we set out to attempt the cyclodehydrogenation of **92** to obtain the fully annulated TBTQ derivative **129** with a novel type of protective group in the bay positions.

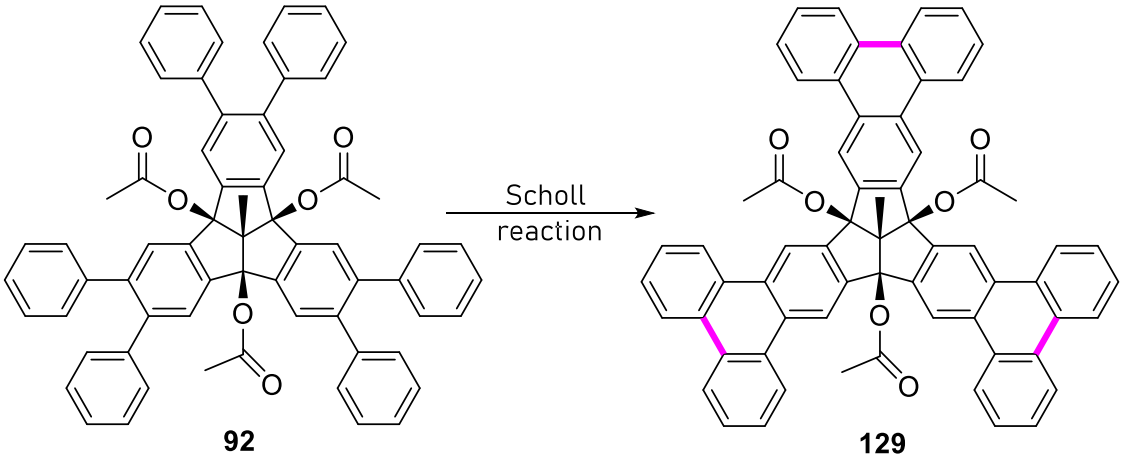

Figure 74. Schematic representation of proposed Scholl reaction to **129**.

Table 3 summarizes the various types of attempting Scholl reactions according to literature. As it is known, the mechanism of the Scholl reaction is currently still under investigation. Several different reaction conditions and proposed mechanisms were reported until now. Many literature protocols exist for the Scholl reaction, which were categorised first of all by the choice of Lewis acid and oxidant. Commonly used reagents include: $FeCl_3$, $MeNO_2$[112-114], $AlCl_3$[76, 97, 117], (bis(trifluoroacetoxy)iodo)benzene (PIFA) / $BF_3 \cdot Et_2O$ [121], $MoCl_5$ [115-116], and DDQ.[119-120, 185]

In this section, the attempted Scholl reaction results will be discussed. It can be seen from **Table 3** that several reagents have been used under different reaction conditions, such as different duration or temperature.

Table 3. Scholl reaction conditions for the attempted threefold cyclodehydrogenation of Me-TBTQ(OAc)$_3$Ph$_6$, **92**

Reaction No	Lewis acid, oxidant	Solvent	Time and conditions	Result
1	$FeCl_3$ (6.0 eq. per C-C)	dry DCM	r.t. 1.5 h, N_2	**130** and **131** as product
2	$FeCl_3$, CH_3NO_2 (6.0.eq per C-C, 1.5 mL nitromethane)	dry DCM	r.t., 2 h, N_2	**130** and **131** as product
3	$FeCl_3$, CH_3NO_2 (8.0.eq per C-C, 2.0 mL nitromethane)	dry DCM	r.t., 4 h, Ar	**130** and **131** as product
4	$FeCl_3$, CH_3NO_2 (10.0.eq per C-C, 3.0 mL nitromethane)	dry DCM	reflux, 12 h, N_2	complex product mixture
5	$FeCl_3$, dry CH_3NO_2 (10.0.eq per C-C, 3.0 mL nitromethane)	dry DCM	r.t., overnight then reflux 3 h, N_2	complex product mixture
6	$FeCl_3$, dry CH_3NO_2 (10.0.eq per C-C, 3.0 mL nitromethane)	dry DCM	r.t., 45 min., N_2	**130** and **131** as product
7	$FeCl_3$, dry CH_3NO_2 (15.0.eq per C-C, 3.0 mL nitromethane)	dry DCM	r.t., 1 h, N_2	**130** and **131** as product
8	$FeCl_3$, dry CH_3NO_2 (8.0.eq per C-C, 3.0 mL nitromethane)	dry DCM	r.t., 45 min, N_2	**130** and **131** as product
9	$FeCl_3$, dry CH_3NO_2 (8.0.eq per C-C, 3.0 mL nitromethane)	dry DCM	r.t., 30 min., N_2	**130** and **131** as product
10	DDQ, TfOH (1.5 eq. per C-C, 300 eq. TfOH ≈ 1.0 mL)	DCM	0 °C, 45 min., N_2	complex product mixture
11	DDQ, TfOH (1.5 eq. per C-C, 100 eq TfOH ≈ 0.3 mL)	dry DCM 0.67 mM	r.t., 24 h, N_2	complex product mixture
12	DDQ, TfOH (2.0 eq. per C-C, 200 eq TfOH ≈ 0.6 mL)	dry DCM	r.t., 3 h, N_2	complex product mixture

13	DDQ, $MeSO_3H$ (2.0 eq per C-C, 1 mL methanesulfonic acid)	dry DCM	0 °C, 1 h, Ar	no reaction
14	DDQ, TfOH (1.5 eq. per C-C, 100 eq TfOH ≈ 0.3 mL)	dry DCM 0.67 mM	TfOH added in 15min, then stirred r.t., N_2	complex product mixture
15	$MoCl_5$ (6.5 eq per C-C)	dry DCM	r.t., 2 h, N_2	no reaction
16	$MoCl_5$ (5.0 eq per C-C)	dry DCM	$MoCl_5$ added at 0 °C, stirred at r.t., 2 h, N_2	no reaction
17	$MoCl_5$ (5.0 eq per C-C)	dry DCM	r.t., 3 d, N_2	complex product mixture

*(0.054 mmol of **92** was used for all experiments which were done with $FeCl_3$ as a Lewis acid.)

As can be seen from **Table 3**, a large number Scholl reaction conditions were tried. Three different Lewis oxidants, namely $FeCl_3$, DDQ and $MoCl_5$ were used under different conditions. In a first experiment, $FeCl_3$ was used as the Lewis oxidant. 50 mg of starting material **92** was dissolved in 20 ml dry DCM in a Schlenk flask under nitrogen atmosphere. 6 equivalents per C-C bond, 18 eq.in total, of anhydrous $FeCl_3$ was added. The reaction mixture was vigorously stirred and deoxygenated continuously by bubbling N_2 through a needle. After 30 min., the reaction was checked by TLC. There were some new spots, but the starting material prevailed as well. Therefore, the reaction mixture was stirred an additional hour. Although the starting material was not completely consumed, further new spots began to appear on TLC and thus the reaction was stopped by adding MeOH to quench. The solvent mixture was removed under reduced pressure and the residual $FeCl_3$ was washed with additional MeOH until the colour of the solution was gone. The crude product was subsequently submitted to flash column chromatography and two main products were isolated and characterized. The main product, isolated after the shorter retention time, was investigated by ^{1}H-NMR revealing that no cyclodehydrogenation occurred.

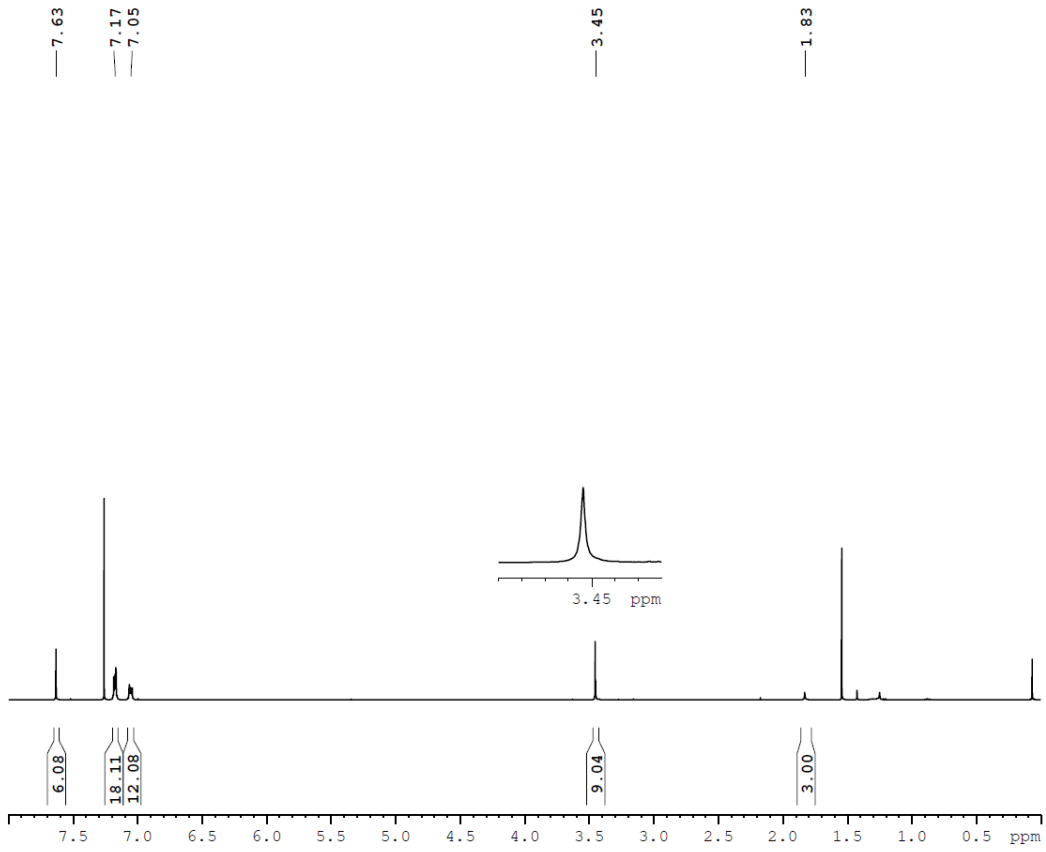

Figure 75. The ^{1}H-NMR spectrum of isolated product Me-TBTQ(OMe)$_3$Ph$_6$ of the attempted Scholl reaction of **129**.

The number of the protons was equal to the starting material **92**. However, the singlet peak, which belongs to the three CH_3 groups of the acetate groups, was shifted from 2.17 ppm to 3.45 ppm indicating the replacement of the acetates. A mass spectrometry was measured by using matrix assisted laser desorption/ionization time-of-light (MALDI-TOF). The most intense peak was at m/z 809, accompanied by very weak peak at m/z 840. The difference between these two values is equal to m/z 31 which corresponds to the molecular weight of OMe. Further, the carbonyl signal of the acetate groups, which is observed at around 170 ppm in ^{13}C-NMR for the starting material, is not present after the attempted Scholl reaction. Furthermore, the FT-IR spectrum also demonstrates a weak peak at 2823 cm^{-1} which is in a typical range for th C-H-vibrations in OMe groups. . Based on all of the spectroscopic results, investigations, and literature examples, it was determined that the first isolated product had three methoxy (OMe) groups instead of acetate (OAc) groups at the bay position and corresponds to Me-TBTQ(OMe)$_3$Ph$_6$, **130** (**Figure 76**).

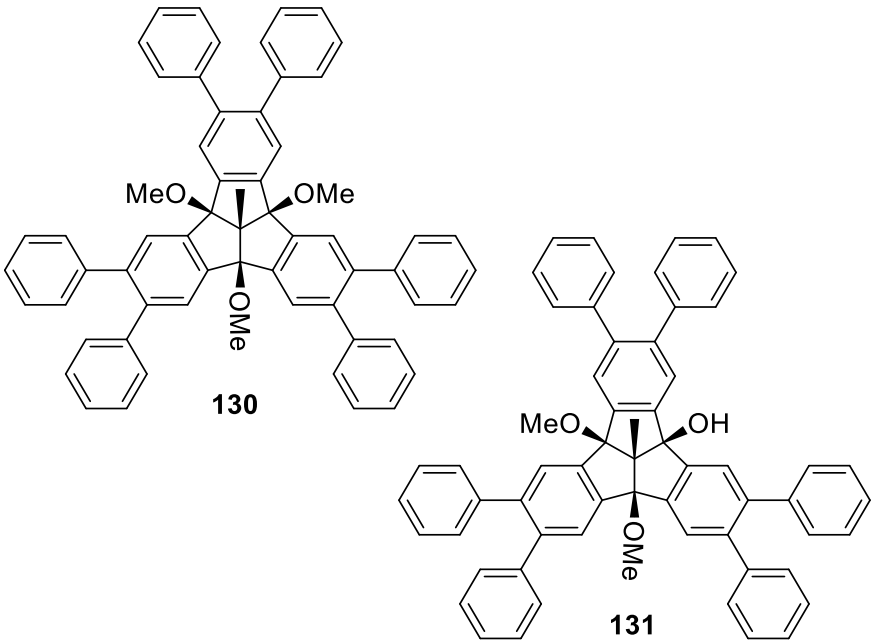

Figure 76. Isolated products **130** and **131** of Scholl reaction.

Normally, chlorination in the bay positions becomes an issue when the cyclodehydrogenation process occurs slowly. In this regard, Me-TBTQ$(OAc)_3Ph_6$ as a relatively electron deficient system compared to other analogues is expected to react slowly in the C-C coupling process. In this case, the chlorination would take place instead of cyclodehydrogenation. As the work-up process includes the addition of MeOH, which is a mild reductive. Thus, chlorinated positions with a high propensity to undergo nucleophilic substitution reactions will undergo the reaction to the respective methylethers. All reactions using $FeCl_3$ resulted in the grafting of methoxy groups in the bay position.

The second isolated product (**131**) revealed two additional singlet peaks in 1H-NMR at δ= 7.64 and 7.63 ppm, both with an integral of 2H. The shifted singlet peak was observed as well. However, the integral showed 6H instead of 9H. Additionally, there was another broad singlet peak around 2.45 ppm with an integral of 1H. The mass spectrometry using MALDI-TOF (+) gave an intense peak at m/z 795, accompanied by a very weak peak at m/z 826. The molecular weight difference between two values again equal to m/z 31 and corresponds to OMe. Based on the spectroscopic findings and the analysis of the first isolated product, the second isolated product was identified as Me-TBTQ$(OMe)_2(OH)Ph_6$.

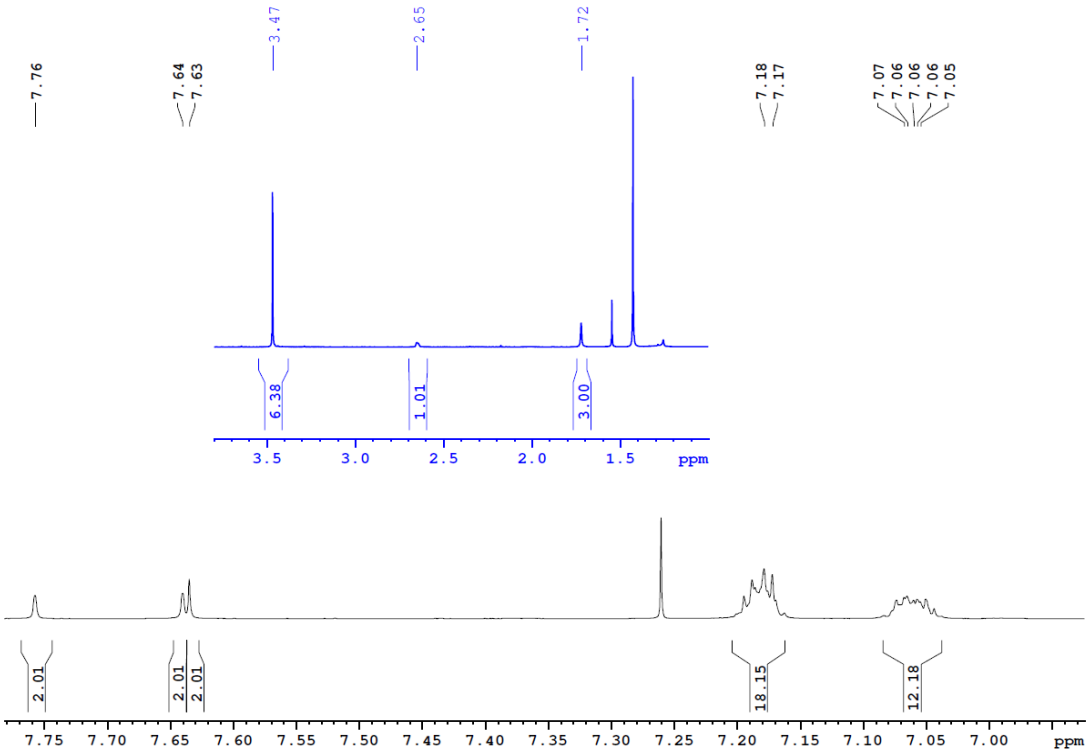

Figure 77. The ^{1}H-NMR spectrum of second isolated product **131** of attempted Scholl reaction.

Following these results, the Scholl reaction with $FeCl_3$ was further investigated and improved. As one modification, $MeNO_2$ was added to the protocol to provide protic acidic environment and reduce the possibility of side product generation. The experiments were carried out under different reaction conditions such as reflux, longer reaction times, changing Lewis acid equivalency per C-C bond. However, under any of the chosen conditions, in the presence of $FeCl_3$/$MeNO_2$, the cyclodehydrogenation reaction of **92** was unsuccessful.

As seen in **Table 3**, further Scholl reaction attempts with DDQ/TfOH and DDQ/MsOH mixtures as a Lewis acid were also carried out. It is reported that DDQ readily oxidizes a variety of aromatic donors such as naphthalene, anthracene, hexaalkylbenzenes etc. in the presence of an acid.[186-189] Furthermore, compared to the commonly used $FeCl_3$, the use of DDQ as an oxidant in Scholl reactions is favourable. It prevents the contamination by chlorinated products and avoids the use of excessive amounts of $FeCl_3$ by using only one equivalent of DDQ per C-C bond formation for the completion of Scholl reactions.[190]

In general, the reactions were carried out as it is described in literature.[172, 185] The starting material was dissolved in anhydrous DCM in a Schlenk flask under inert atmosphere. After adding MsOH or TfOH dropwise, the reaction mixture was treated with DDQ in one portion under ice-bath cooling. The solution colour immediately turned to dark green. The reaction was then quenched by an addition of a saturated aqueous solution of sodium bicarbonate. The dichloromethane layer was separated and washed with aq. $NaHCO_3$. Subsequently, the crude product was subjected to column chromatography. The isolated product was analysed by ^{1}H- NMR spectroscopy. However, it did not show any diagnostic peak neither for the desired product structure nor the starting material. Interestingly, the isolated structure did also not show any OAc, OMe, OH or *centro*-Me peak in ^{1}H-NMR. The only observed peaks were present in the aromatic region of the spectrum. Although there is a quite obvious OH vibration at 3300 cm^{-1} in FT-IR spectrum, any OH peak was not observed in NMR spectroscopy. As mentioned also above, the typical C=O signal belongs to acetyl group comes around 170 ppm in ^{13}C-NMR spectroscopy, however, it was not determined as well. In order to get more information about isolated hydrocarbons, mass spectrometry was measured as well. The APCI mass spectrum shows only two peaks. While one of them is quite intense and located at m/z 930, the weak signal appears at around m/z 947. Both values are greater than either the m/z of starting material or desired product. However, the molecular structure could not be identified even with the help of additional spectroscopic investigations.

As a third oxidant, molybdenum pentachloride ($MoCl_5$) was also used under various conditions. The protocols were adopted from the literature. $MoCl_5$ is known as a selective, one-electron oxidizing reagent and successful to avoid undesired chlorination during Scholl reactions. In general, the C-C coupling is much faster than other side reactions when $MoCl_5$ is used. As a general procedure, the starting material was dissolved in anhydrous DCM in a Schlenk flask under inert atmosphere, then $MoCl_5$ was added in one portion at 0 °C. The reaction solution was stirred at room temperature. The work-up was done by adding MeOH to quench. After removing $MoCl_5$ from the reaction mixture via filtration, the resulting organic solution was extracted with distilled water. The crude product was submitted to column chromatography for further purification. According to ^{1}H-NMR spectroscopy, the isolated product unfortunately did not show any characteristic peak belonging to the desired product. Furthermore, when the resulted spectrum

compared with previous works, it can be seen there is not any shifted peaks. In addition, the methoxy or alcohol groups were not observed, as well. As a result of the prevention of the chlorination process, the methoxylation and/or reduction did not occur, therefore the shifted peaks were not detected.

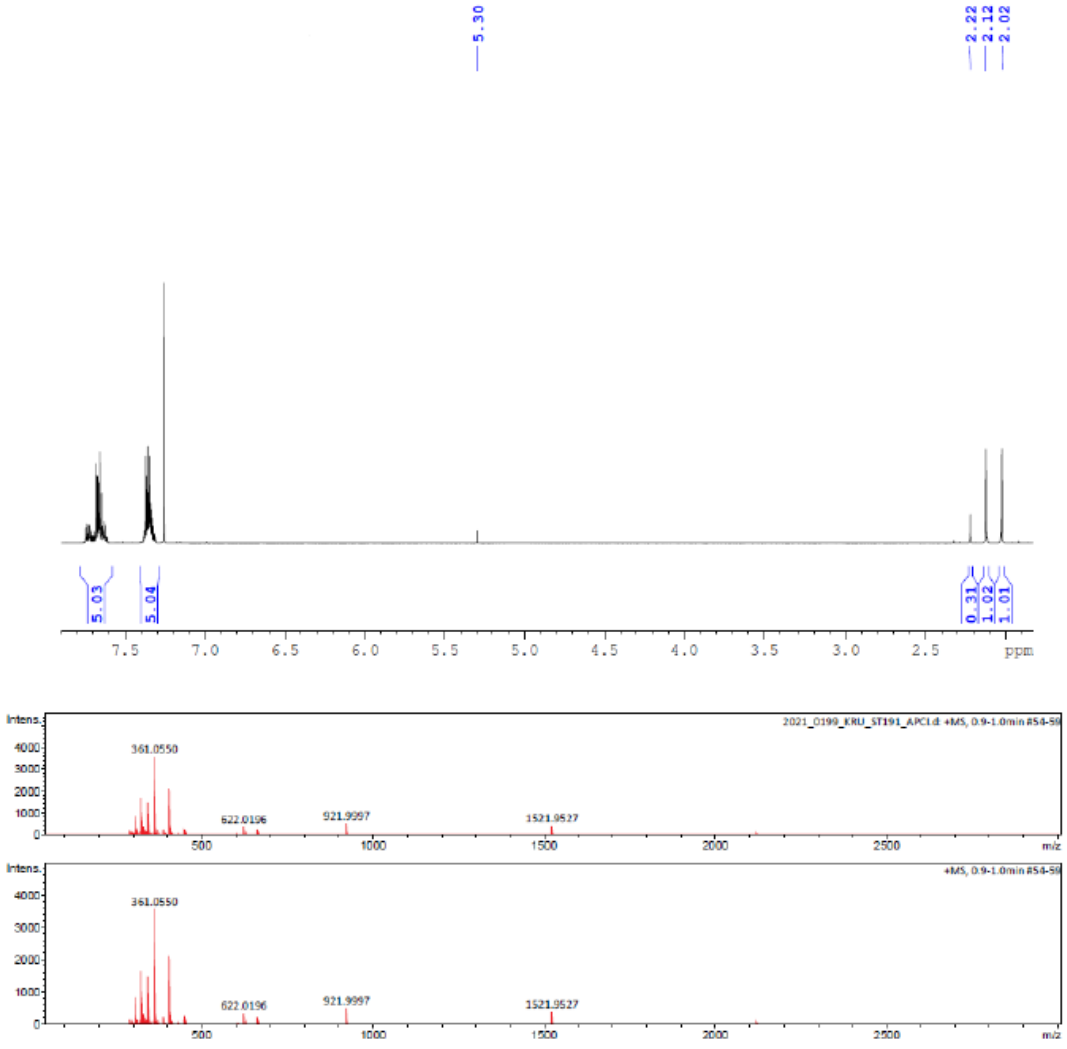

Figure 78. ^{1}H-NMR and APCI spectra of isolated product of **94** after Scholl reaction

Biphenyl substituted TBTQ derivative (Me-TBTQ(OAc)$_3$Bp$_6$, **94**) was also subjected to Scholl reaction after several trials of **92**. The starting material (**94**) was dissolved in dry DCM and FeCl3/ MeNO2 was added to the reaction mixture under Ar atmosphere. The resulting solution was stirred for 30 minutes at room temperature before being stopped by TLC analysis. Toluene was used to extract the solution after it was quenched with Na_2HCO_3. After flash column chromatography with CH/EA the analytical data analyses

were done. As can be seen in ^{1}H-NMR spectrum (**Figure 78**) of an isolated product, there is no specific peak that belongs to the desired product. This reaction produced no relevant results when the integral ratios and mass spectroscopic data were taken into account.

To summarize, it can be clearly understood from the performed Scholl reactions of TBTQ derivatives in this work and previous efforts in literature, that the bond formation during the cyclodehydrogenation depends on several properties of precursor. One of the most important and inducing point of the Scholl reaction is the presence of electron donating substituents in suitable positions in the precursor structure. As it turns out, so far, there is no TBTQ derivate successfully submitted to a Scholl reaction, which does not have any electron donating substituent bound to its backbone. Furthermore, the second important point of precondition for a Scholl reaction is the absence of sterically demanding substituents, particularly in the bay positions. As it was explained, the aim of introducing the acetate groups in the bay position was to eliminate them after cyclodehydrogenation reaction, in order to extend the π-system to the triquinacene core.

However, deacetylation and/or methoxylation reactions were already preferred under the cyclodehydrogenation conditions. This conclusion is consistent with previous work of Kirchwehm. Although the hexaphenyl and hexabiphenyl TBTQ derivatives represent potential candidates for the intramolecular cyclodehydrogenation reaction none of the attempts was successful. Therefore, it can be concluded that the hexaphenyl and hexabiphenyl Me-TBTQ derivative molecules were most likely too electron deficient when comparing them with Kuck´s examples.

1.3.5 Conclusion

To sum up this chapter, acetyl protection of bay-positioned tertiary alcohols was successfully performed. Subsequently, three new π-extended TBTQ derivatives, namely hexaphenyl- (**92**), hexabiphenyl- (**94**), and hexanaphtyl- Me-TBTQ(OAc)$_3$ (**96**) were synthesized via Suzuki cross-coupling reaction. In order to achieve the three-fold Scholl reaction, numerous types of intermolecular oxidative coupling reactions with various Lewis acids under different conditions were tried for **92**. Unfortunately, none of them yielded the desired cyclodehydrogenation products due to the lack of electron donating substituents in the backbone. Therefore, it can be assumed the C_{3v}-symmetric molecules

bearing TBTQ core would not be a favourable candidate for Scholl reactions, unless electron donating substituents are located in suitable positions. However, the molecules are promising to investigate their on-surface supramolecular self-assembly properties by Scanning Tunneling Microscope (STM). This will be discussed in further detail in **Chapter 2**.

1.4. Crystal Structure of Me-TBTQ(OAc)$_3$Ph$_6$

Crystals suitable for X-ray analysis were obtained from **92** upon recrystallization from a cyclohexane/dichloromethane mixture. The data for **92** were collected by Johannes Krebs of the work group of Prof. Dr. Todd Marder (Institute for Inorganic Chemistry, JMU Würzburg) from a shock-cooled single crystal at 100 K. The crystal structure belongs to the triclinic space group $R\overline{3}$ and is shown below in **Figure 79**. It can be seen from the single crystal structure of **92** that one of the phenyl rings on each wing is oriented perpendicular while the other one is parallel to y axis. The longest distance between two phenyl rings was measured as 16.2 Å, while Buschmann reported the distance for the molecule **120** as 15.6 Å.[182] It can be interpreted that the intermolecular cyclodehydrogenation stabilizes the molecule and reduces the length between two neighbouring phenanthrene rings.

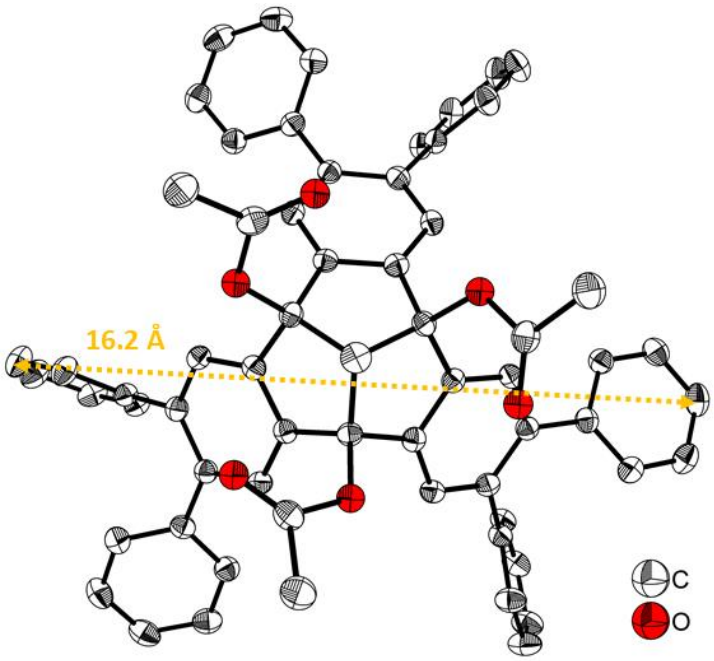

Figure 79. Solid state molecular structure of **Me-TBTQ(OAc)$_3$Ph$_6$, 92,** from single-crystal X-ray diffraction at 100 K. Atomic displacement ellipsoids are drawn at the 50% probability level. Solvent molecules and hydrogen atoms are omitted for clarity. These ORTEP style depictions have been prepared by J. Krebs and are reproduced with permission.

Figure 80 represents the "dimer" structural orientation of Me-TBTQ(OAc)$_3$Ph$_6$, **92**. The molecules are arranged along a three-rotational axis with a bowl-to-bowl orientation. As seen in along the axis are then: Me-TBTQ(OAc)$_3$Ph$_6$-CYH1-CYH2-CYH1- Me-TBTQ(OAc)$_3$Ph$_6$ CYH1 is on the edge and CYH2 is located in the corner of the unit cell, resulting in 1.5 CYH per unit cell.

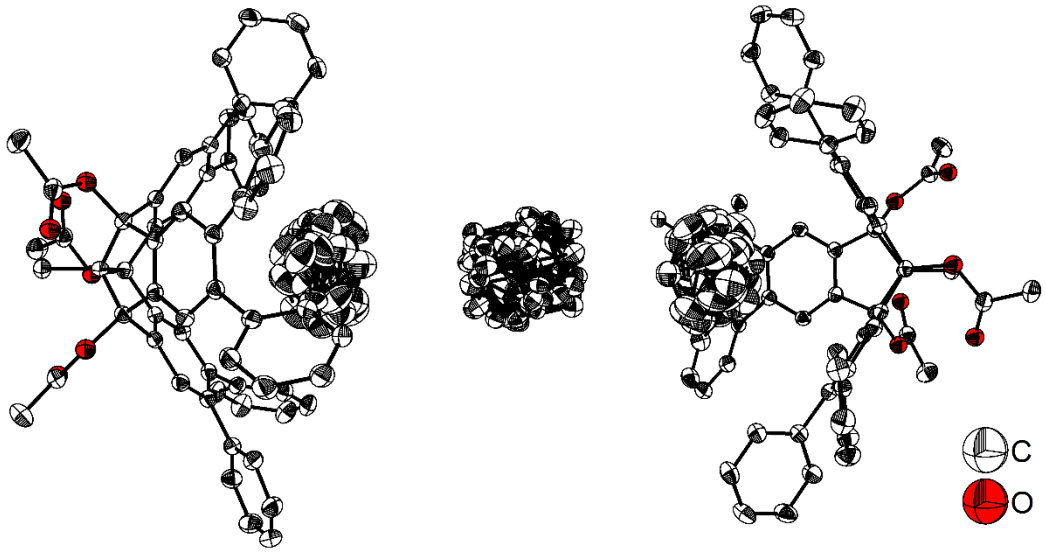

Figure 80. Solid state molecular structure of Me-TBTQ(OAc)$_3$Ph$_6$ derivative **92** from single-crystal X-ray diffraction at 100 K. Atomic displacement ellipsoids are drawn at the 50% probability level and hydrogen atoms are omitted for clarity.

Along the trigonal axis are three cyclohexane solvent molecules enclosed by two Me-TBTQ(OAc)$_3$Ph$_6$ isomers. Image prepared by J. Krebs, reprinted with permission.

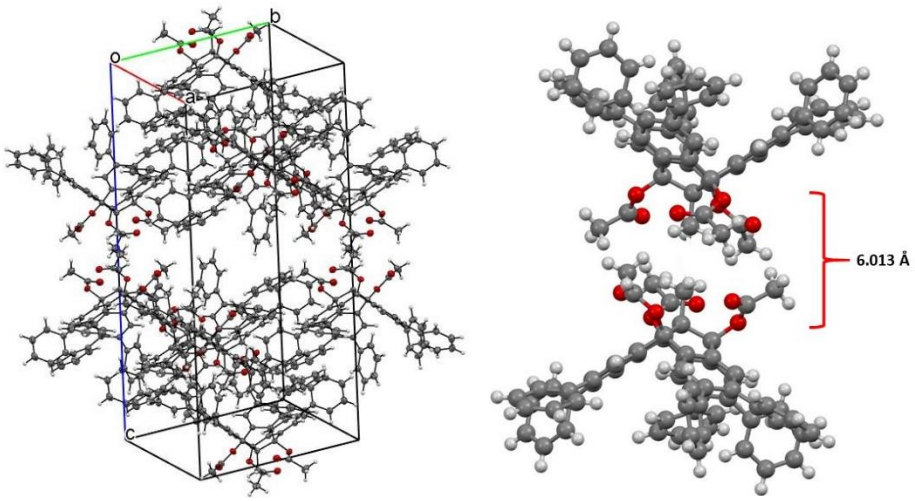

Figure 81. Packing structure of **92** (left), two molecules derived from the packing representation (right), the solvent molecules are omitted for clarity.

The central atoms C12d and C^{Me} locate along the threefold axis, and the molecular symmetry is exactly C_{3v}. As seen in **Figure 81**, unlike parent TBTQ 4**0,** which has molecules stacked in columnar stacks parallel to the c axis and all pointed in the reversed direction, the crystal packing of hexaphenyl derivative shows neighbouring molecules packed in opposite directions: one facing up and one facing down. The intermolecular π–π distance between adjacent molecules is a simple translation with a repeat distance of 6.013 Å. When it is compared with the parent analogue, Me-TBTQ **50**, the distance is increased by around 1 Å, which can be a result of additional acetate groups at the bay positions of the molecule.

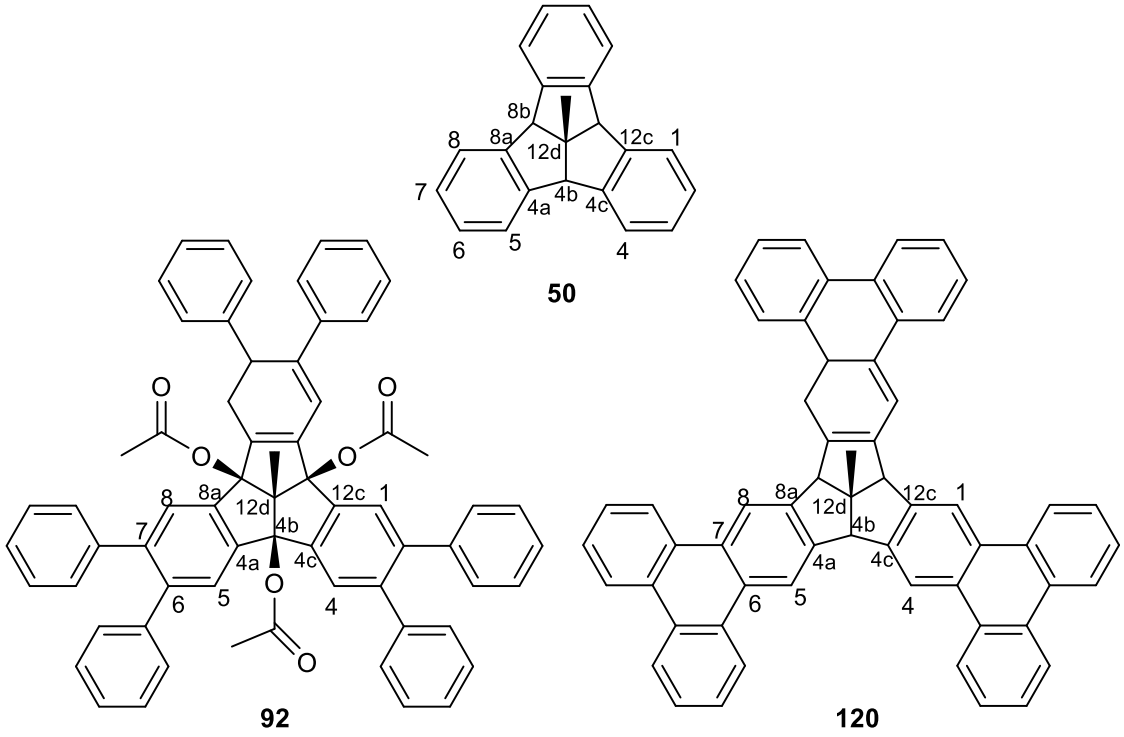

Figure 82. Atom numbering of TBTQs **50, 92** and **120.**

A summary of selected bond lengths, bond angles and torsional angles is presented in **Table 4**. The bond angle C4a-C4b-C4c, which is 113.53° for TBTQ **50,** 117.82° for TBTQ (phenanthrene derivative) **120** and 112.47 for Me-TBTQ$(OAc)_3Ph_6$ **92**, determines the distortion of the triquinacene core. While the deviation is clearly seen for TBTQ (phenanthrene) **120**, there is only 1 Å difference between parent TBTQ and TBTQ(phenanthrene) **120**. The intermolecular cyclodehydrogenation obviously causes the distorted core in TBTQ derivative molecules. Furthermore, the torsional angles C^{Me}-C12d-C4b-C4c, C^{Me}-C12d-C8b-C8c and C^{Me}-C12d-C12b-C12c in Me-TBTQ$(OAc)_3Ph_6$ **92** deviate between 1.8° and 11.4° from their counterpart angles in TBTQ **20.** However, similar to the bond angle C4a-C4b-C4c, there are quite small deviations in bond lengths (≈ 1 Å) between TBTQ derivative **92** and its parent analogue **50**.

Table 4 Selected bond lengths, bond angles and torsional angles for Me-TBTQ **50**, TBTQ(phenantrene) **120** and Me-TBTQ$(OAc)_3Ph_6$ **92**, the values for Me-TBTQ **50** are from data reported by Kuck et. al.[149]

Bond	Bond Length [Å]			Bond	Bond Angle [°]		
	50	**120**	**92**		**50**	**120**	**92**
C12d- C4b	1.5658	1.569	1.582	**C4b-C12d-C8b**	106.61	106.01	105.29
C12d-C12b	1.566	1.561	1.582	**C4c-C4b-C12d**	105.12	105.63	105.26
C12d-C8b	1.565	1.571	1.581	**C4b-C4c-C8a**	111.52	111.62	112.27
C4b-C4c	1.5142	1.504	1.503	**C4a-C4b-C4c**	113.53	117.82	112.47
C4c-C8a	1.400	1.397	1.381	**C12a-C12b-C12c**	113.53	113.89	112.47
C4c-C5	1.3961	1.380	1.386	**C8a-C8b-C8c**	113.53	111.20	112.47
C5-C6	1.3956	1.4109	1.395	**C4c-C8a-C8b**	111.52	113.34	116.98
C6-C7	1.396	1.415	1.416	**C4b-C4c-C5**	128.00	127.97	126.47
C12d-C^{Me}	1.524	1.522	1.520	**C8-C8a-C8b**	127.76	128.60	128.72
Bond	**Torsional Angle [°]**			**C4c-C5-C6**	119.04	120.78	120.35
	50	**120**	**92**	**C7-C8-C8a**	119.04	120.87	120.28
C4b-C4c-C5-C6	176.53	178.85	177.86	**C5-C6-C7**	120.29	118.77	118.71
C12d-C4b-C4c-C5	179.23	178.86	176.98	**C8a-C4c-C5**	120.42	120.40	121.25
C^{Me}-C12d-C4b-C4c	119.97	121.78	120.39	**C4c-C8a-C8**	120.42	119.92	119.41
C^{Me}-C12d-C8b-C8c	119.95	125.52	120.37				
C^{Me}-C12d-C12b-C12c	119.95	108.55	120.65				

CHAPTER 2

2.1. Introduction

2.1.1 Scanning Tunneling Microscope (STM)

Science at the nanoscale is one of the most productive and exciting fields in the current physics of condensed matter. Major breakthroughs have become possible over the past decades through impressive new experimental methods that enable scientists to examine surfaces with extremely high spatial resolution. One important and well-established set of methods is summarized as Scanning Probe Methods. They all enforce the same simple principle: a nanoscale probe is approached towards the sample surface of interest until some physical process occurs which can be used to characterize the sample.

Scanning Tunneling Microscope (STM) was invented in the early 80's by two physicists namely, G. Binnig and H. Rohrer at IBM Laboratory in Zurich, for which they were awarded the Nobel Prize a few years later.[191-192] The principle of quantum mechanical tunneling led to the development of the Scanning Tunneling Microscope (STM) which had a profound impact on chemical, biological and material science research.

**The results detailed in this chapter will be submitted as a scientific paper.*

As a matter of fact, it provides a tool for measuring the conductance of the tunnel at the atomic level. Following this first example of a scanning probe microscope (SPM), a large number of variations have been developed.

In this way, these techniques make it possible to study the atomic arrangements of surfaces. It is obvious that this atomic resolution is more difficult to achieve for closely packed metal surfaces than for relatively open semiconductor surfaces. However, the STM's application to metallic surfaces has proven to open exciting new possibilities. In combination with the ability to manipulate atoms on these surfaces, very spectacular images were generated.

2.1.2 Scanning Tunneling Microscopy: Principle and Instrumentation

Since it was invented, the Scanning Tunneling Microscope (STM) has become a widely used instrument in surface science. By incorporating scanning capacity into tunnelling capability, STM allows us to observe the surfaces of conducting samples and study their electronic properties up to atomic scales.

The fundamental components of an STM consist of a sharp metal tip; a piezoelectric scanning element, which controls the vertical and lateral movement of the tip; a coarse positioning unit; which brings the tip-sample separation to a distance within the tunneling range on a scale of 0.01 Å, a vibration isolation stage; and a set of electronics, which detects the small tunneling current, (10pA-1 nA), controls the piezo-tube scanner with feedback, and initiates the coarse positioning.

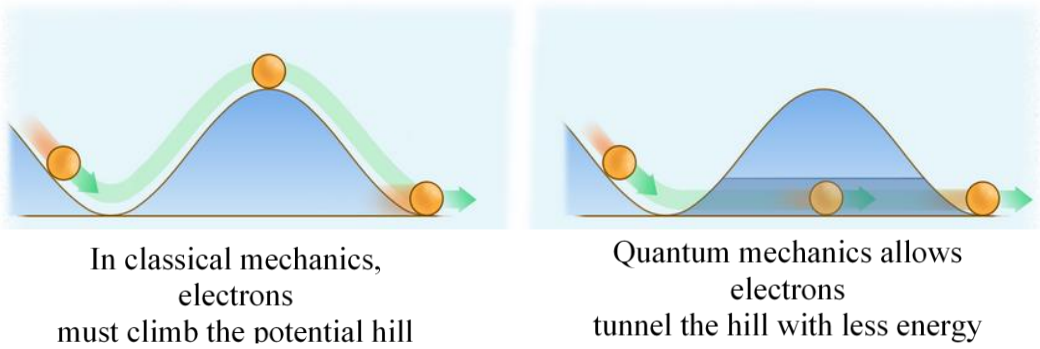

Figure 83. Comparing classical (over the barrier) motion vs. quantum (through the barrier) motion

The phenomenon behind STM is the quantum tunneling of electrons. When two electrodes are separated by a thin potential barrier such as an oxide or vacuum, electrons have a non-zero probability to tunnel through the barrier. This phenomenon, prohibited in classical physics, is permitted in quantum mechanics. In scanning tunneling microscopy, there are two electrodes i.e., the first electrode is the tip and the second one is the sample.

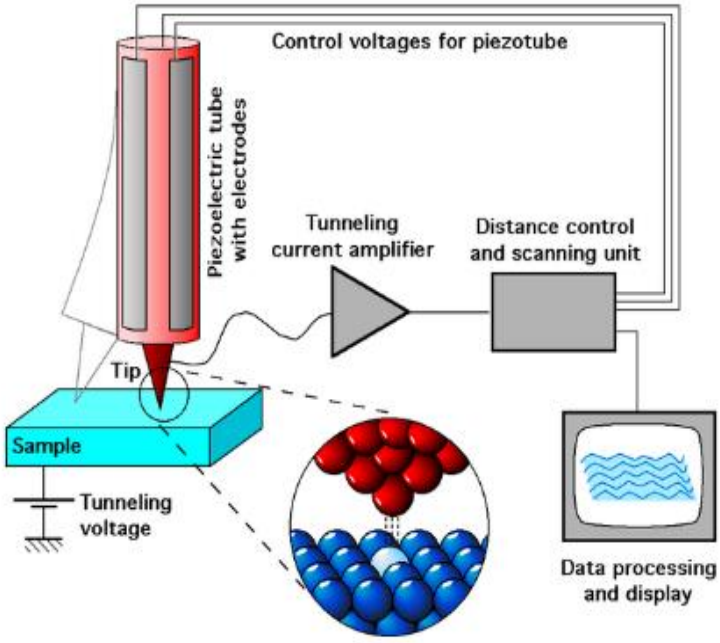

Figure 84. Basic setup of Scanning Tunneling Microscope (STM), Figure: Michael Schmid, TU Wien.[193]

To initiate the tunnelling process, the STM tip is brought several Angstroms from the sample surface. When a bias voltage is applied to the system, the quantum-mechanical tunneling effect causes an electron tunneling current to flow between the tip and the sample before they make mechanical contact. Following the establishment of the tunneling contact, the tip scans over the sample surface with the assistance of a piezoelectric driver, the extension of which can be controlled in three dimensions (x, y, and z) to obtain a two-dimensional map of the surface. The distance between the tip and the sample has a large influence on the tunneling current. This is required for the detection of small surface corrugations. Even minor surface details, such as depressions or protrusions, cause a significant change in the tunneling current. A computer records the data and displays it as an image using STM software (**Figure 84**).[194-195]

2.1.3 Experimental aspects of STM

As mentioned above, the tunneling current IT exponentially depends on the distance d between tip and sample. It is an essential point to achieve a vertical resolution, on the z axis of the tip, of about a picometer:

$$I_T \sim e^{-2kd} \quad with \quad k = \sqrt{\frac{2m\Phi}{\hbar^2}} \qquad \textbf{eqn 2.1}$$

The work function of metals, Φ, is mostly of 4eV. Therefore, the tunnel current decreases by a factor 3 when increasing the tip-sample distance of 1Å. The lateral resolution is mainly dependent on wave functions and the tip-sample distance. As a result, the STM offers the possibility to obtain images in real space at the atomic level.

2.1.3.1 Topographic mode

The scanning tunneling microscope enables to collect topographic and spectroscopic data locally. There are two modes to reveal the topography of a surface (**Figure 85**).

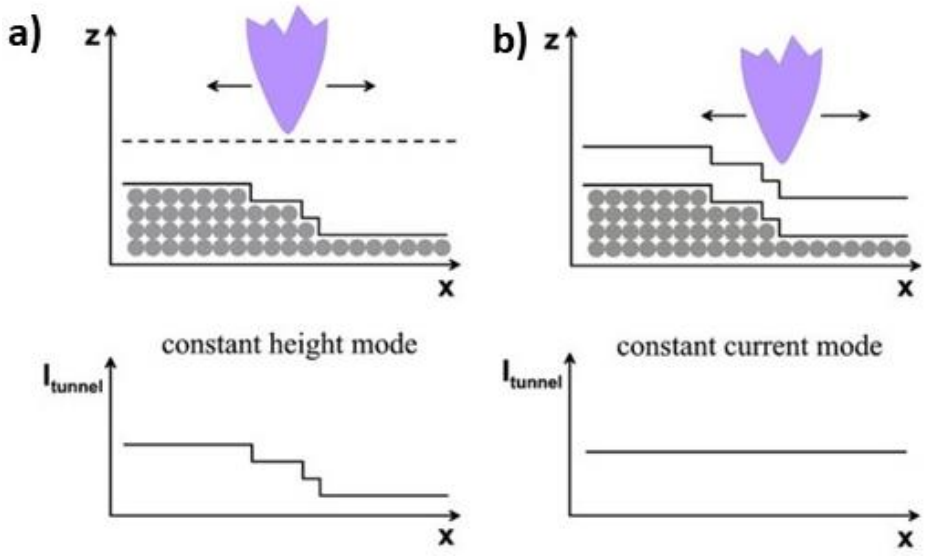

Figure 85. Schematic representation of the STM operating modes: (**a**) constant height, where changes of current are recorded and (**b**) constant current, where variations of height are measured.[196]

As can be seen in **Figure 85**, it demonstrates the topographic STM modes. The two modes, constant height which is shown in (**a**) and constant current, which is shown in (**b**) are explained in more detail in the following.

2.1.3.1.1 Constant height imaging

In constant height mode, the tip is scanned across the surface at nearly constant height. As a function of tip position, the variation of the tunneling current depends on the topography and local electronic surface properties of the sample **Figure 85** (**a**). The constant height mode has the advantage of allowing high scan speeds due to the feedback loop being slowed or turned off completely, thereby avoiding drift effects. However, because surface defects or contaminations may cause the tip to crash, this mode is limited to very flat surfaces and small areas.

2.1.3.1.2 Constant current imaging

In the constant current mode, the tip is scanned across the surface while the feedback loop controls the tip's height to maintain a constant tunneling current **Figure 85** (**b**). The height of the tip z (x, y) as a function of position can be obtained by recording the voltage applied to the piezoelectric driver in order to keep the tunneling current constant, resulting in a topographical image with atomic resolution. Because it allows probing of surfaces that are not necessarily atomically flat, the constant current mode is the most commonly used in STM imaging. However, because of the finite response time of the feedback loop and the piezoelectric driver, this mode has a limited scan speed.

2.1.4 Molecular self-assembly on surfaces

Supramolecular Chemistry[1] was born out of the realization that organic molecules could interact in specific ways to condense into well-ordered structures held together by non-covalent interactions. Supramolecular chemistry can be characterized as *chemistry beyond the chemical bond,* has taught us how to make regulated structures using non-covalent bonds. In context, the nature of the interactions is critical for defining a self-assembled arrangement. In particular, the chemical nature of molecules in chemistry and supramolecular chemistry means that such assemblies cannot be driven by forming new

covalent bonds, as this would undoubtedly disrupt some of the bonds that had already been established within the molecule. Therefore, only noncovalent interactions such as hydrogen-bonds[197-199], dipole–dipole[200-201] and van der Waals interactions[202], metal–ligand coordination[203-204], or a combination of several of them are considered as relevant interactions to chase the self-assembly process. Among them, hydrogen bonds and metal–ligand coordination are relatively strong and strongly directional; thus, they are the most commonly observed supramolecular interactions that define the self-assembly of molecules on a surface.[205]

The nature and spatial distribution of functional groups in the periphery of the molecular backbone also play a major role in the self-assembly of organic molecules. (**Figure 86**).

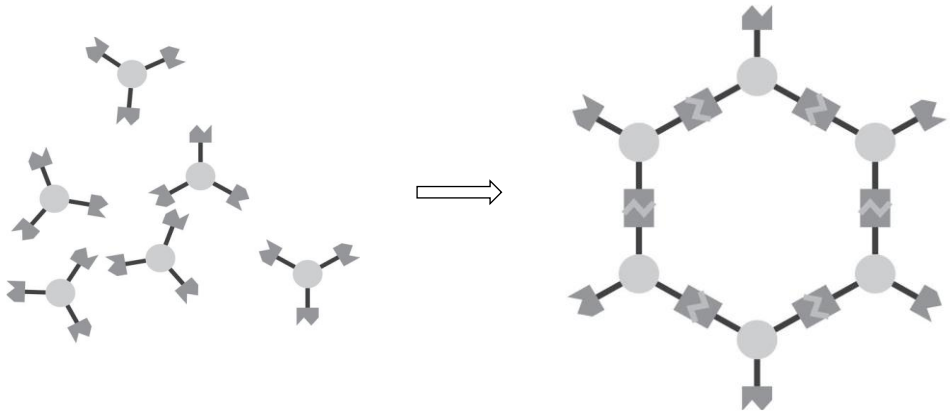

Figure 86. Schematic representation of the molecular self-assembly process of organic molecules [206] (Copyright © 2011 WILEY-VCH Verlag GmbH & Co. KGaA, Weinheim)

Most of the early research in supramolecular chemistry focused on solution-based processes. The dynamic structure of supramolecular assemblies and supermolecules was elucidated using a combination of structural and spectroscopic research techniques. However, there were no real-time visualization tools with sufficient resolution available until the STM was invented, to show information at the (sub)-molecular level of these often-complicated liquid architectures.

The STM has evolved into a very flexible and effective instrument in the field of surface and nanoscale science since its invention. Although the STM was created to obtain useful knowledge on the atomic-scale structure of pristine metal and semiconductor surfaces[191, 207-210], it has since been used for a variety of applications, including extensive analyses of the properties of adsorbates on metals[208-209], *in situ* monitoring of growth processes[208, 210], and studying the conformations of large organic molecules on different substrates. Over the years, the STM has become an efficient method for manipulating nanoscale artefacts such as single atoms and molecules on a surface, including lateral displacements and vertical transfer. Moreover, it has been shown that using an STM tip, single chemical bonds can be selectively broken and formed.[211-214] The ability to manipulate matter with atomic-scale accuracy not only opens up new possibilities for creating artificial, orderly structures at the nanoscale[215], but it can also be used to obtain profound new insights into the precise binding and ordering of molecules on surfaces, leading to valuable new knowledge about chemical bonds.[216]

2.1.4.1 Basic principles of two-dimensional self-assembling process

Spontaneity is the distinguishing characteristics of molecular self-assembly. The intrinsic tendency to minimize Gibbs free energy drives the self-assembling molecular behaviour. Because of the development of intermolecular bonding, the molecules assemble themselves into an ordered configuration as the Gibbs free energy decreases. From a microscopic perspective, the two-dimensional self-assembling process is caused by a delicate equilibrium between molecule-molecule and molecule-substrate interactions.[217]

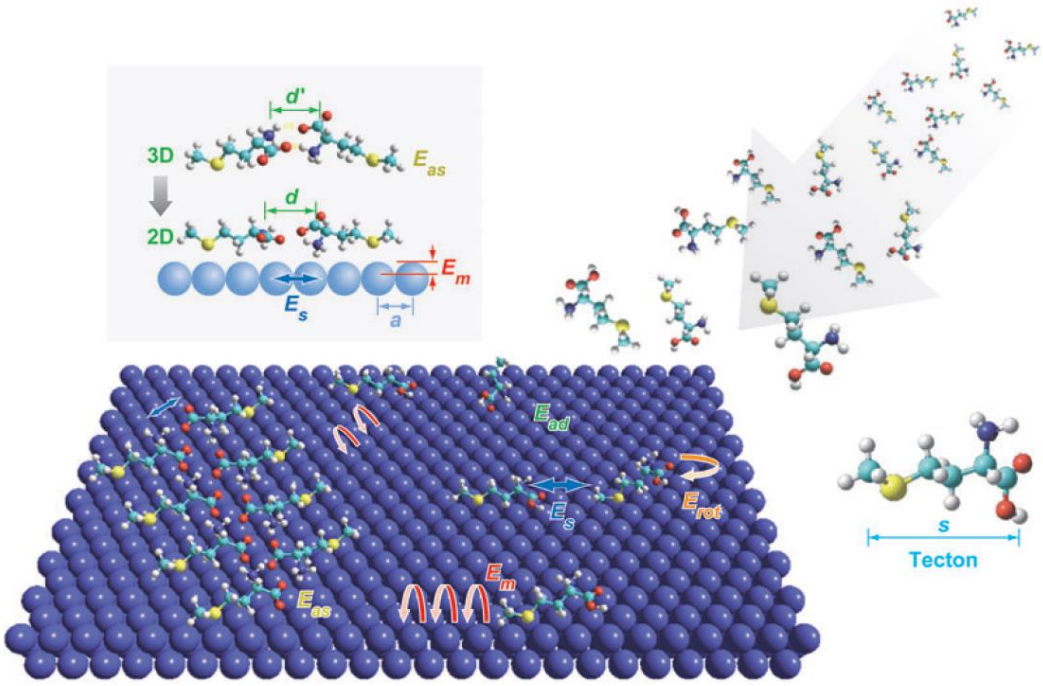

Figure 87. Demonstration of the basic processes of molecular self-assembly on surfaces. (Adapted with permission from reference[217], Copyright 2007, Annual Reviews)

Firstly, as the molecules are deposited on the surface, they interact with the substrate. The interaction between the molecule and substrate should be strong enough to avoid desorption of molecules from the surfaces. Otherwise, if the adsorption energy E_{ad} is too low to keep the molecules on the surface, the molecules would not be able to remain, causing the self-assembling process to fail.

Secondly, as molecules are adsorbed on a surface, they must be able to diffuse on the surface so that they can interact with one another and generate non-covalent bonds. The diffusion mechanism of molecules on surfaces can be explained by the following equation,

$$\Gamma_{diff} = \nu_{diff}\, exp\left[-\frac{E_{diff}}{k_B T}\right] \qquad \textbf{eqn. 2. 2}$$

where Γ_{diff} is the hopping rate of the molecule on the surface, ν_{diff} is a prefactor with a value between 10^{10} and 10^{14} s^{-1} for large species.[218-220] E_{diff} is the diffusion barrier for the molecules on the surface, k_B is the Boltzmann constant and T is the temperature of

the system. Apparently, the hopping rate of the molecule is regulated by E_{diff} and k_BT. In the case of $E_{diff} << k_BT$ the molecules can move quite effortlessly on the surface and are not limited to a certain location. Therefore, molecules can easily disperse on the surface and reach other molecules to form bonds between them. In the opposite case, when the $E_{diff} >> k_BT$, the hopping rate is very low because of the large diffusion barrier. In this situation, the molecules cannot move on the surface and the self-assembled process would be disrupted, and there would most likely be no orderly structure created.

Thirdly, in the case of site-based molecular bonding, the molecules must rotate on the surface in order to form a specific configuration with respect to the underlying surface. Hence, the minimum-energy structure will thus be achieved. As can be seen from the **eqn. 2.2**, temperature and the rate of rotation movement of molecules on the surface have an exponential interaction, like for diffusion movement.[221] In this context, temperature plays an essential role since it can be used to regulate both the rotation and diffusion of molecules.

Lastly, following the adsorption, diffusion and rotation process, the molecules will bond to the surface via non-covalent interactions. Since non-covalent bonds are highly reversible, defect-free molecular structures can be accomplished by molecular self-assembly.[206, 222] When all of these parameters are balanced, a self-assembled two-dimensional molecular pattern can be successfully created.

2.1.4.2 Molecule -molecule interactions

As it is mentioned in section **2.1.4 ,** in molecular self-assembly**,** molecules are connected to each other via non-covalent interactions. Besides, intermolecular interactions play a "sticking" role in the assembling process. As a result, understanding molecule-molecule interactions is critical for achieving controlled tuning of the assembly process. The following section gives a short overview on the main interactions in self-assembly process e.g. van der Waals forces, halogen bonding, hydrogen bonding, and metal-ligand bonding.

2.1.4.2.1 Van der Waals forces Dispersive and long-range inductive forces between molecules are classified as van der Waals interactions. It is caused by the polarization of electron clouds between species that are close to each other.[223-224] Van der Waals forces can be divided into three categories in general: London dispersion force, which is the force between two spontenaously induced dipoles, Debye force, which is the force between a permanent dipole and a corresponding induced dipole and Keesom force, which is the electrostatic interactions between two permanent dipoles. Principally, van der Waals forces are quite weak and non-directional and in general less than 5 kJ/mol. However, as they are attractive forces, their cumulative effect can also play a major role in molecular self-assembly.[225-229] For example, self-assembly of 5-amino[6]chelicene on Cu(100) and Au(111) constructed through van der Waals forces was reported by Ascolani *et al*.[229] STM images **(Figure 88**) demonstrated that the 5- amino[6]helicene molecules formed a porous network structure with a rhombic unit cell. According to their findings, the primary difference between the two studied surfaces is the origin of the molecule-surface interaction. In the case of Cu(100), the C6 rings-surface interaction is dominant, whereas the amino–surface interaction is critical on Au(111). The amino group does not induce polar interactions via hydrogen bonding in either case, but rather the maximization of van der Waals interactions drives the self-assembly. Density functional theory (DFT) calculations also revealed that intermolecular van der Waals forces drove the self-assembly process.

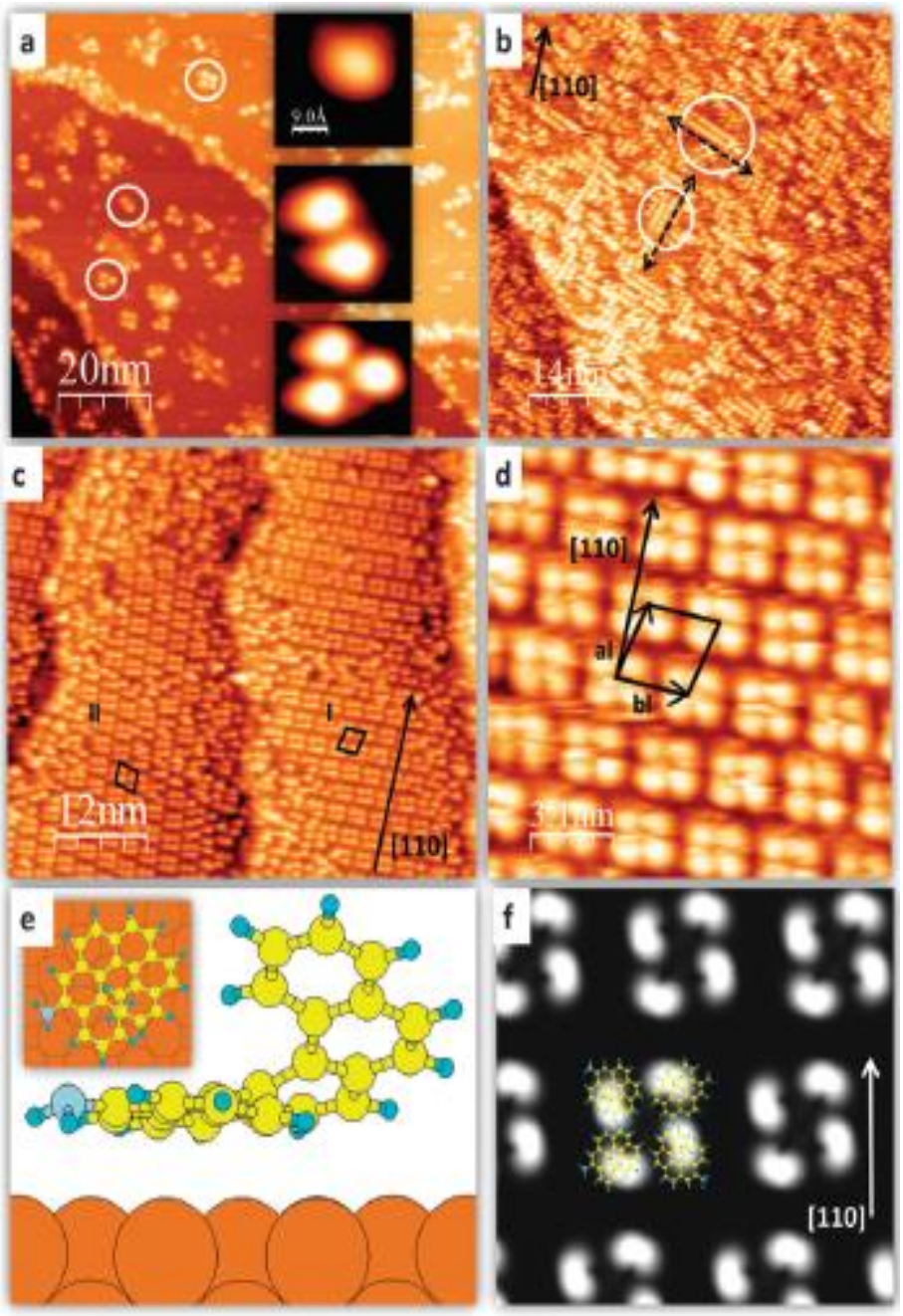

Figure 88. STM images of 5-amino[6]helicene on Cu(100). (a) Low coverage, insets and circles show the single molecules, duplets, triplets and quadruplets diffusing on the surface (-2 V, 50 pA). (b) 60% monolayer coverage, the circles and arrows indicate the formation of double rows (-2 V, 15 pA) (c, d) 90% monolayer coverage, in black the unit cells for the 90° rotamers (I, II) (al = bl = 2.4 nm) (2.2 V, 10 pA), (e) DFT model of the single molecules on Cu(100), top and lateral view, (f) simulated image of calculated cell (Adapted with permission from reference[229] Copyright 2014, Royal Society of Chemistry)

2.1.4.2.2 Hydrogen bonding Hydrogen bonding is a special type of dipole-dipole attraction between molecules. It results from the attractive force between a hydrogen atom bonded to a strongly electronegative atom such as O, N, S, X (F, Cl, Br, I), that exists in the vicinity of another electronegative atom with a lone pair of electrons of unsaturated system.[230-231] Hydrogen bonds are generally stronger than ordinary dipole-dipole and dispersion forces. Its strengths range is from 4 kJ to 50 kJ per mole of hydrogen bonds. Hydrogen bonding is taken into account as one of the most important interaction in molecular self-assembly and supramolecular chemistry because of its comparatively strong and highly directional structure. Intermolecular hydrogen bonding has been used to build a number of two-dimensional supramolecular nanostructures on surfaces. [232-236] For example, in 2015 Steiner and co-workers studied the self-assembly and stability of hydrogen bonded carboxyl (CDTPA) and diaminotriazinyl substituted (ADTPA) dimethylene bridged triphenylamine derivatives on Au(111) and on Cu(111)[237] (**Figure 89**). The self-assembled molecules demonstrated two-dimensional honeycomb networks. Carboxyl groups are often used in hydrogen-bonded self-assemblies. The cyclic dimer, connected by two O···H···O bonds, is the favoured supramolecular synthon. [238-240] Both networks can be assigned to hydrogen-bonded structures, with all molecules interacting on the regular and molecular arrangement. They determined that the molecules are interconnected and mainly driven by intermolecular hydrogen bond interactions throughout the network.

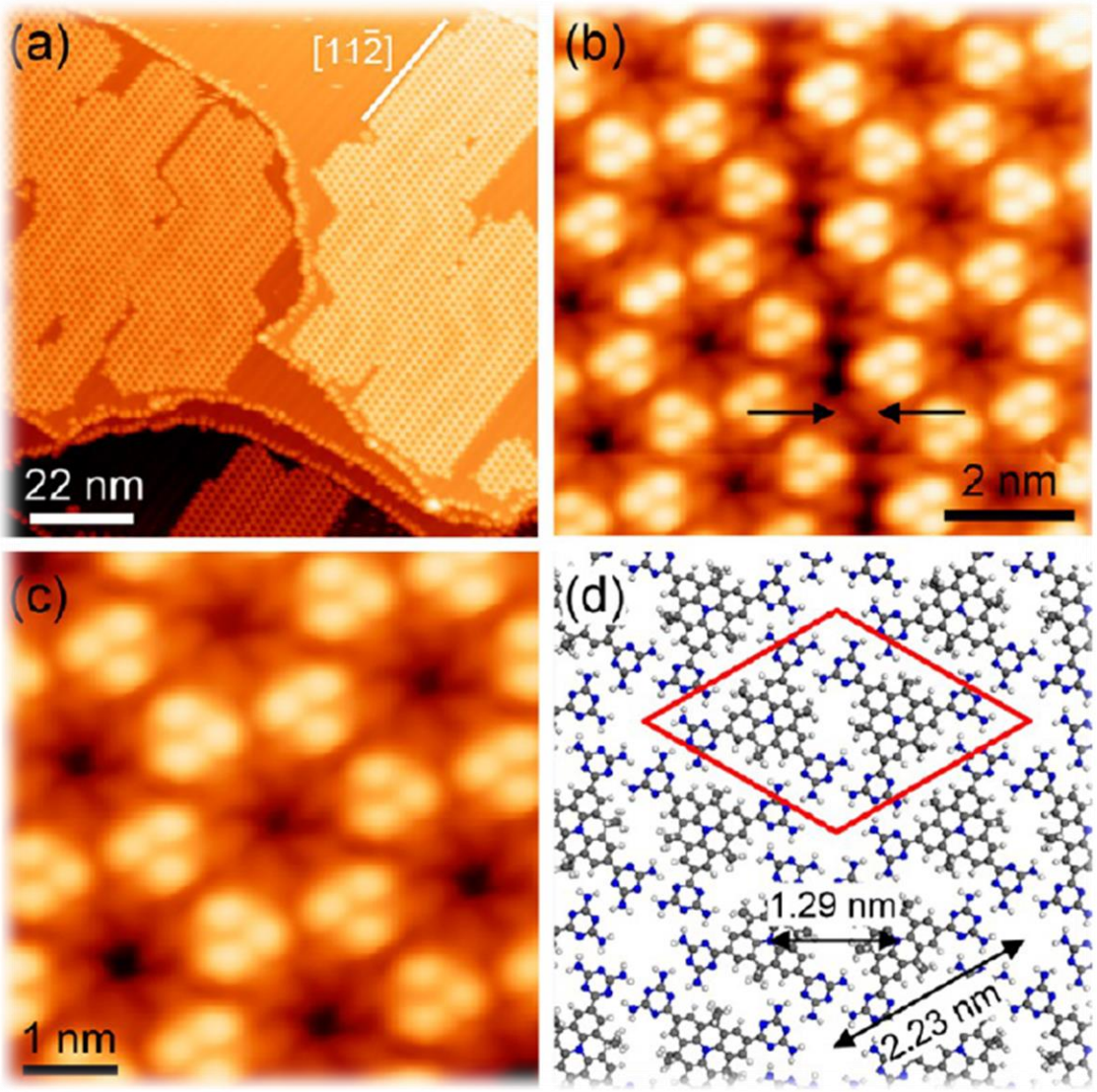

Figure 89. STM images of ADTPA on Au(111) deposited at RT. (a) Overview image of extended hydrogen-bonded networks. (b) High resolution STM topography of a domain boundary between two honeycomb domains that are connected by hydrogen bonds with a tip to-tip bonding motif (black arrows). (c) High-resolution STM image of the honeycomb network with a tip-to-side bonding motif. (d) DFT optimized structure (PBE+D3) of a gas phase ADTPA monolayer with the tip-to-side bonding motif. The unit cell is highlighted by a red frame. STM parameters: (a) U = −1.25 V, I = 510 pA; (b) and (c) U = −800 mV, I = 150 pA. (Adapted with permission from reference[237], Copyright 2015, Royal Society of Chemistry).

2.1.4.2.3 Halogen Bonding Halogen bonding is a type of linear attraction between a nucleophile and an electrophilic site on the terminus of halogen atom bonded to an electron-withdrawing group[241-243] Because of their high electronegativity, halogen atoms tend to be negatively partially charged when bonded to other elements. The anisotropic distribution of surface electrostatic potential around a halogen atom in the molecule is critical for the formation of a halogen bond. The electrostatic attraction between a nucleophile's partial negative charge and either a hydrogen atom's partial positive charge or a small area of partial positive charge on the halogen atom's terminus known as a σ-hole. This σ-hole is usually centred on the C-X axis and surrounded by a negative electrostatic potential belt. The presence of a σ-hole causes an attractive interaction with the nucleophilic region of another molecular body, which is the primary source of halogen bonding.[244]

The terms "hydrogen bonding" and "halogen bonding" are often interchanged. The word "halogen bonding" is derived from the well-known term "hydrogen bonding." Halogen bonding has a higher bonding strength and greater directionality than hydrogen bonding. Exchanging halogen atoms will also alter the bonding power of halogen bonds.[245-247] As a result, halogen bonding is gaining prominence as a technique for constructing molecular nano-architectures.[248-250] For example, Yang *et. al.* reported the halogen-bonded supramolecular self-assembly of graphyne-like molecules (**Figure 90**) on Au(111) driven by both intermolecular halogen and hydrogen bonding. They demonstrated a supramolecular approach to fabricate highly ordered monolayered halogen-bonded graphyne-like two-dimensional (2D) materials from triethynyltriazine derivatives on Au(111).[251] They deposited the molecules on Au(111) at 90K, which subsequently form small self-assembled islands at sub-monolayer coverage. As they observed, the molecules have three bright protrusions, which correspond to Br atoms and confirm that Br-TET adsorbs on Au(111). They investigated that the self-assembled structure was driven by $N_{triazine}$···Br-C(sp) halogen-bonds instead of hydrogen bonded molecules.

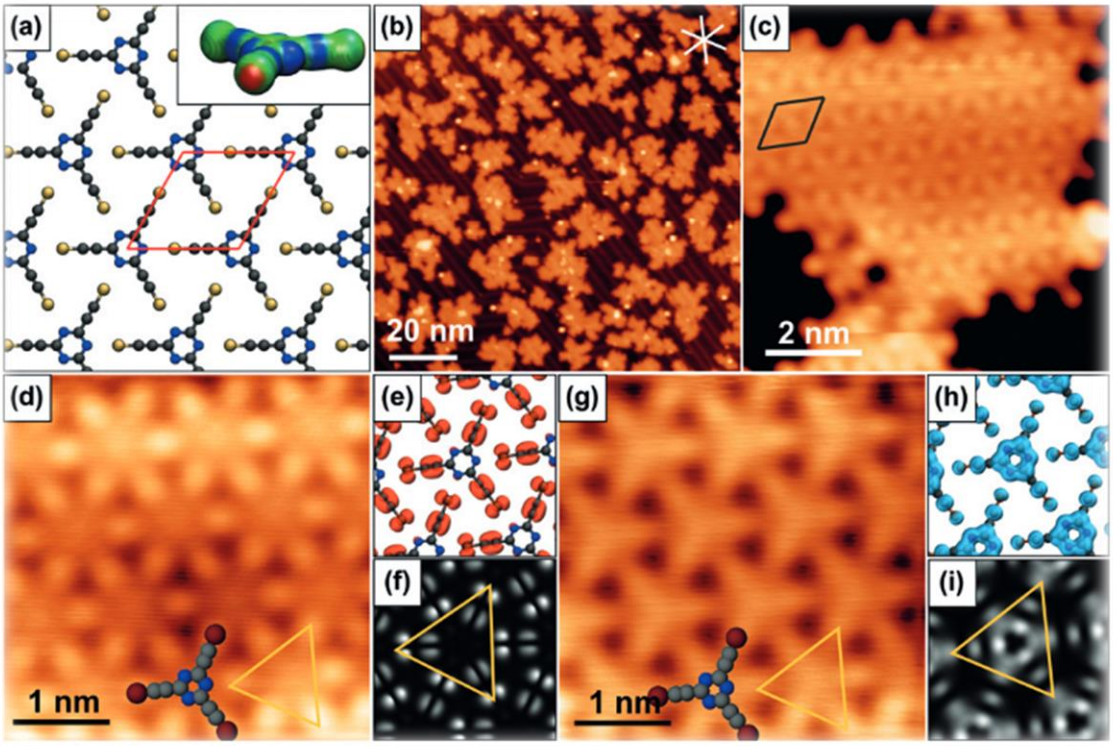

Figure 90. Br-TET on Au(111) upon deposition at 90K. a) Structural model from DFT of halogen-bonded graphyne-like networks. The corresponding electrostatic potential distributions of Br-TET in the inset shows the positive potential in red and the negative potential in blue at isodensity surfaces. b–d, g) STM images of halogen bonded graphyne-like networks. The high-resolution images at (d) U= -0.2 V and (g) U=1.8 V demonstrate the bias dependent STM topography with the corresponding (e,h) partial density of states and f,I) calculated STM images at -0.6 V and +2.5 V that provide a good match to the experiment. The shift towards negative energies in the experiment compared to DFT in gas phase originates from a charge transfer from the surface to the Br-TET-networks. STM parameters: b) U= -1.0 V, I=50 pA; c) U=-1.0 V,I=30 pA; d) U= -0.2 V,I=100 pA; g) U=1.8 V,I=100pA. Colour code: carbon, dark gray; nitrogen, blue; silver, light gray; bromine, brown (Adapted with permission from reference[251] Copyright 2015, Royal Society of Chemistry)

2.1.4.2.4 Metal-ligand bonding Metal-ligand bonding can be interpreted as a coordination association between metal atoms and their accompanying molecules in molecular self-assembly. The metal supplies empty orbitals for the creation of the metal-ligand bonding, while the ligand provides a lone pair of electrons. For the formation of a metal-ligand bond, the lone pair electrons of metal overlaps with the empty orbital of metal.[204, 252-253] Metal-ligand interaction is commonly used to create metal-organic complexes, which have shown great promise in light harvesting, gas storage, and sensor development.[254-258] Metal-ligand interaction has been used to create 1D and 2D metal-organic structures on surfaces for more than a decade.[259-262] Metal-ligand bonding is viewed to be an ideal method for constructing long-range ordered nanostructures on sufficiently stable surfaces. An example of a molecular porous network built via metal–ligand bonding is given by Stulz and co-workers. They have recently published the formation of metal-organic coordination networks via C-Ag-C and C=O-Ag interactions supported by precursor self-assembly on Ag surfaces.[263] (**Figure 91**) They studied the self-assembly and reaction products of 3,6-dibromo-9,10-phenanthrenequinone (DBPQ) on Ag(100) and Ag(110). As they reported, the results of low temperature STM under UHV conditions revealed that the self –assembly of DBPQ at room temperature was driven by hydrogen and halogen bonds on Ag(100). However, they found the DBPQ molecules readily disassociate Br atoms at room temperature and following post annealing at 300 ℃ induce the formation of metal-organic coordination networks including a combination of organometallic species characteristics of Ullmann-like coupling reactions and carbonyl complexes. The molecular row motif formed by DBPQ molecules on Ag(100) is visible in the self-assembly structure. It was discovered to carry over through the thermally induced reaction phase, resulting in ladder-like substructures within the broader metal-organic coordination network. The ladder-like substructures were discovered to be the product of two forms of coordination bonds, C···Ag···C and =O…Ag.

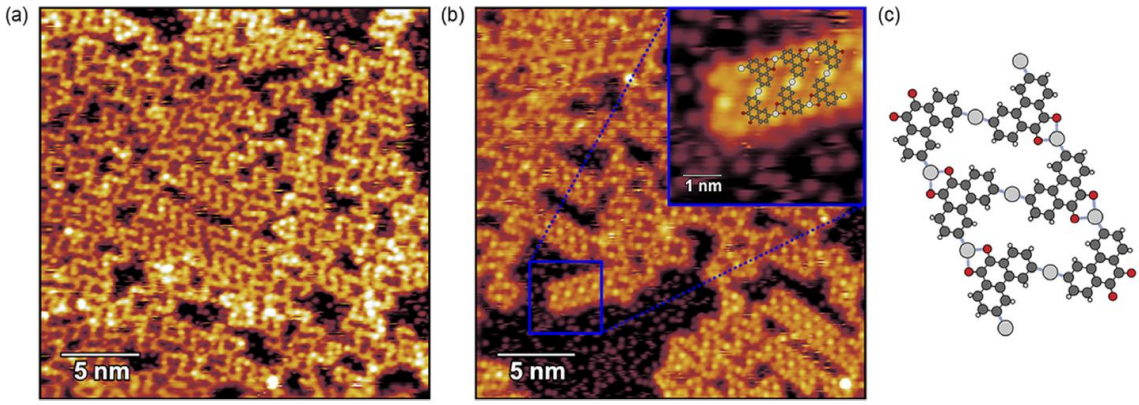

Figure 91. STM images and model showing the metal–organic coordination network of DBPQ that forms on Ag(100) following a thermal anneal to 300 °C. The bromine atoms are observed, adsorbed on the surface and surrounding the coordinated organometallic network. (a) and (b) Scanning at different applied biases results in contrast differences for the Ag adatoms involved in the coordination bonded structure. (a) At a positive bias (U = +1.0 V, I = 100 pA). (b) With a negative bias, the Ag adatoms appear significantly brighter. The inset highlights a recurring ladder-like substructure with molecular models overlaid (U = −1.0 V, I = 100 pA). (c) Model of the ladder-like substructure observed in the metal–organic coordination network highlighting the coordination bonds with blue dashed lines. (Adapted with permission from reference[263], Copyright 2021, AIP Publishing)

Table 5 Summary of energy range, bond length, and character of several noncovalent bond types based on Barth [217] and Metrangolo [264] et al.

Bond type	Energy range [eV]	Bond length [Å]	Character
Van der Waals forces	≈ 0.02 – 0.1	< 10	nonselective
Hydrogen bonding	≈ 0.05 – 0.7	≈ 1.5 – 3.5≈ 2 – 5	selective, directional
Halogen bonding	≈ 0.05 – 1.9	long range	selective, directional
Metal-ligand interaction	≈ 0.05 – 2.5	≈ 1.5 – 2.5	nonselective

Table 5 summarizes various intermolecular interactions. From van der Waals force to halogen bonding, the bonding strength is increasing. Higher bonding strength results in more compact molecular systems, but it also limits the system's versatility. As a result, for the efficient fabrication of the necessary molecular nanoarchitectures, a detailed design of the molecular building block is required.

As previously stated, non-covalent interactions drive the molecular self-assembly process. However, not just one of them is in charge of the process; in most cases, a combination of interactions is observed. One of the most important studies from this thesis, is the temperature dependent molecular self-assembly properties of Me-TBTQ$(OAc)_3Ph_6$ molecules on Cu(111), which will be explained in the following section.

2.2 Results and Discussion

2.2.1 Temperature Dependent self-assemblies of Me-TBTQ(OAc)3Ph6 on Cu (111)

As it was mentioned above in **Chapter 1**, the hexaphenyl substituted Me-TBTQ triacetate molecules, **92,** were obtained using a nine-step synthetic route. The molecules were purified first with column chromatography then recrystallized from a dichloromethane--cyclohexane solvent mixture (see the details in experimental section). Identity and purity of the substance was demonstrated with different spectroscopic methods such as NMR, HPLC and APCI-MS. The spectrum and the chromatogram of molecule **92** can be seen in the appendix section. The molecules were deposited on a Cu(111) crystal and their self-assembly behaviour at different temperatures was studied. Detailed study results will be given in the following sections.

2.2.1.2 Material and Methods

The STM measurements were carried out under ultra-high vacuum (UHV) conditions (base pressure p $\leq 1 \leq 10^{-10}$ mbar). The preparation of samples and analyses were performed in two different chambers. The Cu(111) single crystal was prepared by multiple cycles of 30 min Ar^+ sputtering at an ion energy of 1 keV and a temperature of 650K followed by annealing at 750 K for 15 min. Me-TBTQ$(OAc)_3Ph_6$ molecules were deposited onto the clean Cu(111) surface by a Knudsen-cell evaporator (Dodecon) with a filament-heated crucible. The crystal was heated by a resistive heater after evaporation, and the temperature was determined using a thermocouple attached directly to the manipulator. The corresponding coverages are classified as low and high for coverages that are far below and close to one monolayer, respectively. The samples were loaded into the sample slot of a home-built low-temperature scanning tunneling microscope (STM) of the group of Prof. Matthias Bode (Experimental Physic, JMU Würzburg) with an operating temperature of about 4.5 K after being transferred *in vacuo* to the other UHV chamber. For tip conditioning, STM probe tips were electrochemically engraved from polycrystalline tungsten wires before being gently dipped into the Ag(111) substrate. Manipulation of single **92** molecules were executed with the STM tip at the tunneling parameters of U = 20-50 mV and I = 0.5-50 pA.

2.2.2 Dimer formation at low coverages

First, the molecules, Me-TBTQ(OAc)$_3$Ph$_6$, **92,** were deposited on a clean Cu(111) surface for 9 minutes at 240 °C. However, there were only few molecules observed especially at the step edges (seen in **Figure 92**, a)). Therefore, the duration and the temperature were increased to 18 min. and 260 °C. Despite this, the number of adsorbed molecules on the Cu(111) surface was well below than a monolayer (**Figure 92**, b)).

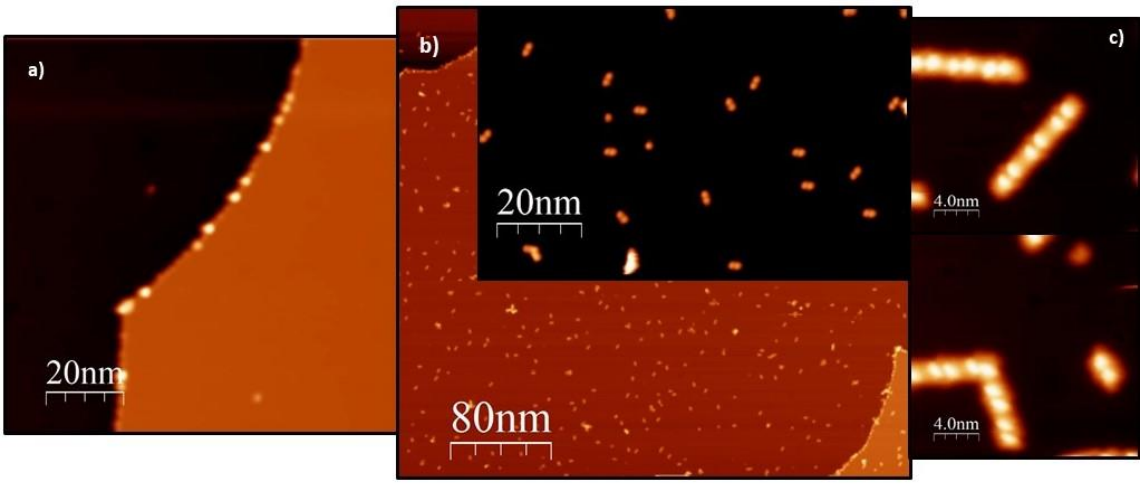

Figure 92. Low coverage deposition of **92** on Cu (111) a) 9 min. long deposition, structures observed only at step edges, U=1V, I=100 pA b) 18 min. long deposition, the dimeric structure started to form, U=500 mV, I= 50 pA c) 54 min. deposition, the molecules initiated to arrange longer chains including dimers, U=1 V, I=50 pA

Hence, the molecules were deposited on the same surface 36 minutes more and the temperature was also increased to 270 °C. (the given temperatures belong to the crucibles, the crystal was at room temperature). The observation of these changes was that the molecules tend to adsorb at step edges first, then form the dimeric structures, the trimers and chains-like structures respectively (seen in **Figure 92**, c)).

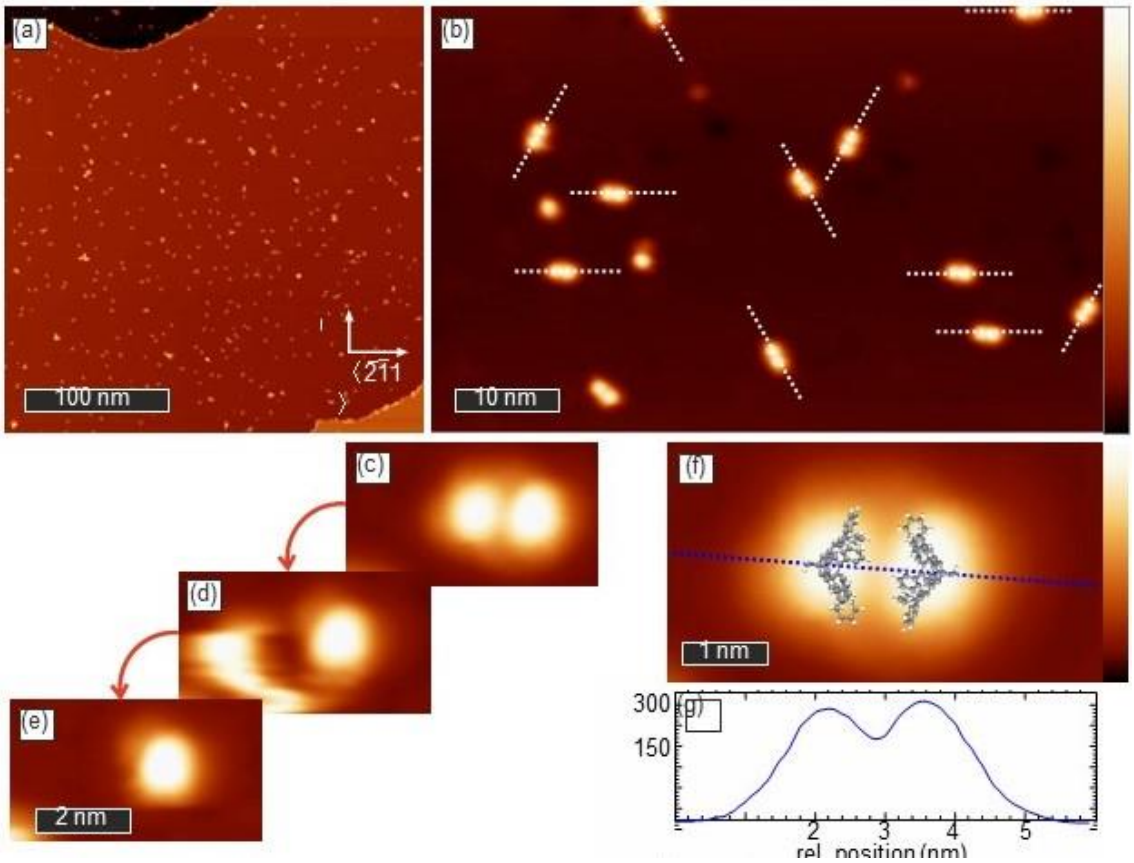

Figure 93. Low coverage deposition of **92** on a Cu (111) surface at room temperature. (a) Topography of a large terrace with monomers, dimers (both appear as small protrusions) and clusters (brighter spots). Preferred adsorption on the crystals step edges can be observed in the upper left and lower right corner. (b) Closer look of several dimers and two monomers. The two protrusions in the upper part correspond to defects of the substrate. As marked by dashed lines, the dimers arrange along the $\langle 2\bar{1}\bar{1} \rangle$ directions of the Cu crystal. (c)-(e) Single molecule STM-Tip manipulation: Starting with a dimer (c), the molecule on the left has been removed (d), resulting in a monomer (e). (f) Enlarged topography of a dimer with the supposed orientation of the two molecules. (g) Height profile of the dimer measured at the dashed line in (f). (f). The inter-molecular distance results in d_{di} = (1.3± 0.2) nm. STM scan parameters (a)-(c), (e), (f): U = 0.5 V, I = 50 pA; (d): U = 0.05 V, I = 50 p

As can be seen from the STM topography in **Figure 93** (a), the molecules appear to adsorb on the step edges of crystal, implying a high mobility at the room temperature. Clusters with two protrusions tend to be the dominant shape on the terraces, as seen in the expanded scan in **Figure 93** (b). In addition, two single protrusions can also be seen in the middle left part of (b), which may be caused by substrate defects. STM-induced molecule modulation facilitates the decomposition of a cluster. (c.f. **Figure 93** (c)) by scanning over the structure (c.f. **Figure 93** (d)) to a single bump (c.f. Figure 2 (e)). This unambiguously shows that each protrusion depicts one single molecule, defining the observed clusters as dimers. The orientation of these dimers is along the $\langle 2\bar{1}\bar{1} \rangle$ directions of the substrate, as highlighted by dashed lines in **Figure 93** (b). On the other hand, subtle tilts away from the symmetry axis are observed and it could be caused by various adsorption sites of the molecules on the surface lattice. The height profile in **Figure 93** (g), taken at the dashed line in **Figure 93** (f), results in d ≈ 300 pm. In fact, this corresponds to the diameter of the triquinacene core. Therefore, it was assumed that the molecules are arranged bowl-to-bowl in dimers based on these findings and supported by the arrangement seen in the the X-ray crystal structure, as presented in **Figure 93** (f) by true-to scale models. The height profile shows that the molecules quench along the central axis, resulting in a slightly smaller bowl diameter than in the crystal arrangement. This orientation influences intermolecular π-stacking, which can be determined by hydrogen-bonding as well as the - association of delocalized electronic systems.

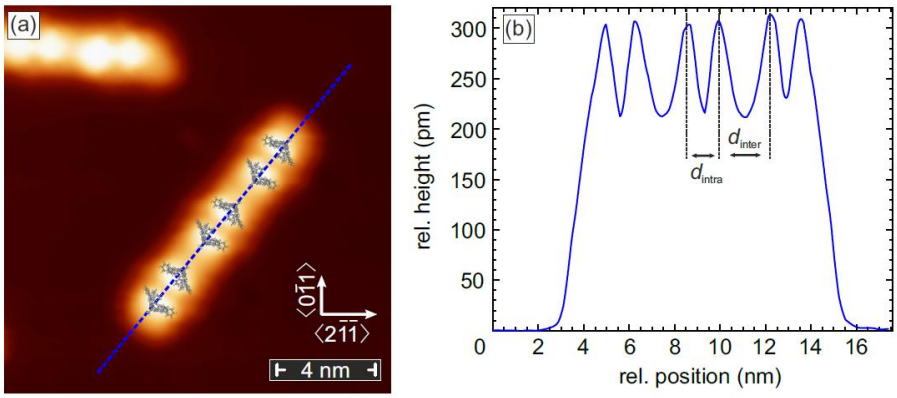

Figure 94. Low coverage deposition of **92** on Cu (111) at RT. Chains of molecules can be observed, as shown in **(a)**, which are oriented along the $\langle 2\bar{1}\bar{1} \rangle$ substrates directions. As can *be* seen in the topography and in the line profile in **(b)**, taken along the dashed

line in **(a)**, the distance between single molecules varies periodically. Scan parameters: U = 1 V, I = 50 pA.

During low coverage deposition, dimeric chains of **92** can be formed on Cu(111) at room temperature, as shown in **Figure 94**. These chains are found near monomers and dimers. A closer look at the chain in **(a)** shows that the distance between adjacent molecules varies. This is particularly apparent in the height profile shown in **(b)**, which is taken along the dashed line in **(a)**. Two distances can be characterized: d_{intra} = (1.25 ± 0.1) nm and d_{inter} = (2.1 ± 0.1) nm. While the first one is almost identical to the molecule-to-molecule distance of free-standing dimers, the second one is 1.7 times greater. As a result, the chains were thought to be dimers, as seen by the overlaid molecular structures in **Figure 94 (a)**: two molecules standing in bowl-to-bowl orientation build a dimer with a distance of d_{intra} = (1.25 ± 0.1) nm, while the *centro* methyl groups extend the distance between two dimers to d_{inter} = (2.1 ± 0.1) nm.

2.2.3 Honeycomb self-assembly arrangement on Cu (111)

Me-TBTQ$(OAc)_3Ph_6$ (**92**) molecules self-assemble into strongly organized structures when the volume of the molecules is increased to high coverage. Furthermore, by deposition at a certain crystal temperature, the structure of the reconstruction can be altered. The temperature-dependent growth behaviour of one fixed coverage is examined in the following for a better comparison.

As shown in **Figure 95** (a), for growth temperatures RT < T_M < 393K we observe islands with typical diameters around 100 nm, which exhibit a honeycomb lattice. Aside from these dominating structures, smaller islands in a state of transformation can be identified. (lower part in **Figure 95** (a)) surrounded by randomly arranged molecular clusters. The honeycomb arrangement can be seen in two orientations, as highlighted by the scan in **Figure 95** (b). The dotted lines indicate the directions along the honeycomb's hollow side. The right (left) domain is tilted by $\alpha_{+(-)}$ = +(-) (13±2) ° from one of the $\langle 0\bar{1}1 \rangle$ directions (solid line). Each protrusion of the honeycomb ring represents one single molecule, according to single molecule manipulation. Two single molecules were pushed out of a system one by one (white arrows) as seen in **Figure 95** (c)-(e), which is in strong alignment with the observations at low coverage.

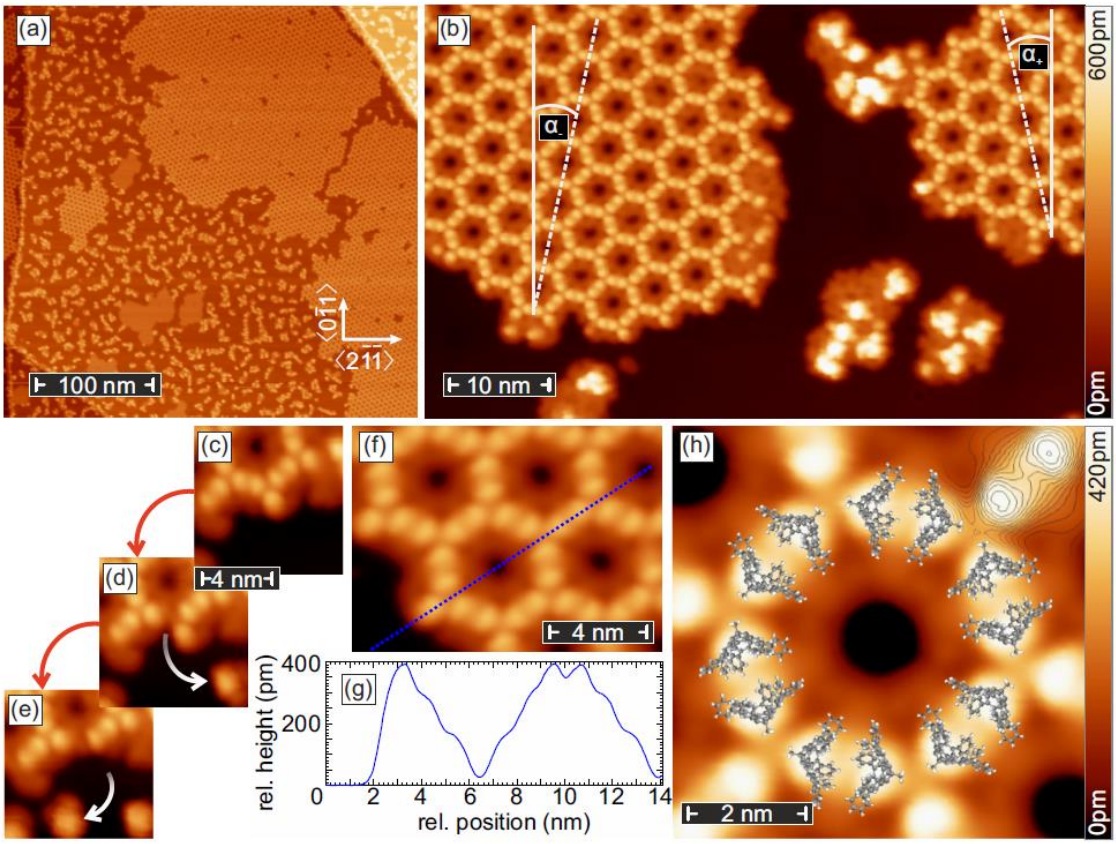

Figure 95. Higher coverage deposition of **92** on a Cu(111) surface at $T_M \approx 363$ K. (a) Wide honeycomb reconstructed islands of molecules coexist with a few tiny islands in a transition state on the topography of a large terrace. Adsorption on the step edges, as well as unordered molecular clusters, can be seen. (b) Enlarged scan of the two phases found for the honeycomb structure. The tilt of $\alpha_{+(-)} = +(-)\ (13\pm2)\ °$ for the right (left) island towards the high symmetry axes is highlighted by dashed lines. (c)-(e) Single molecule manipulation: Starting with an intact structure (c); Two single molecules were moved one at a time, as shown by white arrows. (d)-(e); as a consequence of which a honeycomb is opened and two single molecules are formed (e). (f) Topography at the edge of an island where a height profile is taken along the dashed line. The resulting corrugation along this path is presented in (g). The lattice constant for the honeycomb unit cell is $a_{hoc} = (4.4\pm0.2)$ nm. (h) Enlarged scan of a honeycomb ring with the molecular orientation. A dimer is located on each edge of the structure. Based on the handedness of the molecules an intradimer S-shape can be observed, as highlighted by the overlaid contour plot on the top right. STM scan parameters: U = 1 V, I = 50 pA.

Figure 95 (f) (f) depicts the height profile around the edge of an island (dashed line) (g). The corrugation is approximately 100 pm higher than that seen on the dimer, although the inter-molecular gap decreases to d_{hoc} = (1.15±0.1) nm. In contrast to free-standing dimers, this implies a decreased quench of the arms, which can be explained by increased molecular interactions. The lattice constant of the honeycomb unit cell results in a_{hoc} = (4.4 ± 0.2) nm. Based on these results, a molecular arrangement as depicted in **Figure 95** (h) is proposed. According to this model, each edge of the honeycomb is thus made up of a dimer, as seen in **Figure 95** (f). As mentioned in the results and discussion section of the mass spectrometry results of Me-TBTQ$(OAc)_3Ph_6$, acetate groups at bay positions can easily, be cleaved from the structure, even at room temperature. When the crucible temperature is considered, as well as the STM results, it was assumed that the molecular orientation of the molecules supports that a single molecule **92** has lost one of the acetate groups and that they are self-assembled through metal-ligand interaction with the help of the remaining acetate groups, which is very typical for these types of bonds. Furthermore, the methyl groups are pointing to the corners, while the bowl shape is facing towards each other. A closer look at **Figure 95**, (h) shows an S-shape in the connecting section of a dimer, which is illustrated by the contour plot on the top right. This feature's orientation mirrors that of the second domain. As it is observed in the crystal structure as well, **92** represents two different chiral orientation. The dimeric crystal structure of **92** demonstrates both enantiomers and the S-shape is in accordance with this orientation. Therefore, it was suggested that each domain contains molecules of one handedness, as it is described in **Figure 96** (c), thereby inducing the symmetrical tilt towards the high-symmetry axes.

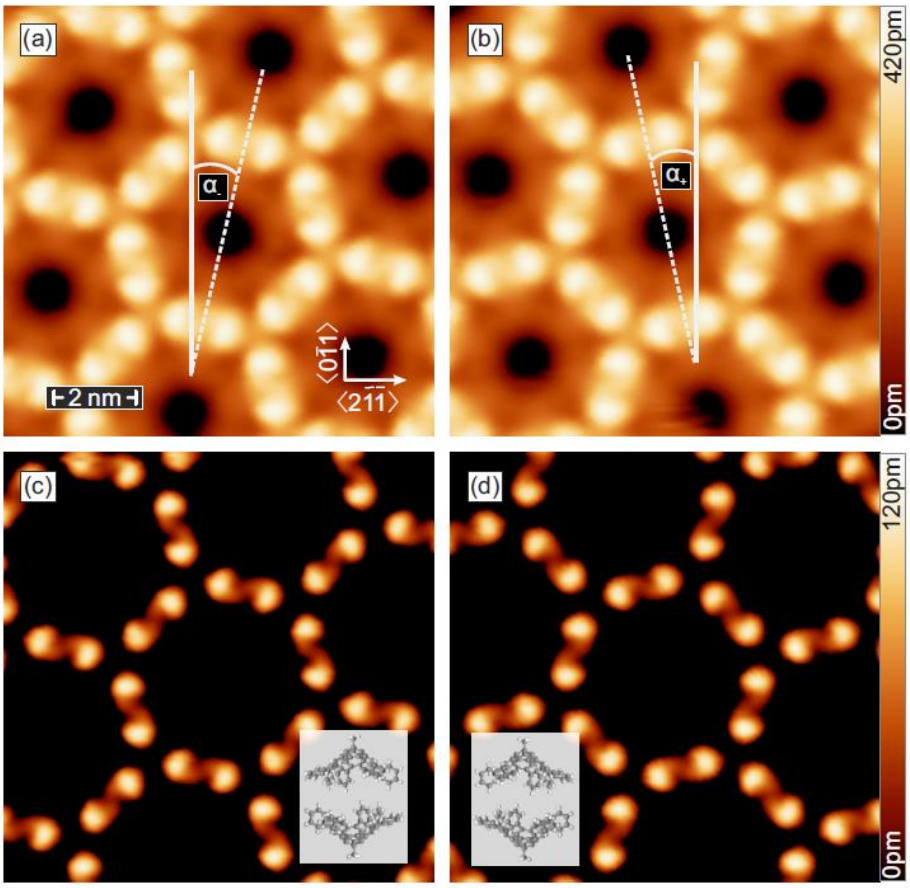

Figure 96. High coverage deposition of Me-TBTQ(OAc)$_3$Ph$_6$ on Cu(111) at T_M 363 K. The two observed orientations of the honeycomb reconstruction are shown in (a) and (b) with a tilt of $\alpha_{+(-)}$ = +(-) (13±2) ° from one of the $\langle 0\bar{1}1 \rangle$ directions. In (c) and (d) reduced topographies of the corresponding scans in (a) and (b) are shown, which highlight the S-shape of the connecting parts between two molecules of each dimer. The insets represent the assumed chirality of the molecules in each orientation. U = 1 V, I = 50 pA.

2.2.4 Triangular self-assembly arrangement on Cu (111)

By increasing the temperature to 393K ≤ T_M < 453 K, a change can be monitored in the appearance of the highly oriented molecules. Instead of a honeycomb lattice, islands appear with an arrangement which we refer to as a transitional state. As can be seen in **Figure 97** (a) Also, the size of these islands ranges from tens to hundreds of nanometres. **Figure 97** represents a zoom in (b) It shows that the islands are made up of a triangular substructure.

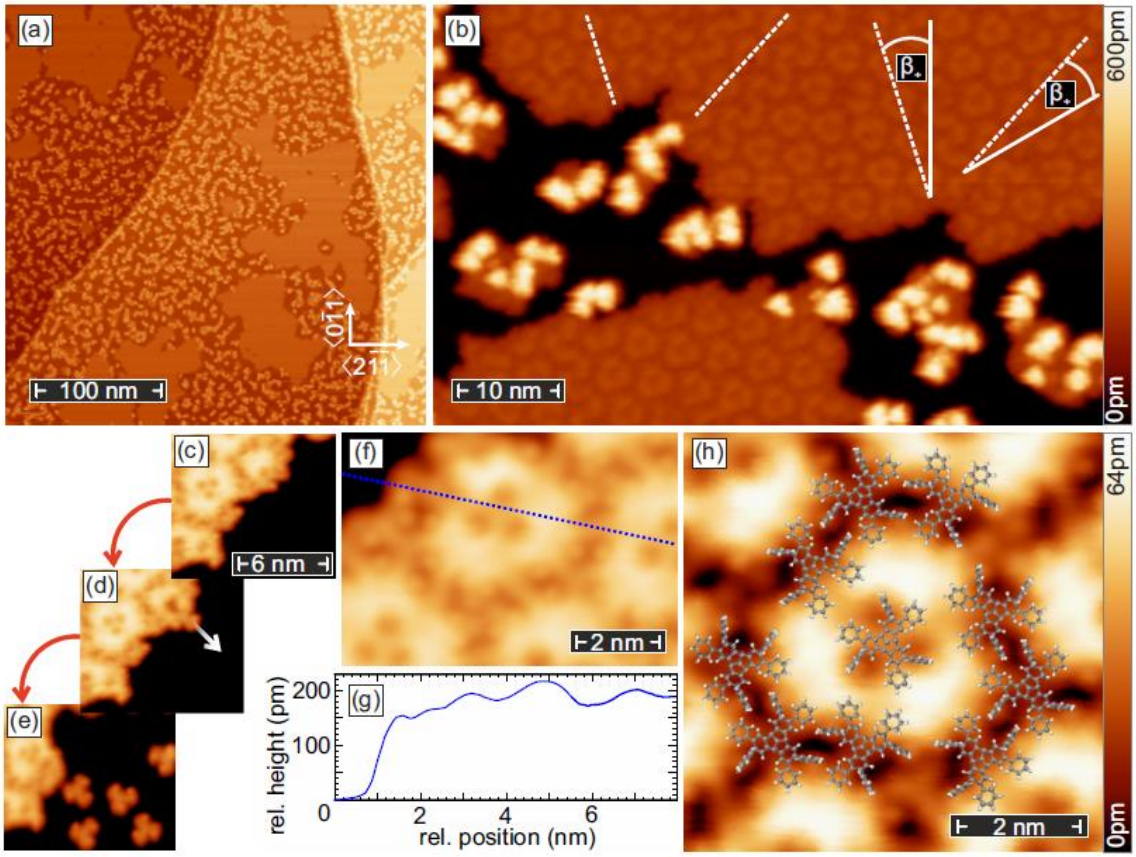

Figure 97. High coverage deposition of **92** on a Cu(111) surface at $T_M \approx 393$ K. (a) Several terraces show large islands of molecular structures in a transitional state. Adsorption could be seen on the step-edges, as well as random clusters. (b) Two islands are shown in an expanded topography, which includes two domains and domain borders with one orientation. The islands seem to have a triangular shape. As marked by dashed lines, both domains are tilted by $\beta = +(18 \pm 2)$ from one of the $\langle 0\bar{1}1 \rangle$ directions. (c)-(e) A halved triangle is detached (c) in two steps of single molecule manipulation: First, a single molecule has been pulled out slightly, as shown by a white arrow (d), whereas five molecules were eliminated at the end (e). (f) A height profile over 1.5 lattice constants is taken along the dotted line of a triangular configuration on the side of an island. The related graph is depicted in (g). The lattice constant for the triangular unit cell is a_{tri} = (4.3 ± 0.2) nm. (h) The molecular orientation is defined by the overlaid structures in this high-resolution scan of the triangular lattice. A symmetrical fan-shaped molecule can be located in the middle and three corners, while six of the molecules on the edges have broken C_3-symmetry. STM scan parameters: U = 1 V, I = 50 pA.

Two orientations of islands with a rotation of β= +(18 ± 2)° from one of the $\langle 0\bar{1}1 \rangle$ substrates high symmetry directions can be found. Two domains regions that are rotated by 60 degrees with respect to one another can be identified for both orientations, as shown by dotted white lines in **Figure 97** (b). By means of single molecule manipulation, half of a triangle was decomposed, as seen in **Figure 97** (c)-(e), yielding five single molecules. As a result of the manipulation, it was found that the appearance of a single molecule in the self-assembled structure is changed. As mentioned above, each single molecule of **92** has a propeller-like C_3-symmetry and one of the two phenyl rings on each arm was observed as a bright protrusion due to its upright position in the overall structure. This assignment was based on the finding that each molecule is considered as a flat lying object in accordance with previous results; the arms are characterized by in-plane phenyl rings, with bright dots representing the phenyl rings pointing out of the molecular plane. Furthermore, the x-ray study of a single molecule in the crystal structure supports this assignment as well (**Figure 79**). However, after the single molecule manipulation, both phenyl rings attached to one arm can flip their orientation, resulting in four non-equivalent configurations with two of them exhibiting reduced symmetry. The height profile in **Figure 97** (g), taken along the dashed line in Figure 4 (f), reveals a corrugation of about 220 pm. The lattice constant for the triangular unit cell is a_{tri} = (4.3±0.2) nm. After combining these findings, it was determined that the orientation of single molecules in the triangular structure shown in **Figure 97** (h). As a result, it was concluded that one unit cell of triangular oriented structure includes a C_3-symmetrical single molecule at the centre and as well as on three edges. Each edge possesses three single molecules, however, only middle one conserves the C_3-symmetry. Furthermore, it was observed that the two single molecules which are located towards to unoccupied corner, lost their C_3-symmetry. The three spherical protrusions in these corners have been assumed as methyl groups based on our observations. As a result, it was concluded that the demethylation of the flat lying molecules in this transition state is yielding bare TBTQ-Ph_6. The following facts support this hypothesis: (i) The observed corrugation of around 220 pm is very low in comparison to the crystal structure's height of 600 pm.; (ii) unlike Me-TBTQ in our previous study[265], there is no protrusion in the molecular center (iii) It was obtained (5)10 molecules for (half)one triangle by detaching half of a triangle and one full triangle. The orientation of the removed molecules, as well as their location before and after the movement, allowed this accurate reconstruction,

with only single protrusions in the unfilled corners.; (iv) It has previously been stated that methyl groups in a hexagonal lattice on (111)-surfaces appear spherical[266-269] (v) The cleavage of methyl groups from organic molecules has previously been defined as an on-surface reaction.[270-271]

2.2.5 Hexagonal self-assembly arrangement on Cu (111)

By increasing the temperature to 453K ≤ T_M < 493K the final self-assembled structure was obtained. **Figure 98** (a) shows around 50nm wide islands.

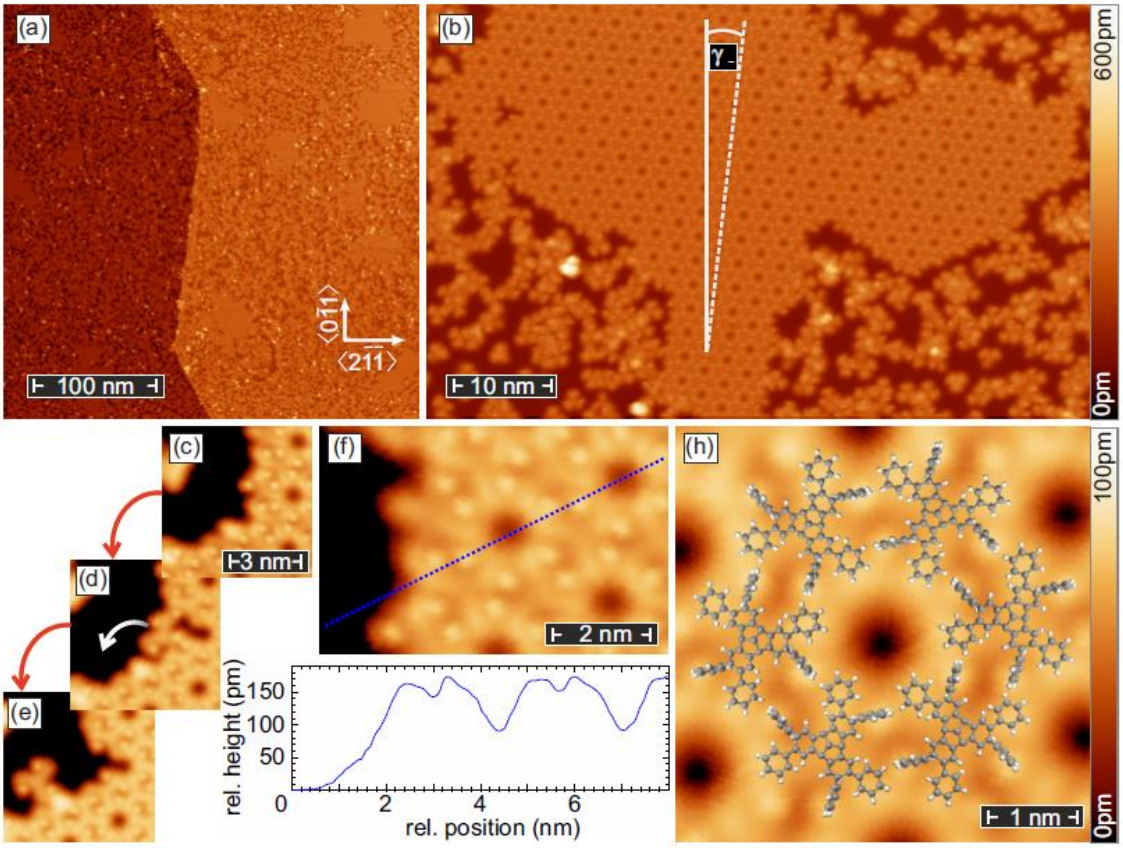

Figure 98. High coverage deposition of **92** on a Cu(111) surface at TM ≤ 468 K. a) On two terraces, islands of around 50nm diameter can be seen, while unorganized molecules occupy large areas. (b) The oriented structure for these islands is hexagonal. The tilt of the given island is γ +(-) = +(-) (6 ± 2) °. (c)-(e) Manipulation of a single molecule as shown by a white arrow, one C_3-symmetrical molecule is pulled out in two steps from the edge of a hexagonal structure. (f) The hexagonal structure's topography has been enlarged, and a height profile has been taken over the dotted blue axis. The resulting

corrugation is given in (g). The lattice constant hexagonal unit cell is a_{hex} = (2.4± 0.2) nm. (h) High-resolution scan of the hexagonal lattice with an overlaid structural model using a ball-stick model with a fan-shaped molecular orientation. STM scan parameters: U = 1 V, I = 50 pA.

As shown in **Figure 98** (b), these islands have a hexagonal configuration, and the two observed orientations are tilted from the surface directions by γ +(-) = +(-) (6 ± 2) °. Single molecules with a C_3-symmetry were removed using molecule manipulation, as seen in **Figure 98** (c)-(e). As a result, for each of the island orientations, a fixed handedness was observed, i.e., a (counter)clockwise orientation of the dots for γ + (-). The structure has a corrugation of about 180 pm, according to the height profile in (g), taken along the dashed line in (f), whereas the lattice constant is a_{hex} = (2.4±0.2) nm. Based on these results, it was determined that one hexagon unit cell is made up of six C_3-symmetrical molecules, as shown in **Figure 98** (h). The lack of single spherical protrusions and the decreased height contribute to the hypothesis that the methyl-groups desorb from the surface when the substrate is heated to a suitable temperature. This assertion is reinforced further by the fact that the desorption of methyl on a Cu(111) surface has been studied in many experiments at equal crystal temperatures of about 450 K.[272-274] Additionally, at intermediate temperatures, a hexagonal arrangement reveals partial methyl-group desorption.[270-271]

2.3 Conclusion

In summary, the substrate temperature dependent self-assembly of Me-TBTQ$(OAc)_3Ph_6$ (**92**) molecules on Cu(111), shows the following evolution of orientations. At room temperature, molecules form dimers, which construct a higher-coverage honeycomb lattice. Furthermore, one of the acetyl group located in the bay positions of the TBTQ core is cleaved and the remaining two induce the metal-molecule interaction. Hereby, the molecular bowls are standing towards each other as face-to-face hemispheres. It was presumed that by increasing the temperature to 393 K, the remaining acetyl and methyl groups would be eliminated from the molecular structure. As it was mentioned above and can be also seen in **Figure 97**, extracted methyl species were observed as spherical bright spots on the surface, while the molecules were self-assembled in a triangular shape. However, the methyl molecules on-surface sterically disturbs the arrangement of the

molecules and thus breaks their C_3-symmetry. It was observed, that at even higher temperatures, the methyl groups desorb from the surface. In addition, the smaller TBTQ-Ph_6 molecules preferably lie flat on Cu(111) crystal and allowing the molecules to settle into a C_3-symmetry and form a dense hexagonal structure.

3. Summary and Outlook

Tribenzotriquinacene (**50**, TBTQ) is a polycyclic aromatic framework with a particularly rigid, C_{3v} symmetrical, bowl-shaped core bearing three mutually fused indane wings. It has been discussed as a defect center for a nanographene by Kuck and colleagues. Therefore, extended TBTQ structures (**40**) are promising models for saturated defect structures in graphene and graphene like molecules and could be used to investigate the role of defects for the electronic properties of graphene.

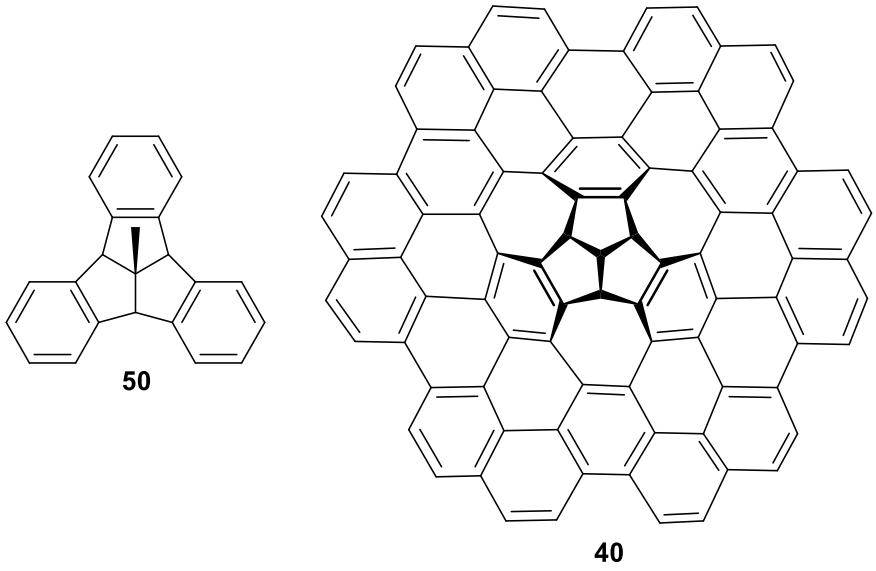

Figure 99. The molecular structures of Me-TBTQ (**50**) and an extended defective graphene flake containing TBTQ at its centre (**40**).

With this motivation, several π-extended TBTQ derivatives have been synthesized in this work. The Suzuki-Miyaura cross coupling reactions between bay position protected iodo TBTQ (**85**) and different types of boronic acids carrying substituents such as phenyl (**91**), biphenyl (**93**), naphthyl (**95**) were successfully performed after multistep synthetic procedures to the precursor molecules, leading to synthetic sequences comprising nine steps in their optimized versions.

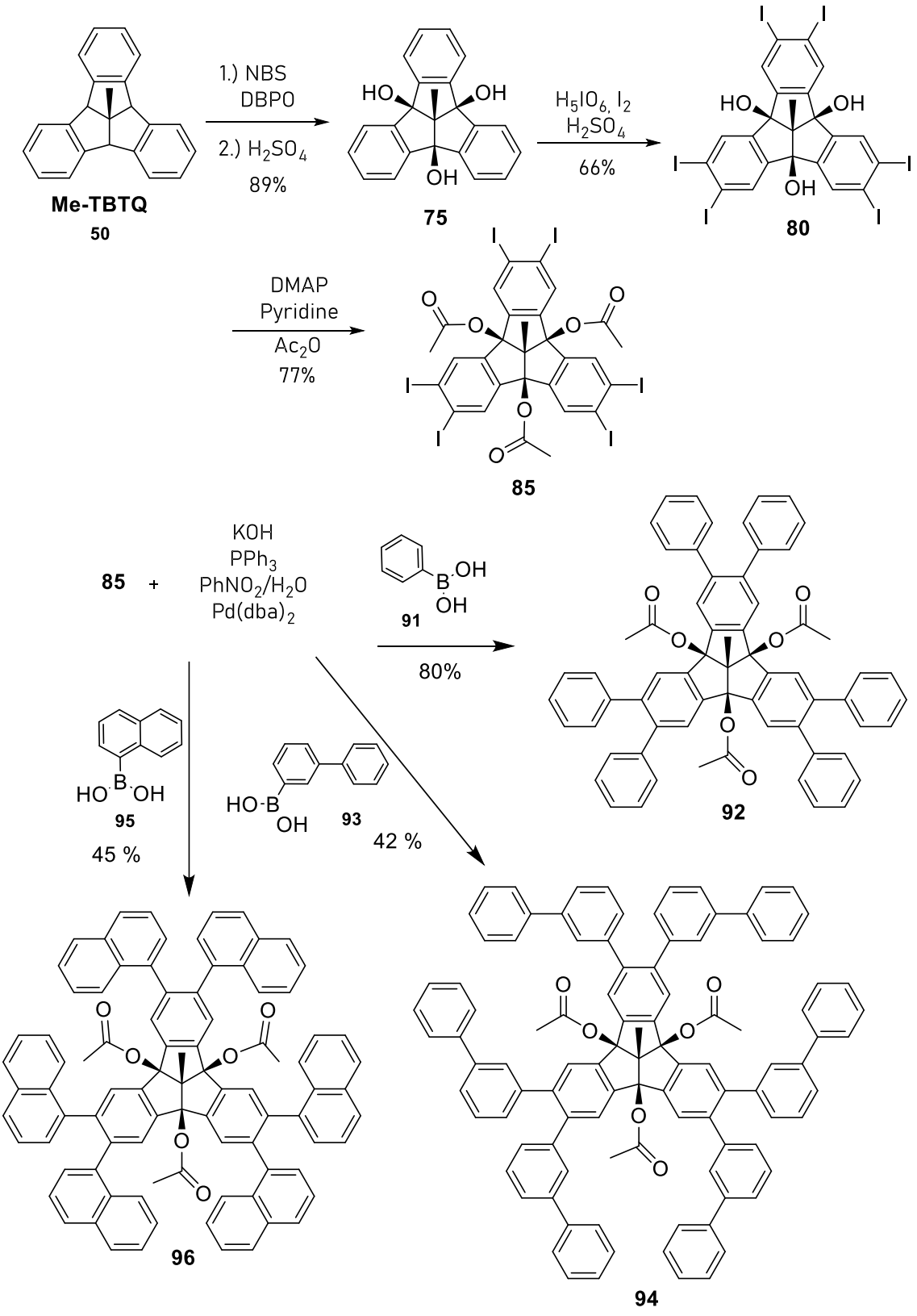

Figure 100. Summarized synthetic pathway to π- extended TBTQs, **92**, **94**, **96.**

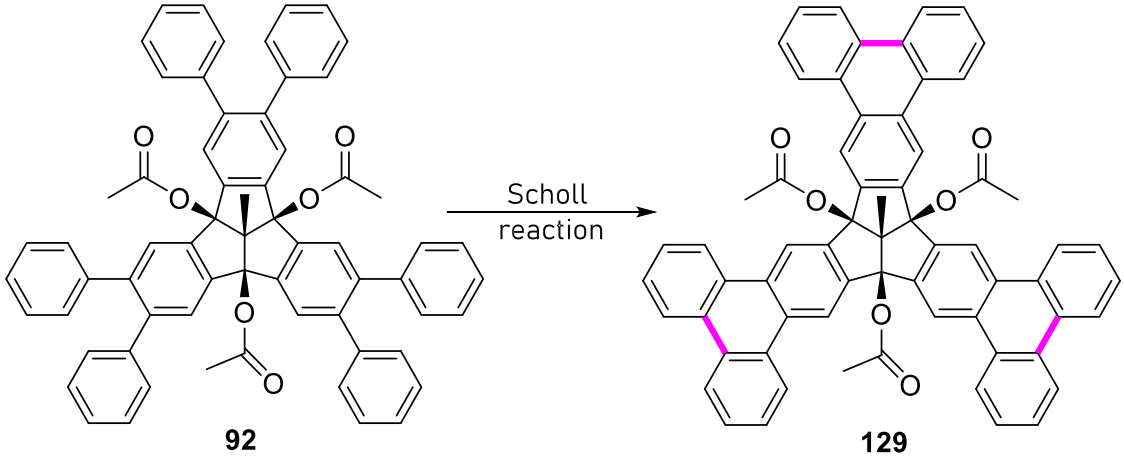

Figure 101. Schematic representation of proposed Scholl reaction to **129**.

The attempted Scholl reaction to **129** is depicted in **Figure 101** Several different Scholl reaction conditions were tried to obtain fully annulated product of hexaphenyl substituted TBTQ (**92**), (**Table 3**). The desired benzannulated TBTQ derivative (**129**) could not be obtained due to unfavourable electron density in the respective positions of the precursor and increased reactivity of the bay position of the molecule **92**. The molecules (**130** and **131**) with MeO and OH groups at bay positions were synthesized instead of the proposed triple benzannulation. As discussed in chapter I the Lewis acids used in the Scholl reaction are mostly chlorine-containing, resulting in chlorination and/or methoxylation of the starting material.[179-180, 182]

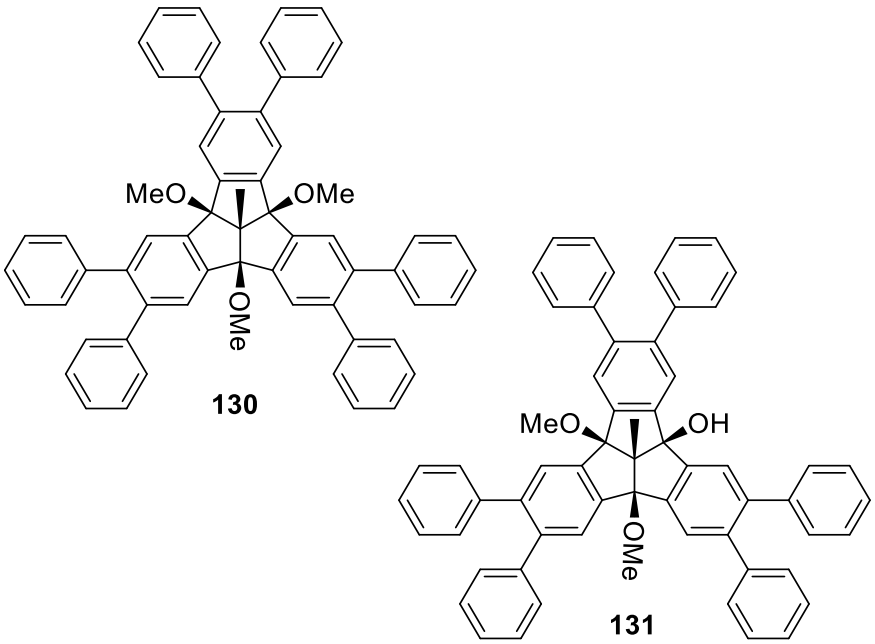

Figure 102. Isolated products of attempted Scholl reactions.

Another method for benzannulation is the on-surface synthesis of graphene flakes and can be carried out using electron beams e.g. in a tunneling microscope (STM).[174] Furthermore, recent high resolution STM experiments (collaboration with the group of Prof. Bode of the Physics Dept.) with the parent system TBTQ (**42**) and *centro*-methyl TBTQ (**50**) on silver and gold surfaces showed that the gas phase deposition of these molecules gives rise to the formation of highly ordered two-dimensional assemblies with unique structural features.[265] This shows the feasibility for the formation of defective graphene networks starting from the parent structures. Therefore, the same deposition technique was used to deposit Me-TBTQ$(OAc)_3Ph_6$, **92** and investigate the molecular self-assembly properties directly on the surface of Cu (111).

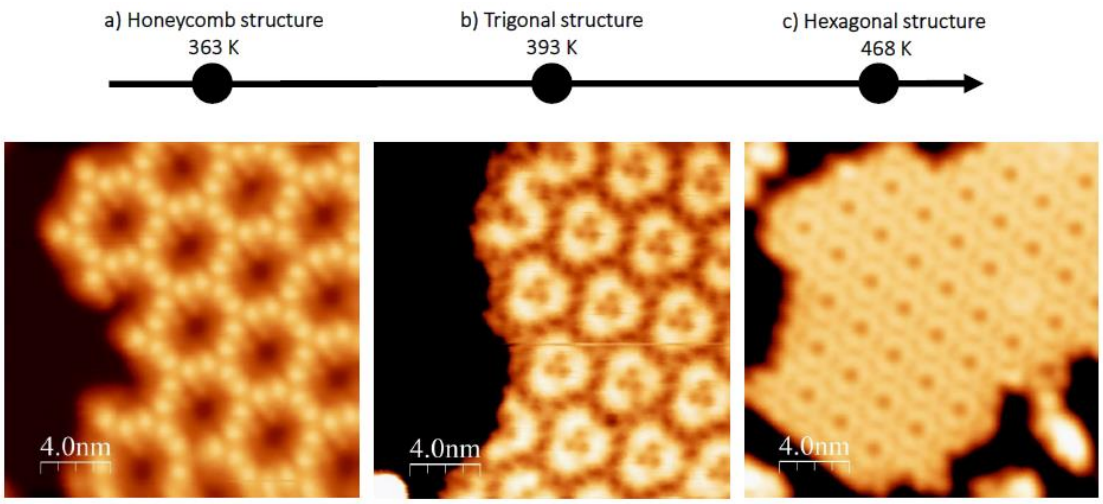

Figure 103. Temperature dependent molecular self-assembly structures of Me-TBTQ(OAc)$_3$Ph$_6$, **92** on Cu(111) surface.

In summary, the substrate temperature dependent self-assembly of Me-TBTQ(OAc)$_3$Ph$_6$ (**92**) molecules on Cu(111), shows the following evolution of orientations. At high surface coverage, molecules form a honeycomb lattice at 363 K (**Figure 103**, **a**). Furthermore, one of the acetyl group located in the bay positions of the TBTQ core is cleaved and the remaining two induce the metal-molecule interaction. Therefore, the molecular bowls are standing towards each other as face-to-face hemispheres. It was presumed that by increasing the temperature to 393 K, the remaining acetyl and methyl groups would be eliminated from the molecular structure. Extracted methyl species were observed as spherical bright spots on the surface, while the molecules were self-assembled in a triangular shape (**Figure 103**, **b**). However, the methyl molecules on-surface sterically disturb the arrangement of the molecules and thus breaks their C_3-symmetry. It was observed, that at even higher temperatures, the methyl groups desorb from the surface. In addition, the smaller TBTQ-Ph$_6$ molecules preferably lie flat on Cu(111) crystal, allowing the molecules to settle into a C_3-symmetry and form a dense hexagonal structure (**Figure 103**, **c**).

4. Zusammenfassung und Ausblick

Tribenzotriquinacen (**50**, TBTQ) ist eine polyzyklische aromatische Verbindung mit einem besonders starren, C_{3v}-symmetrischen, schalenförmigen Kern, der drei anellierte Indan-Flügel trägt. Es wurde von Kuck und Kollegen als Defektzentrum für Nanographen untersucht. Daher sind erweiterte TBTQ-Strukturen (**40**) vielversprechende Modelle für gesättigte Defektstrukturen in Graphen und graphenähnlichen Molekülen, die dazu verwendet werden können, um die Rolle Defekten auf die Ausprägung der elektronischen Eigenschaften von Graphen zu untersuchen.

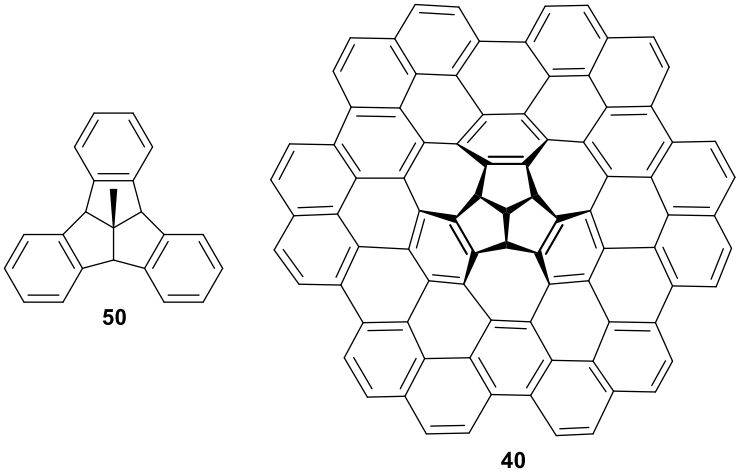

Abb. 1. Die molekularen Strukturen von Me-TBTQ (**50**) und einer ausgedehnten defekthaltigen Graphen-Flocke, die TBTQ in ihrem Zentrum enthält (**40**).

Mit dieser Motivation wurden in dieser Arbeit einige TBTQ-Derivate mit erweitertem π-System synthetisiert. Die Suzuki-Miyaura-Kreuzkupplungsreaktionen zwischen in den Bay-Positionen geschütztem Iodo-TBTQ (**85**) und verschiedenen Arten von Boronsäuren mit Phenyl- (**91**), Biphenyl- (**93**), Naphthyl-Substituenten (**95**) wurde erfolgreich durchgeführt, nachdem die Vorläuferverbindungen durch mehrstufige Synthesen, die in ihren optimierten Versionen insgesamt neun Schritte umfassen, synthetisiert werden konnten.

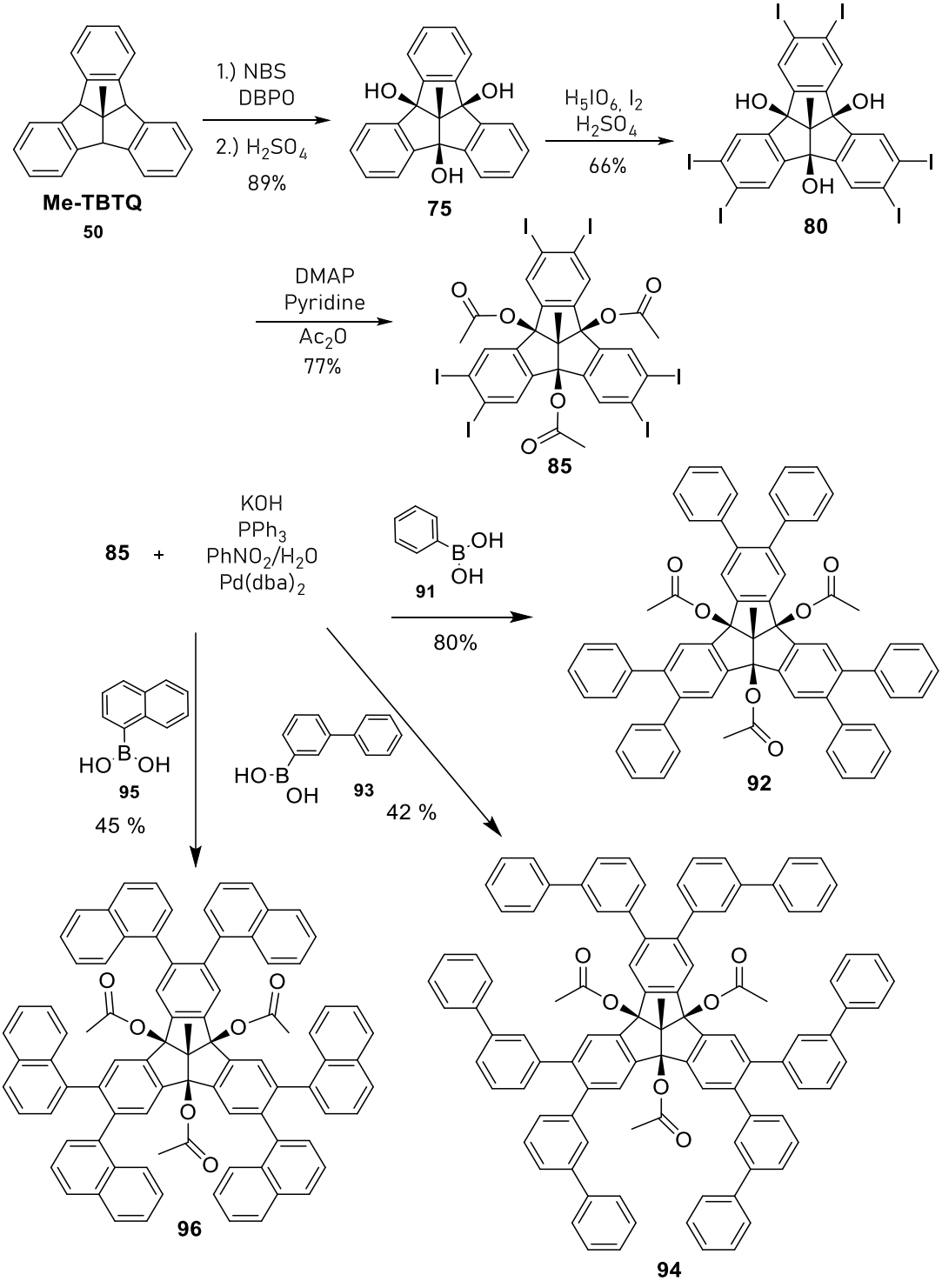

Abb. 2. Zusammengefasster Syntheseweg zu TBTQ-Derivaten **92**, **94** und **96** mit erweitertem π-System.

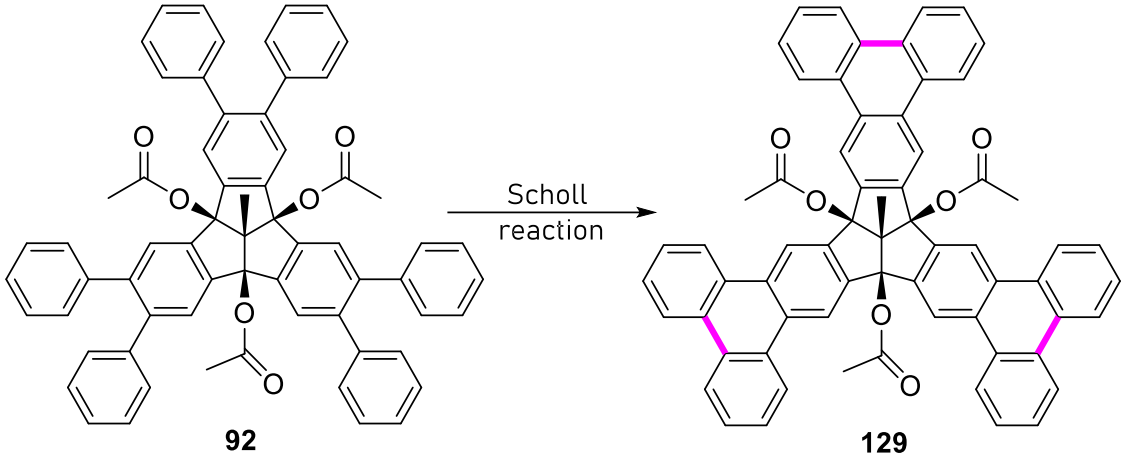

Abb. 3. Schematische Darstellung der vorgeschlagenen Scholl-Reaktion angewendet auf **129**.

Um im Anschluss eine vollständige Annellierung und damit Konjugation des p-Systems zu erreichen, wurden verschiedene Scholl-Reaktionen getestet, um das dreifach anellierte Produkt aus hexaphenylsubstituiertem TBTQ (**92**) zu erhalten (**Tabelle 3**). Das gewünschte benzannulierte TBTQ-Derivat (**129**) konnte aufgrund der relativ geringen Elektronendichte an den Annellierungspositionen und der erhöhten Reaktivität der Bay-Positionen des Moleküls **92** nicht erhalten werden. Die Moleküle (**130** und **131**) mit MeO- und OH-Gruppen an den Bay-Positionen wurden anstelle der vorgeschlagenen Dreifachen-Benzannulation synthetisiert. Wie in Kapitel I besprochen, sind die in der Scholl-Reaktion verwendeten Lewis-Säuren meist chlorhaltig, was zu einer Chlorierung und/oder Methoxylierung (nach Aufarbeitung in MeOH) des Ausgangsmaterials führt.[179-180, 182]

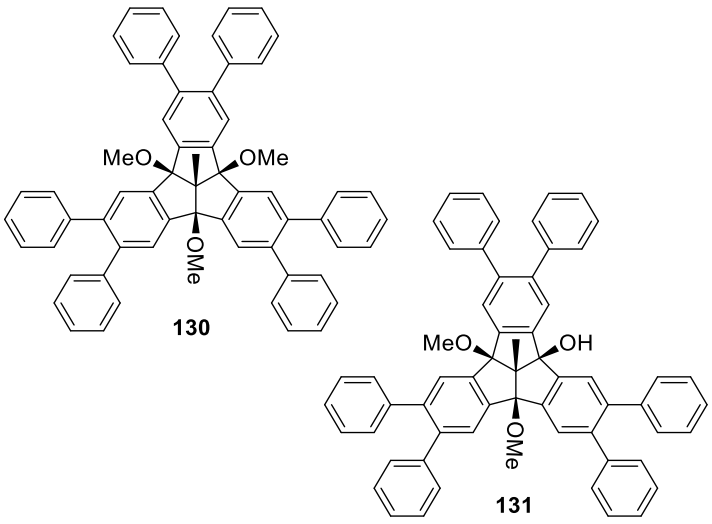

Abb. 4. Isolierte Produkte von getesteten Scholl-Reaktionen.

Eine weitere Möglichkeit zur Annellierung von Nanographenen besteht in der On-Surface-Synthese. Diese kann mit Elektronenstrahlen z.B. in einem Rastertunnelmikroskop (STM) durchgeführt werden.[174] Darüber hinaus war durch hochauflösende STM-Experimente mit dem Stammsystem TBTQ (**42**) und *centro*-methyl TBTQ (**50**) auf Silber- und Goldoberflächen (Kooperation Prof. Bode, Fakultät für Physik) bekannt, dass die Gasphasenabscheidung dieser Moleküle zur Bildung hochgeordneter zweidimensionaler Assemblierte mit einzigartigen strukturellen Eigenschaften führt. Dies zeigt die Möglichkeit zur Bildung von defekthaltigen Graphen-Netzwerken ausgehend von den Stammsystemen. Daher wurde hier die gleiche Abscheidungstechnik verwendet, um für Me-TBTQ$(OAc)_3Ph_6$ (**92)** die molekulare Selbstanordnung auf der Oberfläche von Cu(111) untersuchen.

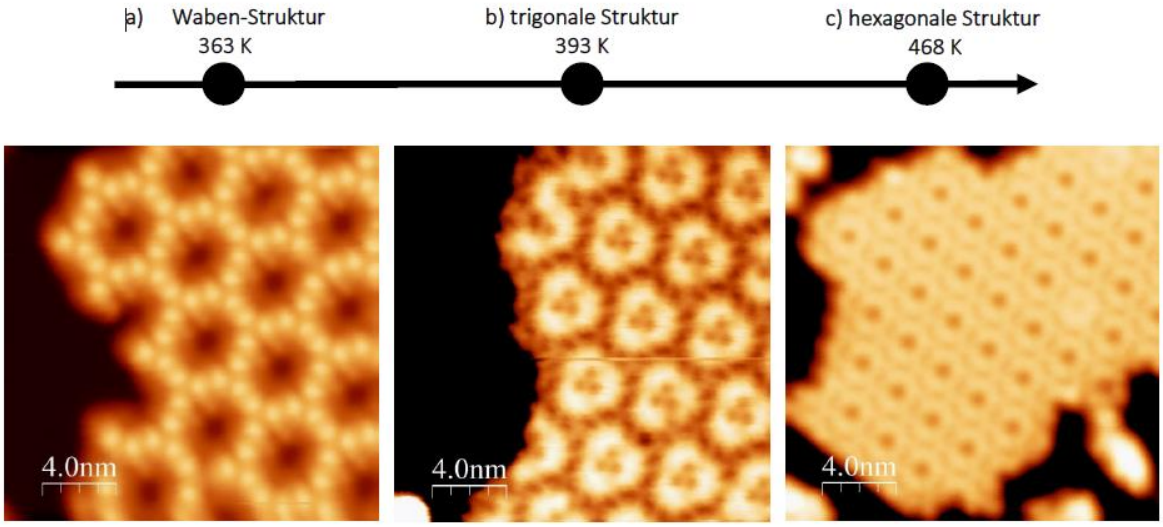

Abb. 5. Temperaturabhängige molekulare Selbstanordnung von Me-TBTQ$(OAc)_3Ph_6$, **92** auf der Cu(111)-Oberfläche.

Zusammenfassend zeigt die Selbstorganisation von Me-TBTQ$(OAc)_3Ph_6$ (**92**) auf Cu(111) eine ausgeprägte Temperaturabhängigkeit. Die Moleküle bilden bei 363 K ein höheres Wabengitter aus (**Abb. 5**, **a**). Außerdem wird eine der Acetylgruppen, die sich in den Bay-Positionen des TBTQ-Kerns befinden, abgespalten und die verbleibenden Gruppen wechselwirken mit der Metalloberfläche. Daher stehen sich die Molekülschalen als einander zugewandte Halbkugeln gegenüber. Es wird vermutet, dass durch die Erhöhung der Temperatur auf 393 K die verbleibenden Acetyl- und Methylgruppen aus der Molekülstruktur eliminiert werden, da die experimentellen Befunde auf diesen

Prozess hindeuten. Extrahierte Methylgruppen wurden als kugelförmige helle Flecken auf der Oberfläche beobachtet, während sich die Moleküle selbst in einer dreieckigen Form anordneten (**Abb. 5**, **b**). Allerdings stören die Methylgruppen an der Oberfläche sterisch die Anordnung der Moleküle und brechen so deren C_3-Symmetrie. Es wurde beobachtet, dass bei noch höheren Temperaturen die Methylgruppen von der Oberfläche desorbieren. Außerdem liegen die kleineren TBTQ-Ph_6-Moleküle bevorzugt flach auf dem Cu (111) -Kristall, so dass sich die Moleküle in der C_3-Symmetrie anordnen und eine dichte hexagonale Struktur bilden (**Abb. 5**, **c**).

5. Experimental Section

5.1 General Methods

Chemicals: Commercial chemicals from Acros Organics, Alfa Aesar, Fluka, Merck or Sigma Aldrich were used without further purification, unless stated otherwise. Solvents were distilled or dried before use, using standard procedures. Dried solvents were used immediately after distillation. Nitrogen and argon (purity: 99.99990%) were used from Linde, which were dried using calcium chloride and silica gel.

Vacuum pumps: Vacuubrand diaphragm pumps and Leybold oil pumps of different kinds were used.

Melting points: Melting points were measured using a Reichert Austria Kofler Heizbank or an Optimelt MPA 100 (>350°C) and are un-corrected.

NMR spectroscopy: ^{1}H and ^{13}C NMR spectra were measured using a Bruker AVANCE 400 FTNMR- Spectrometer (^{1}H: 400 MHz, ^{13}C: 100 MHz) and a Bruker DMX 600 FT-NMRSpectrometer (^{1}H: 600 MHz, ^{13}C: 150 MHz). Chemical shifts (δ) are listed in parts per million (ppm) and are reported relative to internal standards. The internal standard came from the deuterated solvents used:

^{1}H: $CDCl_3$ δ = 7.26, $(CD_3)_2CO$ δ = 2.05, CD_2Cl_2 δ = 5.32.

^{13}C: $CDCl_3$ δ = 77.16, $(CD_3)_2CO$ δ = 29.84. 13C: $CDCl_3$ δ = 77.16, $(CD_3)_2CO$ δ = 29.84, CD_2Cl_2 δ = 53.84.

Coupling constants (*J*) are quoted in Hertz (Hz). The following abbreviations are used to describe nuclear spin coupling: s: singlet, br s: broad singlet, d: doublet, br d: broad doublet, t: triplet, q: quartet, and m: multiplet. ^{13}C NMR, DEPT and standard two-dimensional techniques (COSY, HSQC, HMBC, and NOESY) were used to assign the signals. Deuterated chloroform was filtered through neutral aluminium oxide before sample preparation.

TLC: Thin layer chromatography was carried out using Merck TLC-aluminium coated silica 60 F254 plates (thickness: 0.2 mm) and suitable TLC stains were used when necessary. Solvent mixtures are given in volume percent (v/v).

Chromatography: Column chromatography was carried out using compressed air. Silica gel from Merck (particle size 0.04-0.063 mm) was used and columns of varying sizes and widths were used. Solvent mixtures are given in volume percent (v/v).

HPLC: The following instruments were used: Jasco MD-2010 Plus Multiwavelength Detector, Jasco DG-2080-53 3-Line Degasser, Jasco LC-Net II/ADC, Jasco PU-2080 Plus Intelligent HPLC Pump. The following columns were used: Reprosil C-18-PQ-JASCO, 5 μm, 250 mm × 4 mm, Reprosil C-18-PQ-JASCO column, 5 μm, 250 mm × 10 mm and an Interchim Uptisphere US5SI silica column, 5 μm, 250 mm × 4.6 mm. HPLC solvents were used and given in volume percent (v/v). A rate of 2.5 ml/min was used for semi-preparative columns, and a rate of 1 ml/min was used for analytical columns.

UV/Vis spectroscopy: UV/Vis measurements were carried out using a *Jasco* V-630 spectrometer in 1 cm quarz cuvettes. If not stated otherwise, the solvent used was HPLC grade dichloromethane. The measurements range was 200-800 nm using a quartz cuvette with a layer thickness of 10 mm.

Mass spectromety: The following mass spectrometers were used: Electrospray Ionisation (ESI): Bruker Daltonics micro-TOF Focus II. MAT 90 Varian MS 320. Atmospheric-pressure chemical ionization (APCI) Bruker Daltonics micro TOF Focus II and high-resolution measurements are accurate to < 2 ppm (EI) and < 3 ppm (ESI, APCI), MALDI-TOF measurements were performed with a Bruker Daltonics autoflex II mass spectrometer, equipped with a 337 nm MidiNitrogen laser MNL. All MALDI-TOF spectra were acquired in the linear positive mode.

FT-IR spectroscopy: FT-IR spectra were recorded with a Jasco FT-IR equipped with an ATR unit. The intensity of the adsorption bands is denoted: vs: very strong, s: strong, m: medium, and w: weak.

Elemental Analysis: Measurements for the determination of the chemical composition were carried out using an Elementar Vario Micro. V_2O_5 was added when necessary, to aid combustion.

5.2 Syntheses

2-Methyl-1H-indene-1,3(2H)-dione (44)[275]

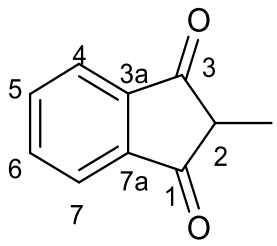

4.72 g (0.123 mol, 1.06 eq.) of a 60% NaH suspension in mineral oil were placed under N_2 atmosphere and washed with 30 ml anhydrous pentane with cold trap via vacuum pump three times to remove the paraffin oil. After anhydrous benzene (122 ml) was poured into NaH, dimethyl phthalate (0.12 mmol 24.4 g, 1.08 eq.) and pentan-3-one (0.12 mmol, 10.0 g, 1.0 eq) were added dropwise, subsequently. The reaction mixture was heated to reflux for 72 h. A deep red solid formed. After cooling the reaction mixture to room temperature, the solids were collected by filtration then dried *in vacuo*. The crude product was dissolved in water (4000 ml), and the solution was acidified with concentrated HCl (≈10 ml). The dione **44** was isolated as yellowish crystals in 62 % yield.

Yield: 23.8 g (0.15 mol, 62 %, lit.[276] 68 %),

Melting Point: 79 − 83 °C (lit.[275] 83 − 84 °C),

R_f: 0.70 (cyclohexane / ethyl acetate 2:1),

^{1}H-NMR (400 MHz, $CDCl_3$): δ = 7.99 -7.97 (2H, m, 4/7-H), 7.86 - 7.84 (2H, m, 5/6-H), 3.05 (1H, q, $^3J_{Me,2}$ = 7.7 Hz, 2-H), 1.42 (3H, d, $^3J_{Me,2}$ = 7.7 Hz, CH_3) ppm,

^{13}C NMR (100 MHz, $CDCl_3$): δ = 201.2 (C_q, C=O), 142.0 (C_q, C-3a/7a), 135.7 (C_t, C-5/6), 123.3 (C_t, C-4/7), 48.9 (C_t, C-2), 10.6 (C_p, CH_3) ppm,

FT-IR: ῦ = 3431 (w, ν(C=O), 3068 (w, ν(C-H_{arom})), 2972 (w, ν(C-H)), 2925 (m, ν(C-H)), 2871 (w, ν(C-H)), 2854 (w, ν(C-H)), 1741 (s, ν(C=O)), 1699 (vs, ν(C=O)), 1589 (s, (C=C_{arom})), 1450 (m, (C=C_{arom})), 1369 (m), 1350 (m), 1327 (m), 1286 (s), 1230 (s), 1155 (m), 1124 (w), 1083 (m), 1039 (w), 976 (w), 931 (s), 800 (m), 741 (vs), 688 (s), 611 (w) cm^{-1}.

UV/Vis (CH_2Cl_2, lg ε): λmax = 303 (0.07), 292 (0.09), 247 (1.26), 223 (3.17) nm.

The spectroscopic data correspond to the data reported in the literature.[276]

2-benzhydryl-2-methyl-1H-indene-1,3(2H)-dione (47)[146]

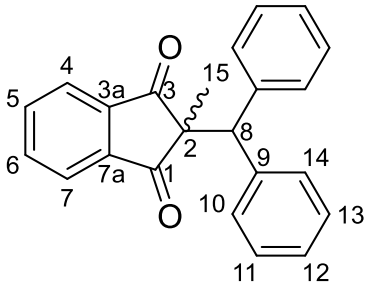

10.0 g (62 mmol, 1.00 eq.) of methylindenedione, 11.5g benzhydrol (62 mmol, 1.00 eq.) and 0.6 g (3.75 mmol. 0.05 eq.) of p-TsOH monohydrate were dissolved in 75 ml of benzene. The reaction mixture was heated to reflux for 5h using a Dean-Stark trap to remove the water produced in the reaction. The solvent was removed *in vacuo* and the residue was dissolved in 50 ml $CHCl_3$, then extracted twice using each time 40 ml of 5% sodium carbonate solution and 40 ml distilled water. The organic phase was dried over sodium sulfate and the solvent was removed *in vacuo*. The remaining orange oil was suspended in 25 ml MeOH and allowed to cool to 5 °C overnight. Before drying, the beige crystals were filtered and washed with MeOH. The dione (**47**) was isolated as a cream-colored powder in 84% yield.

Yield: 18.0 g (93.0 mmol, 84 %, lit.[146] 90 %),

Melting Point: 117 − 120 °C (lit.[146] 122 °C),

R_f (silica): 0.63 (cyclohexane / ethyl acetate 3:1),

^{1}H-NMR (400 MHz, $CDCl_3$): δ = 7.83 -7.81 (2H, m, 4/7-H), 7.70 - 7.68 (2H, m, 5/6-H), 7.47 - 7.44 (4H, m, 10,14-H), 7.18 - 7.14 (4H, m, 11,13-H), 7.07 (2H, t, ^3J = 7.4 Hz, 12-H), 4.57 (1H, s, C*H*$(Ph)_2$), 1.30 (3H, s, CH_3) ppm,

^{13}C NMR (100 MHz, $CDCl_3$): δ = 204.3 (C_q, C=O), 141.4 (C_q, C-3a/7a), 139.7 (C_q, C-1'), 135.5 (C_t, C-5/6), 129.7 (C_t, C-2'/6'), 128.3 (C_t, C-3'/5'), 126.8 (C_t, C-4'), 123.1 (C_t, C-4/7), 58.2 (C_q, C-2), 57.9 (C_t, $CH(PhMe)_2$), 20.0 (C_p, C(2)CH_3) ppm,

FT-IR: ϑ̃ = 3064 (w, ν(C-H)), 3030 (w, ν(C-H)), 2924 (w, ν(C-H)), 2856 (w, ν(C-H)), 1736 (m, ν(C=O)), 1699 (vs, ν(C=O)), 1593 (m, ν(C=C_{arom})), 1495 (m, ν(C=C_{arom})),

1450 (m, δ(CH_3)), 1269 (s), 1244 (m), 987 (m), 766 (s, δ(CH_3)), 731 (m), 704 (vs), 617 (m) cm^{-1}.

UV/Vis (CH_2Cl_2, lg ε): λmax = 304 (0.07), 246 (1.36), 232 (2.51) nm.

HRMS (APCI, pos): calc. for [$C_{23}H_{18}O_2$ + H] m/z 325.1234; found m/z 325.1233.

The spectroscopic data corresponded to the data reported in the literature.[146]

(1R,2s,3S)-2-benzhydryl-2-methyl-2,3-dihydro-1H-indene-1,3-diol (49)[146]

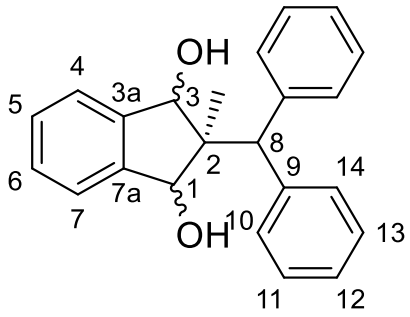

2.11 g (27.5 mmol 1.0 eq.) of $LiAlH_4$ was added under N_2 atmosphere in 100 ml THF. 18.0 g (27.5 mmol) of dione was dissolved in 60.0 ml THF and slowly added into vigorous stirring $LiAlH_4$ mixture. The reaction was heated to reflux for 4h. After cooling down the reaction mixture to room temperature, THF was removed in *vacuo* and the residue was dissolved in 150 ml diethyl ether. The excess $LiAlH_4$ was hydrolyzed by careful addition of ice. The organic phase was decanted, and the aqueous phase was extracted six times with 20 m diethyl ether each time until thin layer chromatography revealed no product. The solvent was removed in *vacuo.* This gave the diol as colorless crystals in the isomer ratio 17:83 (all cis: cis-trans).

Yield: 28.8 g (85.4 mmol, 83 %, lit.[146] 82 %),

all cis-49:

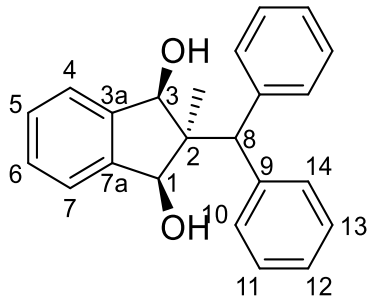

Yield: 4.86 g (0.051 mmol, 17%)

Melting Point.: 193−194 °C; Lit.[146] 191−192 °C,

R_f: 0.37 (Cyclohexane/ethyl acetate 5:1),

^{1}H-NMR (400 MHz, $CDCl_3$)**:** δ = 7.58 (4H, d, ^3J= 8.0 Hz, 10,14-H), 7.44 (2H, m, 5/6-H), 7.36 (4H, t, ^3J = 8.0 Hz, 3a,7a,11,13H), 7.24 (2H, tt, ^3J = 7.4 Hz, ^4J = 1.3 Hz), 5.23 (1H, s, C*H*Ph_2), 4.57 (2H, d, ^3J= 7.2, C*H*OH), 2.26 (2H, d, ^3J = 7.2 Hz, O*H*), 0.84 (3H, s, CH_3) ppm,

^{13}C NMR (100 MHz, $CDCl_3$)**:** δ = 144.72 (C_q, C-3a/7a), 141.80 (C_q, C-1'), 129.93 (C_t, C-3'/5'), 129.17 (C_t, C-2'/6'), 128.54 (C_t, C-4'), 126.49 (C_t, C-4/7), 126.14 (C_t, C-5/6), 81.73 (C_t, C-3/1), 53.46 (C_q, C-2), 48.82 (C_t, $CHPh_2$), 20.48 (C_p, C-(2) *C*H_3) ppm,

FT-IR: ϑ = 3427 (br, *ν*(O-H)), 3249 (br, *ν*(O-H)), 3082 (w, *ν*(C-H_{arom})), 3057 (w, *ν*(C-H_{arom})), 3024 (w, *ν*(C-H_{arom})), 2960 (m, *ν*(C-H)), 2918 (m, *ν*(C-H)), 2854 (w, *ν*(C-H)), 1597 (w, *ν*(C=C_{arom})), 1493 (m, *ν*(C=C_{arom})), 1448 (m, δ(CH_3)), 1412 (m, δ(CH_3)), 1369 (m, δ(CH_3)), 1340 (m), 1315 (m), 1282 (w), 1255 (m), 1209 (m), 1173 (w), 1155 (m), 1134 (w), 1072 (m), 1007 (vs), 949 (m), 922 (m), 847 (m), 796 (s), 760 (s), 739 (s), 698 (vs) cm^{-1}.

UV/Vis (CH_2Cl_2, lg ε): λ_{max} = 271 (1.47), 266 (1.39), 228 (0.84) nm

HRMS (APCI, +): calc. for [$C_{23}H_{22}O_2$+H] m/z 329.1547; found m/z 329.1548

cis-trans 49:

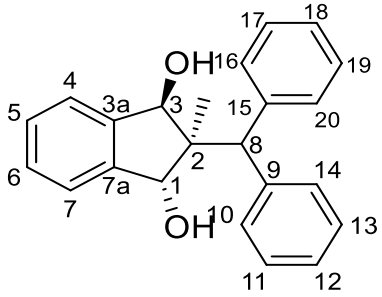

Melting Point.: 69 − 71 °C (lit.[146] 70 − 73 °C),

R_f: 0.40 (cyclohexane/ ethyl acetate 5:1)

^{1}H-NMR (400 MHz, $CDCl_3$)**:** δ = 7.66 (2H, dd, $^3J_{4/7,\ 5/6}$ = 28.2 Hz, $^4J_{4/7,\ 6/5}$ = 8.2 Hz, 4/7-H), 7.59 (2H, dd, $^3J_{5/6,\ 4/7}$ = 28.2 Hz, 4/7-H, $^4J_{5/6,\ 7/4}$ = 8.2 Hz, 5/6-H), 7.41 - 7.28 (10H, m, 4,5,6,7,11,12,13,17,18,19-H), 5.51 (1H, d, $^3J_{3,\ OH}$ = 4.3 Hz, C*H*OH), 4.90 (1H, s, C*H*Ph), 4.77 (1H, d, $^3J_{OH,\ 3}$ = 4.3 Hz, O*H*), 1.72 (1H, d, $^3J_{1,\ OH}$ = 4.5 Hz, C*H*OH), 1.11 (3H, s, CH_3), 1.00 (1H, d, $^3J_{OH,\ 1}$ = 4.5 Hz, O*H*) ppm,

^{13}C NMR (100 MHz, $CDCl_3$)**:** δ = 144.3 (C_q, C-3a/7a), 142.7 (C_q, C-9/15), 142.1 (C_q, C-9/15), 141.2 (C_q, C-3a/7a), 130.2 (C_t, C-16,20/10,14), 129.8 (C_t, C-16,20/10,14), 129.1 (C_t, *C*H), 128. (C_t, *C*H), 128.4 (C_t, *C*H), 127.6 (C_t, *C*H), 127.4 (C_t, *C*H), 127.25 (C_t, *C*H), 126.7 (C_t, *C*H), 125.1 (C_t, *C*H), 124.7 (C_t, *C*H), 81.3 (C_t, C-1), 81.2 (C_t, C-2), 55.8 (C_q, C-2), 55.4 (C_t, *C*HPh_2), 15.4 (C_t, *C*H_3) ppm,

FT-IR: ῡ = 3562 (br, *ν*(O-H)), 3427 (br, *ν*(O-H)), 3059 (w, *ν*(C-H_{arom})), 3028 (w, *ν*(C-H_{arom})), 2970 (w, *ν*(C-H)), 2925 (w, *ν*(C-H)), 1597 (w, *ν*(C=C_{arom})), 1493 (m, *ν*(C=C_{arom})), 1450 (m, δ(CH_3)), 1385 (m, δ(CH_3)), 1331 (w), 1296 (w), 1255 (w), 1207 (m), 1174 (m), 1128 (w), 1076 (w), 1057 (m), 1012 (s), 949 (w), 912 (m), 887 (w), 852 (w), 816 (w), 791 (w), 758 (s), 702 (vs), 660 (s), 629 (s) cm^{-1}.

UV/Vis (CH_2Cl_2, lg ε): λ_{max} = 271 (0.09), 264 (0.12), 228 (0.56), nm.

HRMS (APCI, +): calc. for [$C_{23}H_{22}O_2$+H] m/z 329.1547; found m/z 329.1548

The spectroscopic data corresponded to the data reported in the literature.[146]

12d-methyl-4b,4b1,8b,12b-tetrahydrodibenzo[2,3:4,5]pentaleno[1,6-ab]indene, (Me-tribenzotriquinacene, 50)[146]

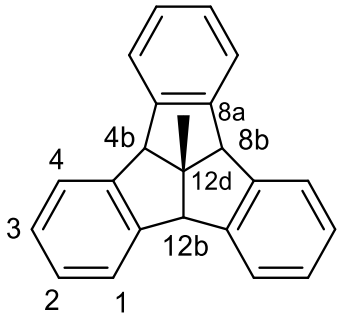

27.8 g (86.9 mmol, 1.0 eq.) of the diol **49** was dissolved in 280 ml *p*-xylene. 4.33 ml (81.0 mmol, 0.93 eq.) of orthophosphoric acid was added and the reaction mixture was heated to reflux at 180 ° C for 3 h using a Dean-Stark apparatus. The hot solution was filtered over potassium carbonate and the one third of the solvent was removed in *vacuo*. Colourless crystals precipitated out on the cooling mixture. These resulting crystals were filtered and washed with *p*-xylene. The procedure was repated two more times to collect the resulting crystals. The product **50** was obtained with a yield of 29%.

Yield: 7.50 g (25.5 mmol, 29 %, lit.[146] 33 %),

Melting Point: 242 °C; lit.[146] 244 °C,

R_f: 0.88 (cyclohexane / ethyl acetate 8:1),

^{1}H-NMR (400 MHz, $CDCl_3$)**:** δ = 7.45-7.42 (6H, m, 1/4-H), 7.21- 7.17 (6H, m, 2/3-H), 4.48 (3H, s, 4b/8b/12b-H), 1.70 (3H, s, C*H*$_3$) ppm,

^{13}C NMR (100 MHz, $CDCl_3$)**:** δ = 145.5 (C_q, C-8a/4c/4a/12c/12a/8a), 127.5 (C_t, C-7/6/3/ 2/10/11), 124.4 (C_t, C-8/5/4/1/12/9), 63.6 (C_t, C-4b/8b/12b), 60.7 (C_q, C-12d), 27.6 (C_t, C(12d)*C*H$_3$) ppm,

FT-IR: ϑ̃ = 3062 (w, ν(C-H$_{arom}$)), 3002 (w, ν(C-H$_{arom}$)), 2960 (w, ν(C-H)), 2893 (w, ν(C-H)), 2362 (w), 2335 (w), 1477 (s, ν(C=C$_{arom}$)), 1456 (m, ν(C=C$_{arom}$)), 1309 (w), 1207 (m), 1155 (m), 1084 (w), 1026 (m), 953 (w), 820 (w), 748 (vs), 731 (vs), 660 (s) cm^{-1}.

UV/Vis (CH_2Cl_2, lg ε): λ_{max} = 276 (0.43), 269 (0.38), 262 (0.64), 228 (0.86) nm.

HRMS (ASAP, pos): calc. for [$C_{23}H_{19}$+H] m/z 295.14813; found m/z 295.14891

The spectroscopic data corresponded to the data reported in the literature.[146]

1,4,7-Tribromo-12d-methyltribenzotriquinacene (Me-TBTQBr$_3$, 55)[153]

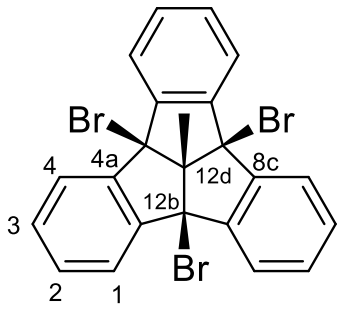

10-methyltribenzotriquinacene (**50**, 5.6 g, 19.0 mmol), NBS (11.2 g, 10.9 mmol) and 75% benzoyl peroxide (9.0 g, 0.33 mmol) were suspended in $CHCl_3$ (300 ml) under N_2 atmosphere. The reaction mixture was heated to reflux for 3 h. The resulting reaction mixture was cooled to the room temperature and the solvent was removed under reduced pressure. The solid residue was suspended in cold MeOH (200 ml) and washed three times with cold MeOH (75 ml). Creamy colored solid was obtained as a tribromide with the yield of 95 %.

Yield 8.3 g (19.8 mmol, 95 %, lit.[153] 100 %),

Melting Point: 328 − 330 °C (decomp.); lit.[153] > 330 °C (decomp.),

R$_f$: 0.75 (cyclohexane / ethyl acetate 8:1),

^{1}H-NMR (400 MHz, $CDCl_3$)**:** δ = 7.70 - 7.68 (6H, m, 8/5/4/1/9/12-H), 7.34 - 7.32 (6H, m, 7/6/3/2/10/11-H), 2.32 (3H, s, C*H*$_3$) ppm,

^{13}C NMR (100 MHz, $CDCl_3$)**:** δ = 143.4 (C_q, C-4a/8c), 130.5 (C_t, C-3/2), 126.0 (C_t, C-4/1), 80.2 (C_t, C-12b), 75.2 (C_q, C-4b^1), 40.0 (C_t, C(12d) *C*H$_3$) ppm,

FT-IR: ϑ̃ = 3074 (w, ν(C-H$_{arom}$)), 3028 (w, ν(C-H$_{arom}$)), 2987 (w, ν(C-H$_{arom}$)), 2362 (w), 1965 (w), 1471 (m, ν(C=C$_{arom}$)), 1460 (m, ν(C=C$_{arom}$)), 1442 (m, δ(CH$_3$)), 1381 (w, δ(CH$_3$)), 1304 (w), 1271 (m), 1215 (m), 1178 (m), 1155 (w), 1078 (w), 1020 (w), 949 (w) 910 (m), 876 (m), 831 (s), 750 (vs), 692 (m), 658 (s), 638 (s) cm^{-1}.

UV/Vis (CH_2Cl_2, lg ε): λ_{max} = 232 (2.21) nm.

HMRS (APCI, pos) calc. for [M$^+$-Br, $C_{23}H_{15}Br_2$] m/z 448.95350; found m/z 448.95506

The spectroscopic data corresponded to the data reported in the literature.[153]

12d-methyldibenzo [2,3:4,5] pentaleno [1,6-ab] indene-4b,8b,12b(4b1H)-triol (Me-TBTQ(OH)$_3$, 75)[140]

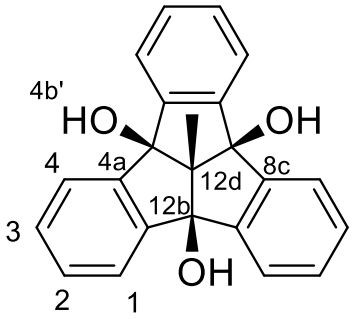

7.35g (0.013 mmol) of tribromide **55** was dissolved in 420.0 ml THF and 138.0 ml H_2SO_4 (20%) was added to mixture then heated to reflux for 3 h. The mixture was cooled down to room temperature and neutralized with concentrated aqueous sodium carbonate. After separating the organic layer, the aqueous layer was extracted two times with tetrahydrofuran then dried over sodium sulfate. The solvent was removed in *vacuo*. The residue was recrystallized from tetrahydrofuran/*n*-heptane (1:7). **75** was obtained as a cream-colored powder with a yield of 89 %.

Yield: 0.79 g (2.31 mmol, 89 %, lit.[148] 94 %),

Melting Point: 312 − 315 °C; lit.[148] 334 °C,

R_f: 0.38 (cyclohexane / ethyl acetate 8:1),

^{1}H-NMR (400 MHz, DMSO-d_6)**:** δ = 7.64 - 7.62 (6H, m, 1/4-H), 7.28 - 7.26 (6H, m, 2/3-H), 5.71 (3H, s, O*H*), 1.25 (3H, s, CH_3) ppm,

^{13}C NMR (100 MHz, $CDCl_3$)**:** δ = 146.3 (C_q, C-8a/4c/4a/12c/12a/8a), 129.1 (C_t, C-7/6/3/2/10/11), 124.5 (C_t, C-8/5/4/1/12/9), 90.0 (C_t, C-4b/8b/12b), 76.4 (C_q, C-12d), 13.1 (C_p, C(12d)CH_3) ppm,

FT-IR: ϑ = 3411 (br, *ν*(O-H)), 3263 (br, *ν*(O-H)), 3068 (w, *ν*(C-H_{arom})), 3032 (w, *ν*(C-H_{arom})), 2939 (w, *ν*(C-H_{arom})), 2875 (w), 2146 (w), 1967 (w), 1589 (w), 1477 (w, *ν*(C=C_{arom})), 1456 (m, (C=C_{arom})), 1363 (m, δ(CH_3)), 1238 (m), 1196 (s), 1149 (w), 1090 (s), 1047 (s), 1032 (s), 962 (m), 914 (s), 891 (m), 787 (w), 767 (vs), 752 (vs), 700 (s), 623 (s) cm^{-1}.

UV/Vis (CH_2Cl_2, lg ε): λ_{max} = 276 (0.38), 269 (0.31), 262 (0.19), 232 (1.1 3) nm.

HMRS (APCI, pos): calc. for [M^+-OH, $C_{23}H_{18}O_2$] m/z 326.13350; found m/z 326.12476

The spectroscopic data corresponded to the data reported in the literature.[148]

2,3,6,7,10,11-hexaiodo-12d-methyldibenzo[2,3:4,5]pentaleno[1,6-ab]indene-4b,8b,12b(4b1H)-triol (Me-TBTQ(OH)$_3$I$_6$, 80)[148]

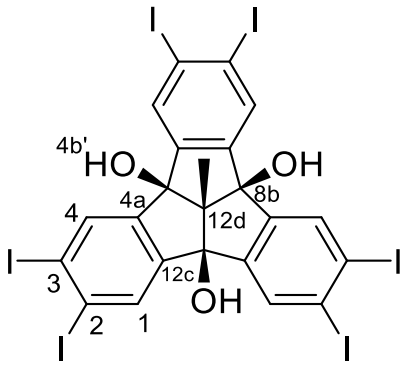

6.0 g (26.4 mmol) periodic acid was dissolved in 150 ml concentrated sulfuric acid in an ice/water bath. First 13.1 g (44.2 mmol) of potassium iodide then 1.2 g (1.64 mmol) trihydroxy tribenzotriquinacene (**75**) were added in small portions. The reaction mixture was stirred at ambient temperature for 18 h. The deep violet mixture was poured into ice and the solid part was separated by suction. The brown residue was heated repeadately with methanol (80 ml total volume) under reflux and recollected by filtration to give hexaiodotriol **80** as an off-white solid with the yield of 66%.

Yield 2.13 g (1.94 mmol, 66 %, lit.[148] 63 %),

Melting Point.: 317 − 320 °C; lit.[148] 314 °C,

R_f: 0.88 (Tetrahydrofuran / cyclohexane 1:1),

^{1}H-NMR (400 MHz, DMSO-d_6)**:** δ = 8.19 (6H, s, 1/4-H), 6.08 (3H, s, O*H*), 1.10 (3H, s, C*H*$_3$) ppm,

^{13}C NMR (100 MHz, DMSO-d_6)**:** δ = 147.03 (C_t, C-8/5/4/1/12/9), 135.19 (C_q, C-8a/4c/4a/12c/12a/8a), 109.88 (C_q, C-7/6/3/2/10/11), 88.52 (C_t, C-4b/8b/12b), 77.70 (C_q, C-12d), 12.1 (C_p, C(12d)*C*H$_3$) ppm,

FT-IR: $\tilde{\upsilon}$ = 3286 (br, ν(O-H)), 2974 (w, ν(C-H_{arom})), 2935 (w, ν(C-H_{arom})), 2871 (w), 2125 (w), 1915 (w), 1618 (w), 1576 (w), 1444 (m, ν(C=C_{arom})), 1390 (m, $\delta(CH_3)$), 1338 (m), 1232 (s), 1182 (s), 1078 (vs), 1038 (vs), 972 (s), 933 (s), 885 (vs), 754 (s), 727 (m), 679 (s), 646 (s) cm^{-1}.

UV/Vis (CH_2Cl_2, lg ε): λ_{max} = 302 (0.03), 291 (0.03), 250 (0.26), 235 (0.26) nm.

HMRS (APCI, pos) calc. for [$C_{23}H_{12}I_6O_3$] 1097.5049; found m/z 1097.5047

The spectroscopic data corresponded to the data reported in the literature.[148]

(4b,8b,12b)-2,3,6,7,10,11-hexaiodo-12d-methyldibenzo[2,3:4,5] pentaleno[1,6-ab] indene-4b,8b,12b(4b1H)-triyl triacetate (Me-TBTQ(OAc)$_3$I$_6$, 85)

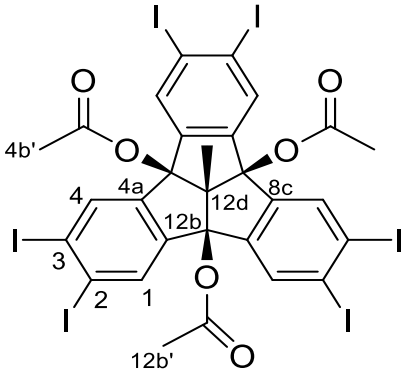

Version A (Microwave): 100.0 mg (9.1 μmol, 1 eq.) hexaiodotriol, **80**, 37.0 mg (0.27 mmol, 3.0 eq.) potassium carbonate, 42 mg (4.5 eq., ~0.1 ml) acetic anhydride with 130.0 mg (4.5 eq.) tetra-butyl ammonium bromide were placed into microwave tube and insert in a microwave oven which is equipped magnetic stirrer under atmospheric pressure at 100 °C by 1000 Watt for a period of 10 minutes. After cooling the reaction mixture to room temperature, the crude product was dissolved in 50 ml EtOAc and filtered over celite and then purified with silica-gel column chromatography (2:1 CH/EA). The product was isolated as a white powder with the yield of 45 %.

Version B: 300 mg (0.273 mmol, 1 eq.) hexaiodotriol, **80**, was dissolved in 50 ml DCM with the help of ultrasonic bath. Then 9 ml Ac_2O (0.97 mol) 15 ml pyridine and 210 mg DMAP were added into the solution. The resulting mixture was stirred at ambient temperature for 3d. The solution was diluted with 300 ml Et_2O and extracted with 2N HCl, saturated $NaHCO_3$, distilled water and Brine two times of each (800 ml total volume). The organic phase was dried over $MgSO_4$ and the solvent was removed under

reduced pressure. The extracted product was recrystallized with DCM and **85** was obtained as white powder with the yield of 77%.

Yield: 214 mg (77%)

Melting Point: 330 °C (decomposed)

R_f: 0.44 (cyclohexane/ ethyl acetate 2:1)

^{1}H-NMR (400 MHz, DMSO-d_6)**:** δ = 7.90 (6H, s, 8/5/4/1/12/9-H), 2.16 (9H, s, C(O)-CH_3), 1.45 (3H, s, CH_3) ppm,

^{13}C NMR (100 MHz, $CDCl_3$)**:** δ = 169.69 (C_q, -OC(O)Me), 142.35 (C_t, C-8/5/4/1/12/9), 133.90 (C_q, C-8a/4c/4a/12c/12a/8a), 110.02 (C_q, C-7/6/3/2/10/11), 94.53 (C_t, C-4b/8b/12b), 30.97 (C_q, C-12d), 21.79 (C_p, C(O)-CH3), 12.39 (C_t, C(12d)CH_3) ppm,

FT-IR: $\tilde{\upsilon}$ = 3012 (w, ν(C-H_{arom})), 2969 (w, ν(C-H_{arom})), 2945 (w, ν(C-H_{arom})), 2902 (w), 2889 (w), 2827 (w), 2191 (w), 2164 (w), 2141 (w), 1743 (s), 1624 (w), 1583 (w), 1444 (m, ν(C=C_{arom})), 1367 (m, δ(CH_3)), 1348 (m), 1277 (m), 1213 (vs), 1082 (m), 1053 (s), 1007 (s), 984 (s), 957 (m), 899 (m), 870 (s), 756 (w), 721 (w), 681 (m), 617 (m) cm^{-1}.

UV/Vis (CH_2Cl_2, lg ε): λ_{max} = 306 (0.26), 296 (0.26), 252 (2.06), 238 (2.02) nm.

HRMS (APCI, pos): calc. for [$C_{65}H_{48}O_6$ + H] m/z 1223.54, found [M^+-OAc] m/z 1164.5224.

EA: calc**. C:** 28.46; **H:** 1.48; **I:** 62.21; **O:** 7.84; found **C:** 28.36; **H:** 1.70

12d-methyl-2,3,6,7,10,11-hexaphenyldibenzo[2,3:4,5]pentaleno[1,6-ab]indene-4b,8b,12b(4b1H)-triyl triacetate (Me-TBTQ(OAc)$_3$Ph$_6$, 92)

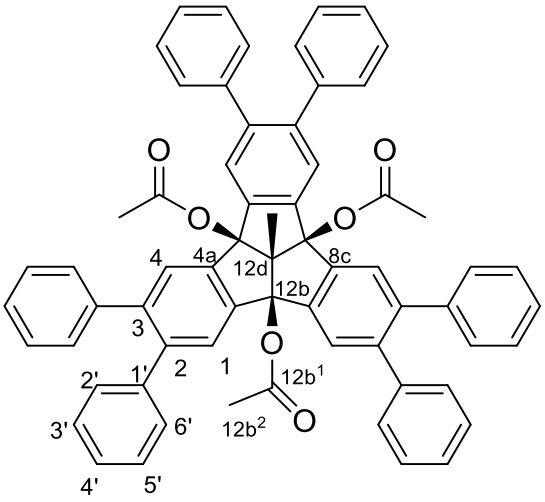

500.0 mg (1.0 eq., 0.41 mmol) of hexaiodotriacetate TBTQ, **85**, 1.70 g (34 eq., 14.0 mmol) of phenyl boronic acid (**91**), 0.45 g (4.16 eq., 1.70 mmol) of PPh_3 and 3.40 g (147.0 eq., 60mmol) of KOH were dissolved in nitrobenzene (60.0 ml) and water (25.0 ml) mixture which were placed into the Schlenk flask under nitrogen atmosphere. The solution was degassed three times then the $Pd(dba)_2$ catalyst (45 mg) was added. The resulting mixture was degassed once more and heated to reflux overnight. The resulting reaction medium was cooled down to room temperature then diluted with 500.0 ml of Et_2O. The mixture was extracted with 2M KOH, 0.1 M HCl, dist. H_2O and Brine solutions respectively.The organic phase was dried over $MgSO_4$ and the solvent was removed under *vacuo*. The crude product was purified with flash column chromatography (4:1:1, CH/EA/DCM). Further purification was done by HPLC with Reprosil C-18-PQ-JASCO semi preparation column, (5 μm, 250 mm × 10 mm) and using ACN as an eluent for STM investigations. The product was isolated as a creamy coloured crystal with the yield of 80 %. Single crystals for X-Ray crystallography were obtained using Rigaku Oxford Diffraction XtaLAB Synergy diffractometer with a semiconductor HPA-detector (HyPix-6000) and multi-layer mirror mono chromated Cu-Kα radiation at 100 K.

Yield 2.13 g (1.94 mmol, 80%)

Melting Point: 248-252 °C

R_f: 0.54 (cyclohexane/ ethyl acetate 2:1)

^{1}H-NMR (600 MHz, DMSO-d_6)**:** δ = 7.83 (s, 6H, 1/4-H), 7.24-7.17 (*J*=m, 18H, 3'/4'/5'-H), 7.03-7.01(dt, *J*=1.910 Hz, 12H, 2'/6'-H), 2.16 (s, 9H, 4b^2/8b^2/12b^2-H), 1.56 (3H, s, C*H*$_3$) ppm,

^{13}C NMR (600 MHz, DMSO-d_6)**:** δ = 169.66 (C_q, -OC(O)Me, C-4b^1/8b^1/12b^1), 141.79 (Cq, C-1'), 140.97 (C_q, C-8a/4c/4a/12c/12a/8a), 140.55 (C_q, C-7/6/3/2/10/11), 128.02 (C_t, C-3',4'), 126.82 (C_t, C-5'), 125.58 (C_t, C-2', 6'), 125.45 (Ct, C-1/4/5/8/9/12), 95.95 (Cq, C-4b/8b/12b), 76.94 (Cq, C-12d), 21.72 ((O)CH_3, C-4b^2/8b^2/12b^2), 12.28 (C_p, C(12d)CH_3) ppm,

FT-IR: ϑ̃ = 3056 (w, *ν*(C-H$_{arom}$)), 3027 (w, *ν*(C-H$_{arom}$)), 2921 (w, *ν*(C-H$_{arom}$), 2848 (m, *ν*(C-H$_{arom}$)), 1745 (s, *ν*(C=O)), 1600 (w, *ν*(C=C$_{arom}$)) 1571 (w, *ν*(C-, C=C$_{arom}$)), 1477 (m), 1446 (m) 1369 (m, δ(CH_3)), 1326 (w), 1213 (s, *ν*(C- C=O)), 1176 (m), 1074 (w), 1037 (s), 1018 (s), 983 (s), 946 (m), 902 (m), 879 (m), 813 (w), 763 (s), 698 (s), 640 (w), 609 (w) cm^{-1}.

UV/Vis (CH_2Cl_2, lg ε): λ_{max} = 302 (0.47), 256 (2.92), 231 (2.41), nm.

HRMS (APCI, +): calc. for [$C_{65}H_{48}O_6$ + H] m/z 925.3492, found m/z 925.3414.

EA: calc. **C:** 84.39; **H:** 5.23; **O:** 10.38 found **C:** 84.33 **H:** 5.51

12d-methyl-2,3,6,7,10,11-hexa(naphthalen-1-yl)dibenzo[2,3:4,5]pentaleno[1,6-ab]indene-4b,8b,12b(4b1H)-triyl triacetate (Me-TBTQ(OAc)$_3$Np$_6$, 96)

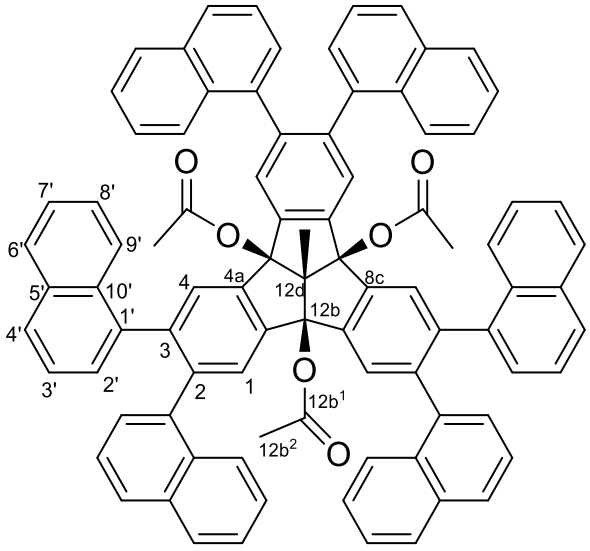

250.0 mg (1.0 eq., 0.2 mmol) of hexaiodotriacetate TBTQ, **85**, 1.20 g (34 eq., 6.95 mmol) of 1-naphtaleneboronic acid (**95**), 1.69 g (147.0 eq., 30.1 mmol) of potassium hydroxide and 220.0 mg (4.16 eq., 0.85mol) of triphenyl phosphine were dissolved in nitrobenzene (35 ml)/ dist. Water (12 ml) mixture under nitrogen atmosphere. The reaction mixture was degassed three times before $Pd(dba)_2$ cat. (25 mg) was added. After adding the catalyst, the solution was degassed once more then heated to reflux for 2 days. The resulting reaction medium was cooled down to room temperature then diluted with 250 ml diethyl ether and extracted with 2M KOH, 0.1 M HCl, dist. water and brine solutions respectively. The organic phase was dried over magnesium sulfate and the solvent was removed under reduced pressure. The crude product was purified with flash column chromatography (4:1, CH/EA). Further purification was done by HPLC with Reprosil C-18-PQ-JASCO semi preparation column, (5 μ m, 250 mm × 10 mm) and using ACN as an eluent for STM investigations. The product was isolated as a pale pink coloured powder with the yield of 45%.

Yield 110.0 mg (0.09 mmol, 45%)

Melting Point: 265 °C,

R_f: 0.63 (cyclohexane / ethyl acetate 2:1),

^{1}H-NMR (600 MHz, DMSO-d_6)**:** δ = 8.06 (s, 6H, 1/4/5/8/9/12-H), 7.49-7.50 (dt, *J*=, 6H, 6'-H), 7.34-7.36 (dt, *J*=1.910 Hz, 12H, 2'/4'-H), 7.27-7.32 (m, 30H, 8'/9'/10'/11'/12'-H) 713-7.14 (dt, 3'-H) 2.19 (s, 9H, $4b^2$/$8b^2$/$12b^2$-H), 1.62 (3H, s, CH_3) ppm,

^{13}C NMR (600 MHz, DMSO-d_6)**:** δ = 170.3 (C_q, -O*C*(O)Me,), 142.3 (C), 142.1 (C), 141.3 (C), 140.1 (C), 139.8 (C), 139.6 (C), 139.3 (C), 139.0 (C), 138.6 (C), 133.6 (C), 133.5 (C), 133.4 (C), 133.3 (C), 133.2 (C), 132.8 (C), 132.6 (C), 132.5 (C), 132.3 (C), 131.7 (C), 131.6 (C), 131.5 (C), 129.1 (C), 128.8 (CH), 128.7 (CH), 128.5 (CH), 128.4 (CH), 128.2 (CH), 128.0 (CH), 127.8 (CH), 127.6 (CH), 127.4 (CH), 127.3 (CH), 126.9 (CH), 126.8 (CH), 126.7 (CH), 126.4 (CH), 126.3 (CH), 126.2 (CH), 125.8 (CH), 125.5 (CH), 125.3 (CH), 125.2 (CH), 125.1 (CH), 124.7 (CH), 124.6 (CH), 124.5 (CH), 124.4 (CH), 124.3 (CH), 122.3 (CH), 97.0 (C), 78.2 (C), 77.9 (C), 67.4 (C), 60.4 (C), 25.9 (C), 22.1 (C), 21.2 (C), 12.8 (12d-*CH*$_3$).ppm,

FT-IR: ῡ = 3046 (w, ν(C-H_{arom})), 2923 (w), 2846 (w), 2119 (w), 2082 (w), 1745 (s, ν(C=O)), 1592 (w), 1508 (m, ν(C=C_{arom})), 1428 (w), 1390 (m, δ(CH_3)), 1365 (m), 1214

(s, ν(C- C=O)), 1118 (s), 1047 (m), 1008 (m), 981 (m), 906 (m), 887 (m), 800 (s), 775 (s), 738 (m), 674 (m), cm^{-1}.

UV/Vis (CH_2Cl_2, lg ε): λ_{max} = 292 (2.89), 238 (3.68), nm.

HRMS (ESI, pos) calc. for 1247.4282 [$C_{89}H_{60}O_6$+ Na] found m/z 1247.4234

EA: calc. **C:** 87.23; **H:** 4.94; **O:** 7.83 found **C:** 87.02 **H**: 5.41

2,3,6,7,10,11-hexa([1,1'-biphenyl]-3-yl)-4b1 methyldibenzo[2,3:4,5] pentaleno [1,6-ab]indene-4b,8b,12b(4b1H)-triyl triacetate (Me-TBTQ(OAc)$_3$Bp$_6$, 94)

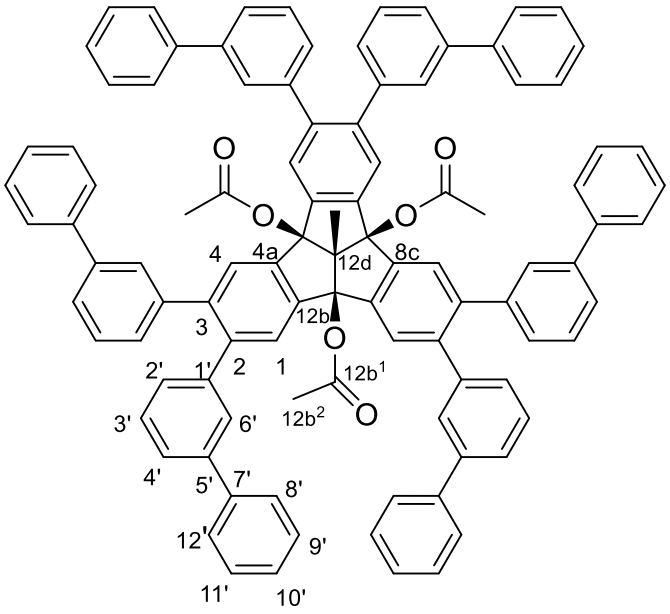

250.0 mg (1.0 eq., 0.2 mmol) of hexaiodotriacetate TBTQ, **85**, 1.38 g (34 eq., 6.95 mmol) of 2-biphenylboronic acid (**93**), 1.69g (147.0 eq., 30.1 mmol) of potassium hydroxide and 220.0 mg (4.16 eq., 0.85mol) of triphenyl phosphine were dissolved in nitrobenzene (37.5 ml)/ dist. Water (12.5 ml) mixture under nitrogen atmosphere. The reaction mixture was degassed three times before $Pd(dba)_2$ catalyst (25 mg) was added. After adding the catalyst, the solution was degassed once more then heated to reflux for 2 days. The resulting reaction medium was cooled down to room temperature then diluted with 250 ml diethyl ether and extracted with 2M KOH, 0.1 M HCl, dist. water and brine solutions respectively. The organic phase was dried over magnesium sulfate and the solvent was removed under reduced pressure. The crude product was purified with flash column chromatography (4:1:1, CH/EA/DCM). Further purification was done by HPLC with Reprosil C-18-PQ-JASCO semi preparation column, (5 μm, 250 mm × 10 mm) and

using ACN as an eluent for STM investigations. The product was isolated as a white-colored powder with the yield of 42%.

Yield 65.0 mg (0.09 mmol, 42%)

Melting Point: 263 °C,

R_f: 0.75 (cyclohexane/ ethyl acetate 2:1),

^{1}H-NMR (600 MHz, DMSO-d_6)**:** δ = 8.06 (s, 6H, 1/4/5/8/9/12-H), 7.49-7.50 (m, 6H, 6'-H), 7.34-7.36 (m, 12H, 2'/4'-H), 7.27-7.32 (m, 30H, 8'/9'/10'/11'/12'-H) 713-7.14 (m, 3'-H) 2.19 (s, 9H, 4b^2/8b^2/12b^2-H), 1.62 (3H, s, CH_3) ppm,

^{13}C NMR (600 MHz, DMSO-d_6)**:** δ = 169.71 (C_q, -OC(O)Me, C-4b^1/8b^1/12b^1), 141.79 (Cq, C-7'), 141.19 (C_q, C-1'), 141.04 (C_q,C-5'), 139.99 (Cq, C-4a/4c/8a/8c/12a/12c), 139.85 (cq, C-2/3/6/7/10/11), 128.79 (C_t, C-9',11'), 128.72 (C_t, C-8'/12'), 128.62 (C_t, C-3'), 128.55 (Ct, C-10'), 127.41 (C_t, C-4'), 126.6 (C_t, C-2'), 125.50 (C_t, C-1/4/5/8/9/12), 125.26 (C_t, C-6'), 95.97 (Cq, 4b/8b/12b), 76.72 (Cq, C-12d), 21.38 (Cq, ((O)CH_3, C-4b^2/8b^2/12b^2), 12.28 (C_p, C(12d)CH_3) ppm,

FT-IR: ϑ = 3054 (w, ν(C-H_{arom})), 3031 (w, ν(C-H_{arom})), 2881(w, ν(C-H_{arom})), 2807 (w, ν(C-H_{arom})), 2019 (w), 1751 (s, ν(C=O), 1598 (m, ν(C=C_{arom})), 1573 (m, ν(C=C_{arom})), 1471 (m), 1452 (w), 1425 (w), 1407 (w), 1365 (m, δ(CH_3)), 1332 (w), 1211, (s, ν(C-C=O)), 1168 (w), 1049 (m), 1020 (m), 985 (m), 948 (m), 890 (m), 835 (m) 802 (m) cm$^-$

UV/Vis (CH_2Cl_2, lg ε): λ_{max} = 301 (0.52), 256 (3.11) nm.

HRMS (APCI, pos): calc. for m/z 1380.5162 [$C_{101}H_{72}O_6$] found m/z 1380.5323

EA: calc. **C:** 87.80**; H:** 5.25**; O:** 6.95 found **C:** 87.17 **H:** 5.51

2-benzylidene-1,3-diphenylpropane-1,3-dione (53)[147]

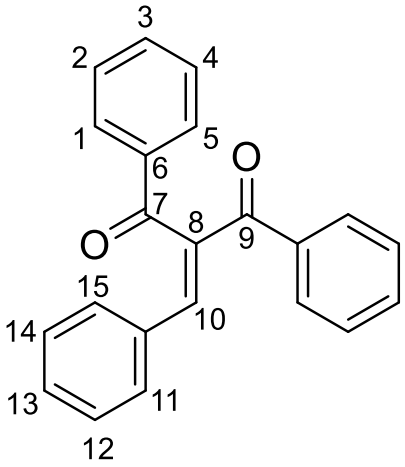

12.2 g (1.0 eq., 11.7 ml, 115 mmol) benzaldehyde, **52**, and 25.9 g (1.0 eq., 115 mmol) dibenzoylmethane, **51**, were dissolved in 350.0 ml toluene. Hexanoic acid (0.25 eq., 3.66 ml) and piperidine (0.13 eq., 1.51 ml) were added and the reaction mixture was heated to reflux for 40 h using a Dean-Stark trap. After cooling the mixture to the room temperature, the solution was washed with a 10 % $NaHCO_3$ solution (500 ml), 5 % AcOH (500ml) and brine (500 ml). the organic phase was dried over $MgSO_4$, and the solvent was removed *in vacuo*. The desired diketone (**53**) was obtained after column chromatography (silicagel, pentane/ethyl acetate 9:1) as a pale-yellow oil in 46% yield

Yield: 16.7 g (115 mmol, 46% lit.[147] 66%).

Rf: 0.18 (pentane/ethyl acetate 9:1)

^{1}H NMR (400 MHz, $CDCl_3$): δ = 7.96-7.99 (2H, m, 1,5-H), 7.86-7.89 (2H, m, 11,15-H), 7.59 (1H, t, ^3J = 7.4 Hz), 7.55-7.47 (4H, m, 3,12,14,16-H), 7.43-7.39 (2H, m, 2,4-H), 7.35-7.33 (2H, m, 18,22-H), 7.31-7.22 (3H, m, 19,20,21-H) ppm.

^{13}C NMR (100 MHz, $CDCl_3$): δ = 197.1 (C_q, C-7), 195.1 (C_q, C-9), 144.1 (C_t, C-16), 139.6 (C_q, C-8), 137.5 (C_q, C-10), 136.4 (C_q, C-6), 134.0 (C_t, C-3), 133.2 (C_q, C-17),132.7 (C_t, C-13), 130.6 (C_q, *C*H), 130.2 (C_t, C-18,22), 129.7 (C_t, C-11,15), 129.5 (C_t, C-1,5,), 129.0 (C_t, C-2,4), 128.9 (C_t, *C*H), 128.7 (C_t, C-12,14) ppm.

FT-IR (ATR): ῡ = 3060 (w, *ν*(C-H_{arom})), 1733 (w), 1671 (m, *ν*(C=O)), 1635 (m, *ν*(C=O)), 1597 (m, ν(C=C_{arom})), 1576 (w), 1493 (w), 1446 (w). 1373 (w), 1319 (w),

1259 (s), 1228 (vs), 1174 (w), 1115 (w), 1074 (w), 1026 (w), 978 (m), 933 (w), 872 (w), 758 (m), 733 (m), 688 (vs), 644 (w) cm^{-1}

UV/Vis (CH_2Cl_2, lg ε): λmax = 300 (11 500), 259 (14 100) nm.

The spectroscopic data corresponded to the data reported in the literature.[147]

2-Benzylidene-1,3-diphenylpropane-1,3-diol (54)[147]

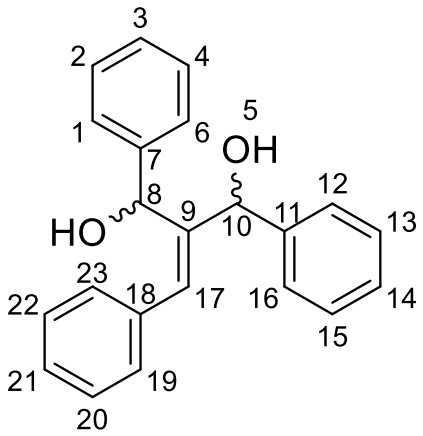

1.50 g of diketone, **53**, (1.0 eq., 4.80 mmol) was dissolved in anhydrous DCM (25 ml) in a schlenk flask under nitrogen atmosphere. After cooling the mixture to -78 ^oC 0.4 M $CeCl_3.7H_2O$ (2.50 g, 1.4 eq., 6.72 mmmol) in MeOH (17 ml) solution was added to the reaction medium. 15 min. later $NaBH_4$ (0.38 g, 10.1 mmol) was added to the reaction mixture, and it was stirred for 30 min. at -78 ^oC. The solution was warmed up to room temperature and stirred for 1h. The reaction was checked with TLC to verify to complete. The reaction mixture was diluted with Et_2O (40 ml) and quenched with 0.5 M HCl (25 ml) solution. After separateing the phases, water phase was extracted with Et_2O (2* 25 ml) and combined organic phases were washed with brine (2*100 ml) and dried over $MgSO_4$. The solvent was removed *in vacuo*. The resulted product was purified and the diastereoisomers were seperated with flash column chromatography (silica, chloroform/ ethyl acetate 98:2) with a combined yield of 79 % of syn and anti-isomers.

2-Benzylidene-1,3-diphenylpropane-cis-1,3-diol (*syn- 54*)

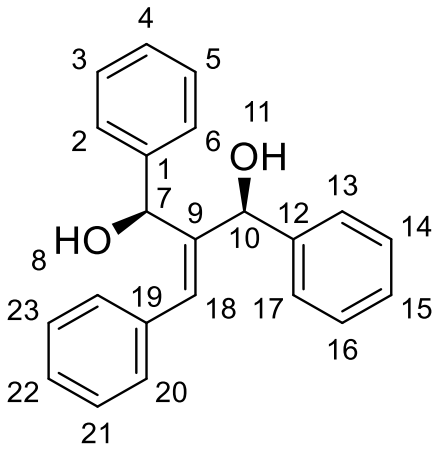

Yield: 223 mg, 705 µmol, 15%.

Melting Point:109–111°C (Lit.[147] 108-109°C).

Rf: 0.34 ($CHCl_3$/ethyl acetate 98:2)

^{1}H NMR (400 MHz, $CDCl_3$): δ = 7.40–7.22 (15H, m, C*H*), 7.07 (1H, s, 18-H), 5.95 (1H, d, ^3J = 6.2 Hz, 7-H), 5.29 (1H, d, ^3J = 3.6 Hz, 10-H), 3.79 (1H, d, ^3J = 6.2 Hz, 11-H), 2.80 (1H, d, ^3J = 3.76 Hz, 8-H) ppm.

^{13}C NMR (100 MHz, $CDCl_3$): δ = 141.0 (C_q), 138.6 (C_q), 138.4 (C_q, C-9), 135.4 (C_q), 131.7 (C_t), 128.8 (C_t), 128.5 (C_t), 128.4 (C_t), 128.3 (C_t), 128.2 (C_t), 127.5 (C_t), 127.8 (C_t), 127.6 (C_t), 125.5 (C_t), 74.5 (C_t, C-10), 72.0 (C_t, C-7) ppm.

FT-IR (ATR): ϑ̃ = 3301 (m, *ν*(O-H)), 3024 (w, *ν*(C-H_{arom})), 1599 (w), 1492 (w), 1448 (w), 1255 (w), 1209 (w), 1130 (w), 1076 (w), 1043 (m), 1007 (s), 920 (w), 863 (w), 766 (m), 742 (w), 696 (vs), 629 (w) cm^{-1}.

UV/Vis (CH_2Cl_2, lg ε): λ_{max} = 248 (4.07) nm.

The spectroscopic data corresponded to the data reported in the literature.[147]

2-Benzylidene-1,3-diphenylpropane-1,3-diol (*anti-54*)

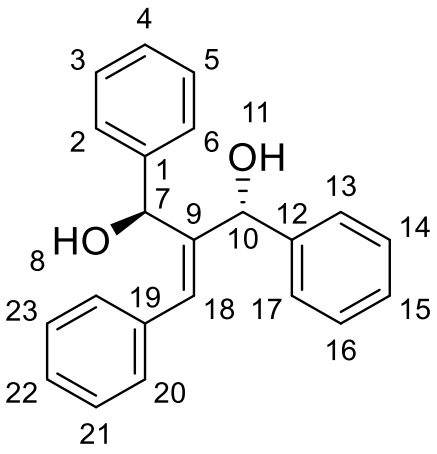

Yield: 797 mg (252 mmol, 67%, lit.[147] 93%)

Rf: 0.27 ($CHCl_3$/ethyl acetate 98:2)

^{1}H NMR (400 MHz, $CDCl_3$): δ = 7.40–7.23 (15H, m, C*H*), 7.07 (1H, s, 18-H), 5.96 (1H, d, ^3J = 6.2 Hz, 7-H), 5.37 (1H, d, ^3J = 3.6 Hz, 10-H), 2.05 (1H, d, ^3J = 6.2 Hz, 11-H), 2.03 (1H, d, ^3J = 3.76 Hz, 8-H) ppm.

^{13}C NMR (100 MHz, $CDCl_3$): δ = 142.6 (Cq), 141.7 (Cq), 140.5 (Cq), 134.3 (Cq), 133.2 (C_t,

C-18), 128.9 (C_t), 128.5 (C_t), 128.5 (C_t), 128.4 (C_t), 127.9 (C_t), 127.6 (C_t), 127.2 (C_t), 127.2

(C_t), 125.7 (Ct), 74.9 (Ct, C-10), 72.2 (Ct, C-7) ppm.

FT-IR (ATR): $\tilde{\upsilon}$ = 3301 (m, ν(O-H)), 3024 (w, ν(C-H_{arom})), 1599 (w), 1492 (w), 1448 (w), 1255 (w), 1209 (w), 1130 (w), 1076 (w), 1043 (m), 1007 (s), 920 (w), 863 (w), 766 (m), 742 (w), 696 (vs), 629 (w) cm^{-1}.

UV/Vis (CH_2Cl_2, lg ε): λmax = 247 (0.88) nm.

HRMS (APCI, pos): accurate mass calcd for [$C_{22}H_{20}O_2^+$-2 H_2O] m/z 280.1355, found m/z 281.12942

The spectroscopic data corresponded to the data reported in the literature.[147]

4b,12d,8b,12b-Tetrahydrodibenzo[2,3:4,5]pentaleno[1,6-ab]indene(TBTQ, 42)[147]

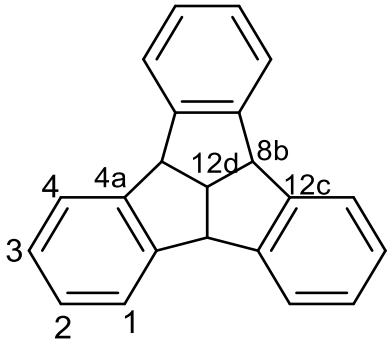

The alcohol, **54** (130 mg, 0.41 mmol) was dissolved in 2.0 ml chlorobenzene and polyphosphoric acid was added to the solution. The reaction mixture was heated to reflux at 130 ^{o}C under nitrogen and stirred vigorously for 20 h. After cooling the reaction mixture to room temperature, the product was precipitated in the fridge. The crude product was filtered and washed with acetone then dried to obtain **42** as a white powder with the yield of 38%.

Yield: 60 mg, 0.21 mmol, 38% (Lit.[147] 32%).

m.p: 321°C (Lit.[147] 322°C, decomp.)

Rf: 0.44 (cyclohexane/CH_2Cl_2 95:5)

^{1}H NMR (400 MHz, $CDCl_3$): δ = 7.47–7.43 (6H, m, 1,4-H), 7.22–7.15 (6H, m, 2,3-H), 4.96 (3H, d, ^{3}J = 9.7 Hz, 4b,8b,12b-H), 4.47 (1H, q, ^{3}J = 9.7 Hz, 12d-H) ppm.

^{13}C NMR (100 MHz, $CDCl_3$): δ = 145.9 (C_q, C-4a, 12c), 127.5 (C_t, C-2,3), 124.4 (C_t, C-1,4), 56.0 (C_t, C-4b,8b,12b), 51.2 (C-12d) ppm.

FT-IR (ATR): ῡ = 3068 (w, *ν*(C-H_{arom})), 3020 (w, *ν*(C-H_{arom})), 2974 (w, *ν*(C-H)), 2900 (w, *ν*(C-H)), 1683 (w), 1603 (w), 1480 (m, *ν*(C=C_{arom})), 1474 (m, *ν*(C=C)$_{arom}$), 1456 (m, δ(C-H)), 1315 (w), 1295 (w), 1274 (w), 1255 (w), 1199 (w), 1172 (w), 1157 (w), 1083 (w), 1033 (w), 1025 (w), 1012 (w), 975 (w), 959 (w), 935 (w), 888 (w), 877 (w), 866 (w), 832 (w), 750 (s, δ(C-H_{arom})), 741 (s, δ(C-H_{arom})), 711(s, δ(C-H_{arom})), 662 (w), 647 (w), 630 (w), 617 (w), 603 (m) cm^{-1}.

UV/Vis (CH_2Cl_2, lg ε): λ_{max} = 276 (0.74), 269 (0.63), 230 (1.33) nm.

HRMS (APCI, pos): calc. for m/z 281.13265 [$C_{22}H_{17}$] found m/z 281.13303

The spectroscopic data corresponded to the data reported in the literature.[147]

[2,3:4,5]pentaleno[1,6 ab]indene-4b, 8b, 12b(12dH)-tri-carbonitrile (132)[148]

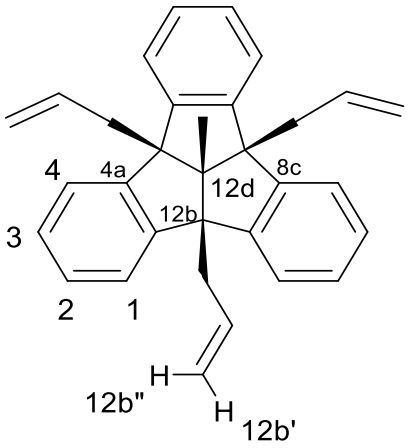

0.50 g of tribromide **55** (942 µmol) was dissolved in 30 ml dry DCM under argon atmosphere. After adding 0.58 ml (3.18 mmol) $SnCl_4$ to the solution, allyl trimethylsilane (95%) (0.46 ml, 2.81 mmol,) was injected dropwise during 30 min. The reaction was stirred at room temperature for 12 h. The crude mixture was hydrolysed by adding distilled water (200 ml). The precipitating inorganic salts were filtered off and the phases were separated. The water phase was extracted with DCM while the organic phase was washed with dist. water several times. he combined organic phases were dried over sodium sulfate and the solvent was removed under pressure. The crude product was recrystallized using MeOH. The product was obtained as colourless needles with the yield of 72 %.

Yield: 310 mg, (0.83mol, 72 %**,** lit.[148] 75%)

Melting point: 178 °C, lit.[148] 177-179 °C

Rf: 0.57 (cyclohexane/ ethyl acetate 3:1)

^{1}H NMR (400 MHz, $CDCl_3$): δ = 7.34- 7.29 (6H, m, 1,4-H), 7.18- 7.14 (6H, m, 2,3-H), 5.61- 5.51 (3H, m, $4b^2$, $8b^2$, $12b^2$-H), 5.13- 5.04 (3H, dd, ^3J= 17.2 Hz, ^4J= 1.86 Hz 4b',8b', 12b'-H), 4.98- 4.91 (3H, dd, ^3J= 10.4 Hz, ^4J= 1.82 Hz 4b",8b", 12b"-H), 3.04 (6H, d, ^3J= 6.56 Hz $4b^1$, $8b^1$, $12b^1$-H), 1.67 (3H, s, CH_3) ppm.

^{13}C NMR (100 MHz, $CDCl_3$): δ = 147.58 (Cq, C-4a/4c/8a/8c/12a/12c), 137.21 (C-$4b^1$, 8b1, $12b^1$), 127.59 (Ct, C-7/6/3/2/10/11), 123.39 (Ct, C-1/4/5/8/9/12), 116.34 (Ct), 72.90

(Cq, C- 4b/8b/12b), 66.20 (Cq, C-12d), 42.59 (Ct, C-4b1/8b1/12b1), 17.16 (Cq, C-*C*H3) ppm

FT-IR: (ATR): ϑ = 3068 (w, *ν*(C-H_{arom})), 3019 (w, *ν*(C-H_{arom})), 2977 (w, *ν*(C-H)), 2912 (w, *ν*(C-H)), 2885 (w), 2831 (w), 11639 (w) 1596 (m) 1477 (m, *ν*(C=C_{arom})), 1428 (m, *ν*(C=C)$_{arom}$), 1295 (w), 1259 (w), 1153 (w), 1083 (w), 1083 (w), 1033 (w), 912 (m), 802 (m), 752(s, δ(C-H_{arom})), 694 (s, δ(C-H_{arom})), 651 (s, δ(C-H_{arom})), 599 (s), 565 (s) cm^{-1}

UV/Vis (CH_2Cl_2, lg ε): λ_{max} = 277 (0.19), 269 (0.18), 230 (0.99) nm.

HRMS (APCI.pos): calc. for [$C_{32}H_{31}$] m/z 415.24258; found m/z 425.24170

The spectroscopic data corresponded to the data reported in the literature.[148]

(4bs,8bs,12bs)-4b,8b,12b-tris(methoxymethoxy)-12d-methyl-4b,4b1,8b,12b tetrahydrodibenzo [2,3:4,5] pentaleno[1,6-ab]indene (Me-TBTQ(OMOM)$_3$, 76)

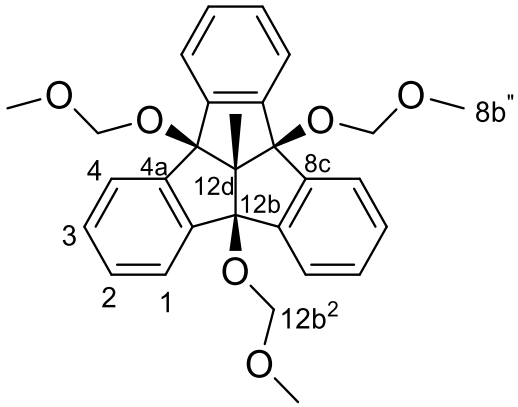

2.0 g of TBTQ(OH)$_3$, **75**, (1 eq., 5.8 mmol) and 15 ml N,N-diisopropylamine (15 eq., 87 mmol) were added into a solution of 125 ml toluene and 4.40 ml methoxymethyl chloride (10 eq, 58 mmol, 4.67 g) respectively. The reaction mixture was heated to reflux for 18 h. The reaction was checked with TLC to ensure complete consuming the starting material. Then, the resulting solution was first cool down to room temperature. The solution was mixed with EtOAc (30 ml) and sat. NH_4Cl (50 ml) and stirred vigorously for 30 min. to allow decomposition of residual starting material. Then the phases were separated. The organic phase was washed with $NaHCO_3$ (2x30 ml) and brine (2x30 ml) and dried over $MgSO_4$. The resulting solvent was removed under *vacuo*. The product was obtained as creamy coloured powder with the yield of 87%.

Yield: 2.42 g (5.10 mmol, 87%)

R_f: 0.59 (Cyclohexane/ethyl acetate 2:1)

Melting point: 107 °C

^{1}H NMR (400 MHz, $CDCl_3$): δ = 7.66-7.62 (6H, m, 1,4-H) 7.33-7.31 (6H, m, 2,3-H), 4.70 (6H, s, $4b^1$,$8b^1$,$12b^1$), 3.51 (9H, s, $4b^2$,$8b^2$, $12b^2$), 1.32 (3H, s, C*H*$_3$) ppm.

^{13}C NMR (100 MHz, $CDCl_3$): δ = 142.66 (C_q, C-8a/4c/4a/12c/12a/8a), 129.65 129.1 (C_t, C-7/6/3/2/10/11), 125.14(C_t, C-8/5/4/1/12/9), 96.92 (C_t, C-4b/8b/12b), 93.07 (Ct, C-$4b^1$/$8b^1$/$12b^1$), 55.80 (C_q, C-12d), 21.50 C_t, C-$4b^2$/$8b^2$/$12b^2$), 14.80 (C_p, C(12d)CH_3) ppm

FT-IR: (ATR): ῡ = 2943 (w, *v*(C-H_{arom})), 2887 (w, *v*(C-H_{arom})), 2817 (w, *v*(C-H)), 2360 (w, *v*(C-H)), 1716 (w), 1461 (w), 1282 (m), 1236 (m), 1149 (s),1097 (s), 1018 (s), 981 (s), 921 (s), 757 (s), 694 (m)

UV-Vis (CH_2Cl_2, lg ε): 276 (0.16), 268 (0.14), 230 (1.32) nm.

HRMS: (ESI. Pos) calc. for [M^++Na, $C_{29}H_{30}NaO_6$] m/z 497.1935, found m/z 497.1918

EA: calc. **C:**73.40. **H:**4.37 **O:**20.23, found **C:**73.17, **H:** 6.87

4b,8b,12b-tribromo-2,3,6,7,10,11-hexaiodo-12d-methyl-4b,4b1,8b,12b-tetrahydrodibenzo[2,3:4,5]pentaleno[1,6-ab]indene (Me-TBTQBr$_3$I$_6$, 133)

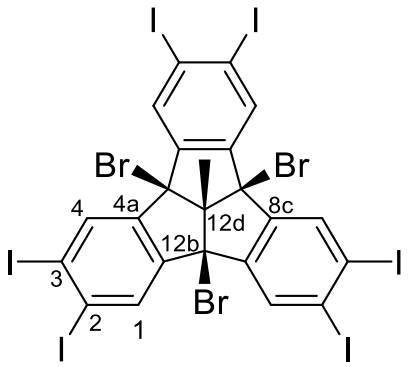

200 mg of hexaiodotriol (**80**) was dissolved in 40 ml anhydrous THF and the flask was placed under Ar atmosphere. 1.02 ml of PBr_3 was slowly added at 0°C. The resulted reaction mixture was stirred at ambient temperature for 16 h. The mixture was poured into 50 g of ice and stirred until it came to room temperature. The solution was extracted with $CHCl_3$ (3x100 ml) and the combined organic phases dried over $MgSO_4$ and removed under reduced pressure. The crude product was purified with column chromatography. (5:1 CH/EA) The product was isolated as a white powder with the yield of 53 %.

Yield: 115 mg (53%, lit.[148] 55%)

R_f: 0.86 (cyclohexane/ ethyl acetate 5:1)

Melting point: 255°C (decomp., lit.[148] 254 °C decomp.)

^{1}H-NMR (600 MHz, $CDCl_3$)**:** δ = 8.07 (s, 6H, 1/4/5/8/9/12), 2.15 (s, 3H, 12d-C*H*$_3$) ppm

^{13}C-NMR (600 MHz, $CDCl_3$): δ = 143.8 (Cq, C-4a/4c/8a/8c/12a/12c-C), 136.0 (Ct, C-1/4/5/8/10/11-C), 111.1 (Cq, C-2/3/6/7/9/10), 75.6 (Cq, C-4b/8b/12b), 53.4 (Cq, C-12d), 36.6 (Cq, C-12d(*C*H$_3$)) ppm

FT-IR (ATR) : ϑ = 3070 (w, *ν*(C-H$_{arom}$)), 2990 (w, *ν*(C-H$_{arom}$)), 2958 (w, *ν*(C-H$_{arom}$)), 2947 (w, *ν*(C-H$_{arom}$)), 2941 (w), 2929 (w), 1573 ((m, *ν*(C=C$_{arom}$)) , 1436 ((m, *ν*(C=C$_{arom}$)), 1379(m, *ν*(C-H), 1346 (m), 1267 (m), 1244 (m), 1211 (m), 1084 (m), 921 (s, δ(C-H$_{arom}$)), 848 ((s, δ(C-H$_{arom}$)), 825 (s), 748 (s), 701(s), 671 (s), 603 (s), 576(s, δ(C-Br)), 511(s, δ(C-Br))

UV-Vis (CH_2Cl_2, lg ε): 320 (0.18), 259 (0.99) nm.

MS: (APCI, +) calc. for $C_{23}H_9Br_3I_6$ m/z 1286. 25; found [M^+-Br] m/z 1206. 3682

EA: calc. **C**: 21.47; **H**: 0.71; **Br**: 18.63; **I**: 59.19, found **C:**21.22, **H:** 0.78

The spectroscopic data corresponded to the data reported in the literature.[148]

12d-Methyl-4b,8b,12b-tri-n-propyl 4b,8b,12b,12dtetrahydrodibenzo [2,3:4,5] pentaleno [1,6-ab] indene [12d-methyl-4b,8b,12b-tri (n-propyl) tribenzotriquinacene, (134)

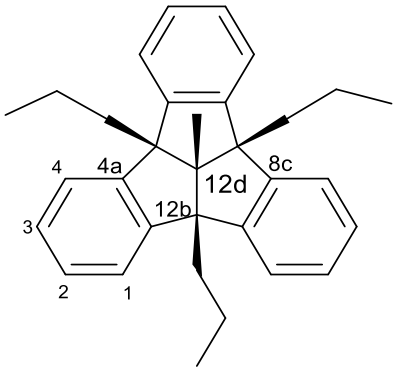

A solution of triallyltribenzotriquinacene, (**132**, 207 mg, 0.5 µmol, 1 eq.) in anhydrous EtOAc (15 ml) was mixed with 20 mg of Pd/Charcoal (10 %) under the hydrogen atmosphere. Hydrogenation was applied via H_2 filled balloon. The reaction mixture was vigorously stirred at ambient temperature and pressure for 24 h. The resulted solution was filtered off over the silica pad and the solvent was removed under vacuo. The colourless solid was recrystallized over EtOH (10 ml) and it gave the colourless needle as a product with the afforded yield of 78 %.

Yield: 93 mg (0. 79 mol 78 %, lit.[141] 90%)

Melting Point: 242 °C, (lit.[141] 240-241 °C)

Rf: 0.37 (cyclohexane/ ethyl acetate 3:1)

^{1}H-NMR (400 MHz, $CDCl_3$)**:** δ = 7.27-7.29 (m, 6H, 2/3/6/7/10/11-H), 7.12-7.10 (m, 6H, 1/4/5/8/9/12-H), 2.14-2.17 (m, 6H, $4b^2$, $8b^2$, $12b^2$-H), 1.61 (s, 3H, 12d-CH_3), 1.15-1.21 (6H, m, $4b^1$, $8b^1$, $12b^1$-H), 0.92 (s, 9H, CH_3) ppm

^{13}C-NMR (100 MHz, $CDCl_3$)**:** δ = 151.6 (Cq, C-4a/4c/8a/8c/12a/12c), 126,7 (Ct, C-2/3/6/7/9/10), 123.4 (Ct, C-1/4/5/8/9/12), 61.6 (Cq, C-4b/8b/12b), 52.1 (Cq, C-12d),

41.7 (Ct, C-4b^1/8b^1/12b^1), 18.7 (Ct, C-4b^2/8b^2/12b^2), 17.6 (Cq, C-12d (*C*H$_3$)), 14.7 (Cq, C4b^3/8b^3/12b^3)

FT-IR: 2956 (w, *ν*(C-H$_{arom}$)), 2867 (w, *ν*(C-H$_{arom}$)), 2190 (w, *ν*(C-H$_{arom}$)), 1716 (w, *ν*(C-H$_{arom}$)), , 1477 (w, *ν*(C-H$_{arom}$)), 1454 (s) , 1373 (s), 1286 (m), 1153 (m), 1027 (s), 973 (s), 910 (s),

UV-Vis (CH_2Cl_2, lg ε): 270 (0.15), 273 (0.11), 277 (0.16) nm.

HRMS (APCI, pos) calc. for [$C_{32}H_{37}$] m/z 421.28953; found m/z 421.28801

The spectroscopic data corresponded to the data reported in the literature.[141]

5.3 X-ray crystal structures

Crystallographic data deposited with the Cambridge Data Centre (as denoted by a CCDC number: 2093789) can be accessed free of charge at www.ccdc.cam.ac.uk/data_request/cif

5.3.1 Structure detemination of Me-TBTQ$(OAc)_3Ph_6$, 92

The measurements and structure determination of TBTQ **92** was carried out by Johannes Krebs (Institute of Inorganic Chemistry, Universität Würzburg).

A crystal suitable for single-crystal X-ray diffraction was selected, coated in polybutyl oil, mounted on a polyimide microloop (MicroMounts from MiTeGen) and transferred to a stream of cold nitrogen (Oxford Cryostream 800). Diffraction data of Me-TBTQ$(OAc)_3Ph_6$ was collected on a Rigaku Oxford Diffraction XtaLAB Synergy diffractometer with a semiconductor HPA-detector (HyPix-6000) and multi-layer mirror mono chromated Cu-Kα radiation at 100 K. The images were processed and corrected for Lorentz-polarization effects and absorption (empirical scaling) using the CrysAlisPro software from Rigaku Oxford Diffractio. The structures were solved using the intrinsic phasing method (SHELXT)[277] and Fourier expansion technique. All non-hydrogen atoms were refined in anisotropic approximation, with all hydrogen atoms 'riding' in idealized positions, by full-matrix least squares against F^2 of all data, using SHELXL[278] software and the SHELXLE[279] graphical user interface. Diamond[280] software was used for graphical representation. Crystal data and experimental details are listed in **Table 6**; full structural information has been deposited with the Cambridge Crystallographic Data Centre. CCDC-2093789

5.3.2 Crystal structure data and parameters

Table 6 Details on single-crystal X-ray diffraction data and structure refinements of Me-TBTQ(OAc)$_3$Ph$_6$, **92**

Data	Me-TBTQ(OAc)$_3$Ph$_6$
CCDC-Nummer	2093789
Empirical formula	C74H66O6
ρ_{calc}/g·cm^{-3}	1.222
F(000)	3348
Crystal size/mm^3	0.094×0.084×0.014
Crystal color, habit	colourless plate
μ/mm 1	0.596
Mr/g·mol^{-1}	1051.34
Temperature/K	100(2)
Radiation, λ/Å	CuK$_{\alpha,}$ 1.54184
Crystal system	trigonal
Space group	R^{-}3
Unit cell dimensions	
a/Å	18.3167(2)
b/Å	18.3167(2)
c/Å	29.5097(5)
α/°	90
β/°	90
γ/°	120
Volume/Å3	8574.1(2)
Z	6
2Θ/°	6.33-155.39
Unique reflections	3982
Parameters / restraints	498/390
GooF on F2	1.056
R1 [I>=2σ (I)]	0.0519
wR2 [all data]	0.1531
Max./min. residual electron density/ e Å^{-3}	0.54 / –0.59

6. List of Abbrevations

Å Angström
Abb. *Abbildung*
APCI atmospheric pressure chemical ionisation
APEX annulative π-extension aq. aqueous solution
arom. aromatic
ATR attenuated total reflection
BDPTQ benzodiphenanthrenotriquinacene
bpin pinacol boronate ester
BPTQ benzophenanthrenotriquinacene
BTPTQ benzotriphenanthrenotriquinacene
n-BuLi *n*-butyllithium
t-BuOK potassium *tert*-butoxide
calc. calculated
CCDC Cambridge crystallographic data centre
CDFC cyclodehdrogenofluorination
CDHC cyclodehydrochlorination
conc. concentrated
COSY correlation spectroscopy
DBU 1,8-Diazabicyclo(5.4.0)undec-7-ene
DDQ 2,3-dichloro-5,6-dicyano-1,4-benzoquinone
DEPT distortionless enhancement by polarisation transfer
DFT density functional theory
DIBAL-H diisobutylaluminium hydride
DIPA diisopropylamine
DL double layer
DMF *N*,*N*-dimethylformamide
DMSO dimethylsulfoxide
ε extinction coefficient
EA elemental analysis
EI eletron ionisation
ESI electrospray ionisation
eq. equivalents
Et_2O diethylether
EtOH ethanol
fcc face centered cubic
FVP Flash vacuum pyrolysis
FT-IR fourier transform infraredspectroscopy
IR infrared
hcp hexagonal close-packed
HMBC heteronuclear multiple bond correlation
HPLC high pressure liquid chromatography
HRMS high resolution mass spectrometry
HSQC heteronuclear single quantum coherence
LDA lithium diisopropylamide
LiHMDS lithium bis(trimethylsilyl)-amide
M molar concentration
MALDI-TOF matrix assisted laser desorption ionisation-time of flight
Me methyl
MeLi methyllithium

MeOH methanol
m.p. melting point
MPLC medium pressure liquid chromatography
MS mass spectrometry
NBS *N*-bromosuccinimide
NIS *N*-iodosuccinimide
NOESY nuclear OVERHAUSER enhancement and exchange spectroscopy
NMR nuclear magnetic resonance
Otf trifluoromethanesulfonate
PAH polycyclic aromatic hydrocarbon
PCC pyridinium chlorochromate
PCDHF photocyclodehydrofluorination
PIFA (Bis(trifluoroacetoxy)-iodo)benzene
ppm parts per million
quant. quantitative yield
rac- racemic mixture
Rf retention factor
RP-HPLC reverse phase high pressure liquid chromatography
rt room temperature
sh shoulder
SPhos 2-Dicyclohexylphosphino-2',6'-dimethoxybipheny
STM scanning tunneling microscopy
TFA trifluoroacetic acid
TBTQ tribenzotriquinacene
TfOH trifluoromethanesulfonic acid
THF tetrahydrofuran
TLC thin layer chromatography
UV/Vis ultraviolet/visible
% v/v volume percent
λmax wavelength of maximum absorption

Abbreviations in NMR spectroscopy:

s singulet
d doublet
t triplet
q quartet
m multiplet
br s broad singulet
br d broad doublet
Cq quaternary carbon
Ct tertiary carbon
Cp primary carbon
J coupling constant
δ chemical shift

Abbreviations in IR spectroscopy:

vs very strong
s strong
m medium
w weak

7. References

1. Novoselov, K. S.; Geim, A. K.; Morozov, S. V.; Jiang, D.; Zhang, Y.; Dubonos, S. V.; Grigorieva, I. V.; Firsov, A. A.,. *Science* **2004,** *306* (5696), 666-669.
2. Chen, J. H.; Jang, C.; Xiao, S. D.; Ishigami, M.; Fuhrer, M. S.,. *Nat Nanotechnol* **2008,** *3* (4), 206-209.
3. Geim, A. K.; Kim, P., *Sci Am* **2008,** *298* (4), 90-97.
4. Ishigami, M.; Chen, J. H.; Cullen, W. G.; Fuhrer, M. S.; Williams, E. D., *Nano Lett* **2007,** *7* (6), 1643-1648.
5. Lee, C.; Wei, X. D.; Kysar, J. W.; Hone, J., *Science* **2008,** *321* (5887), 385-388.
6. Kuzmenko, A. B.; van Heumen, E.; Carbone, F.; van der Marel, D., *Phys Rev Lett* **2008,** *100* (11).
7. Englert, J. M.; Hirsch, A.; Feng, X. L.; Mullen, K., *Angew Chem Int Edit* **2011,** *50* (37), A17-A24.
8. Dalal, M. H.; Lee, C. Y.; Wallace, G. G., *J Mater Sci* **2021,** *56* (4), 3612-3622.
9. Gilje, S.; Han, S.; Wang, M.; Wang, K. L.; Kaner, R. B., *Nano Letters* **2007,** *7* (11), 3394-3398.
10. Stankovich, S.; Dikin, D. A.; Dommett, G. H. B.; Kohlhaas, K. M.; Zimney, E. J.; Stach, E. A.; Piner, R. D.; Nguyen, S. T.; Ruoff, R. S., *Nature* **2006,** *442* (7100), 282-286.
11. Stankovich, S.; Piner, R. D.; Chen, X. Q.; Wu, N. Q.; Nguyen, S. T.; Ruoff, R. S., *J Mater Chem* **2006,** *16* (2), 155-158.
12. Stankovich, S.; Dikin, D. A.; Piner, R. D.; Kohlhaas, K. A.; Kleinhammes, A.; Jia, Y.; Wu, Y.; Nguyen, S. T.; Ruoff, R. S., *Carbon* **2007,** *45* (7), 1558-1565.
13. Wu, J. S.; Pisula, W.; Mullen, K. *Chem Rev* **2007,** *107* (3), 718-747.
14. Schwierz, F., Graphene transistors. *Nat Nanotechnol* **2010,** *5* (7), 487-496.
15. Rutter, G. M.; Crain, J. N.; Guisinger, N. P.; Li, T.; First, P. N.; Stroscio, J. A., *Science* **2007,** *317* (5835), 219-222.
16. Pedersen, T. G.; Flindt, C.; Pedersen, J.; Mortensen, N. A.; Jauho, A. P.; Pedersen, K., *Phys Rev Lett* **2008,** *100* (13).
17. Cortijo, A.; Vomediano, M. A. H., *Nucl Phys B* **2007,** *763* (3), 293-308.
18. Araujo, P. T.; Terrones, M.; Dresselhaus, M. S., *Mater Today* **2012,** *15* (3), 98-109.

19. Banhart, F.; Kotakoski, J.; Krasheninnikov, A. V.,. *Acs Nano* **2011,** *5* (1), 26-41.

20. Liu, L. L.; Qing, M. Q.; Wang, Y. B.; Chen, S. M.,. *J Mater Sci Technol* **2015,** *31* (6), 599-606.

21. Jing, N. N.; Xue, Q. Z.; Ling, C. C.; Shan, M. X.; Zhang, T.; Zhou, X. Y.; Jiao, Z. Y., *Rsc Adv* **2012,** *2* (24), 9124-9129.

22. Mortazavi, B.; Ahzi, S., *Carbon* **2013,** *63*, 460-470.

23. Henderson, M. A., *Surface Science* **1999,** *419*, 174-187.

24. Stone, A. J.; Wales, D. J., *Chem Phys Lett* **1986,** *128* (5-6), 501-503.

25. Savin, A. V.; Kivshar, Y. S., *Physical Review B* **2013,** *88* (12).

26. Ugeda, M. M.; Brihuega, I.; Guinea, F.; Gomez-Rodriguez, J. M., *Phys Rev Lett* **2010,** *104* (9).

27. Gass, M. H.; Bangert, U.; Bleloch, A. L.; Wang, P.; Nair, R. R.; Geim, A. K., *Nat Nanotechnol* **2008,** *3* (11), 676-681.

28. Meyer, J. C.; Kisielowski, C.; Erni, R.; Rossell, M. D.; Crommie, M. F.; Zettl, A., *Nano Lett* **2008,** *8* (11), 3582-3586.

29. Huang, P. Y.; Ruiz-Vargas, C. S.; van der Zande, A. M.; Whitney, W. S.; Levendorf, M. P.; Kevek, J. W.; Garg, S.; Alden, J. S.; Hustedt, C. J.; Zhu, Y.; Park, J.; McEuen, P. L.; Muller, D. A., *Nature* **2011,** *469* (7330), 389-+.

30. Yazyev, O. V.; Louie, S. G., *Phys Rev B* **2010,** *81* (19).

31. Lahiri, J.; Lin, Y.; Bozkurt, P.; Oleynik, I. I.; Batzill, M., *Nat Nanotechnol* **2010,** *5* (5), 326-329.

32. Yazyev, O. V.; Louie, S. G., *Nature Materials* **2010,** *9* (10), 806-809.

33. Kotakoski, J.; Mangler, C.; Meyer, J. C. *Nat Commun* **2014,** *5*.

34. Kotakoski, J.; Krasheninnikov, A. V.; Kaiser, U.; Meyer, J. C., From Point Carbon. *Phys Rev Lett* **2011,** *106* (10).

35. Blanc, N.; Jean, F.; Krasheninnikov, A. V.; Renaud, G.; Coraux, J., *Phys Rev Lett* **2013,** *111* (8).

36. Robertson, A. W.; Montanari, B.; He, K.; Allen, C. S.; Wu, Y. A.; Harrison, N. M.; Kirkland, A. I.; Warner, J. H., *Acs Nano* **2013,** *7* (5), 4495-4502.

37. Moktadir, Z.; Hang, S.; Mizuta, H.,. *Carbon* **2015,** *93*, 325-334.

38. Stauber, T.; Peres, N. M. R.; Guinea, F., *Phys Rev B* **2007,** *76* (20).

39. Hentschel, M.; Guinea, F., *Phys Rev B* **2007,** *76* (11).

40. Eizenberg, M.; Blakely, J. M., C *Surf Sci* **1979,** *82* (1), 228-236.

41. Reina, A.; Jia, X. T.; Ho, J.; Nezich, D.; Son, H. B.; Bulovic, V.; Dresselhaus, M. S.; Kong, J., Large Area, Few-Layer *Nano Lett* **2009,** *9* (1), 30-35.

42. Berger, C.; Song, Z. M.; Li, X. B.; Wu, X. S.; Brown, N.; Naud, C.; Mayou, D.; Li, T. B.; Hass, J.; Marchenkov, A. N.; Conrad, E. H.; First, P. N.; de Heer, W. A., *Science* **2006,** *312* (5777), 1191-1196.

43. Chen, J. H.; Cullen, W. G.; Jang, C.; Fuhrer, M. S.; Williams, E. D., *Phys Rev Lett* **2009,** *102* (23).

44. Wang, C. L.; Dong, H. L.; Hu, W. P.; Liu, Y. Q.; Zhu, D. B., A Material Odyssey of Organic Electronics. *Chem Rev* **2012,** *112* (4), 2208-2267.

45. Dong, H. L.; Zhu, H. F.; Meng, Q.; Gong, X.; Hu, W. P., O*Chem Soc Rev* **2012,** *41* (5), 1754-1808.

46. Jiang, W.; Li, Y.; Wang, Z. H.,. *Accounts Chem Res* **2014,** *47* (10), 3135-3147.

47. Shi, K.; Lei, T.; Wang, X. Y.; Wang, J. Y.; Pei, J., *Chem Sci* **2014,** *5* (3), 1041-1045.

48. Mei, J. G.; Diao, Y.; Appleton, A. L.; Fang, L.; Bao, Z. N., *J Am Chem Soc* **2013,** *135* (18), 6724-6746.

49. Chase, D. T.; Rose, B. D.; McClintock, S. P.; Zakharov, L. N.; Haley, M. M., *Angew Chem Int Edit* **2011,** *50* (5), 1127-1130.

50. Fix, A. G.; Deal, P. E.; Vonnegut, C. L.; Rose, B. D.; Zakharov, L. N.; Haley, M. M., *Org Lett* **2013,** *15* (6), 1362-1365.

51. London, G.; Rekowski, M. V.; Dumele, O.; Schweizer, W. B.; Gisselbrecht, J. P.; Boudon, C.; Diederich, F., *Chem Sci* **2014,** *5* (3), 965-972.

52. Martin, N.; Scott, L. *Chem Soc Rev* **2015,** *44* (18), 6397-6400.

53. Kroto, H. W.; Heath, J. R.; Obrien, S. C.; Curl, R. F.; Smalley, R. E.,. *Nature* **1985,** *318* (6042), 162-163.

54. Iijima, S., Helical Microtubules of Graphitic Carbon. *Nature* **1991,** *354* (6348), 56-58.

55. Xiao, W.; Passerone, D.; Ruffieux, P.; Ait-Mansour, K.; Groning, O.; Tosatti, E.; Siegel, J. S.; Fasel, R., *J Am Chem Soc* **2008,** *130* (14), 4767-71.

56. Takeda, M.; Hiroto, S.; Yokoi, H.; Lee, S.; Kim, D.; Shinokubo, H., *J Am Chem Soc* **2018,** *140* (20), 6336-6342.

57. Kanagaraj, K.; Lin, K. J.; Wu, W. H.; Gao, G. W.; Zhong, Z. H.; Su, D.; Yang, *Symmetry-Basel* **2017,** *9* (9).

58. Arnaya, T.; Seki, S.; Moriuchi, T.; Nakamoto, K.; Nakata, T.; Sakane, H.; Saeki, A.; Tagawa, S.; Hirao, T., *J Am Chem Soc* **2009,** *131* (2), 408-+.

59. Schmidt, B. M.; Seki, S.; Topolinski, B.; Ohkubo, K.; Fukuzumi, S.; Sakurai, H.; Lentz, D., *Angew Chem Int Ed Engl* **2012,** *51* (45), 11385-8.

60. Jackson, E. A.; Steinberg, B. D.; Bancu, M.; Wakamiya, A.; Scott, L. T., *J Am Chem Soc* **2007,** *129* (3), 484-485.

61. Steinberg, B. D.; Jackson, E. A.; Filatov, A. S.; Wakamiya, A.; Petrukhina, M. A.; Scott, L. T.,. *J Am Chem Soc* **2009,** *131* (30), 10537-10545.

62. Amaya, T.; Ito, T.; Hirao, T., *Angew Chem Int Edit* **2015,** *54* (18), 5483-5487.

63. Mebs, S.; Weber, M.; Luger, P.; Schmidt, B. M.; Sakurai, H.; Higashibayashi, S.; Onogi, S.; Lentz, D., *Org Biomol Chem* **2012,** *10* (11), 2218-2222.

64. Faust, R., Fullerene Model Compounds -*Angewandte Chemie-International Edition in English* **1995,** *34* (13-14), 1429-1432.

65. Frash, M. V.; Hopkinson, A. C.; Bohme, D. K., Corannulene as a Lewis base: *J Am Chem Soc* **2001,** *123* (27), 6687-6695.

66. Vijay, D.; Sakurai, H.; Subramanian, V.; Sastry, G. N., *Phys Chem Chem Phys* **2012,** *14* (9), 3057-3065.

67. Scanlon, L. G.; Balbuena, P. B.; Zhang, Y.; Sandi, G.; Back, C. K.; Feld, W. A.; Mack, J.; Rottmayer, M. A.; Riepenhoffl, J. L., *J Phys Chem B* **2006,** *110* (15), 7688-7694.

68. Okamoto, T.; Nakahara, K.; Saeki, A.; Seki, S.; Oh, J. H.; Akkerman, H. B.; Bao, Z. N.; Matsuo, Y., A*Chem Mater* **2011,** *23* (7), 1646-1649.

69. Wu, H. W.; Zhao, P.; Li, X.; Chen, W. B.; Agren, H.; Zhang, Q.; Zhu, L. L., *Acs Appl Mater Inter* **2017,** *9* (4), 3865-3872.

70. Barth, W. E.; Lawton, R. G., Dibenzo[Ghi,Mno]Fluoranthene. *J Am Chem Soc* **1966,** *88* (2), 380-&.

71. Barth, W. E.; Lawton, R. G., Synthesis of Corannulene. *J Am Chem Soc* **1971,** *93* (7), 1730-&.

72. Amaya, T.; Hirao, T., *Pure Appl Chem* **2012,** *84* (4), 1089-1100.

73. Stabel, A.; Herwig, P.; Mullen, K.; Rabe, J. P., *Angewandte Chemie-International Edition in English* **1995,** *34* (15), 1609-1611.

74. Rieger, R.; Mullen, K., *J Phys Org Chem* **2010,** *23* (4), 315-325.

75. Iyer, V. S.; Wehmeier, M.; Brand, J. D.; Keegstra, M. A.; Mullen, K.,. *Angewandte Chemie-International Edition in English* **1997,** *36* (15), 1604-1607.

76. Simpson, C. D.; Brand, J. D.; Berresheim, A. J.; Przybilla, L.; Rader, H. J.; Mullen, K., *Chem-Eur J* **2002,** *8* (6), 1424-1429.

77. Yang, W. L.; Monteiro, J. H. S. K.; de Bettencourt-Dias, A.; Catalano, V. J.; Chalifoux, W. A., *Angew Chem Int Edit* **2016,** *55* (35), 10427-10430.

78. Echavarren, A. M.; Gomez-Lor, B.; Gonzalez, J. J.; de Frutos, O., *Synlett* **2003,** (5), 585-597.

79. Sato, T.; Shimada, S.; Hata, K.,. *J Chem Soc Chem Comm* **1970,** (12), 766-&.

80. Sato, T.; Shimada, S.; Hata, K., *B Chem Soc Jpn* **1971,** *44* (9), 2484-+.

81. Daigle, M.; Picard-Lafond, A.; Soligo, E.; Morin, J. F., *Angew Chem Int Edit* **2016,** *55* (6), 2042-2047.

82. Miyaura, N.; Yanagi, T.; Suzuki, A., *Synthetic Commun* **1981,** *11* (7), 513-519.

83. Stille, J. K., *Angewandte Chemie-International Edition in English* **1986,** *25* (6), 508-523.

84. Hatanaka, Y.; Hiyama, T., *J Org Chem* **1988,** *53* (4), 918-920.

85. Tamao, K.; Sumitani, K.; Kumada, M., *J Am Chem Soc* **1972,** *94* (12), 4374-&.

86. Negishi, E.; King, A. O.; Okukado, N., *J Org Chem* **1977,** *42* (10), 1821-1823.

87. Mallory, F. B.; Gordon, J. T.; Wood, C. S.; Lindquist, L. C.; Savitz, M. L., Photochemistry of Stilbenes .1. *J Am Chem Soc* **1962,** *84* (22), 4361-&.

88. Mallory, F. B.; Wood, C. S.; Gordon, J. T., *J Am Chem Soc* **1964,** *86* (15), 3094-&.

89. Shen, Y.; Chen, C. F., *Chem Rev* **2012,** *112* (3), 1463-1535.

90. Ito, H.; Segawa, Y.; Murakami, K.; Itami, K., *J Am Chem Soc* **2019,** *141* (1), 3-10.

91. Amsharov, K. Y.; Merz, P.,. *J Org Chem* **2012,** *77* (12), 5445-5448.

92. Amsharov, K. Y.; Kabdulov, M. A.; Jansen, M.,. *Angew Chem Int Edit* **2012,** *51* (19), 4594-4597.

93. Löwe, J., *Z Chemie* **1868**, 603-304.

94. Weitzenböck, R. S. C. S. R., *Ber. Dtsch. Chem. Ges* **1910,** *43*, 1734–1746.

95. Grzybowski, M.; Sadowski, B.; Butenschon, H.; Gryko, D. T., *Angew Chem Int Edit* **2020,** *59* (8), 2998-3027.

96. Buchta, E.; Bosche, J., *Liebigs Ann Chem* **1962,** *660* (Dec), 33-+.

97. Avlasevich, Y.; Kohl, C.; Mullen, K., *J Mater Chem* **2006,** *16* (11), 1053-1057.

98. Grzybowski, M.; Skonieczny, K.; Butenschon, H.; Gryko, D. T., *Angewandte Chemie-International Edition* **2013,** *52* (38), 9900-9930.

99. Agranat, I.; Oded, Y. N.; Mala'bi, T.; Pogodin, S.; Cohen, S., *Struct Chem* **2019,** *30* (5), 1579-1610.

100. Nagarajan, S.; Barthes, C.; Girdhar, N. K.; Dang, T. T.; Gourdon, A., *Tetrahedron* **2012,** *68* (46), 9371-9375.

101. Horibe, T.; Ohmura, S.; Ishihara, K., *J Am Chem Soc* **2019,** *141* (5), 1877-1881.

102. Sarhan, A. A. O.; Bolm, C., *Chem Soc Rev* **2009,** *38* (9), 2730-2744.

103. Zhai, L. Y.; Shukla, R.; Wadumethrige, S. H.; Rathore, R., *J Org Chem* **2010,** *75* (14), 4748-4760.

104. Ding, K. L.; Xu, G. G.; Wang, Y.; Liu, J. X.; Yu, Z. Y.; Du, B. S.; Wu, Y. J.; Koshima, H.; Matsuura, T., N. *Chem Commun* **1997,** (18), 1815-1815.

105. Ding, K. L.; Wang, Y.; Zhang, L. J.; Wu, Y. J.; Matsuura, T., *Tetrahedron* **1996,** *52* (3), 1005-1010.

106. A. Zinke and R. Dengg, *Monatsh. Chem.* **1922,** *43*, 125-128.

107. Berresheim, A. J.; Muller, M.; Mullen, K., *Chem Rev* **1999,** *99* (7), 1747-1785.

108. Watson, M. D.; Fechtenkotter, A.; Mullen, K., *Chem Rev* **2001,** *101* (5), 1267-1300.

109. Narita, A.; Wang, X. Y.; Feng, X. L.; Mullen, K., *Chem Soc Rev* **2015,** *44* (18), 6616-6643.

110. Stepien, M.; Gonka, E.; Zyla, M.; Sprutta, N., H*Chem Rev* **2017,** *117* (4), 3479-3716.

111. Hammerich, O.; Parker, V. D., *Adv Phys Org Chem* **1984,** *20*, 55-189.

112. Chaolumen; Murata, M.; Wakamiya, A.; Murata, Y., *Chem Lett* **2017,** *46* (4), 591-593.

113. Alameddine, B.; Anju, R. S.; Shetty, S.; Baig, N.; Al-Mousawi, S.; Al-Sagheer, F., *J Polym Sci Pol Chem* **2017,** *55* (21), 3565-3572.

114. Zhao, J.; Xu, Z. Q.; Oniwa, K.; Asao, N.; Yamamoto, Y.; Jin, T. N., **2016,** *55* (1), 259-263.

115. Fujikawa, T.; Mitoma, N.; Wakamiya, A.; Saeki, A.; Segawa, Y.; Itami, K., *Org Biomol Chem* **2017,** *15* (21), 4697-4703.

116. Schubert, M.; Franzmann, P.; von Leupoldt, A. W.; Koszinowski, K.; Heinze, K.; Waldvogel, S. R., *Angew Chem Int Edit* **2016,** *55* (3), 1156-1159.

117. Oded, Y. N.; Pogodin, S.; Agranat, I.,. *J Org Chem* **2016,** *81* (22), 11389-11393.

118. Fujikawa, T.; Segawa, Y.; Itami, K., S. *J Am Chem Soc* **2015,** *137* (24), 7763-7768.

119. Little, M. S.; Yeates, S. G.; Alwattar, A. A.; Heard, K. W. J.; Raftery, J.; Edwards, A. C.; Parry, A. V. S.; Quayle, P.,. *Eur J Org Chem* **2017,** *2017* (13), 1694-1703.

120. Nobusue, S.; Fujita, K.; Tobe, Y.,. *Org Lett* **2017,** *19* (12), 3227-3230.

121. King, B. T.; Kroulik, J.; Robertson, C. R.; Rempala, P.; Hilton, C. L.; Korinek, J. D.; Gortari, L. M., Controlling the Scholl reaction. *J Org Chem* **2007,** *72* (7), 2279-2288.

122. Ormsby, J. L.; Black, T. D.; Hilton, C. L.; Kumar, B.; King, B. T.,. *Tetrahedron* **2008,** *64* (50), 11370-11378.

123. Terrones, H.; Lv, R. T.; Terrones, M.; Dresselhaus, M. S.. *Rep Prog Phys* **2012,** *75* (6).

124. Liu, J. Z.; Narita, A.; Osella, S.; Zhang, W.; Schollmeyer, D.; Beljonne, D.; Feng, X. L.; Mullen, K.,. *J Am Chem Soc* **2016,** *138* (8), 2602-2608.

125. Chaolumen; Murata, M.; Wakamiya, A.; Murata, Y., U. *Angew Chem Int Edit* **2017,** *56* (18), 5082-5086.

126. Scott, L. T., *Pure Appl Chem* **1996,** *68* (2), 291-300.

127. Tsefrikas, V. M.; Scott, L. T., *Chem Rev* **2006,** *106* (12), 4868-4884.

128. Wu, Y. T.; Siegel, J. S., *Chem Rev* **2006,** *106* (12), 4843-4867.

129. Wu, Y. T.; Wu, T. C.; Chen, M. K.; Hsin, H. J., *Pure Appl Chem* **2014,** *86* (4), 539-544.

130. Tan, Q.; Higashibayashi, S.; Karanjit, S.; Sakurai, H.,. *Nat Commun* **2012,** *3*.

131. Juricek, M.; Strutt, N. L.; Barnes, J. C.; Butterfield, A. M.; Dale, E. J.; Baldridge, K. K.; Stoddart, F.; Siegel, J. S., *Nat Chem* **2014,** *6* (3), 222-228.

132. Xiao, W.; Passerone, D.; Ruffieux, P.; Ait-Mansour, K.; Groning, O.; Tosatti, E.; Siegel, J. S.; Fasel, R., *J Am Chem Soc* **2008,** *130* (14), 4767-4771.

133. Stockl, Q.; Bandera, D.; Kaplan, C. S.; Ernst, K. H.; Siegel, J. S., *J Am Chem Soc* **2014,** *136* (2), 606-9.

134. Higashibayashi, S.; Sakurai, H., *J Am Chem Soc* **2008,** *130* (27), 8592-+.

135. Bandera, D.; Baldridge, K. K.; Linden, A.; Dorta, R.; Siegel, J. S., *Angew Chem Int Ed Engl* **2011,** *50* (4), 865-7.

136. Liu, J. Z.; Ma, J.; Zhang, K.; Ravat, P.; Machata, P.; Avdoshenko, S.; Hennersdorf, F.; Komber, H.; Pisula, W.; Weigand, J. J.; Popov, A. A.; Berger, R.; Mullen, K.; Feng, X. L., *J Am Chem Soc* **2017,** *139* (22), 7513-7521.

137. Di Giovannantonio, M.; Urgel, J. I.; Beser, U.; Yakutovich, A. V.; Wilhelm, J.; Pignedoli, C. A.; Ruffieux, P.; Narita, A.; Mullen, K.; Fasel, R., *J Am Chem Soc* **2018,** *140* (10), 3532-3536.

138. Pradhan, A.; Dechambenoit, P.; Bock, H.; Durola, F.,. *J Org Chem* **2013,** *78* (6), 2266-2274.

139. Kawasumi, K.; Zhang, Q. Y.; Segawa, Y.; Scott, L. T.; Itami, K., *Nat Chem* **2013,** *5* (9), 739-744.

140. Mughal, E. U.; Kuck, D., *Chem Commun* **2012,** *48* (71), 8880-8882.

141. Mughal, E. U.; Kuck, D.,. *Org Biomol Chem* **2010,** *8* (23), 5383-5389.

142. Fernandez-Garcia, J. M.; Evans, P. J.; Rivero, S. M.; Fernandez, I.; Garcia-Fresnadillo, D.; Perles, J.; Casado, J.; Martin, N., *J Am Chem Soc* **2018,** *140* (49), 17188-17196.

143. Tellenbroker, J.; Kuck, D., *Angew Chem Int Edit* **1999,** *38* (7), 919-922.

144. Dhara, A.; Beuerle, F., *Synthesis-Stuttgart* **2018,** *50* (15), 2867-2877.

145. Kuck, D.,. *Angewandte Chemie-International Edition in English* **1984,** *23* (7), 508-509.

146. Kuck, D.; Lindenthal, T.; Schuster, *Chemische Berichte-Recueil* **1992,** *125* (6), 1449-1460.

147. Markopoulos, G.; Henneicke, L.; Shen, J.; Okamoto, Y.; Jones, P. G.; Hopf, H., Tribenzotriquinacene. *Angew Chem Int Edit* **2012,** *51* (51), 12884-12887.

148. Kuck, D.; Schuster, A.; Krause, R. A.; Tellenbroker, J.; Exner, C. P.; Penk, M.; Bogge, H.; Muller, *Tetrahedron* **2001,** *57* (17), 3587-3613.

149. Brandenburg, J. G.; Grimme, S.; Jones, P. G.; Markopoulos, G.; Hopf, H.; Cyranski, M. K.; Kuck, D., U. *Chem-Eur J* **2013,** *19* (30), 9930-9938.

150. Beuerle, F.; Gole, B.,. *Angew Chem Int Edit* **2018,** *57* (18), 4850-4878.

151. Tellenbroker, J.; Kuck, D., . *Beilstein J Org Chem* **2011,** *7*, 329-337.

152. Kuck, D.,. *Pure Appl Chem* **2006,** *78* (4), 749-775.

153. Beaudoin, D.; Rominger, F.; Mastalerz, M., *Synthesis-Stuttgart* **2015,** *47* (24), 3846-3848.

154. Zhou, L.; Zhang, T. X.; Li, B. R.; Cao, X. P.; Kuck, D., *J Org Chem* **2007,** *72* (17), 6382-6389.

155. Linke, J.; Bader, N.; Tellenbroker, J.; Kuck, D., *Synthesis-Stuttgart* **2018,** *50* (1), 175-183.

156. Bredenkotter, B.; Henne, S.; Volkmer, D., *Chemistry* **2007,** *13* (35), 9931-8.

157. Bredenkotter, B.; Grzywa, M.; Alaghemandi, M.; Schmid, R.; Herrebout, W.; Bultinck, P.; Volkmer, D., *Chem-Eur J* **2014,** *20* (29), 9100-9110.

158. Henne, S.; Bredenkotter, B.; Baghi, A. A. D.; Schmid, R.; Volkmer, D. *Dalton T* **2012,** *41* (19), 5995-6002.

159. Wang, T.; Li, Z. Y.; Xie, A. L.; Yao, X. J.; Cao, X. P.; Kuck, D., *J Org Chem* **2011,** *76* (9), 3231-3238.

160. Liu, S. Y.; Wang, X. R.; Li, M. P.; Xu, W. R.; Kuck, D., *Beilstein J Org Chem* **2020,** *16*, 2551-2561.

161. Li, Z. M.; Hu, D.; Wei, J.; Qi, Q. L.; Cao, X. P.; Chow, H. F.; Kuck, D., *Synthesis-Stuttgart* **2018,** *50* (7), 1457-1461.

162. Wang, T.; Hou, Q. Q.; Teng, Q. F.; Yao, X. J.; Niu, W. X.; Cao, X. P.; Kuck, D., *Chem-Eur J* **2010,** *16* (41), 12412-12424.

163. Zhang, Y. F.; Cao, X. P.; Chow, H. F.; Kuck, D., *J Org Chem* **2017,** *82* (1), 179-187.

164. Ng, C. F.; Chow, H. F.; Kuck, D.; Mak, T. C. W., *Cryst Growth Des* **2017,** *17* (5), 2822-2827.

165. Klotzbach, S.; Beuerle, F.,. *Abstr Pap Am Chem S* **2014,** *248*.

166. Klotzbach, S.; Scherpf, T.; Beuerle, F., *Chem Commun* **2014,** *50* (83), 12454-12457.

167. Leonhardt, V.; Fimmel, S.; Krause, A. M.; Beuerle, F., *Chem Sci* **2020,** *11* (32), 8409-8415.

168. Kirchwehm, Y.; Damme, A.; Kupfer, T.; Braunschweig, H.; Krueger, A.,. *Chem Commun* **2012,** *48* (10), 1502-1504.

169. Dhara, A.; Weinmann, J.; Krause, A. M.; Beuerle, F., *Chemistry-a European Journal* **2016,** *22* (35), 12473-12478.

170. Mughal, E. U.; Neumann, B.; Stammler, H. G.; Kuck, D.. *Eur J Org Chem* **2014,** *2014* (33), 7469-7480.

171. Ip, H. W.; Ng, C. F.; Chow, H. F.; Kuck, D.,. *J Am Chem Soc* **2016,** *138* (42), 13778-13781.

172. He, L. S.; Ng, C. F.; Li, Y. K.; Liu, Z. F.; Kuck, D.; Chow, H. F.,. *Angew Chem Int Edit* **2018,** *57* (41), 13635-13639.

173. Ho-Wang Ip, Y. L., Dietmar Kuck, and Hak-Fun Chow,. *The Journal of Organic Chemistry* **2021,** *86*, 5546-5551.

174. Mishra, S.; Beyer, D.; Eimre, K.; Liu, J. Z.; Berger, R.; Groning, O.; Pignedoli, C. A.; Mullen, K.; Fasel, R.; Feng, X. L.; Ruffieux, P., *Journal of the American Chemical Society* **2019,** *141* (27), 10621-10625.

175. Berliner, M. A.; Belecki, K., *J Org Chem* **2005,** *70* (23), 9618-9621.

176. Selvakumar, K.; Lingam, K. A. P.; Varma, R. V. L.,. *Rsc Adv* **2014,** *4* (69), 36538-36543.

177. Hofle, G.; Steglich, W.; Vorbruggen, H., *Angew Chem Int Edit* **1978,** *17* (8), 569-&.

178. Tellenbröker, J., Ph.D. Thesis. *University of Bielefeld* **1999**.

179. Zhou, Y.; Liu, W. J.; Zhang, W.; Cao, X. Y.; Zhou, Q. F.; Ma, Y. G.; Pei, J., *J Org Chem* **2006,** *71* (18), 6822-6828.

180. Rempala, P.; Kroulik, J.; King, B. T.,. *J Org Chem* **2006,** *71* (14), 5067-5081.

181. Zhai, L. Y.; Shukla, R.; Rathore, R., *Organic Letters* **2009,** *11* (15), 3474-3477.

182. Buschmann, R.. University of Wuerzburg, 2019.

183. Ip, H. W.; Chow, H. F.; Kuck, D., *Org Chem Front* **2017,** *4* (5), 817-822.

184. Buschmann, R.. Universität Würzburg, Wuerzburg, 2019.

185. Reinhard, D.; Rominger, F.; Mastalerz, M., *J Org Chem* **2015,** *80* (18), 9342-9348.

186. Rathore, R.; Kochi, J. K., *Acta Chem Scand* **1998,** *52* (1), 114-130.

187. Rathore, R.; Zhu, C. J.; Lindeman, S. V.; Kochi, J. K., *J Chem Soc Perk T 2* **2000,** (9), 1837-1840.

188. Handoo, K. L.; Gadru, K.,. *Curr Sci India* **1986,** *55* (18), 920-922.

189. Eberson, L.; Hartshorn, M. P.; Persson, O., *J Chem Soc Perk T 2* **1997,** (2), 195-201.

190. Wang, X. Y.; Yao, X. L.; Mullen, K., *Sci China Chem* **2019,** *62* (9), 1099-1144.

191. Binnig, G.; Rohrer, H.; Gerber, C.; Weibel, E., 7*Phys Rev Lett* **1983,** *50* (2), 120-123.

192. Binning, G.; Rohrer, H.; Gerber, C.; Weibel, E., Surface Studies by Scanning Tunneling Microscopy. *Phys Rev Lett* **1982,** *49* (1), 57-61.

193.Schmid,M.https://www.iap.tuwien.ac.at/www/surface/stm_gallery/stm_schematic.

194. Chen, C. J., *Introduction to Scanning Tunneling Microscopy*. Second Edition ed.; 1993; p 488.

195. Bai, C., *Scanning Tunneling Microsocpy and Its applications*. Springer Series in Surface Science: 2000.

196. Pandelov, S. Investigation of the structure and reactivity of nanostructured surfaces Technische Universität München, 2007.

197. Barth, J. V.; Weckesser, J.; Cai, C. Z.; Gunter, P.; Burgi, L.; Jeandupeux, O.; Kern, K., *Angew Chem Int Edit* **2000,** *39* (7), 1230-+.

198. Llanes-Pallas, A.; Matena, M.; Jung, T.; Prato, M.; Stohr, M.; Bonifazi, D., *Angew Chem Int Edit* **2008,** *47* (40), 7726-7730.

199. Otero, R.; Schock, M.; Molina, L. M.; Laegsgaard, E.; Stensgaard, I.; Hammer, B.; Besenbacher, F., *Abstr Pap Am Chem S* **2005,** *229*, U772-U772.

200. Wintjes, N.; Hornung, J.; Lobo-Checa, J.; Voigt, T.; Samuely, T.; Thilgen, C.; Stohr, M.; Diederich, F.; Jung, T. A., Su*Chem-Eur J* **2008,** *14* (19), 5794-5802.

201. Yokoyama, T.; Yokoyama, S.; Kamikado, T.; Okuno, Y.; Mashiko, S., *Nature* **2001,** *413* (6856), 619-621.

202. Lei, S.; Surin, M.; Tahara, K.; Adisoejoso, J.; Lazzaroni, R.; Tobe, Y.; De Feyter, S., *Nano Lett* **2008,** *8* (8), 2541-2546.

203. Langner, A.; Tait, S. L.; Lin, N. A.; Chandrasekar, R.; Meded, V.; Fink, K.; Ruben, M.; Kern, K., *Angew Chem Int Edit* **2012,** *51* (18), 4327-4331.

204. Barth, J. V., *Surf Sci* **2009,** *603* (10-12), 1533-1541.

205. Elemans, J. A. A. W.; Lei, S. B.; De Feyter, S., *Angew Chem Int Edit* **2009,** *48* (40), 7298-7332.

206. Otero, R.; Gallego, J. M.; de Parga, A. L. V.; Martin, N.; Miranda, R., Molecular. *Adv Mater* **2011,** *23* (44), 5148-5176.

207. Rohrer, H., *Surf Sci* **1994,** *299* (1-3), 956-964.

208. Besenbacher, F., *Rep Prog Phys* **1996,** *59* (12), 1737-1802.

209. Rosei, F.; Rosei, R.,. *Surf Sci* **2002,** *500* (1-3), 395-413.

210. Voigtlander, B., *Surf Sci Rep* **2001,** *43* (5-8), 127-+.

211. Hla, S. W.; Meyer, G.; Rieder, K. H.,. *Chem Phys Lett* **2003,** *370* (3-4), 431-436.

212. Kaiser, K.; Scriven, L. M.; Schulz, F.; Gawel, P.; Gross, L.; Anderson, H. L., *Science* **2019,** *365* (6459), 1299-+.

213. Grill, L.; Dyer, M.; Lafferentz, L.; Persson, M.; Peters, M. V.; Hecht, S., *Nat Nanotechnol* **2007,** *2* (11), 687-691.

214. Ho, W., Single-molecule chemistry. *J Chem Phys* **2002,** *117* (24), 11033-11061.

215. Li, Q. L.; Cao, R. X.; Ding, H. F.,. *Appl Phys Lett* **2020,** *117* (6).

216. Gustafsson, A.; Paulsson, M., *J Phys-Condens Mat* **2017,** *29* (50).

217. Barth, J. V., *Annu Rev Phys Chem* **2007,** *58*, 375-407.

218. Weckesser, J.; Barth, J. V.; Kern, K., M*Phys Rev B* **2001,** *64* (16).

219. Weckesser, J.; Barth, J. V.; Kern, K., *J Chem Phys* **1999,** *110* (11), 5351-5354.

220. Schunack, M.; Linderoth, T. R.; Rosei, F.; Laegsgaard, E.; Stensgaard, I.; Besenbacher, F., *Phys Rev Lett* **2002,** *88* (15).

221. Lauhon, L. J.; Ho, W., *J Chem Phys* **1999,** *111* (13), 5633-5636.

222. Goronzy, D. P.; Ebrahim, M.; Rosei, F.; Arramel; Fang, Y.; De Feyter, S.; Tait, S. L.; Wang, C.; Beton, P. H.; Wee, A. T. S.; Weiss, P. S.; Perepichka, D. F., *Acs Nano* **2018,** *12* (8), 7445-7481.

223. Steed, J. A., J., *Supramolecular Chemistry*. John Wiley & Sons: 2013.

224. Steed, J., et al., John Wiley & Sons: 2007.

225. Jung, T. A.; Schlittler, R. R.; Gimzewski, J. K., **1997,** *386* (6626), 696-698.

226. Yokoyama, T.; Yokoyama, S.; Kamikado, T.; Mashiko, S., *J Chem Phys* **2001,** *115* (8), 3814-3818.

227. Xiao, W. D.; Feng, X. L.; Ruffieux, P.; Groning, O.; Mullen, K.; Fasel, R., *J Am Chem Soc* **2008,** *130* (28), 8910-+.

228. Marbach, H.; Steinruck, H. P., *Chem Commun* **2014,** *50* (65), 9034-9048.

229. Ascolani, H.; van der Meijden, M. W.; Cristina, L. J.; Gayone, J. E.; Kellogg, R. M.; Fuhr, J. D.; Lingenfelder, M., *Chem Commun* **2014,** *50* (90), 13907-13909.

230. Gilli, G., Gilli, Paola, Oxford University Press: 2009.

231. Jeffrey, G., Oxford University Press: 1997.

232. Makoudi, Y.; Palmino, F.; Arab, M.; Duverger, E.; Cherioux, F., *J Am Chem Soc* **2008,** *130* (21), 6670-+.

233. Silly, F.; Shaw, A. Q.; Castell, M. R.; Briggs, G. A. D.; Mura, M.; Martsinovich, N.; Kantorovich, L., *J Phys Chem C* **2008,** *112* (30), 11476-11480.

234. van den Brom, C. R.; Arfaoui, I.; Cren, T.; Hessen, B.; Palstra, T. T. M.; De Hosson, J. T. M.; Rudolf, P.,. *Adv Funct Mater* **2007,** *17* (13), 2045-2052.

235. Wasio, N. A.; Quardokus, R. C.; Forrest, R. P.; Lent, C. S.; Corcelli, S. A.; Christie, J. A.; Henderson, K. W.; Kandel, S. *Nature* **2014,** *507* (7490), 86-+.

236. Theobald, J. A.; Oxtoby, N. S.; Phillips, M. A.; Champness, N. R.; Beton, P. H., *Nature* **2003,** *424* (6952), 1029-1031.

237. Steiner, C.; Gliemann, B. D.; Meinhardt, U.; Gurrath, M.; Meyer, B.; Kivala, M.; Maier, S., *J Phys Chem C* **2015,** *119* (46), 25945-25955.

238. Ivasenko, O.; Perepichka, D. F., *Chem Soc Rev* **2011,** *40* (1), 191-206.

239. Lackinger, M.; Heckl, W. M., *Langmuir* **2009,** *25* (19), 11307-11321.

240. MacLeod, J. M.; Ivasenko, O.; Fu, C. Y.; Taerum, T.; Rosei, F.; Perepichka, D. F., *J Am Chem Soc* **2009,** *131* (46), 16844-16850.

241. Metrangolo, P.; Neukirch, H.; Pilati, T.; Resnati, G., Halogen bonding based recognition processes:. *Accounts Chem Res* **2005,** *38* (5), 386-395.

242. Politzer, P.; Murray, J. S.; Clark, T., *Phys Chem Chem Phys* **2010,** *12* (28), 7748-7757.

243. Cavallo, G.; Metrangolo, P.; Milani, R.; Pilati, T.; Priimagi, A.; Resnati, G.; Terraneo, G., The Halogen Bond. *Chem Rev* **2016,** *116* (4), 2478-2601.

244. Kellett, C. W.; Kennepohl, P.; Berlinguette, C. P., *Nat Commun* **2020,** *11* (1).

245. Priimagi, A.; Cavallo, G.; Metrangolo, P.; Resnati, G.,. *Accounts Chem Res* **2013,** *46* (11), 2686-2695.

246. Clark, T.; Hennemann, M.; Murray, J. S.; Politzer, P., *J Mol Model* **2007,** *13* (2), 291-296.

247. Huber, S. M.; Scanlon, J. D.; Jimenez-Izal, E.; Ugalde, J. M.; Infante, I., *Phys Chem Chem Phys* **2013,** *15* (25), 10350-10357.

248. Chung, K. H.; Park, J.; Kim, K. Y.; Yoon, J. K.; Kim, H.; Han, S.; Kahng, S. J., *Chem Commun* **2011,** *47* (41), 11492-11494.

249. Gutzler, R.; Fu, C. Y.; Dadvand, A.; Hua, Y.; MacLeod, J. M.; Rosei, F.; Perepichka, D. F., *Nanoscale* **2012,** *4* (19), 5965-5971.

250. Pham, T. A.; Song, F.; Nguyen, M. T.; Stohr, M.,. *Chem Commun* **2014,** *50* (91), 14089-14092.

251. Yang, Z. C.; Fromm, L.; Sander, T.; Gebhardt, J.; Schaub, T. A.; Gorling, A.; Kivala, M.; Maier, S.,. *Angewandte Chemie-International Edition* **2020,** *59* (24), 9549-9555.

252. E A Moore, R. J., *Metal-Ligand Bonding*. RSC 2004.

253. Dong, L.; Gao, Z. A.; Lin, N., *Prog Surf Sci* **2016,** *91* (3), 101-135.

254. Resendiz, M. J. E.; Noveron, J. C.; Disteldorf, H.; Fischer, S.; Stang, P. J., *Org Lett* **2004,** *6* (5), 651-653.

255. Ahrens, M. J.; Sinks, L. E.; Rybtchinski, B.; Liu, W. H.; Jones, B. A.; Giaimo, J. M.; Gusev, A. V.; Goshe, A. J.; Tiede, D. M.; Wasielewski, M. R., *J Am Chem Soc* **2004,** *126* (26), 8284-8294.

256. Lee, J.; Li, J.; Jagiello, J., *J Solid State Chem* **2005,** *178* (8), 2527-2532.

257. Sumida, K.; Rogow, D. L.; Mason, J. A.; McDonald, T. M.; Bloch, E. D.; Herm, Z. R.; Bae, T. H.; Long, J. R., *Chem Rev* **2012,** *112* (2), 724-781.

258. Uzun, A.; Keskin, S., *Prog Surf Sci* **2014,** *89* (1), 56-79.

259. Messina, P.; Dmitriev, A.; Lin, N.; Spillmann, H.; Abel, M.; Barth, J. V.; Kern, K., *J Am Chem Soc* **2002,** *124* (47), 14000-14001.

260. Spillmann, H.; Dmitriev, A.; Lin, N.; Messina, P.; Barth, J. V.; Kern, K., *J Am Chem Soc* **2003,** *125* (35), 10725-10728.

261. Dmitriev, A.; Spillmann, H.; Lin, N.; Barth, J. V.; Kern, K.,. *Angew Chem Int Edit* **2003,** *42* (23), 2670-2673.

262. Liu, J.; Chen, Q. W.; Xiao, L. H.; Shang, J.; Zhou, X.; Zhang, Y. J.; Wang, Y. F.; Shao, X.; Li, J. L.; Chen, W.; Xu, G. Q.; Tang, H.; Zhao, D. H.; Wu, K., *Acs Nano* **2015,** *9* (6), 6305-6314.

263. Schultz, J. F.; Yang, B.; Jiang, N.,. *J Chem Phys* **2021,** *154* (4).

264. Metrangolo, P.; Resnati, G.; Pilati, T.; Liantonio, R.; Meyer, F., Engineering functional materials by halogen bonding. *J Polym Sci Pol Chem* **2007,** *45* (1), 1-15.

265. Vogt, M.; Buschmann, R.; Toksabay, S.; Schmitt, M.; Schwab, M.; Bode, M.; Krueger, A., *J Phys Chem C* **2019,** *123* (9), 5469-5478.

266. Marcinkowski, M. D.; Darby, M. T.; Liu, J. L.; Wimble, J. M.; Lucci, F. R.; Lee, S.; Michaelides, A.; Flytzani-Stephanopoulos, M.; Stamatakis, M.; Sykes, E. C. H., *Nat Chem* **2018,** *10* (3), 325-332.

267. Chan, Y. L.; Pai, W. W.; Chuang, T. J., *J Phys Chem B* **2004,** *108* (3), 815-818.

268. Pai, W. W.; Chan, Y. L.; Chuang, T. J., *Chinese J Phys* **2005,** *43* (1), 212-218.

269. Yu, H. B.; Webb, L. J.; Ries, R. S.; Solares, S. D.; Goddard, W. A.; Heath, J. R.; Lewis, N. S., *J Phys Chem B* **2005,** *109* (2), 671-674.

270. Schlutter, F.; Rossel, F.; Kivala, M.; Enkelmann, V.; Gisselbrecht, J. P.; Ruffieux, P.; Fasel, R.; Mullen, K.,. *J Am Chem Soc* **2013,** *135* (11), 4550-4557.

271. Bieri, M.; Blankenburg, S.; Kivala, M.; Pignedoli, C. A.; Ruffieux, P.; Mullen, K.; Fasel, R., *Chem Commun* **2011,** *47* (37), 10239-10241.

272. Chuang, T. J.; Chan, Y. L.; Chuang, P.; Klauser, R., *J Electron Spectrosc* **1999,** *98*, 149-173.

273. Lin, J. L.; Bent, B. E., *J Am Chem Soc* **1993,** *115* (7), 2849-2853.

274. Chiang, C. M.; Bent, B. E.,. *Surf Sci* **1992,** *279* (1-2), 79-88.

275. Mosher, W. A.; Soeder, R. W., *J Org Chem* **1971,** *36* (11), 1561-&.

276. Mosher, W. A.; Soeder, R. W., *Chem* **1971,** *8* (5), 855-&.

277. Sheldrick, G. M., SHELXT - Integrated space-group and crystal-structure determination. *Acta Crystallogr A* **2015,** *71*, 3-8.

278. Sheldrick, G. M., A short history of SHELX. *Acta Crystallogr A* **2008,** *64*, 112-122.

279. Hubschle, C. B.; Sheldrick, G. M.; Dittrich, B., ShelXle: a Qt graphical user interface for SHELXL. *J Appl Crystallogr* **2011,** *44*, 1281-1284.

280. Brandenburg, H. P., K, Diamond Version 4.2.0. Crystal and Molecular Structure Visualization, Crystal Impact, Bonn (Germany), 2016. 2016.

8. Appendix

List of Figures

List of Tables

MALDI-TOF Mass spectrum of Me-TBTQ(OAc)$_3$Np$_6$, 96

Comment 1	Sinem Toksabay
Comment 2	ST19_1; Matrix: DCTB 1:3 in Chloroform
Analysis Name	2020_0969_KRU_ST139_1\0_H16\1
File Name	D:\Data\Specs\Spektren2020\2020_0969_KRU_ST139_1\0_H16\1

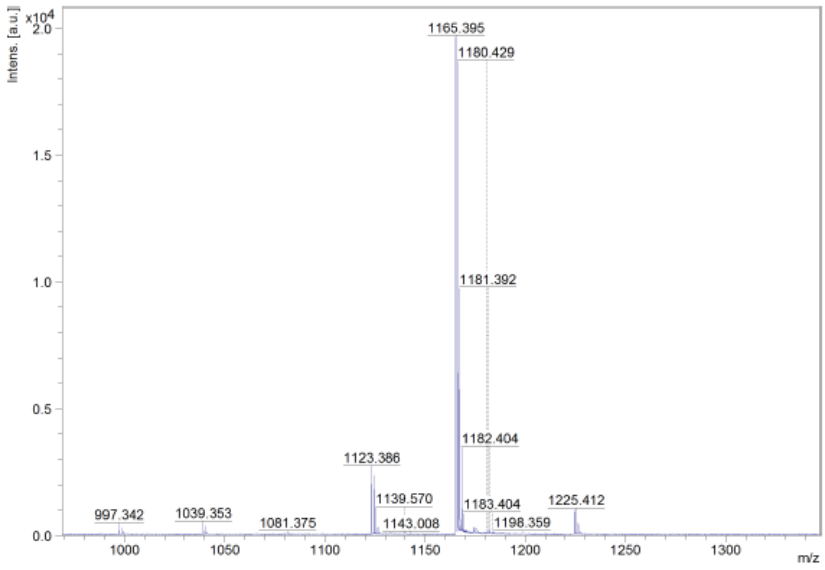

Acquisition Parameter

Spectrometer

positive voltage polarity	POS
PIE delay	140 ns
Ion source voltage 1	20 kV
Ion source voltage 2	17.8 kV
Lens voltage	8 kV
Linear detector voltage	2.909 kV
Deflection on	
Deflection mass	
Reflector voltage 1	20.8 kV
Reflector voltage 2	10.9 kV
Reflector detector volt.	1.985 kV
Acquisition method name	D:\Methods\flexControlMethods\Standard Methods\RP_700-3500_Da.par

Instrument Info

Instrument

Instrument type	ultraflexTOF/TOF
Instrument serial	8275601.00641
Name of computer	UTX-541
Operator ID or name	BDAL@DE
flexControl version	flexControl 3.4.135.7
flexAnalysis version	

Target

Target type	0280784
Target serial number	1004038
Position	H16

^{1}H-NMR Spectrum of of Me-TBTQ(OAc)$_3$Np$_6$, 96

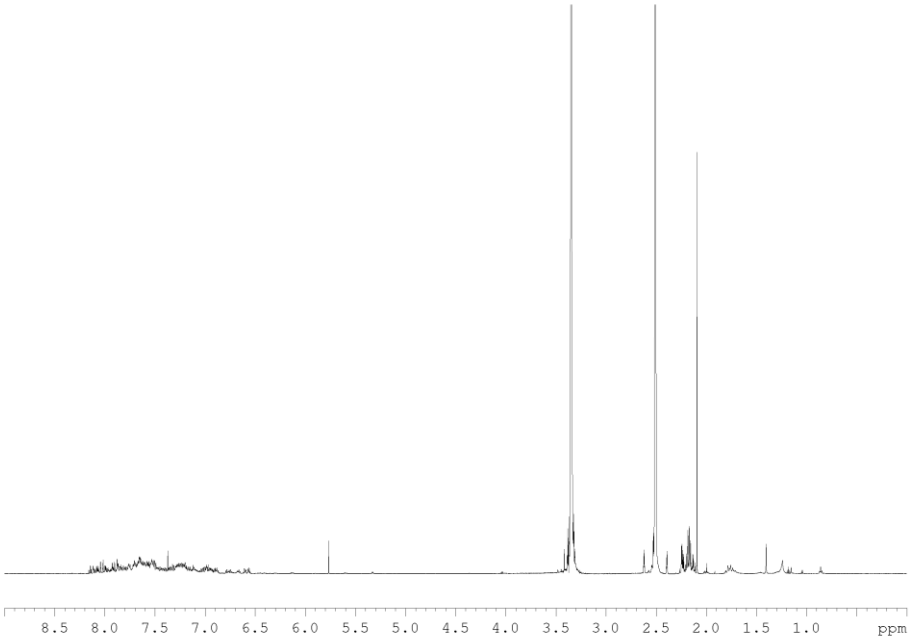

^{13}C-NMR Spectrum of Me-TBTQ(OAc)$_3$Np$_6$, 96